Investigation and Enhancement of Zn-Ce Redox Flow Battery Performance Through Experimental and Modeling Studies

by

Hao Yu

A thesis

presented to the University of Waterloo

in fulfillment of the

thesis requirement for the degree of

Doctor of Philosophy

in

Chemical Engineering

Waterloo, Ontario, Canada, 2025

© Hao Yu 2025

Examining Committee Membership

The following served on the Examining Committee for this thesis. The decision of the Examining Committee is by majority vote.

External Examiner	Prof. Emin Caglan Kumbur Dept. of Mechanical Engineering and Mechanics
Supervisors:	Prof. Mark Pritzker Dept. of Chemical Engineering, University of Waterloo
	Prof. Jeff Gostick Dept. of Chemical Engineering, University of Waterloo
Internal Member:	Prof. Michael Pope Dept. of Chemical Engineering, University of Waterloo
Internal Member:	Prof. Michael Fowler Dept. of Chemical Engineering, University of Waterloo
Internal-external Member:	Prof. Xiaoyu Wu Dept. of Mechanical and Mechatronics Engineering, University of Waterloo

Author's Declaration

This thesis consists of material all of which I authored or co-authored: see Statement of Contributions included in this thesis. This is a true copy of the thesis, including any required final revisions, as accepted by my examiners.

I understand that my thesis may be made electronically available to the public.

Statement of Contribution

Portions of this thesis are based upon a combination of the following published studies:

Yu H, Pritzker M, Gostick J. Use of mixed methanesulfonic acid/sulfuric acid as positive supporting electrolyte in Zn-Ce redox flow battery. Journal of the Electrochemical Society. 2023 Feb 28;170(2):020536.

Yu H, Pritzker M, Gostick J. Improving performance of hybrid Zn–Ce redox flow battery by controlling ion crossover and use of mixed acid positive electrolyte. Journal of Applied Electrochemistry. 2024 Sep 4:1-8.

Abstract

The transformation from energy based on fossil fuels to that based on sustainable options such as wind, solar and hydroelectric sources is crucial to reduce air/water pollution and carbon emissions. However, the production of electricity from these sustainable sources is typically intermittent in nature and can perturb the stability of the existing power grid. Redox flow batteries (RFB) have emerged as promising devices for grid-scale energy storage to stabilize power systems and improve their efficiency. Among the different types of RFBs, zinc- and cerium-based RFBs are promising for large-scale applications that require high output power density due to their low cost and high cell voltage. Motivated by its potential for future applications, this work focuses on the performance improvement of Zn-Ce RFBs through both experimental and modeling studies. Many of the findings and general ideas for RFB performance improvement are also applicable to other RFB systems and to commercial scale RFBs in real-life scenarios.

In this work, the effect of different positive supporting electrolytes on the performance of a bench-scale Zn-Ce RFB has been studied. The effectiveness of mixed methanesulfonic/sulfuric acid, mixed methanesulfonic/nitric acid and pure methanesulfonic acid has been assessed and compared. The Ce(III)/Ce(IV) reaction exhibits faster kinetics and the battery exhibits higher coulombic efficiency in the mixed 2 mol/L MSA-0.5 mol/L H_2SO_4 electrolyte compared to that achieved in the commonly used 4 mol/L MSA electrolyte due to lower H^+ crossover and higher Ce(IV) solubility. The rate of the fade in coulombic efficiency in the mixed MSA-H_2SO_4 electrolyte is 0.55% per cycle over 40 charge-discharge cycles, while the fade rate is 1.26% in the case of 4 mol/L MSA. Furthermore, the positive electrode reaction is no longer the limiting half-cell reaction even at the end of long-term battery charge-discharge operation.

The effect of ion crossover on the overall Zn-Ce RFB performance has also been investigated through the measurement of the Zn(II), Ce(III), Ce(IV) and H^+ concentrations on both sides of a Nafion 117 membrane during charge-discharge cycles. As much as 36% of the initial Zn(II) ions transfer from the negative to the positive electrolyte and 42.5% of the H^+ in the positive electrolyte has crossed over to the negative side after 30 charge-discharge cycles. Both of these phenomena contribute to the steady fade in battery performance over the course of operation. Based on these findings, experiments aimed at reducing the concentration gradient driving crossover by

intentionally adding different amounts of Zn(II) to the positive electrolyte at the outset of operation have been conducted. This approach has been shown to reduce the crossover of Zn(II) from the negative side to the positive side, improve both the battery coulombic and voltage efficiencies and reduce the decay of battery performance. Since the ion crossover phenomena is very commonly observed, this strategy to improve battery overall performance and reduce ions crossover by minimizing concentration gradient is not only applicable to similar lab-scale RFB research, but also beneficial for real-life RFB applications.

Since the positive electrode reaction becomes the limiting half-cell reaction during the course of battery operation, two strategies have been investigated to regenerate the positive electrolyte by converting the accumulated Ce(IV) ions back to Ce(III) ions. The first strategy which utilizes RuO_2 as a catalyst for Ce(IV) reduction improves the voltage efficiency from 71.1% to 77.8% over 16 cycles but reduces the coulombic efficiency from 74.1% to 57.8% due to the leakage of RuO_2 catalyst through the porous filter into the positive electrolyte. The method utilizing H_2O_2 to regenerate the positive electrolyte improves the average coulombic efficiency from 63.7% to 68.3% and the average voltage efficiency from 56.8% to 76.1% over 30 cycles. Similar battery performance and life-cycle improvement can also be expected if these electrolyte regeneration methods are applied on a commercial scale. Furthermore, the implementation of these regeneration methods should also reduce the overall operating costs since it will reduce the frequency with which electrolytes have to be replaced.

Finally, a transient 2-D model for the Zn-Ce RFB that accounts for the crossover of different electroactive species through the membrane has been developed. All three modes of transport (migration, diffusion and convection) coupled with electrode kinetics of Zn/Zn(II) and Ce(III)/Ce(IV) redox couples as well as HER and OER side reactions are included in the model. This model has been successfully validated against measurements of the evolution of the cell voltage, negative and positive electrode potentials and ion crossover during the course of 5 charge-discharge carried out in our laboratory. The validated model is then used to simulate the battery behaviour when operated under various operating conditions and using positive electrodes with different geometries. The results obtained provide useful information for the future design of Zn- or Ce-based RFBs with the aim of further improving their performance.

Acknowledgements

First and foremost, I would like to express my heartfelt gratitude to my supervisors, Professor Mark Pritzker and Professor Jeff Gostick, for their guidance, encouragement and unwavering patience throughout this process. Their expertise, insightful feedback and commitment to my work have been instrumental in shaping this research. Having them as my supervisors is one of the luckiest thing that has happened to me in my life.

To my family, I owe a debt of gratitude that words cannot fully capture. To my parents, thank you for your unconditional love, understanding and constant encouragement. Your faith in me provided the foundation on which this achievement stands and your sacrifices have been a source of strength throughout my journey.

To my friends, colleagues and peers, thank you for your companionship and encouragement along the way. Your support, whether through late-night discussions, shared frustrations, having lunch together or simply being there to listen has made this journey more fulfilling and enjoyable. To everyone who contributed in any way, thank you from the bottom of my heart.

Table of Contents

List of Figures xiii

List of Tables xxi

Nomenclature xxii

Chapter 1 Introduction and Research Objectives 1

1.1 Introduction 1

1.2 Research Objectives 8

1.3 Thesis Outline 9

Chapter 2 Literature Review 10

2.1 Development of Redox Flow Batteries 10

2.2 Popular RFBs 13

2.2.1 All-V RFBs 13

2.2.2 Fe-Cr RFBs 14

2.2.3 Metal-free RFBs 16

2.2.4 Zn-Br RFBs 17

2.2.5 Zn-Ce RFBs 19

2.3 RFB Modelling 32

2.3.1 Modelling application 33

2.3.2 Zn-Ce RFB modelling 39

Chapter 3 Experimental and Methods 42

3.1 Components of redox flow batteries 42

3.2 Electrochemical measurements 44

3.2.1 Half-cell measurement 44

3.2.2 Bench-scale full-cell system 45

3.3 Measurement of Ce(IV), H^+ and Zn(II) concentrations and electrolyte properties 47

3.4 Battery performance evaluation metrics 48

Chapter 4 Use of Mixed Methanesulfonic Acid/Sulfuric Acid as Positive Supporting Electrolyte in Zn-Ce Redox Flow Battery 52

4.1 Introduction 52

4.2 Experimental 54

4.2.1 Reagents 54

4.2.2 Electrochemical Experiments 54

4.3 Results and Discussion 56

4.3.1 Cyclic voltammetry 56

4.3.2 Battery cycling performance 58

4.3.3 Evolution of H^+ concentration in negative electrolyte and Ce(IV) concentration in positive electrolyte 70

Chapter 5 Improving performance of hybrid Zn–Ce redox flow battery by controlling ion crossover and use of mixed acid positive electrolyte 74

5.1 Introduction 74

5.2 Experimental 76

5.2.1 Preparation of electrolyte 76

5.2.2 Measurement of Ce(IV), H^+ and Zn(II) concentrations and electrolyte properties 76

5.3 Results and Discussion 79

5.3.1 Crossover in battery operating with 4 mol/L MSA positive supporting electrolyte 79

5.3.2 Effect of addition of Zn(II) to MSA and MSA-H_2SO_4 mixed acid positive supporting electrolytes on battery performance 82

5.3.3 Effect of current density on battery efficiency 95

5.3.4 Effect of Zn(II) on Ce(III)/Ce(IV) redox couple and O_2 evolution 97

5.3.5 Discharge polarization curves of batteries operating with various positive electrolytes 101

Chapter 6 Regeneration of positive electrolyte using RuO_2 and H_2O_2 104

6.1 Introduction 104

6.2 Experimental 106

6.3 Results and Discussion 109

6.3.1 Catalytic regeneration of positive electrolyte using RuO_2 109

6.3.2 Regeneration of positive electrolyte using H_2O_2 111

Chapter 7 Two-Dimensional Transient Model of a Zn-Ce RFB Incorporating Ion Crossover 119

7.1 Introduction 119

7.2 Experimental 119

7.3 Model Description 121

7.3.1 Electrolyte flow equations 123

7.3.2 Species transport equations in negative compartment 124

7.3.3 Species transport equations in positive compartment 126

7.3.4 Species transport equations in membrane 131

7.3.5 Tank model 132

7.3.6 Initial and boundary conditions 133

7.3.7 initial conditions 139

7.3.8 Details concerning numerical solution of model 141

7.4 Results and Discussion 147

7.4.1 Model validation 147

7.4.2 Use of validated model to investigate battery behaviour 153

7.4.3 Effect of applied current density on molar fluxes 156

7.4.4 Effect of flow rate 161

7.4.5 Effect of positive electrode geometry and specific surface area 170

7.4.6 Effect of negative electrode thickness 176

Chapter 8 Conclusions and Recommendations for Future Work 184

8.1 Conclusions 184

8.2 Future work 187

8.2.1 Inhibition of HER 187

8.2.2 Optimization of positive electrolyte composition 188

8.2.3 Minimization of undesired ion crossover 188

8.2.4 Further improvement of multi-physics model 189

8.2.5 Regeneration of positive electrolyte 190

8.2.6 Low-cost positive electrode material 191

Letters of Copyright Permission 193

References 196

Appendix 215

List of Figures

Figure 1.1. Schematic of a typical redox flow battery (reproduced with permission).[14] 3

Figure 2.1. Chronological summary of major flow battery developments. 13

Figure 2.2. Solubilities of Ce(III) and Ce(IV) in MSA measured at 298°K (reproduced with permission).[127] 25

Figure 3.1. Pt-Ti positive electrode used in this work. 42

Figure 3.2. Components of bench-scale flow battery used in this study (reproduced with permission) [129]: Pt-Ti mesh positive electrode (1), silicone rubber gaskets (2, 4, 6, 8), acrylic flow channels (3, 7), ion exchange membrane (5), PVE negative electrode (9) and copper current collector (10). 43

Figure 3.3. Diagram showing the connection between the RFB, external electrolyte reservoir tanks and reference electrodes inserted to monitor the positive and negative electrode potentials during battery operation (reproduced with permission).[38] 44

Figure 3.4. Schematic of three-electrode system used in this research. 45

Figure 4.1. Cyclic voltammograms of the Ce(III)/Ce(IV) redox couple obtained in different supporting electrolytes at a scan rate of 50 mV/s. Each of the listed supporting electrolytes contains 0.8 mol/L Ce(III) in its initial state. 57

Figure 4.2. Cell voltage during 40 galvanostatic charge-discharge cycles at 25 mA/cm^2 and 50°C when 4 mol/L MSA is used as the positive supporting electrolyte. 59

Figure 4.3. Cell voltage during 40 galvanostatic charge-discharge cycles at 25 mA/cm^2 and 50°C when 2 mol/L MSA-0.5 mol/L H_2SO_4 mixed acid is used as the positive supporting electrolyte. 60

Figure 4.4. Negative and positive electrode potentials during 40 galvanostatic charge-discharge cycles at 25 mA/cm^2 and 50°C when 4 mol/L MSA is used as the positive supporting electrolyte. 60

Figure 4.5. Negative and positive electrode potentials during 40 galvanostatic charge-discharge cycles at 25 mA/cm^2 and 50°C when 2 mol/L MSA-0.5 mol/L H_2SO_4 is used as the positive supporting electrolyte..... 61

Figure 4.6. Coulombic efficiency of Zn-Ce redox flow battery operating with different positive electrolytes over 40 galvanostatic charge-discharge cycles. The current density during each charge-discharge cycle is 25 mA/cm^2 and the charge duration is 1 hour during each cycle. 64

Figure 4.7. Voltage efficiency of Zn-Ce redox flow battery operating with different positive electrolytes over 40 galvanostatic charge-discharge cycles. The current density during each charge-discharge cycle is 25 mA/cm^2 and the charge duration is 1 hour during each cycle. 66

Figure 4.8. Energy efficiency of Zn-Ce redox flow battery operating with different positive electrolytes over 40 galvanostatic charge-discharge cycles. The current density during each charge-discharge cycle is 25 mA/cm^2 and the charge duration is 1 hour during each cycle. 67

Figure 4.9. Polarization curve of Zn-Ce redox flow battery operating with 4 mol/L MSA and 2 mol/L MSA-0.5 mol/L H_2SO_4 mixed acid as positive supporting electrolyte. 68

Figure 4.10. Variation of the H^+ concentration in the negative electrolyte over the course of 40 charge/discharge cycles when 4 mol/L MSA and 2 mol/L MSA-0.5 mol/L H_2SO_4 are used as the supporting positive electrolytes. 71

Figure 4.11. Variation in the Ce(IV) concentration in the positive electrolyte over the course of 40 charge/discharge cycles when 4 mol/L MSA and 2 mol/L MSA-0.5 mol/L H_2SO_4 are used as the supporting positive electrolytes. 73

Figure 4.12. (a) Comparison of the positive electrolytes remaining after 40 charge-discharge cycles: 4 mol/L MSA (left) and 2 mol/L MSA-0.5 mol/L H_2SO_4 mixed acid (right) supporting electrolytes. (b) 4 mol/L MSA and (c) 2 mol/L MSA-0.5 mol/L H_2SO_4 mixed acid supporting electrolyte. ... 73

Figure 5.1. Variation of (A) Zn(II) concentration in the positive and negative electrolytes, (B) H^+ concentration in the negative electrolyte and (C) total soluble Ce(III)+Ce(IV) concentration in the positive and negative electrolytes obtained over 30 cycles at 25 mA/cm^2 using 4 mol/L MSA

positive supporting electrolyte. Effect of Zn(II) concentration added to the positive electrolyte containing mixed acid (triangle) or MSA-only (square) on the resulting (D) average coulombic efficiency, (E) voltage efficiency and (F) energy efficiency of the battery over 30 cycles at 25 mA/cm^2. 82

Figure 5.2. Cell voltage of the Zn-Ce redox flow battery over 30 cycles at 25 mA/cm^2 obtained when the fresh positive electrolyte contains 0.8 mol/L Ce(III) in 4 mol/L MSA(blue), 2/0.5 MA(black), 0.6 mol/L Zn(II) added to 4 mol/L MSA (orange) and 0.4 mol/L Zn(II) added to 2/0.5 MA (green). The fresh negative electrolyte contains 1.5 mol/L Zn(II) in 1 mol/L MSA. 86

Figure 5.3. Variation of (A) H^+ concentration in the negative electrolyte, (B) Zn(II) concentration in the positive (half-filled symbols) and negative electrolytes (fully-filled symbols) and (C) total soluble Ce(III) + Ce(IV) concentration in the positive (half-filled symbols) and negative (fully-filled symbols) electrolyte over 30 cycles at 25 mA/cm^2 obtained using the various positive electrolytes. The fresh positive electrolyte contains 0.8 mol/L Ce(III) in 4 mol/L MSA(blue), 2/0.5 MA(black), 0.6 mol/L Zn(II) added to 4 mol/L MSA (orange) and 0.4 mol/L Zn(II) added to 2/0.5 MA (green). The fresh negative electrolyte contains 1.5 mol/L Zn(II) in 1 mol/L MSA. 88

Figure 5.4. Effect of zinc(II) methanesulfonate concentration on the electrical conductivities (A) and viscosities (B) of the MSA (blue) and 2/0.5MA (orange) electrolytes in this study. 91

Figure 5.5. Energy efficiency of each charge-discharge cycle when the battery is operated for 30 cycles at 25 mA/cm^2. The fresh positive electrolyte contains 0.8 mol/L Ce(III) in 4 mol/L MSA(blue), 2/0.5 MA(black), 0.6 mol/L Zn(II) added to 4 mol/L MSA (orange) and 0.4 mol/L Zn(II) added to 2/0.5 MA (green). The fresh negative electrolyte contains 1.5 mol/L Zn(II) in 1 mol/L MSA 94

Figure 5.6. Effect of applied current density on the (A) coulombic, (B) voltage and (C) energy efficiencies of the Zn-Ce redox flow battery operating over 3 successive cycles. The fresh positive electrolyte contains 0.8 mol/L Ce(III) in 4 mol/L MSA(blue), 2/0.5 MA(black), 0.6 mol/L Zn(II) added to 4 mol/L MSA (orange) and 0.4 mol/L Zn(II) added to 2/0.5 MA (green). The fresh negative electrolyte contains 1.5 mol/L Zn(II) in 1 mol/L MSA 97

Figure 5.7. Effect of zinc(II) methanesulfonate concentration on the cyclic voltammograms for the Ce(III)/Ce(IV) redox couple in (A) 4 mol/L MSA and (B) 2/0.5 MA positive supporting electrolytes initially containing 0.8 mol/L Ce(III). Scan rate = 50 mV/s. (C) Discharge polarization (solid lines, square symbols) and power density (dashed lines, triangle symbols) curves of Zn-Ce redox flow battery operating with different positive electrolytes after being charged at 50 mA/cm^2 for 90 minutes to reach SOC of 50%. The battery is discharged for 20 s at each of the applied current densities followed by a 20 s rest period. 99

Figure 6.1. Schematic diagram of the custom-made catalytic bed used in this study for the electrolyte regeneration using RuO_2 as catalyst 108

Figure 6.2. Cell voltage during 16 consecutive charge-discharge cycles of the Zn-Ce RFB operating at a current density of 25 mA/cm^2, temperature of 323°K, electrolyte flow rate of 66 mL/min and charge duration of 1 hour with (black) and without (blue) regeneration using RuO_2 catalyst. The negative electrolyte contains 1.5 mol/L Zn(II) in 1 mol/L MSA and the positive electrolyte contains 0.8 mol/L Ce(III) in 4 mol/L MSA at the start of the cycles 110

Figure 6.3. Cell voltage during 30 consecutive charge-discharge cycles of the Zn-Ce RFB operating at a current density of 25 mA/cm^2, temperature of 323°K, electrolyte flow rate of 66 mL/min and charge duration of 1 hour with (black) and without (blue) regeneration by H_2O_2 addition. The negative electrolyte contains 1.5 mol/L Zn(II) in 1 mol/L MSA and the positive electrolyte contains 0.8 mol/L Ce(III) in 4 mol/L MSA at the start of the cycles 111

Figure 6.4. (A) Positive and (B) negative electrode potentials measured during 30 consecutive charge-discharge cycles of the Zn-Ce RFB operating at a current density of 25 mA/cm^2, temperature of 323°K, electrolyte flow rate of 66 mL/min and charge duration of 1 hour with (black) and without (blue) regeneration by H_2O_2 addition. The negative electrolyte contains 1.5 mol/L Zn(II) in 1 mol/L MSA and the positive electrolyte contains 0.8 mol/L Ce(III) in 4 mol/L MSA at the start of the cycles. Red arrows indicate the addition of H_2O_2 to the positive electrolyte. 114

Figure 6.5. Ce(IV) concentration in the positive electrolyte measured during 30 consecutive charge-discharge cycles of the Zn-Ce RFB operating at a current density of 25 mA/cm^2,

temperature of 323°K, electrolyte flow rate of 66 mL/min and charge duration of 1 hour with (black) and without (blue) regeneration by H_2O_2 addition. The negative electrolyte contains 1.5 mol/L Zn(II) in 1 mol/L MSA and the positive electrolyte contains 0.8 mol/L Ce(III) in 4 mol/L MSA at the start of the cycles. The red dots represent the Ce(IV) concentration immediately after electrolyte regeneration. 116

Figure 6.6. (A) Coulombic efficiency, (B) voltage efficiency and (C) energy efficiency during 30 consecutive charge-discharge cycles of the Zn-Ce RFB operating at a current density of 25 mA/cm^2, temperature of 323°K, electrolyte flow rate of 66 mL/min and charge duration of 1 hour with (black) and without (blue) regeneration by H_2O_2 addition. The negative electrolyte contains 1.5 mol/L Zn(II) in 1 mol/L MSA and the positive electrolyte contains 0.8 mol/L Ce(III) in 4 mol/L MSA at the start of the cycles. 118

Figure 7.1. Schematic showing the geometry of the two-dimensional Zn-Ce redox flow battery described in the model. 122

Figure 7.2. Boundary conditions applied to the Zn-Ce redox flow battery model. 135

Figure 7.3. Comparison of model-fitted values of cell voltage (A) and electrode potential (B) with experimental measurements over 5 consecutive charge-discharge cycles operating at a current density of 25 mA/cm^2, 323°K temperature, negative and positive electrolyte flow rates of 66 mL/min and charge duration of 1 hour. The negative electrolyte initially contains 1.5 mol/L Zn^{2+} in 1 mol/L MSA and the positive electrolyte contains 0.8 mol/L Ce^{3+} in 4 mol/L MSA. 149

Figure 7.4. Comparison of experimental and model-fitted concentrations of (A) Zn^{2+} in the negative electrolyte, (B) Zn^{2+} in the positive electrolyte, (C) total Ce in the negative electrolyte, (D) total Ce in the positive electrolyte, (E) H^+ in the negative electrolyte. The H^+ concentration in the positive electrolyte as determined by the model is shown in (F). 152

Figure 7.5. Variation of the (A) surface density of zinc deposit on the negative electrode, (B) surface Ce^{3+} and $CeOH^{3+}$ concentrations in the positive electrolyte, (C) bulk Ce^{3+} and $CeOH^{3+}$ concentrations in the positive electrolyte, (D) H^+ concentrations in the positive and negative electrolytes, (E) current density of OER and (F) current density of HER over the 5 consecutive

charge-discharge cycles. The charge-discharge cycles were conducted at a current density of 25 mA/cm^2, temperature of 323°K and charge duration of 1 hour and positive and negative electrolyte flowrates of 66 mL/min. The negative electrolyte contains 1.5 mol/L Zn^{2+} in 1 mol/L MSA and the positive electrolyte contains 0.8 mol/L Ce^{3+} in 4 mol/L MSA at the start of the 1st cycle. 155

Figure 7.6. Breakdown of computed diffusional and migrational molar fluxes of each species across the membrane obtained at t = 30 min during charge (A, C and E) and t = 30 min during discharge (B, D and F) of the 3rd cycle computed using the model for battery operation at 323°K, charge duration of 1 hour and positive and negative electrolyte flowrates of 66 mL/min. The negative electrolyte contains 1.5 mol/L Zn^{2+} in 1 mol/L MSA and the positive electrolyte contains 0.8 mol/L Ce^{3+} in 4 mol/L MSA at the start of the 1st cycle. 158

Figure 7.7. Variation of H^+ concentration in the negative electrolyte over 5 consecutive charge-discharge cycles when the Zn-Ce RFB is operated at different current densities..... 160

Figure 7.8. Effect of electrolyte flowrate on (A) cell voltage, surface concentration of (B) Ce^{3+} and (C) $CeOH^{3+}$ during the 1st charge-discharge cycle and (D) surface density of the zinc deposit at the end of the 1st discharge cycle. The charge-discharge cycles are conducted at a current density of 25 mA/cm^2, temperature of 323°K, charge duration of 1 hour and at various flow rates of the positive and negative electrolytes. The negative electrolyte contains 1.5 mol/L Zn^{2+} in 1 mol/L MSA and positive electrolyte contains 0.8 mol/L Ce^{3+} in 4 mol/L MSA at the start of the cycle. 163

Figure 7.9. Effect of positive and negative electrolyte flowrates on the overpotential of Ce^{3+}/$CeOH^{3+}$ reaction. Charge-discharge cycle is conducted at current density of 25 mA/cm^2, temperature of 323°K and charge duration of 1 hour. The negative electrolyte contains 1.5 mol/L Zn^{2+} in 1 mol/L MSA and positive electrolyte contains 0.8 mol/L Ce^{3+} in 4 mol/L MSA at the start of the cycle. 165

Figure 7.10. (A) Effect of electrolyte flowrate on the Zn^{2+} concentration profiles across the negative compartment at a height of H/2. The solid lines correspond to the profiles during charge and dash lines to the profiles during discharge. The data is taken at the 30 min from the start of battery charge and 30 min from battery discharge. (B) Effect of electrolyte flowrate on the surface

density of the zinc metal deposit on the negative electrode surface after charge. Charge-discharge cycle is conducted at current density of 25 mA/cm^2, temperature of 323°K and charge duration of 1 hour. The negative electrolyte contains 1.5 mol/L Zn^{2+} in 1 mol/L MSA and positive electrolyte contains 0.8 mol/L Ce(III) in 4 mol/L MSA at the start of the cycle. 167

Figure 7.11. Effect of electrolyte flowrate on current density for (A) zinc deposition and (B) HER. Charge-discharge cycle is conducted at current density of 25 mA/cm^2, temperature of 323°K and charge duration of 1 hour. The negative electrolyte contains 1.5 mol/L Zn^{2+} in 1 mol/L MSA and positive electrolyte contains 0.8 mol/L Ce^{3+} in 4 mol/L MSA at the start of the cycle. 168

Figure 7.12. Effect of the electrolyte flowrates on the discharge polarization curves of the Zn-Ce RFB. These polarization simulations are conducted by first charging the battery at 50 mA/cm^2 for 45 minutes to reach an SOC of 50%, followed by battery discharge for 20s at different current densities ranging from 1 to 175 mA/cm^2 until a point is reached where cell voltage drops to the discharge termination criterion of 0.5 V. 169

Figure 7.13. Optical photographs of (A) Pt-Ti mesh, (B), Pt-Ti micromesh, and (C) Pt-Ti felt (reproduced with permission).[195,210] 172

Figure 7.14. (A) Cell voltage, (B) Ce^{3+} surface concentration, (C) $CeOH^{3+}$ surface concentration and (D) zinc deposit remaining on the negative electrode at the end of 1st charge-discharge cycle using the different positive electrodes. 173

Figure 7.15. Polarization curves of the Zn-Ce RFB obtained at 323°K and a flow rate of 66 mL/min when operated using the original Pt-Ti, Pt-Ti mesh, Pt-Ti micromesh and Pt-Ti felt electrodes. The polarization simulation was conducted by first charging the battery at 50 mA/cm^2 for 45 minutes to reach an SOC of 50%, followed by battery discharge for 20s at each of the applied current densities 176

Figure 7.16. Breakdown of the contribution of the different components in the Zn-Ce RFB to its total ohmic resistance based on measurements and the model. 178

Figure 7.17. Effect of the thickness of the negative PVE electrode on the cell voltage obtained during charge and discharge of the Zn-Ce RFB. The charge-discharge cycles are conducted at a

current density of 25 mA/cm^2, temperature of 323°K, charge duration of 1 hour, electrolyte flow rate of 66 mL/min. The negative electrolyte contains 1.5 mol/L Zn^{2+} in 1 mol/L MSA and the positive electrolyte contains 0.8 mol/L Ce^{3+} in 4 mol/L MSA at the start of the cycle. 180

Figure 7.18. Effect of negative PVE electrode thickness on the discharge polarization curves of the Zn-Ce RFB operating at 323°K. The polarization simulation is done by first charging the battery at 50 mA/cm^2 for 45 minutes to reach an SOC of 50%, followed by battery discharge for 20s at each of the applied current densities. 182

Figure 7.19. Resistance of different negative electrodes. 183

Figure S1. Effect of zinc(II) methanesulfonate addition on the cyclic voltammograms for the oxygen evolution reaction in (A) 4 mol/L MSA and (B) 2/0.5 MA in the absence of Ce(III)/Ce(IV) ions. Scan rate = 50 mV/s. 215

Figure S2. Comparison of computed surface and bulk Ce(III) concentrations in the positive compartment when Pi-Ti micromesh positive electrode is used..... 216

Figure S3. Comparison of computed surface and bulk Ce(IV) concentrations in the positive compartment when Pi-Ti micromesh positive electrode is used..... 216

List of Tables

Table 3.1. Quantities and descriptions used to evaluate battery attributes and performance. 50

Table 4.1. Key information from CV curves. 58

Table 5.1 Key information from CV curves 101

Table 7.1. Initial concentrations of various species 140

Table 7.2 Geometric features and operating conditions of the Zn-Ce flow battery in this study 141

Table 7.3. Values of electrochemical and mass transport parameters used in the model..... 143

Table 7.4. Charge numbers of dissolved species and stoichiometric coefficients for the electrode reactions. 145

Table 7.5. Model parameters obtained in this study by fitting model to the experimental data . 148

Table 7.6. Properties of the different positive electrode evaluated in the model simulations. ... 171

Table 7.7. Ohmic resistances of the different components of the Zn-Ce RFB based on measurements and the model. 178

Nomenclature

Parameters	
a	Activity
α_a	Anodic reaction transfer coefficient
α_c	Cathodic reaction transfer coefficient
ε_{pos}	Porosity of the positive electrode
η	Overpotential (V)
μ	Dynamic viscosity (kg/m·s)
υ	Stoichiometric coefficient
ϕ_e	Potential in electrolyte (V)
ϕ_s	Potential in solid phase of positive electrode (V)
ρ	Fluid density (kg/m^3)
σ_s	Conductivity of positive electrode (S/m)
σ_s^{eff}	Effective conductivity of positive electrode (S/m)
$\vec{P}$	Pressure vector (Pa)
$\vec{v}$	Velocity (m/s)
a	Specific area of positive electrode (1/m)
c	Concentration (mol/L)
D	Diffusion coefficient (m^2/s)
D_{eff}	Effective diffusion coefficient (m^2/s)

E	Potential (V)
F	Faraday constant (C/mol)
H	Cell height (m)
I	Current (A)
i	Current density (A/cm^2)
k_m	Mass transfer coefficient (m/s)
K	Intrinsic permeability of positive electrode
L_e	Negative flow channel/positive electrode width (m)
L_m	Membrane width (m)
$\vec{N}$	Molar flux of ion species (mol/m^3·s)
Q	Electrolyte flow rate (mL/min)
R	Gas constant (J/mol·K)
S	Source term (mol/m^3·s)
T	Temperature (K)
t	Time (s)
V	Volume of electrolyte (L)
z	Charge number
Subscript	
$bulk$	Bulk property
$Ce(III)$	Property related to Ce(III)

$Ce(III)$	Property related to Ce(IV)
f	Property related to the fixed sulfonate groups in Nafion membrane
H^+	Property related to H^+ ion
H_2	Property related to HER
In	Property related to the inlet outlet of flow channel
m	Property related to membrane
neg	Property related to the negative compartment/reaction
O_2	Properties related to OER
Out	Property related to the outlet of flow channel
pos	Property related to the positive compartment/reaction
ref	Reference value
s	Electrode surface property
x	Direction perpendicular to negative electrode surface
y	Direction perpendicular to the inlets of battery
Zn	Property related to metal zinc
$Zn(II)$	Property related to Zn(II)

Chapter 1 Introduction and Research Objectives

1.1 Introduction

In 2015, the Paris Agreement was negotiated and signed by 196 parties at the United Nations Climate Change Conference with the long-term goal to limit the temperature increase to 1.5°C above pre-industrial levels. To achieve this goal, greenhouse gas emissions must be reduced as soon as possible and even reach net zero by the middle of the 21st century. The emissions from burning fossil fuels for electricity and heat accounted for 43.5% of the total CO_2 emissions in 2020, which was significantly larger than that from other sources such as transportation (20.4%), manufacturing and construction (17.8%) and the remainder (18.3%). [1] Needless to say, the energy structure worldwide has to be shifted from fossil fuel-based toward a reliable, affordable and, most importantly, sustainable clean energy system.

Renewable energies are obtained from unlimited and naturally replenished resources such as wind, sunlight, tides, waves, biomass and thermal energy. Energy from these sources offers numerous economic and environmental benefits including the reduction of carbon emissions and many types of air pollution. Many major economic powers such as the US, UK, Canada and Germany are aiming to completely shift their power grid to green renewable electricity in combination with a reliable baseload power such as nuclear energy within the next 15 years.[2] By 2030, China plans to generate ~ 50% of its total capacity of 1200 gigawatts of electricity from renewable energy resources. Up to now, 314 cities around the world are operating their power grid using at least 70% of its electricity from renewable sources. Obviously, the number of cities achieving this target is expected to continuously rise.[3] In Canada, the electricity generated from renewable resources made up 73.7% of the total electricity consumed in 2022. This was dominated by hydroelectric power which made up 65.5% of the total, followed by 6.1% from wind, 1.5% from biomass and 0.72% from solar.[4] The above mentioned data refer to electricity usage by residential, commercial and industrial users, but not to transportation and heating which still rely primarily on fossil fuels.

Despite the promising aspects of renewable energy sources mentioned above, one of the main barriers to their widespread adoption is their poor reliability. In many jurisdictions, renewable resources are intermittent in nature and the production of electricity from these sources is very

sensitive to real-time climate conditions. For example, the electricity produced from wind turbines depends on wind speed and air density, which varies dramatically at different times of the year. Solar energy is not available during the night and can be affected by the unpredictable cloudy and rainy conditions above the solar panel area. In fact, an inclusion of as little as 20% renewable energy production can potentially destabilize the existing power grid due to their intermittent nature.[5,6] Therefore, advanced energy harvesting and storage systems must be paired with renewable energy to mitigate short-term fluctuations and interruptions. An effective energy storage technology should meet the following characteristics: 1) highly scalable, 2) fast response time, 3) low cost, 4) high efficiency, 5) long life-cycle and 6) low environmental impact.[7–9] Currently, the most widely employed energy storage techniques involve the use of pumped hydroelectric power, compressed air and flywheels. Over 95% of the large-scale (> 100 MW) energy storage worldwide is based on pumped-hydro systems.[10] However, it is worth noting that this technology is not usually designed to match irregular and periodic production of energy from renewable sources.[11] In addition, the construction of infrastructure associated with this technology poses potential environmental concerns to the surrounding area, not to mention high construction costs and the need for large water bodies.

Redox flow batteries (RFBs) have emerged as a promising technology for grid-scale energy storage due to their unique advantages including flexible modular design and operation, high scalability, short response times, no detrimental effects associated with being fully charged or discharged, relatively minimum maintenance once installed and long life cycles.[12,13] All these features make this technology a promising candidate for the storage of electricity generated by intermittent and irregular renewable resources.

Figure 1.1 shows a schematic of a typical redox flow battery, which is a rechargeable energy storage device that converts electricity to chemical energy during charge and converts chemical energy back to electricity during discharge. Unlike conventional batteries such as Li-ion batteries, the electroactive species of a RFB are stored in two external electrolyte tanks that are separated from reactions sites on the electrodes, which reduces the risks of fire and safety concerns. During battery operation, the negative and positive electrolytes are continuously circulated from the tanks to their corresponding compartment by pumps for energy conversion. Due to the separation in the locations where the electroactive species are stored and the electrode reactions occur, the factors

governing the energy storage capacity of RFBs are different from those that determine the power storage capacity. The energy capacity is determined by the concentration of electroactive species in the electrolyte and the total volume of the electrolytes, whereas the power output is determined by the number of unit cells (i.e., total electrode area) in a RFB stack system. These features give RFBs the unique property that their energy and power capacities can be designed and scaled up independently of each other. In most cases, each unit cell contains an ion exchange membrane which separates it into negative and positive compartments that can be maintained at different electrolyte compositions. In a redox flow battery that employs a cation exchange membrane, an ion such as H^+ would ideally be the only species in the cell that is transported from the positive to the negative compartment during battery charge. During discharge, the same amount of H^+ ions would ideally be transported back to the positive side if electrode side reactions are neglected. When an anion exchange membrane is used, a negatively charged ion such as OH^- would be transported back and forth across the membrane during charge and discharge to maintain the electroneutrality of the system.

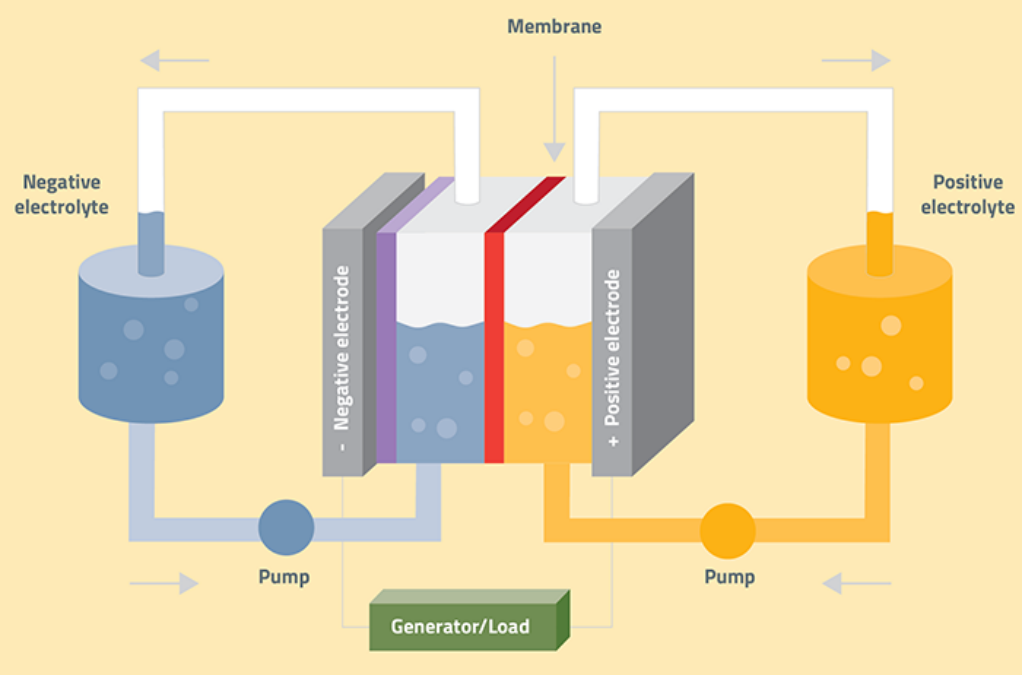


Figure 1.1. Schematic of a typical redox flow battery (reproduced with permission).[14]

Among the different types of RFBs, the Zn-Ce system has attracted attention due to its high open-circuit voltage and low cost. In a Zn-Ce RFB, the Zn^0/Zn(II) redox couple is utilized at the negative electrode and the Ce(III)/Ce(IV) at the positive electrode, while methanesulfonic acid (MSA)-based solutions are used as the supporting electrolytes on the two sides. The electrode reactions and overall reactions are shown as follows:

Negative electrode: $$Zn(II) + 2e^- \underset{Discharge}{\overset{Charge}{\rightleftarrows}} Zn,\ E^0 = -0.959\ V\ vs.Ag|AgCl \quad (1)$$

Positive electrode: $$Ce(III) \underset{Discharge}{\overset{Charge}{\rightleftarrows}} Ce(IV) + e^-,\ E^0 = 1.28 - 1.72\ V\ vs.Ag|AgCl \quad (2)$$

Cell reaction: $$Zn(II) + 2Ce(III) \underset{Discharge}{\overset{Charge}{\rightleftarrows}} Zn + 2Ce(IV), E^0_{cell} = 2.24 - 2.68\ V \quad (3)$$

Due to the highly positive potential of the Ce(III)/Ce(IV) redox couple and negative potential of Zn^0/Zn(II) redox couple, the open-circuit voltage of Zn-Ce RFBs can reach 2.4V, which is among the largest values attainable in aqueous-based flow batteries. It should be noted that the standard potential of the positive reaction lies in a range between 1.28V and 1.72V depending on the supporting electrolyte (such as sulfuric acid or perchloric acid) and the presence of complexing agents which stabilize the Ce(III)/Ce(IV) ions in the solution to prevent hydrolysis and precipitation.[15–17]

Although cerium is classified as a rare earth element, its abundance in the earth's crust is comparable to that of copper and greater than that of common metals such as lead and tin. The abundances of zinc and cerium rank 24th and 25th, respectively, in the continental crust of the earth.[18] In industry, cerium is often generated as a by-product in the production of Nd which is in high demand for use in magnets. In fact, due to the fact that the supply of cerium is higher than its demand, the excess is stored for future applications in order to prevent collapse of its commodity price.[19,20] Overall, zinc and cerium should be excellent choices for use in redox flow battery technology for large-scale energy storage due to their low price and large redox potential gap. Another advantage of this system is that its components are much less toxic than the components of all-vanadium flow batteries.[21,22] For example, the electrolytes of Zn-Ce RFBs are based on

methanesulfonic acid, which is an organic acid and is of less environmental concern than that of sulfuric acid commonly used in other flow batteries. In addition, Zn-Ce RFB does not contain corrosive or highly toxic heavy metals such as Br, Cr(VI) or Pb.

Despite these advantages, key challenges must be addressed in order for Zn-Ce RFBs to be technologically and economically viable for large-scale commercial applications. At the negative electrode, the hydrogen evolution reaction (HER) competes with the zinc deposition reaction during battery charge. Since the HER is irreversible, the electrons that are consumed by HER cannot be used for battery discharge, thereby reducing the coulombic efficiency. The HER also causes an imbalance in the discharge capacity on the two sides of the battery over multiple charge-discharge cycles whereby the Ce(IV) produced during battery charge cannot be fully converted back to Ce(III) ions during discharge. In addition, the accumulation of flammable hydrogen gas could conceivably be a safety hazard, especially in a closed system. Several strategies have been proposed to minimize the HER and its effects on battery performance and life cycle.[23–25]

Another problem on the negative side is the potential formation of zinc dendrites during battery charge. The deposited zinc layer should be uniform and smooth on the electrode surface. However, zinc has a tendency to preferentially nucleate and grow on sites such as minor flaws on the electrode due to the enhancement of local electric field, which can lead to the continuous growth of needle-like and sharp dendrite structures. This is detrimental to the system because dendrites can pierce the ion exchange membrane and cause leakage between the two sides, leading to battery self-discharge and even short-circuiting, especially when operating at high current densities. To solve this problem, the addition of reagents such as organic molecules, surfactants and metal ions to the negative electrolyte has been explored to achieve smooth and uniform zinc deposits.[26–30] Most importantly, the use of methanesulfonic acid (MSA) as supporting electrolyte has been found to be very effective at suppressing zinc dendrite formation, which is one of the reasons that it has been extensively used in zinc-based RFBs.

Another critical challenge is the crossover of electroactive species such as H^+, Zn(II) and Ce(III)/Ce(IV) across the membrane due to the non-ideal behaviour of the ion exchange membrane. This crossover process is caused primarily by the existence of concentration gradients of the various species across the membrane, leading to their diffusion from the concentrated to the dilute

side. The undesired crossover has two critical negative effects on battery performance. The first is the enhancement of the hydrogen evolution side reaction on the negative electrode due to both increased H^+ concentration and reduced Zn(II) concentration in the negative electrolyte, which lowers the columbic efficiency of the battery. The second negative effect is the reduction of the solubility of Ce(IV) ions in the positive electrolyte as its acidity declines due to the net transfer of H^+ ions to the negative side. Over the course of battery operation, hydrogen evolution causes the negative side to limit the battery discharge capacity, thereby preventing some of the Ce(IV) in the positive electrolyte from being reduced to Ce(III) during discharge and resulting in the accumulation of Ce(IV) ions on the positive side. Eventually, Ce(IV) precipitation begins to occur in the positive electrolyte due to this increase in Ce(IV) concentration and the reduction in its solubility due to the lowering of the H^+ concentration. Once Ce(IV) precipitation occurs, the battery capacity is permanently decreased since the precipitate does not redissolve into Ce(IV) ions in the positive electrolyte.[31–34]

To prevent the accumulation of Ce(IV) ions in the positive electrolyte that causes battery performance decay, an effective method to restore the state-of-charge of the positive electrolyte is needed. It is worth mentioning that the undesired crossover of electroactive species has also been widely reported in all-vanadium RFBs. However, the electrolytes in all-vanadium RFBs can be re-balanced by remixing the positive and negative electrolyte periodically. Of course, such a strategy is not positive for the Zn-Ce RFB system because different elements are used on the two sides and cannot be easily separated after remixing. Therefore, a strategy to restore the positive electrolyte periodically is needed to extend battery life and reduce overall costs from electrolytes, especially for long-term battery operation.[8,35,36]

The highly acidic and oxidative environment of positive electrolyte that contains MSA and Ce(III)/Ce(IV) ions is also a concern for the Zn-Ce RFB systems. This causes the corrosion and degradation of different battery components such as the electrode, ion exchange membrane and even the tubing. Some carbon-based positive electrodes (graphite, carbon felt and carbon polyvinyl-ester) have proven to be good surfaces for the Ce(III)/Ce(IV) redox couple, but they are not stable in the aggressive positive electrolyte and are permanently damaged after only a few charge-discharge cycles.[37] Therefore, more stable positive electrodes such as platinum-based materials which are much more expensive have to be used to ensure stable battery performance. It

has also be shown that the use of anion exchange membranes can reduce the amount of undesired H^+ crossover through the membrane and improve battery efficiency.[38] Similar to carbon-based electrode materials, these anion exchange membranes are not chemically durable and tend to be permanently damaged by the highly acidic and oxidizing electrolyte within ~30 hours of battery operation.

While experiments conducted in the laboratory are valuable and can provide real-world data to evaluate the performance of RFBs, the cost of experimental setups and materials such as chemicals, membranes and equipment can be very expensive. The use of multi-physics models to simulate the battery performance is relatively inexpensive and rapid, especially when the battery has to be tested under a wide range of operating conditions and for extended charge-discharge cycles. In addition, insight into internal processes during battery operation such as mass transport, concentration gradients of different species, potential and current distributions can be obtained, which are challenging or impossible to determine directly from laboratory experiments. Most of the models reported have been developed for all-vanadium RFBs since they are the most widely studied and commercialized system to date. The first transient 2-dimensional Zn-Ce RFB model that includes all three modes of transport (diffusion, migration and convection) was developed by Amini and Pritzker in our own group and accurately fit to extensive experimental data.[39] However, one limitation of this model was that the commonly observed crossover of different electroactive species was not considered. This phenomenon is important to include since the crossover of ions changes the acidity and the concentrations of electroactive species, which further affects the reactions kinetics of electrode reactions (including HER and OER side reactions) and the battery efficiency. To further improve the accuracy of the model, the inclusion of ionic crossover across the membrane and correlations for prediction of mass transfer coefficients is strongly recommended. Another limitation of the previous Zn-Ce RFB model was that properties such as mass transfer coefficients of Ce(III) and Ce(IV) used in the model were accurate only for the exact same operating conditions and battery properties used during validation. Therefore, the model was not ideally suited for the investigation of battery performance under different operating conditions and battery properties such as flow rates, electrode porosity and electrode specific surface area. To this end, a more comprehensive multi-physics model should be developed to accurately describe the distribution of the various ions in the two electrolytes and the membrane and to investigate the effect of different operating conditions such as flow rate, applied current density and electrode

porosity on battery performance. Such a model would also allow for the prediction and optimization of battery performance and potentially reduce the time and costs involved in future experimental testing.

1.2 Research Objectives

This work is an extension of research on the Zn-Ce RFB system by Amini [40] and focuses on crucial aspects neglected in this previous study. The aim of this work is to study the performance and identify the limitations of Zn-Ce RFB through experiments and mathematical modeling, with the ultimate goal to provide strategies and solutions to improve battery performance. It is worth noting that some of the findings and proposed ideas should also be applicable to other hybrid flow battery systems as well, such as Zn-I, Zn-Br and H_2-Br. The objectives of this research are to both improve battery efficiency and increase life-cycle and can be summarized as follows:

- Identification of the mechanisms of Zn-Ce RFB performance decay over the course of battery operation by monitoring the electrode reaction kinetics and electroactive species concentrations in the electrolytes.
- Investigation of the overall battery performance using different positive supporting electrolytes such as HNO_3-MSA, H_2SO_4-MSA and MSA at various compositions with the aim of reducing H^+ crossover and improving Ce(IV) ion solubility.
- Measurement of crossover of different electroactive species such as H^+, Zn(II), Ce(III), and Ce(IV) and modification of electrolyte composition to reduce crossover and thereby improve overall performance of the Zn-Ce RFB.
- Development of a simple and efficient strategy to regenerate the positive electrolyte composition during the course of battery operation in order to extend battery life and improve battery efficiency.
- Development of an accurate and comprehensive transient multi-physics model that incorporates crossover of the various electroactive species in order to predict battery performance under different conditions and be used in the design of the various battery components to further improve performance.

1.3 Thesis Outline

Chapter 1 provides an introduction to redox flow batteries and discusses the objectives of this work. Chapter 2 contains a comprehensive literature review of the history of the development of redox flow batteries, electrode reactions of various popular redox flow batteries and mathematical modeling of redox flow batteries, with particular attention on the Zn-Ce system. The experimental methods and the bench-scale Zn-Ce battery setup used in this work are described in Chapter 3. Chapter 4 presents an experimental study on the use of mixed acids such as MSA-H_2SO_4 or MSA-HNO_3 as the positive supporting electrolyte to improve the long-term performance of Zn-Ce redox flow battery by increasing the Ce(IV) solubility and reducing HER on the negative side due to H^+ crossover. An experimental study of the crossover of different electroactive species through the membrane over 30 charge-discharge cycles is described in Chapter 5. Based on the findings from these measurements, the positive electrolyte composition is then modified according to the measured crossover to minimize its effect and further improve battery performance. In Chapter 6, two regeneration methods that convert the accumulated Ce(IV) back to Ce(III) in the positive electrolyte are compared and shown to significantly improve the voltage efficiency. Chapter 7 presents a comprehensive 2-D transient Zn-Ce redox flow battery model incorporating the crossover of different ions. Once this model is successfully validated against extensive experimental data, it is used to predict battery performance under different conditions. Finally, the conclusions obtained from this work and recommendations for future studies are presented in Chapter 8.

Chapter 2 Literature Review

2.1 Development of Redox Flow Batteries

In 1949, an all-chromium redox flow battery operating with a sulfuric acid electrolyte and based on the conversion between Cr^{2+}, Cr^{3+} and Cr^{4+} ions on lead or mercury electrodes for energy storage was developed by Kangro.[41] The patent filed for this device described the first experimental results for a flow battery as we understand it today. It identified the two major advantages of redox flow batteries: feasibility of energy storage from intermittent sources and the decoupled energy and power capacities. However, due to the highly toxic nature of chromium(VI) solutions and the use of heavy metal electrode materials, this type of flow battery drew less attention than others. In addition, Kangro noted another potential redox couple of Ti^{3+}/Ti^{4+} and Cl^-/Cl_2 that should be feasible for use in a redox flow battery. In this system, the Cl_2 gas produced at the positive electrode during charge would be dissolved in CCl_4.

In 1955, Sn-Fe and Sn-Br redox flow battery systems were described in detail for the first time by Posner.[42] Three years later in 1958, Pieper investigated the possibilities of several redox couples such as Ti(III)/Ti(II), V(II)/V(III), V(IV)/V(V), Fe(II)/Fe(III), Cu(I)/Cu(II) and Ce(III)/Ce(IV) as electroactive species for redox flow batteries and finally conducted a study on the Ti-Fe system.[43] Eventually, as many as 11 different flow cell designs were developed by Pieper, together with different electrolyte compositions. With the optimized system, an energy efficiency of 55% was achieved when operated at current densities over the range of 0.5 – 5 mA/cm^2.

In 1973, researchers at the US National Aeronautics and Space Administration (NASA) invented the first redox flow battery using aqueous-based Fe/Cr redox couples.[44] In this system, 1 mol/L $FeCl_2$ and 1 mol/L $CrCl_3$ in 2 mol/L HCl solutions were used as the negative and positive electrolytes, respectively. The battery included an ion-exchange membrane to separate the electrolytes and carbon felts were used as the electrodes. In 1997, Lim et al. introduced a hybrid flow battery based on a Zn-Br redox couple.[45] In this study, these authors introduced the electrolyte circulation system that is currently in use in more modern RFBs.

In the early 1980s, the first all-vanadium RFB was developed by Skyllas-Kazacos and co-workers at the University of New South Wales, inspired by the work at NASA on Fe-Cr RFBs.[46] A charge-

discharge curve of the all-vanadium RFB system operating with 0.1 mol/L vanadium solutions in 2 mol/L sulphuric acid, graphite plates as electrodes and an anion exchange membrane at a current density of 3 mA/cm^2 was reported for the first time. Countless studies have since been conducted to optimize electrolyte composition, ion exchange membrane, electrode materials, flow battery design and operating conditions, with the ultimate goal of achieving better performance at lower cost.[47–52]

In 1981, a redox flow battery system based on iron deposition on the negative electrode and the Fe(II)/Fe(III) reaction at the positive electrode was reported by Hruska et al.[53] Due to its low cost, easy availability and relatively low toxicity, iron has always been considered to be a very desirable material for flow batteries. However, the reaction kinetics of the Fe/Fe(II) redox couple is very sluggish and hydrogen evolution reaction readily occurs on the negative electrode as an undesired side reaction during charge.

In 1988, Matsuda in Japan introduced the first non-aqueous flow battery containing organic species, in which an organic ruthenium complex based on 2,2'-bipyridine ligands in an acetonitrile solvent was used as the electroactive species.[54] However, the high cost of ruthenium and low overall energy efficiency were the main obstacles for large-scale application of this system. Further investigations on organometallic RFBs have become increasingly more common in recent years. Some of the organometallic RFBs systems that have been studied include V(II)/V(III)-L-cysteine(O_2) and V(II)/V(III)-glyoxal(O_2) and a series of different metal acetylacetonates (V, Cr, and Mn) in acetonitrile by the Thompson group at the University of Michigan.[55–57]

In 2004, a hybrid aqueous Pb-Pb flow battery was developed at the University of Southampton, based on the use of methanesulfonic acid to dissolve Pb(II) ions.[58] In the same year, Clarke patented the principles of a Zn-Ce RFB for the first time.[37,59] This was followed by several experimental studies on this system.[22,60–63] Due to the high cell voltage as high as ~2.4V for this system, the Scottish start-up company Plurion commercialized this technology in 2010.

In 2014, the first metal-free aqueous RFB system based on 9,10-anthraquinone-2,7-disulphonic acid (AQDS) and Br^-/Br_2 redox pairs was developed by Michael Aziz's group at Harvard University.[64] Since then, the number of studies on organic RFBs has increased significantly. The development of the above mentioned RFBs is summarized in chronological order in Figure 2.1.

In addition to the above-mentioned flow battery systems, new concepts in RFB design have also been proposed. In 2014, an vanadium-based photocatalytic flow battery was reported.[65] In this design, a TiO_2 photoanode was used as the positive electrode and a Pt-mesh was used as the negative electrode. The battery was charged under light illumination and could switch to discharge when connected to a load. In the same year, an all-Cu thermally regenerable RFB was patented by Peljo et al.[66,67] This battery capitalized on the strong and stable complexation of Cu^+ ions with acetonitrile (ACN). During discharge, an aqueous stream containing Cu(II) ions was pumped into the positive flow channel, while a slurry containing Cu nanoparticles was fed to the negative flow channel. The positive half-cell employed a copper foam electrode, where Cu(II) ions were reduced to Cu(I) ions during discharge. In the negative half-cell, carbon felt was used as the electrode where Cu nanoparticles were oxidized to Cu(I) ions during discharge. An anion exchange membrane separated the cell into the two compartments and the two electrolyte outflow streams were collected in the same tank for electrolyte recharge. The oxidation state of the Cu(I) ions was stabilized by its formation of complexes with ACN in the electrolyte. The battery was recharged by removing the ACN from the collected electrolyte mixture using thermal energy by distillation accomplished using an external device that collected heat from external sources. This resulted in the production of a slurry electrolyte containing Cu(II) for the positive half-cell reaction and Cu^0 nanoparticles for the negative half-cell reaction. After electrolyte separation by centrifugation, the recharged negative and positive electrolytes streams were again ready for battery discharge. The ACN collected by distillation in the previous step was condensed and re-introduced into the two streams of electrolytes before being pumped into the battery. In 2020, the operation of a microbially-charged RFB was reported for the first time.[68] In this battery, electroactive bacteria (geobacter sulfurreducens) were utilized to charge the negative electrolyte of the RFB operating with a 2,6-AQDS/$[Fe(CN)_6]^{4+}$ redox couple.

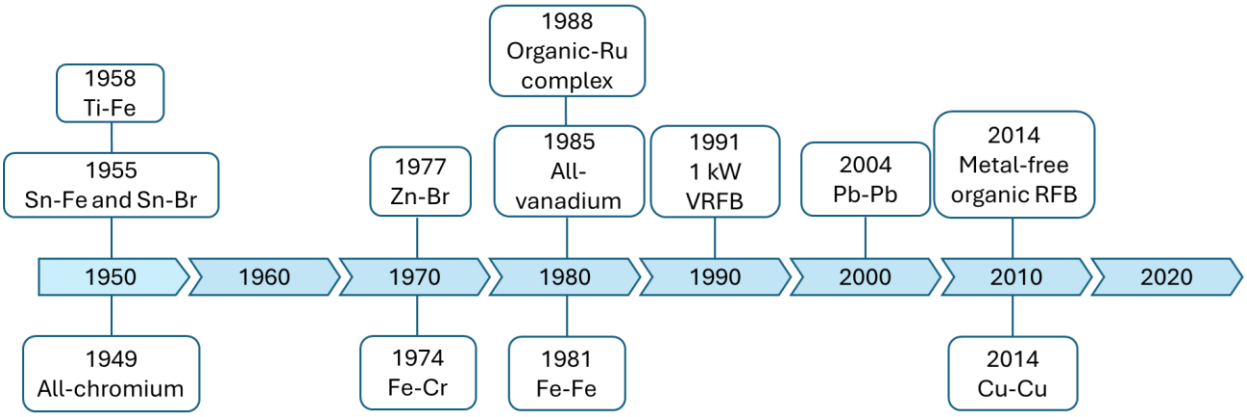


Figure 2.1. Chronological summary of major flow battery developments.

2.2 Popular RFBs

2.2.1 All-V RFBs

The idea of using vanadium ions in its various oxidation states in a battery was first proposed by Pissoort in a patent in 1933. However, no experiments were conducted to prove this concept until Maria Skyllas-Kazacos and co-workers at the University of New South Wales began research on this topic in 1985.[46,69] In an all-vanadium redox flow battery, the V(II)/V(III) redox couple is employed on the negative side and V(IV)/V(V) on the positive side. Sulfuric acid (~5 mol/L) is usually used as the supporting electrolyte on both sides. A fully charged all-vanadium RFB that uses carbon-based electrode materials such as carbon felt or porous fibres has an OCP of ~1.26V at 25°C. The half-cell and overall reactions are as follows:

Negative electrode: $$V^{3+} + e^- \underset{Discharge}{\overset{Charge}{\rightleftarrows}} V^{2+},\ E^0 = -0.25\ V \quad (4)$$

Positive electrode: $$VO^{2+} + H_2O \underset{Discharge}{\overset{Charge}{\rightleftarrows}} VO_2^+ + 2H^+ + e^-, E^0 = 1.00V \quad (5)$$

Overall reaction: $$V^{3+} + VO^{2+} + H_2O \underset{Discharge}{\overset{Charge}{\rightleftarrows}} V^{2+} + VO_2^{+} + 2H^{+} \quad (6)$$

The major advantages of all-vanadium RFBs are that they have relatively high battery efficiencies between 70% and 90% due to lower levels of gas evolution reaction and that the battery can operate with less expensive carbon-based electrode materials.[70] The main disadvantages of all-vanadium RFBs are the high cost of the vanadium-based electrolytes and the toxicity of the vanadium ions and sulfuric acid to the environment. In addition, the low solubility and stability of the V(II), V(III) and V(IV) ions at low temperatures and V(V) ions at high temperatures in sulfuric acid supporting electrolytes reduce the operating temperature to a narrow window between 10 and 40°C controlled by a thermal regulation system and limit the energy density to less than 35 Wh/L.[71–73] In 2010, the use of a mixed acid (H_2SO_4 and HCl) to increase the solubility and stability of vanadium ions in the electrolyte was proposed by researchers at the US DOE Pacific Northwest National Laboratories and was able to improve battery performance by raising the maximum total vanadium species concentration to 2.5 mol/L, representing a ~70% increase in energy capacity compared to that reported in earlier studies.[74]

2.2.2 Fe-Cr RFBs

As the first modern RFB, Fe-Cr RFB was proposed by Thaller in NASA for use in space missions, although it was unsuitable for deep-space travel due to its low energy and power densities.[44] This type of battery was subsequently paired with a photovoltaic cell for stationary energy storage applications, with the aim of overcoming high oil prices resulting from the embargo in 1973. In the early 1980s, an 8×39 cell stack with a capacity of 1 kW/13kW was introduced to match a solar panel array as an energy storage device.[75]

Negative electrode: $$Cr^{3+} + e^- \underset{Discharge}{\overset{Charge}{\rightleftarrows}} Cr^{2+}, E^0 = -0.407V \quad (7)$$

Positive electrode: $$Fe^{2+} \underset{Discharge}{\overset{Charge}{\rightleftarrows}} Fe^{3+} + e^-,\ E^0 = 0.771\ V \quad (8)$$

Overall reaction: $$Fe^{2+} + Cr^{3+} \underset{Discharge}{\overset{Charge}{\rightleftarrows}} Fe^{3+} + Cr^{2+} \quad (9)$$

The major advantage of Fe-Cr RFBs is their low cost since iron is the most abundant element in the earth's crust by mass and the abundance of Cr is ~1000 times higher than that of vanadium.[76] The price of ferrochromium alloys produced throughout the world including Asia, Africa, Europe and Middle East has remained under US$1500/tonne of chromium content since 2019.[77] This alloy contains both of the metallic elements Fe and Cr used in this battery which is another cost-saving feature for the acquisition of the electroactive species. It is estimated that the cost of Fe-Cr RFBs can be as low as $9.4 kW/h, which is comparable to the target cost proposed by the US Department of Energy.[78] Another advantage is its high stability over long-term operation and long life-cycles due to its simple electrode reactions.

When operating the battery, higher temperatures (>50°C) are usually applied to shift the inactive complex ($[Cr(H_2O)_6]^{3+}$) to its electroactive form ($[Cr(H_2O)_5Cl]^{2+}$). Similar to many other types of RFBs, the hydrogen evolution reaction (HER) is one of the main reasons for capacity loss due to the negative potential of the Cr redox reaction. In addition, the relatively low open-circuit voltage (~1.18V) and the use of a highly corrosive HCl electrolyte are also drawbacks of Fe-Cr RFBs that has been the focus of research.[79–81] The discovery that the sluggish Cr(II)/Cr(III) reaction kinetics can be catalyzed by metallic gold and the undesired HER can be suppressed by metallic lead led to the development of a bimetallic negative electrode in which gold and lead nanoparticles are incorporated onto carbon fibres. Of course, the use of gold as an electrocatalyst significantly raises the overall cost especially for grid-scale energy storage.[75,82]

2.2.3 Metal-free RFBs

In 2014, the first metal-free aqueous flow battery was developed by Aziz and co-workers at Harvard University.[64] Their system involved the combination of a (9,10-anthraquinone-2,7-disulphonic acid) AQDS and Br^-/Br_2 redox pair. AQDS undergoes a reversible 2-electron transfer process on a glassy carbon electrode with kinetics that are 1-3 orders of magnitude faster than that of the more common redox couples such as Fe^{2+}/Fe^{3+}, Cr^{2+}/Cr^{3+}, VO^{2+}/VO_2^+, and V^{2+}/V^{3+} on similar electrode materials.[82] Their unit cell was able to achieve ~99% current efficiency when operating at a very large current density (500 mA/cm^2) with a capacity degradation as low as 0.78% per cycle.

The half-cell reactions and overall reaction are listed below:

Negative electrode: $$AQDS + 2H^+ + 2e^- \underset{Discharge}{\overset{Charge}{\rightleftarrows}} \mathrm{AQDSH_2}, E^0 = 0.213V \quad (10)$$

Positive electrode: $$2Br^- \underset{Discharge}{\overset{Charge}{\rightleftarrows}} Br_2 + 2e^-,\ E^0 = 1.087\ V \quad (11)$$

Overall reaction: $$AQDS + 2H^+ + 2Br^- \underset{Discharge}{\overset{Charge}{\rightleftarrows}} \mathrm{AQDSH_2} + Br_2 \quad (12)$$

In a long-term performance test of the AQDS/Br_2 unit cell with a positive electrolyte containing 0.1L 1 mol/L AQDS in 1 mol/L H_2SO_4 and negative electrolyte containing 0.12L 0.5 mol/L Br_2 in 3 mol/L HBr, a coulombic efficiency of 98.35% and capacity retention of 99.84% was achieved over 750 charge-discharge cycles.[83] An AQDS derivative with one hydroxyl group on each benzene ring, namely 1,8-dihydroxy-9,10-anthraquinone-2,7-disulphonic acid, has also been engineered to achieve even better battery performance.[64] This derivative has a lower redox potential and faster reaction kinetics than AQDS, which leads to a larger OCV and better battery performance.

Compared to inorganic RFBs, aqueous redox flow batteries that utilize organic electroactive species as reactants offer some obvious advantages. Firstly, the cost and availability of organic

electroactive species are less constrained by the production and reserves of minerals that contain the key elements (e.g. vanadium, chromium, iron and zinc) since they are usually made from elements such as carbon, hydrogen, nitrogen and oxygen. Secondly, the transition metal elements used in inorganic RFBs must be extracted and purified from ores, whereas the organic electroactive species can be synthesized via green chemistry routes. Thirdly, some of the key physical and electrochemical properties, including solubility and redox potential, can be tailored by the purposeful modification of the structures of the electroactive species molecules. Moreover, some organic species such as quinones are known to undergo two-electron transfer process, which yields a higher energy density.

2.2.4 Zn-Br RFBs

Zinc-bromine RFBs are hybrid systems that utilize the Zn^0/Zn(II) reaction at the negative electrode and the Br^-/Br_2 reaction at the positive electrode. The half-cell and overall cell reactions are listed below:

Negative electrode: $$Zn^{2+} + 2e^- \underset{Discharge}{\overset{Charge}{\rightleftarrows}} Zn(s), E^0 = -0.76V \quad (13)$$

Positive electrode: $$2Br^- \underset{Discharge}{\overset{Charge}{\rightleftarrows}} Br_2 + 2e^-, E^0 = 1.09\,V \quad (14)$$

Overall reaction: $$Zn^{2+} + 2Br^- \underset{Discharge}{\overset{Charge}{\rightleftarrows}} Zn(s) + Br_2 \quad (15)$$

Compared with the most popular and commercialized all-vanadium redox flow battery, Zn-Br RFBs utilize low-cost $ZnBr_2$ as the electroactive material which enables the system to be operated at a cost of $8/kWh. This reported cost is 16 times lower than that of all-vanadium RFBs and 6 times lower than that of Li-ion batteries.[84] In addition, the Zn-Br RFB has a high open-circuit voltage of ~1.82 V and high energy density of ~70 Wh/kg. For comparison, the open-circuit voltage and energy density of all-vanadium RBFs are ~1.5V and 10-50 Wh/kg, respectively.[85,86]

A drawback with this system are the complications associated with bromine. Firstly, extra precautions are required throughout the process and operation of the battery due to the extremely hazardous and corrosive nature of Br_2. Secondly, the operating temperature must be maintained below 50°C to ensure it does not exceed the boiling point of bromine (58.9°C). Even at these lower temperatures, Br_2 is highly volatile. In order to prevent its evaporation from the positive electrolyte, bromine sequestration agents (BSAs) such as N-methyl-N-ethylpyrrolidinium bromide (MEPBr), N-Methyl-N-ethyl morpholinium bromide (MEM), and N-ethylpyridinium bromide (EpyBr) are introduced to the system to capture the Br_2 molecules and form a bromine-rich and dense electrolyte.[87] The Br_2 capture process involving these sequestration agents (denoted as QBr below) can be described by the following reaction:

Br_2 capture: $$QBr + nBr_2 \leftrightarrow QBr_{2n+1} \quad (16)$$

Another critical problem with the operation of Zn-Br RFBs is the uneven zinc layer deposit that tends to form during battery charge. Instead of forming a smooth deposit, small irregularities on the negative electrode surface lead to an uneven current distribution and faster zinc deposition at certain sites, which can grow into needle-like dendrites. During battery operation, portions of these dendrites can break off from the deposited zinc layer into the electrolyte and reduce the columbic efficiency since they can no longer be utilized for battery discharge. Furthermore, the danger exists for the needle-like structure to pierce the separator or membrane used in the battery and lead to self-discharge due to electroactive species crossover and even short-circuiting of the Zn-Br RFB. In addition, the highly corrosive nature of Br_2 may also degrade the separator or membrane, resulting in reduced battery performance and shortened battery lifespan.

2.2.5 Zn-Ce RFBs

2.2.5.1 Zn deposition reaction

Zinc deposition is a well-established industrial process in which zinc ions in an electrolyte are reduced and deposited as metallic zinc on a cathode surface. This process has been widely used in various industrial processes such as electroplating, corrosion protection, battery technology (e.g., zinc alkaline, zinc-air and zinc-nickel batteries) and electrowinning for recovery of metallic zinc from ores and waste materials by cathodic reduction from Zn^{2+}-containing electrolytes in an electrolytic cell.[88–90] At present, conventional zinc electrodeposition is primarily carried out in one of three electrolytes: alkaline zincate (pH>12), acidic chloride (pH 4-6) and acidic sulfate (pH 2-4).[91–93] The use of cyanide zinc baths has been historically one of the most widely used choices due to their excellent throwing power, which describes the ability to deposit zinc uniformly even on recessed and complex surfaces.[94,95] However, cyanide is toxic and poses health and environmental concerns. In addition, the stringent regulations to reduce water pollution and the increasingly high cost of effluent disposal are also reasons that non-cyanide baths have become popular and are now more commonly used for commercial zinc electroplating.

The deposition of zinc is a complicated process mainly governed by electrochemical reactions and influenced by factors such as mass transport and distribution of current. Under the effect of an electric field, the solvated Zn(II) ions migrate toward the anode and gradually de-solvate near the electrode surface. Subsequently, the Zn(II) ions are adsorbed onto the anode surface and gain electrons to be reduced to metallic zinc. This process involves adsorption, electron transfer, nucleation and growth steps and is usually accompanied by the HER side reaction.[96] Zinc electrodeposition in alkaline and neutral/acidic electrolytes operates via different mechanisms and different reactions. In alkaline electrolytes, ZnO first combines with OH^- and H_2O to form zincate ions ($[Zn(OH)_4]^{2-}$), followed by their reduction to form metallic zinc by obtaining electrons on the electrode surface. It is generally accepted that alkaline zinc deposition proceeds by the following steps[97]: 1) mass transfer of zincate ions from the bulk to the electrode surface by migration, diffusion and convection to replace the zincate ions reduced at the electrode surface, 2) transformation of ($[Zn(OH)_4]^{2-}$) to $Zn(OH)_2$ which is generally believed to be the species directly involved in reduction, 3) reduction of $Zn(OH)_2$ via a sequence of two 1-electron transfer steps to adsorbed Zn atoms that can move over the electrode surface, 4) movement of these newly formed

Zn ad-atoms to newly formed metal lattice sites on the electrode surface for crystal growth or gather with other Zn atoms to nucleate new crystals. Since these steps occur in series, the overall deposition rate is determined by the slowest step in this sequence. Step 3) above in the zinc deposition process involves two consecutive one-electron transfer reactions in which an intermediate Zn(I) adatom is generated first, followed by its conversion to elemental Zn(0).[98]

The reaction mechanism of zinc deposition in neutral or acidic environments is different than that in the above mentioned alkaline solutions and involves the following 3 steps: 1) diffusion of Zn(II) from the bulk to the electrode surface where reduction occurs, 2) direct reduction of Zn(II) to form Zn ad-atoms without any pre-conversion steps, 3) nucleation and growth process similar to step 4) above in the case of alkaline deposition by which the Zn ad-atoms form a metallic zinc deposit.[97] As with metal reduction under alkaline conditions, Zn(II) reduction also involves two consecutive one-electron transfer steps with the first step usually being rate-limiting.[99]

Organic additives (organic compounds with high molecular weight) are widely used in zinc electroplating baths to inhibit hydrogen evolution reaction and act as crystal growth modifiers that enable the growth of denser and smoother deposit surfaces.[100,101] The quality and morphology of electrodeposited zinc is also affected by other factors such as temperature, applied current density, electrolyte composition, plating time and the anode-cathode separation distance.[97] Since the behaviour of zinc deposition/dissolution is relatively well understood, the low cost of metallic zinc and low potential of the Zn/Zn(II) redox couple, zinc-based batteries are used for numerous applications ranging from disposable batteries to rechargeable systems. For example, the most commonly used alkaline batteries developed in the 1950s utilize zinc as the negative electrode, manganese dioxide (MnO_2) as the positive electrode and alkaline potassium hydroxide as the electrolyte. During discharge of rechargeable zinc-air batteries, oxidation of the zinc negative electrode to zinc hydroxide in alkaline conditions releases two electrons, which combine with oxygen from the air and water at the positive electrode to form hydroxide ions that replenish the electrolyte. Some of the advantages of zinc-based batteries include low cost, environmental friendliness, high safety and relatively high energy densities.[102]

2.2.5.2 Ce(III)/Ce(IV) redox couple

The ability of Ce(IV) to be a strong one-electron oxidant in acidic aqueous media was recognized as early as 1931 and has led to many studies on the Ce(III)/Ce(IV) redox properties under a variety of conditions.[16,103–105] Ce(IV) salts are reported to be very useful reagents for the functionalization of alkenes and catalysis of esterification reactions. In addition, they are also utilized in the electrosynthesis and initiation of radical polymerization reactions.[19] Ceric ammonium nitrate (CAN) is used as powerful oxidizing agent in organic chemistry.

The standard electrode potentials for the Ce(III)/Ce(IV) redox couple ranging from 1.28V and 1.72V vs. Ag/AgCl have been reported in different acidic electrolyte solutions, reflecting its dependence on the supporting electrolyte medium. A standard potential for the Ce(III)/Ce(IV) redox couple of +1.46 V vs. SCE was measured based on the oxidation of $Ce(ClO_4)_3$ in 1 mol/L $HClO_4$.[105] It was found that the redox potential increased by ~400 mV when the supporting electrolyte was changed from 1 mol/L HCl to 1 mol/L $HClO_4$. This indicates that the potential for Ce(III) oxidation increases when the supporting acid has lower coordinating ability.[15] In addition, it has been reported that the addition of fluoride ions to solutions containing Ce(IV) ions renders them incapable of oxidizing iodide. These studies reveal that the redox properties of the Ce(III)/Ce(IV) couple are sensitive to the nature of the ligands and counter ions in solution.[106] Due to its high standard electrode potential, the Ce(III)/Ce(IV) redox couple has also been widely studied for its potential application as electroactive species in RFBs for large-scale energy storage.[107–109]

Fang et al. conducted voltammetry and constant-current electrolysis experiments to investigate the electrochemical behavior of the Ce(III)/Ce(IV) redox couple at different temperatures and concentrations of the sulfuric acid supporting electrolyte.[107] These researchers observed that the current peaks for both oxidation and reduction decreased with an increase of the sulfuric acid concentration and the separation between the anodic and cathodic peaks increased when the sulfuric acid concentration increased from 0.1 to 2 mol/L, which then decreased with a further rise in the acid concentration. They also found that elevated temperatures were favorable for the Ce(III)/Ce(IV) redox couple. When the temperature was raised from 298°K to 333°K, the peak current increased and the separation between the anodic and cathodic peaks decreased. In another

study by Buchanan et al., the structures of Ce(III) and Ce(IV) ions and the charge transfer mechanism in sulfuric acid supporting electrolyte was studied experimentally using X-ray absorption fine structure spectroscopy (EXAFS) and kinetic measurements and theoretically using density functional theory (DFT).[110] The authors concluded that each Ce(III) ion is coordinated by nine water molecules and proposed that Ce(IV) is complexed by six water molecules and three bisulfates in sulfuric acid electrolytes. A two-step charge transfer process was identified for the conversion of Ce(III) from Ce(IV). In the first step, the Ce(IV) ions in the form of $[Ce(H_2O)_6(HSO_4)_3]^+$ exchange bisulfate anions with water molecule to form $[Ce(H_2O)_9]^{4+}$. This is followed by the rate-determining step whereby the actual electron transfer occurs and Ce(IV) in the form of $[Ce(H_2O)_9]^{4+}$ is reduced to Ce(III) in the form of $[Ce(H_2O)_9]^{3+}$.

2.2.5.3 Overview of Zn-Ce RFBs

The Zn-Ce RFB was introduced by Plurion Inc (UK) in 2005 and has since attracted research interest due to its high cell voltage and low cost.[59] The OCV of the Zn-Ce RFB is ~2.4V, which is almost double that of the all-vanadium RFB. The Zn-Ce RFB is categorized as a hybrid system since an electroactive zinc metal layer is plated on the surface of the negative electrode during battery charge. The half-cell and overall reactions are listed bellow:

Negative electrode:
$$Zn(II) + 2\,e^- \underset{Discharge}{\overset{Charge}{\rightleftarrows}} Zn(s), E^0 = -0.76V \quad (17)$$

Positive electrode:
$$2\,Ce(III) \underset{Discharge}{\overset{Charge}{\rightleftarrows}} 2\,Ce(IV) + 2\,e^-,\ E^0 = 1.67\,V \quad (18)$$

Overall reaction:
$$Zn(II) + 2\,Ce(III) \underset{Discharge}{\overset{Charge}{\rightleftarrows}} Zn(s) + 2\,Ce(IV) \quad (19)$$

Although this technology was patented in 2005, the study of the Ce(III)/Ce(IV) redox couple in acid electrolytes in half-cells stretches back many decades earlier.[111,112] Moreover, the chemistry of zinc deposition and dissolution in various solutions was already well studied because of the

importance of these processes in hydrometallurgical and electroplating industries, not to mention the studies conducted on batteries that use Zn(0)/Zn(II) reaction at the negative electrode.[101,113,114] Zinc is also a very cheap and abundant metal element suitable for application in batteries. As of 2023, the price of zinc was $2870 per tonne, which was significantly lower than that of copper (~$8000), chromium ($10,000) and vanadium ($30,000), although much higher than that of iron (~$120).[115] The price of cerium was ~$3000/tonne as of 2024.[116]

Due to the large OCV, side reactions such as hydrogen evolution reaction (HER) and oxygen evolution reaction (OER) typically occur on the negative and positive electrodes, respectively. The side reactions result in a loss of columbic efficiency of the battery and pH changes near the electrode surface. These side reactions are listed bellow:

Negative side reaction: $$2\,H^+ + 2\,e^- \xrightarrow{charge} H_2\uparrow, E^0 = 0\,V \quad (20)$$

Positive side reaction: $$2\,H_2O \xrightarrow{charge} 4\,H^+ + 4\,e^- + O_2\uparrow,\ E^0 = 1.23\,V \quad (21)$$

Electrode materials: Carbon-based composite materials such as planar carbon polyvinyl-ester composites are commonly used as the negative electrode for the Zn^0/Zn(II) reaction in small laboratory-scale flow batteries for performance investigations.[60,117] The patent on a Zn-Ce RFB filed by Clarke et al. in 2005 described the use of glassy carbon as the electrode for both the negative and positive reactions.[59] In subsequent early trials using commercial products, Pt-Ti electrodes were used on the positive side.[60] Various materials including graphite, carbon polyvinyl-ester, carbon felt and 3-D platinized-titanium mesh have been tested as the positive electrode.[37] The use of carbon felt and the 3-D platinized-titanium mesh yielded the highest conversion rate of Ce(III) to Ce(IV) under the same operating conditions.[37] However, the carbon-based electrode materials either exfoliated or expanded during battery operation and were damaged permanently due to the highly oxidizing nature of Ce(IV) ions. Degradation products (carbon particles and sludge) were found in the electrolyte after only a few battery cycles. In comparison, the 3-D

platinized-titanium mesh showed high stability throughout the charge-discharge cycles, which makes it the preferred positive electrode material.[37]

In the early trials of the commercial-scale Zn-Ce RFB developed by Plurion, a carbon-HDPE (high-density polyethylene) composite materials coated with Ti and Pt using physical vapour deposition was used as the positive electrode. However, due to the corrosion of the carbon materials and formation of pinholes on the coating after battery cycling, the positive electrode material was switched to platinized-titanium mesh in later trials.[60] Later, a ceramic electrode material made of reduced titanium oxide with the general formula of Ti_nO_{2n-1} ($3<n<10$), commercially termed Ebonex® proved to be a suitable electrode material due to its high electrical conductivity, chemical stability and catalytic activity.[118,119] In addition, Ebonex® coated with 2 mg/cm^2 Pt prepared by electrodeposition was shown to have similar electrochemical activity as pure Pt for redox couples such as Ce(III)/Ce(IV), Ag(I)/Ag(II) and $[Fe(CN)_6]^{3-}$/$[Fe(CN)_6]^{4-}$ in acidic solutions.[120] This Pt/Ebonex® electrode was then tested in a flow cell for >500 hours and exhibited no degradation in its properties, thereby demonstrating its excellent stability. On the other side, a 1 mm-thick Ti sheet has been successfully used as the negative electrode for a commercial-scale Zn-Ce RFB.[60]

Electrolyte: As mentioned in the Introduction, MSA is commonly used as the supporting electrolyte in both negative and positive compartments in Zn-Ce RFB systems. The conductivity of MSA is as high as 0.30 S/cm, which is comparable to that of hydrochloric acid and sulfuric acid (0.35 S/cm and 0.44 S/cm) while being much less corrosive.[121] Furthermore, the solubility of Ce(III) and Ce(IV) ions in MSA is much higher than in sulfuric acid, which is important for achieving high battery energy density. At the same time, the solubility of Zn(II) in MSA is as high as 2.16 mol/L.[37] More importantly, the use of MSA has been shown to significantly reduce the tendency of zinc dendrites to form and grow on the negative electrode surface during battery charge.[122] Sulfuric acid is not only very toxic to living things, but is also highly corrosive to the metal components of an RFB system. In addition, sulfuric acid-containing mists generated during industrial processes can cause significant damage to the human respiratory system if they are inhaled. On the other hand, methanesulfonic acid is also toxic and corrosive, but much less

aggressive and hazardous than sulfuric acid. Methanesulfonic acid is also biodegradable and breaks down to relatively benign products such as carbon dioxide and water.[123,124]

An important consideration in the choice of the positive electrolyte composition is that the Ce(III) solubility is highest at lower MSA concentrations, whereas the opposite trend is observed in the case of the Ce(IV) solubility (Figure 3.2). Since it is important that the solubilities of both Ce(III) and Ce(IV) be as high as possible, the use of an MSA concentration of 4 mol/L in the positive electrolyte is optimum since it ensures a solubility of ~1.2 mol/L for both species at room temperature.[125,126] However, it turns out not to be feasible to operate Zn-Ce RFBs at such high Ce(III) concentrations due to the excessive viscosity of such solutions, leading to large drops in both the coulombic and voltage efficiencies. Thus, the optimum Ce(III) concentration in the positive electrolyte in its fully discharged state is found to be 0.8 mol/L.[37] Based on these considerations, the positive electrolyte composition typically used is 0.8 mol/L Ce(III) in 4 mol/L MSA.

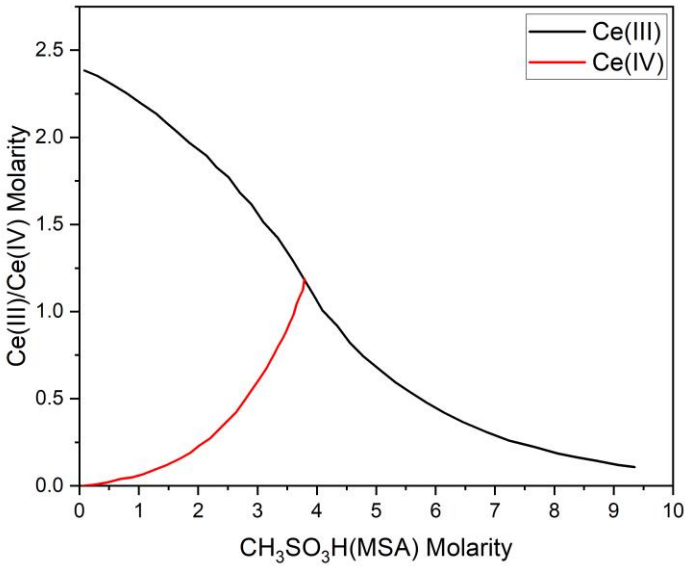


Figure 2.2. Solubilities of Ce(III) and Ce(IV) in MSA measured at 298°K (reproduced with permission).[127]

Experiments on the effect of the Zn(II) concentration in the negative electrolyte showed that it has little effect on the coulombic and voltage efficiencies over the range from 0.5 mol/L to 1.5 mol/L

at an applied current density of 50 mA/cm^2, although higher Zn(II) concentration is beneficial to the battery performance when operating at high current densities to prevent mass transfer limitations.[37] The optimum negative electrolyte composition was found to be 1.5 mol/L Zn(II) in 1 mol/L MSA. The use of a lower MSA concentration than on the positive side helps reduce the extent of the hydrogen evolution side reaction, which benefits the coulombic efficiency.

Several studies have been conducted to study the effect of employing various mixed acids as supporting electrolytes for Zn-Ce RFBs. Nikiforidis et al. conducted comprehensive research on the electrochemical activity of the Ce(III)/Ce(IV) redox couple in mixed acid electrolytes containing MSA as the base electrolyte with different concentrations of hydrochloric, nitric and sulfuric acid.[33] Cyclic voltammetry experiments showed that the reversibility and kinetics of the Ce(III)/Ce(IV) reaction was significantly enhanced when the 4 mol/L MSA base electrolyte was combined with 0.5 – 1 mol/L hydrochloric acid. In addition, higher diffusion coefficients of both Ce(III) and Ce(IV) and exchange current density were obtained when using MSA-H_2SO_4 and MSA-HNO_3 supporting electrolytes, although the reversibility of the Ce(III)/Ce(IV) reaction remained the same.[33] In another study, Chen et al. investigated the viability of an organic supporting electrolyte for a Zn-Ce RFB prepared by dissolving 1-butyl-3-methylimidazolium chloride (BMImCl) in water.[128] The idea behind this approach was to reduce the amount of free water in the electrolyte in order to widen the potential window for water stability to ~ 3 V and lower the extent to which the HER and OER occur on the negative and positive electrodes, respectively, during charge. In their proof-of-concept experiment, the negative electrolyte and the positive electrolyte contained 0.05 mol/L $ZnSO_4$ and 0.1 mol/L $Ce(SO_4)_2$, respectively, in ~ 4.37 mol/L BMImCl. The battery achieved a coulombic efficiency and voltage efficiency of 66% and 73%, respectively, when operated at a current density of 0.075 mA/cm^2, electrolyte flowrate of 20 mL/min and temperature of 298°K, indicating the potential of this organic supporting electrolyte for RFB applications.

As for changes to the negative electrolyte, the use of a solution containing 0.9 mol/L ZnMSA and 0.6 mol/L $ZnCl_2$ in 1 mol/L MSA supporting electrolyte was introduced by Amini and Pritzker in our group.[129,130] The addition of chloride ions significantly increased the amount of deposited zinc layer relative to the hydrogen evolution reaction, reduced the nucleation overpotential and enhanced the exchange current density of the negative electrode reaction. Both the battery

columbic efficiency and voltage efficiency were increased relative to that observed when the negative electrolyte only contained 1.5 mol/L ZnMSA in 1 mol/L MSA. In addition, the use of the mixed MSA-chloride negative electrolyte reduced the build-up of Ce(IV) ions in the positive electrolyte since it enabled a longer discharge time and further improved the battery durability.

2.2.5.4 Challenges of the application of Zn-Ce RFBs

Although having one of the highest open-circuit voltages, the battery efficiency and long-term performance of Zn-Ce RFBs are not as good as that of all-vanadium RFBs. Therefore, some key challenges must be overcome if this technology is to be commercialized for large-scale applications. The challenges listed in this section are the main focuses of our study and can be summarized as 1) parasitic hydrogen evolution reaction on the negative half-cell during battery charge, 2) crossover of electroactive species due to the non-ideal behaviour of the ion exchange membrane, and 3) imbalance in the discharge capacity of the two electrolytes resulting in the accumulation of Ce(IV) ions on the positive side.

1) parasitic hydrogen evolution reaction

While a number of studies have focused on improving the performance of Zn-Ce RFBs, less research has been conducted to investigate its performance decay especially during long-term operation. By measuring the electroactive species concentrations after each charge-discharge cycle and separately recording the potentials of the two electrodes, the limiting half-cell reaction during each cycle can be identified. When the battery containing a negative electrolyte containing 1.5 mol/L ZnMSA in 1 mol/L MSA and positive electrolyte containing 0.8 mol/L CeMSA in 4 mol/L MSA (optimum compositions in MSA-only based solutions) in its fully discharged state is subjected to charge-discharge cycles at a current density of 25 mA/cm^2, charge duration of 60 min and 50°C, the negative half-cell reaction is found to be the limiting reaction by the second cycle.[32] This is caused by the occurrence of the irreversible HER side reaction on the negative electrode surface during battery charge. The electrons consumed by the HER are transferred to hydrogen gas which dissipates away from the electrode and are unavailable for battery discharge. This reduces the amount of zinc that would otherwise be deposited on the negative electrode and available for

battery discharge. This leads to the negative electrode reaction becoming the limiting side during operation of the RFB. However, the situation changes again due to the sustained effects of the HER on the negative electrode and the net transfer of H^+ ions from the positive to the negative electrolyte due to its large concentration gradient. When the H^+ concentration on the positive side becomes low enough, the solubility of Ce(IV) ions decreases to the point that it begins to precipitate out as an oxide. The Ce(IV) ions that precipitate are no longer available for the Ce(III)/Ce(IV) reaction, leading to a significant drop in the energy capacity of the positive electrode reaction so that this side of the cell becomes limiting thereafter.

In fact, the HER is not only observed as an undesirable side reaction in zinc-based batteries but also in many other batteries and electrochemical systems (e.g., electrodeposition of zinc and other metals) and so is a critical issue to be addressed. It has been shown that certain additives can be introduced to the electrolyte to suppress the HER. For example, K_2S and FeS were found to be effective in inhibiting HER when added to the electrolyte in a lead-acid battery by increasing the overpotential of the HER.[131] The use of organic additives such as dimethyl sulfoxide (DMSO), dimethyl carbonate (DMC), acetonitrile (AN), 1,2-dimenthoxyethane (DME) and trimethyl phosphate (TMP) has also been extensively reported to reduce HER, although these organic additives also increase the zinc nucleation overpotential and lower the ionic conductivity of electrolyte when added at higher concentrations.[132–137] Another very effective approach to inhibit HER is by modifying the electrode surface. For example, Zhao et al. incorporated up to 0.04 wt.% of Ga_2O_3 or Bi_2O_3 into a carbon-based negative electrode using a binder, with the aim of reducing the HER in a lead-acid battery.[138] Their experimental results showed that the rate of HER was suppressed and higher battery coulombic efficiency achieved by adding 0.01 wt.% Ga_2O_3 to the carbon-based negative electrode using a carboxymethyl cellulose (CMC) binder.

2) crossover of electroactive species

Another factor that complicates the long-term behaviour of the Zn-Ce RFB system (and other RFBs) is the crossover of H^+ from the positive to the negative electrolyte due to the large H^+ concentration gradient across the membrane, which leads to an increase in acidity and enhancement in the HER on the negative electrode. Ideally, a proton exchange membrane would only allow the transfer of a certain amount of H^+ ions depending on the state of charge of the

battery to conduct electricity and maintain the electroneutrality of the system, while preventing the transfer of more H^+ and the other electroactive species from one side to the other. Unfortunately, Nafion ion exchange membranes typically used in Zn-Ce RFBs are not highly selective and allow the cross-over of most species. As shown in Figure 2.2, the solubility of Ce(IV) ions is reduced at lower MSA concentrations. Therefore, both the build-up of the Ce(IV) concentration (discussed in challenge 3) below) and reduction in the acid concentration in the positive electrolyte eventually lead to the precipitation of Ce(IV) ions, which permanently reduces the battery efficiency and lifespan. Strategies to reduce the undesired hydrogen evolution side reaction and increase the Ce(IV) solubility in the positive electrolyte are critical in order to improve the battery efficiency and lifespan.

One approach to reduce the extent of the HER on the negative electrode is to lower the amount of H^+ crossover during battery operation by lowering the H^+ concentration gradient across the membrane. This would entail reducing the acidity in the positive electrolyte below the 4 mol/L MSA that is typically used, while still maintaining a high Ce(III)/Ce(IV) solubility and favourable reaction kinetics for the Ce(III)/Ce(IV) redox couple.

Another approach is to use an anion exchange membrane instead of a Nafion cation exchange membrane in the Zn-Ce RFB to reduce H^+ crossover. Unfortunately, commercially available anion exchange membranes are not usually as mechanically and chemically stable as Nafion.[38] This is likely to be a particular problem in the case of Zn-Ce RFBs due to the extremely high acidity and presence of highly oxidizing Ce(IV) ions in the positive electrolyte. In a recent study from our group by Amini and Pritzker, a commercially available anion exchange membrane (Fap-375-PP) was used in a Zn-Ce RFB operated at a current density of 25 mA/cm^2 at 50°C with a positive electrolyte initially containing 0.8 mol/L Ce(III) in 4 mol/L MSA.[38] These experiments showed that the anion exchange membrane was permanently damaged after ~15 charge-discharge cycles, leading to a dramatic drop in battery efficiency and eventually to complete battery failure. Several other anion exchange membranes were also tested for potential application in Zn-Ce RFBs, but none exhibited satisfactory performance or stability.[38] To the best of our knowledge, currently no anion exchange membrane that matches the excellent mechanical and chemical stability of Nafion membranes and can withstand the extreme conditions in a Zn-Ce RFB is available. Thus, the

development of reliable anion exchange membranes is critical for performance and lifespan improvement of RFBs operating with Ce(IV)-containing solutions.

Much attention has also been focused on the development of cation exchange membranes that have comparable stability to Nafion. For example, sulfonated poly(arylene thioether ketone) (SPTK) and sulfonated poly(arylene thioether ketone ketone) (SPTKK) were synthesised by Chen et al. using one-pot polymerization method, followed by post-sulfonation using chlorosulfonic acid as the sulfonation agent in dichloromethane solution.[139] These membranes were then tested in an all-vanadium RFB and showed one order of magnitude lower VO^{2+} permeability compared with the Nafion 117 membrane, which led to higher coulombic efficiency. In another study, a quaternized cardo-poly(etherketone) (QPEK-C) anion exchange membrane was synthesised by chloromethylation of the cardo-polyetherketone (PEK-C) polymer followed by reaction with trimethylamine for quaternization with the aim of minimizing ion crossover, while ensuring good ionic conductivity and both excellent mechanical and chemical stability.[140] The V-Ce RFB was able to achieve an average of 97.5% coulombic efficiency and 77% voltage efficiency when operated at 40 mA/cm^2 over 50 cycles. More importantly, no significant changes of the properties of the anion exchange membrane such as ionic conductivity, ultimate tensile strength and elongation at break were observed, suggesting that this membrane might be a promising candidate for RFB applications. Gu et al. developed a double-membrane cell design consisting of both an anion exchange membrane and cation exchange membrane separated by an electrolyte containing 4 mol/L $NaClO_4$.[141] The structure of the battery therefore contains the following sequence of components: electrolyte, anion exchange membrane, electrolyte, cation exchange membrane and electrolyte. This unique cell design allowed for the use of very different supporting electrolytes on the two sides, such as an acidic electrolyte on one side and alkaline on the other. Although proof-of-concept experiments showed that this cell exhibited a very low overall ion crossover rate when operated at a current density of 5 mA/cm^2, the voltage efficiency was compromised due to the large internal resistance of the double-membrane cell design. Since the membrane design and synthesis are not the focus of our study, the possibility of using the aforementioned cell structure is not investigated in our study of the Zn-Ce RFB system.

3) imbalance in the discharge capacity of the two electrolytes resulting in the accumulation of Ce(IV) ions on the positive side.

Since the side reactions are irreversible and the HER occurs to a much greater extent than the OER on the positive electrode, the amount of zinc metal deposited on the negative electrode and Ce(IV) generated in the positive electrolyte do not follow the ideal 2:1 stoichiometry ratio. As a result, this can lead to complete removal of the zinc deposit from the negative electrode during battery discharge before all of the Ce(IV) produced during charge can be converted back to Ce(III) and therefore to the gradual build-up of unreduced Ce(IV) ions in the positive electrolyte from cycle to cycle. Eventually, Ce(IV) reaches its solubility limit and starts to precipitate out from the positive electrolyte, accumulate in the electrolyte tank and thereby reduce battery performance. Therefore, a strategy to regenerate the positive electrolyte by reducing the accumulated Ce(IV) back to Ce(III) in the electrolyte would be beneficial to extend battery life and improve its efficiency. On the other hand, it would not be beneficial to convert all of the Ce(IV) to Ce(III) at the end of each charge-discharge cycle since this will tend to lead to low Ce(IV) concentrations at the start of discharge and possible mass transfer difficulties for reduction of Ce(IV) during discharge. From our experience, an initial Ce(IV) concentration slightly higher than 0 mol/L (e.g., ~0.05 mol/L) would be enough to make sure that the positive electrode reaction does not become the limiting half-cell reaction and reduce battery efficiency.

Another advantage of regenerating the positive electrolyte is that this would avoid having to discard some or all of this solution and thereby reduce the overall cost of Zn-Ce RFBs and make them more competitive. An ideal method to re-balance the positive electrolyte should be easy to operate and inexpensive, while not introducing any contaminants to the electrolyte. One approach investigated in the case of a Ce-V RFB was to use a catalytic bed loaded with RuO_2 or IrO_2 in the Ce half-cell to discharge the positive electrolyte.[142] This method was very effective since RuO_2 and IrO_2 are excellent catalysts for the oxidation of water to O_2 and thereby drive the reduction of Ce(IV) back to Ce(III). Since the same Ce(III)/Ce(IV) redox chemistry occurs in Zn-Ce RFBs, this idea can be readily adapted to regenerate the positive electrolyte in our system.

Another potentially effective and simple method to regenerate the positive electrolyte is to use hydrogen peroxide as a reducing agent to convert the accumulated Ce(IV) back to Ce(III). In fact, the reaction mechanism of the reduction of Ce(IV) by hydrogen peroxide under different conditions was extensively studied as early as in the 1950s.[143] The kinetics of Ce(IV) reduction in the presence of different supporting acid electrolytes was investigated and found to proceed as two

consecutive one-electron steps that went to completion within a few seconds at room temperature even when the Ce(IV) and the hydrogen peroxide were present at only micromolar concentrations.[144,145] A major advantage of this method compared to the use of RuO_2 and IrO_2 micro-particles is that the amount of Ce(IV) ions to be reduced can be precisely controlled since the reduction reaction follows 1:1 stoichiometry between Ce(IV) and H_2O_2. The amount of hydrogen peroxide needed to regenerate the positive electrolyte can be determined once the Ce(IV) present in the electrolyte is measured. Hydrogen peroxide can be easily introduced to the electrolyte tank using a pipette without the need for an extra circulation system to divert the electrolyte from the tank or an external chamber for the reaction to occur. Furthermore, no danger of contamination of the battery that is harmful to its performance exists with this regeneration procedure. This method appears very promising for bench-scale as well as future large-scale Ce-based RFBs.

2.3 RFB Modelling

Experimental investigations of RFBs obviously are aimed at providing important and extensive understanding of these systems. However, certain important information such as the distributions of ion concentrations and potential within the electrolytes and electrodes (in the case of porous electrodes), current distribution and flow patterns of different ion species cannot be obtained from experiments. Moreover, the time and cost to conduct laboratory-based experiment investigations is another consideration that cannot be neglected. In this regard, the development of mathematical models aimed at simulating battery performance, optimizing operating conditions and designing cell components for improved performance can be extremely valuable. With the aid of mathematical modelling, detailed information such as voltage and current distributions, variation of ion concentrations across the electrolytes and the flux of the various soluble species can be systematically analyzed to provide insight into battery design and performance improvement. Accordingly, the relationship between overpotential, current density, flow rate, species concentrations and electrode structure in RFBs have been intensively investigated using various models.

Based on the intended application, RFB simulations can be classified into four different types: i) market, ii) stack-and-system, iii) cell and iv) material. In market-level modeling, cost, safety and

lifespan are the major considerations. For example, an empirical model that describes the overall capital costs is presented as a function of different variables such as power capacity of the battery, cost of the electrolyte, cost of the membrane, battery overall efficiency and operating current density.[146] Stack-and-system models neglect the physicochemical processes inside the flow battery and describe the system in terms of a zero-dimensional transient equivalent circuit and lumped parameter model. RFB models at the cell or mesoscopic level account for 1-, 2- or 3-dimensional transport phenomena occurring within the electrolytes and electrodes and electrochemical reaction kinetics and provide more detailed and hopefully accurate descriptions of unit cell performance. Materials modeling of RFBs provides precise analysis of the effect of micro-structure and molecular/atomic structure on overall battery performance. In the most detailed multi-scale models, phenomena occurring over a range of size scales from molecular/atomic to mesoscopic to macroscopic are considered. The development of these relatively low-cost and time-saving mathematical models has made redox flow battery optimization and design more efficient and accessible. Detailed information concerning the above-mentioned model types is provided in the following paragraphs.

2.3.1 Modelling application

2.3.1.1 Market-level modelling

Cost reduction is one of the most important challenges to be addressed in order to enhance the competitiveness of RFB technology. Accordingly, the primary goals of market-level models are to accurately quantify and analyze the various costs of RFB systems in order to meet market requirements and to account for the factors that affect these costs. One of the most representative models of this type was developed by Zhang et al.[146] in order to determine the overall costs associated with energy and power density of an all-vanadium RFB. These researchers defined a relative sensitivity index to indicate the influence of different cost factors such as electrolyte, membrane, electrode materials and operation current density on the total cost of an RFB system. A higher index indicates that a factor has a greater influence on the cost. A key finding of this analysis was that the overall cost of the RFB system was most sensitive to the costs of the electrolyte and membrane. Another model developed by Viswanathan et al. was used to investigate the relationship between the cost and performance of 4 MWh/1 MW all-vanadium and Fe-V RFB systems.[147] This cost model was composed of 3 sub-models: an electrochemical model, a shunt

current model and a pumping loss model. The electrochemical model was used to calculate the effects of applied current density, state-of-charge, operating temperature, electrolyte flow rate and initial concentration of electroactive species. The current passing through the flow channels and the manifolds was calculated using the shunt current model, while the pump model estimated the energy loss associated with the flow of the electrolytes through the cell and optimized flow channel design. With the help of the model, the operating parameters and battery design conditions such as flow rates, power density, electrode area, number of unit cells and flow channel dimensions could be adjusted to maximize efficiency and minimize capital costs. They found that the cost of the electrolyte and membrane made up 43% and 27%, respectively, of the total cost of the 4 MWh/1 MW all-vanadium RFB system they considered. If this system were down-sized to 0.25 MWh/1 MW, the cost of the membrane became 44% of the total and the electrolyte costs was reduced to 8%.[147] A techno-economic model that calculated specific system costs and broke down the costs of the different components of a 120 kWh/10 kW all-vanadium RFB system was developed by Noack et al.[148] These authors found that the failure of the bipolar plate materials is the biggest problem for RFB systems, although the bipolar plates only contribute a minor part of the total ohmic loss of the stack. Therefore, less expensive bipolar plates made with stronger mechanical properties would be particularly advantageous to reduce the overall cost of flow battery stacks even if they have lower electrical conductivity. They also found that it would be difficult to achieve a competitive RFB system with redox reactions that have low cell voltages smaller than 1 V. Such a system would require a higher number of unit cells to achieve the desired power density and extremely low cell resistance to be economically feasible, which would increase the total costs even with lower material costs.

2.3.1.2 Stack-and-system level modelling

Stack-and-system modeling of RFBs is often done for the purposes of process control where a mathematically simplified yet accurate description of flow battery systems is preferred. Instead of focusing on the detailed spatial and temporal distributions of variables such as current, voltage and ionic concentrations, system-and-stack models concentrate on the system operating parameters to predict stack performance and overall efficiency. To simplify these models, several assumptions

are often made: 1) the concentration of each species is uniform within the cells, pipes and electrolyte tanks, 2) the cells and tanks behave as continuous stirred reactors and 3) the physical properties of the cells and stack such as resistance remain constant throughout battery operation.[149–151] Scamman and Roberts developed a utility-scale model to predict the technical and commercial performance of a 120 MWh/15 MW polysulfide/bromine (PSB) storage plant.[152] This model evaluated the system performance based on various technical and commercial parameters such as operating current density, electrolyte flowrate and temperature. Based on the simulation results, a range of current density and optimal electrolyte flow rates were identified to make the plant economically viable for commercial applications. The model developed by Xing and Zhang focused on the investigation of the shunt current loss in all-vanadium RFB stacks.[153] The shunt current in a RFB stack refers to the unintended current that flows through a parallel path between cells with sufficiently low resistance and thereby diverts a portion of the total current, which is one of the major factors reducing the system efficiency in RFB systems. The model studied the impact of different charge and discharge patterns on shunt current loss. The analysis using this model showed that a reduction in the number of cells connected in a series configuration, decrease in the resistance of manifolds and channels and increase in the power density generated by a single cell would be viable approaches to lowering the shunt current in all-vanadium RFB stacks. Another stack model developed by Tand and Skyllas-Kazacos described the performance of an all-vanadium RFB consisting of 19 unit cells and two cylindrical electrolyte tanks with the aim of studying the effect of temperature variations during operation.[151] Model calculations showed that the electrolyte temperature is most strongly affected by the applied current density, electrolyte flowrate, surrounding temperature and the heat generated by the ohmic cell resistance. Based on these findings, temperature would best be controlled by fabricating the electrolyte tanks made from materials that have high thermal conductivity and designing the tanks with larger surface area to enhance the heat transfer flux to the surroundings in order to maintain the temperature of electrolyte within the desired range.

2.3.1.3 Cell-level modelling

In cell-level RFB models, factors such as fluid flow, reaction kinetics, transport through electrolyte, electrodes and membrane, electronic contact resistance and mass-transfer resistance between the bulk and electrode surface are carefully considered. Compared to stack-and-system models, cell level modelling of RFBs provides more in-depth and comprehensive predictions of single battery operation. The first cell-level RFB model was developed by NASA for the Fe-Cr system as early as 1984.[154] This model incorporated redox kinetics, mass transfer, ohmic effects and the hydrogen evolution side reaction on the negative electrode and was used to determine the optimum electrode thickness and electrolyte flow rate, amount of hydrogen gas produced and the effect of temperature on battery performance. The main limitations of this model were its neglect of the transport of dissolved species due to migration and the directions of convective electrolyte flow other than that parallel to the electrode surface. Later, several Zn-Br RFB models were developed to predict the current and potential distributions within the electrolytes and electrodes, optimum resistivity of electrolytes and energy efficiency of the cell as a function of the state-of-charge, which enabled better understanding of the physical phenomena occurring in the battery.[155,155,156] Based on these models, battery performance was predicted for different design and operating conditions, such as electrolyte flow rate, thickness of electrodes/separators and composition of electrolytes. However, these models did not account for a second bromine-rich phase in the positive electrolyte and a complete circulation system including electrolyte tanks and connecting piping required for time-dependent simulations. Although the authors suggested that such extensions to the model be made, these were not actually done.

To predict all-vanadium RFB performance with higher accuracy, a 2-D single-cell dynamic was developed by Shah et al. and validated by comparison with experimental results.[157] This model was employed to study the effects of different initial electrolyte concentrations, electrolyte flow rates and electrode porosity on the overall battery performance. This model was later extended to incorporate the effects of temperature, heat loss, side reactions such as hydrogen and oxygen evolution reaction to further unravel the mechanisms operating during flow battery operation.[149] Based on the two models presented by Shah et al.[157] and You et al.[158], another stationary and isothermal 3-D all-vanadium RFB model that focused on the negative side of the cell revealed that the electrolyte velocity has a significant impact on the distribution of concentrations, overpotential

and current density.[159] However, the aforementioned models were based on some assumptions that failed to fully capture the physicochemical process of flow batteries. For example, most of the models assume that the ion exchange membrane used in the model is ideal and only permeable to protons. As a result, battery self-discharge resulting from the crossover of different ionic species such as vanadium is neglected. Later, improvements to the prediction of battery voltage and efficiency were achieved by including the side reactions at the two electrodes, vanadium crossover through the membrane and the resulting capacity loss during battery operation in a 2-D model.[160]

A number of successful models to optimize the design and operating conditions of VRFBs have also been developed. For instance, the flow rate of electrolytes in RFBs is a crucial factor that influences the efficiency of batteries because a trade-off has to be made between pump energy consumption and battery power output. When the battery operates at a high flow rate, the efficiency of the system decreases due to the higher energy consumption by the pump. However, the concentration overpotential increases when the electrolyte flow rate is low due to depletion of electroactive species at the surface of electrodes. Detailed models describing the relationship between flow rate and battery efficiency at different states-of-charge have been presented and used to develop a variable flow rate strategy for battery operation to improve battery efficiency and capacity.[161,162] In another model, the architecture of the electrodes in an all-vanadium RFB with interdigitated flow fields was optimized.[163] This model accounted for electrode material properties such as fiber diameter, porosity and thickness of the fibrous electrode.

2.3.1.4 Material-level modelling

Compared with cell-level models, material-level models can be used to evaluate the precise effects of the material micro-structure and molecular/atomic structure on RFB performance. Critical physio-chemical processes in the solid and liquid phase can be resolved at the micro-pore scale to provide insightful information concerning the design of electrode materials and other cell components. A 3-D pore-scale model to investigate the flow patterns of electrolyte in an all-vanadium RFB was presented by Qiu et al.[164] In this work, the detailed geometry of the electrode was obtained using X-ray computed tomography (XCT) and calibrated against experimentally determined pore-scale characteristics, such as pore and fibre diameter, porosity and surface area.

Coupled with the electrochemical processes at the electrolyte/electrode interface, the processed XCT data were then used as inputs describing the electrode material in simulations of fluid flow, species transport and charge transport during battery operation. This analysis enabled detailed information of the local distribution of ion concentrations, overpotentials and current density at each point of the porous electrode to be plotted. The same authors subsequently studied the effects of different electrode morphologies under various operating conditions.[165] In addition to the detailed information of concentration, overpotential and current distribution across the tested 3D electrode domain, the authors concluded that the cell discharge voltage would rise with an increase of the electrolyte flow rates due to the smaller concentration gradient of the vanadium species within the porous electrode.

In addition to the work focusing on electrode materials, models developed to understand the solution chemistry at the molecular/atomic scale using molecular dynamics (MD) and density functional theory (DFT) have also been developed. These models aimed to optimize the solubility and stability of the various vanadium species in the sulfate-based electrolyte, due to the narrow operating temperature range in which V(II), V(III) and V(IV) precipitate below 10°C, while V(V) ions precipitate above 40°C. Using nuclear magnetic resonance (NMR) data and DFT and MD modeling, Vijaykumar et al. discovered that the V(V) existing as $[VO_2(H_2O)_3]^+$ has poor stability at elevated temperatures in the electrolyte and precipitates after deprotonation of H^+ from one of the water molecules coordinated to the V(V) ions.[166] Such deprotonation could be partially avoided and the V(V) ions stabilized in solution by raising the acidity of the electrolytes. In another study conducted by the same group, the structure of V(III) ions in a mixture of vanadium chloride and vanadium sulfate electrolyte was studied using NMR spectroscopy and DFT modelling.[167] This analysis showed that complexes involving sulfate and chloride counter ions and V(III) ions are energetically more favourable than those that form between water molecules and V(III) cations (i.e., $[V(H_2O)_6]^{3+}$). The authors found that aside from the solution temperature, the vanadium-to-proton ratio in the electrolyte is also an important factor that controls V(III) precipitation. One of the possible pathways for this process proposed by the authors is that the deprotonated V(III)-sulfate complexed molecules act as seeds for continuous nucleation which eventually leads to precipitation.

2.3.2 Zn-Ce RFB modelling

Compared with the more popular and commercialized all-vanadium RFBs, much less work has been reported on the modeling of Zn-Ce RFBs. The only comprehensive two-dimensional transient model of Zn-Ce RFB incorporating the different transport modes (migration, diffusion and convection) and electrode kinetics was developed by Amini and Pritzker and solved using COMSOL.[39] This model accounted for the charge, mass, and momentum transport coupled with electrochemistry on the electrode and was fitted to an extensive set of experimental data obtained in our laboratory. This model also included the HER and OER side reactions on the negative and positive electrodes, respectively. The experimental data included full-cell voltages, positive and negative electrode potentials (versus Ag/AgCl reference electrodes) and the Ce(IV) ion concentration in the positive electrolyte measured over the course of 5 charge-discharge cycles. The fitted model showed an excellent match with the experimental data. Once validated, the model was then used to make further predictions of the performance of the bench-scale Zn-Ce RFB under a variety of conditions. Simulations of battery operation at current densities of 15, 25 and 35 mA/cm^2 revealed that a higher discharge voltage would be achieved at the lowest current density due to reduced electrode polarization and ohmic losses in the system. In addition, a rise in the charge cell voltage during cycling at the highest current density of 35 mA/cm^2 was observed and found to stem from the rise in the positive electrode potential. Analysis of the model clearly showed that this increase of the positive electrode potential was due to the build-up of Ce(IV) ions and the depletion of Ce(III) ions in the electrolyte, leading to a higher overpotential for the oxidation of Ce(III) to Ce(IV).

The effect of the mass transfer of Ce(III) and Ce(IV) on battery performance was also examined by Amini and Pritzker.[39] The mass transfer coefficients of these two species were assumed to be similar in this analysis. The voltage efficiency improved from 78% to 86% when the mass transfer coefficient of both species was increased from $\approx 10^{-5}$ m/s to $\approx 10^{-4}$ m/s. It should be noted that a mass transfer coefficient of 10^{-5} m/s applies to the case when a coarse grid electrode similar to that used in their experiments (dimensions of 45mm × 6mm × 20mm, porosity of 0.758 and mesh fibre diameter of 1.5 mm), whereas a mass transfer coefficient of 10^{-4} m/s corresponds to the situation when a micro-mesh positive electrode is used. The discharge voltage was found to be higher and more stable due to the higher Ce(IV) concentration at the electrode surface. The model also

predicted that the positive electrode potential would not drop even at the end of battery discharge when the mass transfer coefficient was $\approx 10^{-4}$ m/s, indicating a sufficient Ce(IV) concentration at the electrode surface and that the battery efficiency would not be limited by mass transfer of Ce(IV) from the bulk to the electrode surface. On the other hand, when the mass transfer coefficients were reduced to $\approx 10^{-6}$ m/s, the battery was not able to discharge at all due to the extremely slow mass transfer of the Ce(IV) ions from the bulk to the electrode surface. Although the Ce(III) concentration was found to be very high during battery charge of the first cycle, the mass transfer of Ce(III) became increasingly difficult and a much higher cell voltage was observed when the mass transfer coefficients were $\approx 10^{-6}$ m/s. A conclusion from this analysis was that the use of positive electrodes such as a Pt-Ti micromesh or felt electrode with much higher surface area to improve mass transfer of cerium ions could greatly improve the performance of the Zn-Ce RFB.

Since the positive half-cell reaction was no longer the limiting reaction when mass transfer to and from the positive electrode was enhanced, Amini and Pritzker then focused on improvement of the negative electrode reaction to enhance battery performance and overall efficiency. A previous experimental study had shown that the exchange current density for the zinc redox reaction could be increased from 7.4×10^{-3} A/cm^2 to 53.4×10^{-3} A/cm^2 when an alternative MSA-HCl mixed acid instead of the MSA was used as negative supporting electrolyte.[130] Therefore, simulations of the model using this higher exchange current density for the zinc redox reaction were carried out to determine the battery performance while keeping the properties of the positive half-cell the same (mass transfer coefficient $= 10^{-4}$ m/s). The charge efficiency was found to increase from 75% to 80%, while the voltage efficiency increased from 83% to 85%. The increase in charge efficiency could be attributed to the larger amount of zinc deposited on the negative electrode during charge, which enabled a longer battery discharge time. This prolonged discharge time ensured that more Ce(IV) ions in the positive electrolyte could be converted back to Ce(III) during each cycle and slowed the gradual accumulation of Ce(IV) from cycle to cycle. The improvement in voltage efficiency occurred due to the reduction in the activation overpotential for the Zn(0)/Zn(II) reaction. Although the exchange current density increased by more than 7-fold, the model still predicted that the negative half-cell reaction would be the limiting reaction due to the irreversible HER side reaction, which still led to Ce(IV) accumulation and precipitation. In this regard, the inhibition of

the HER side reaction on the negative electrode is the most critical problem to be resolved for further improvement of Zn-Ce RFB overall performance.

It should be noted that an important assumption made by Amini and Pritzker in this 2D transient Zn-Ce RFB model is that the cation exchange membrane is permeable to protons only so that crossover of the other ions is neglected. However, as will be shown later in this thesis, this is not the actual case during operation of our Zn-Ce battery. In fact, the crossover of different ion species through cation exchange membranes is a widely reported phenomenon in other flow battery systems.[168–171] Crossover in the Zn-Ce system should not be neglected since it will reduce the Zn(II) and Ce(III)/Ce(IV) ion concentrations available for the electrode reactions and enhance the undesired irreversible HER side reaction, both of which tend to lower the battery efficiencies and performance. Therefore, the development of a Zn-Ce RFB model that more accurately describes the behaviour of the cation exchange membrane used in our laboratory experiments is needed to further improve its accuracy. In addition, such a model could be used to determine the optimum membrane choice that reduces crossover while enabling better battery performance and longer life.

Another improvement of the model could be the determination of the mass transfer coefficient of the Ce(III) and Ce(IV) ions. In the past model of Amini and Pritzker, these coefficients were fitted according to the cell voltage and electrode potential, which was accurate but only valid for the exact conditions applied to the Zn-Ce RFB. Any change in the operating parameters and battery properties such as flow rate, electrode porosity, electrode mesh diameter and electrolyte viscosity would change the actual mass transfer coefficient in the battery system, which leads to inaccurate predictions of the battery performance if the mass transfer coefficient used in the model remain unchanged. Consequently, the use of a correlation linking the mass transfer coefficients of the various species to factors such as electrolyte flow rate, viscosity of electrolyte and porosity and surface area of the positive electrode should be applied to more accurately describe mass transfer at the positive electrode during battery operation under many operating conditions. In addition, the effect of cell geometry and design of the various cell components such as flow channel, electrode thickness, electrode porosity and electrode specific surface area on battery performance and mass/charge transport process should be investigated. This information will be insightful and valuable for the further design and performance improvement of the Zn-Ce RFB at lower cost.

Chapter 3 Experimental and Methods

3.1 Components of redox flow batteries

As shown in Figure 3.1, the redox flow battery unit cell used in this study is composed of a Pt-Ti mesh (Metakem GmbH) positive electrode having a Pt loading level of 7 mg/cm^2, grid wire diameter of 1.5 mm, porosity of 0.758 and superficial area of 9 cm^2 (2 cm × 4.5 cm). A polyvinyl ester (PVE) carbon sheet (TDM Fuel Cells) with an area of 9 cm^2 and thickness of 6 mm is used together with a copper current collector (McMaster-Carr) as the negative electrode. The negative and positive flow channels are made from acrylic sheet (CIP Wholesale) to distribute the electrolytes to the chambers. A piece of Nafion 117 ion exchange membrane (Fuel Cell Store) with a dimension of 4 cm × 8 cm is used in the unit cell to conduct ions as well as prevent the two electrolytes from mixing with each other. Silicone rubber gaskets (CS Hyde Company) are placed between different parts of the unit cell to prevent electrolyte leakage. The size of the active area of the negative electrode is also 9 cm^2 (2 cm × 4.5 cm). The different components are assembled together in the order as shown in Figure 3.2.

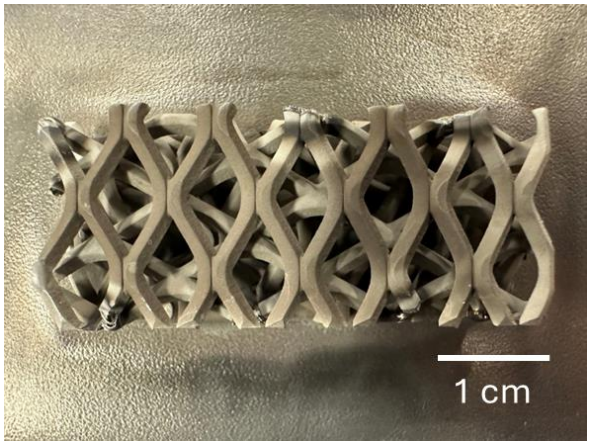


Figure 3.1. Pt-Ti positive electrode used in this work.

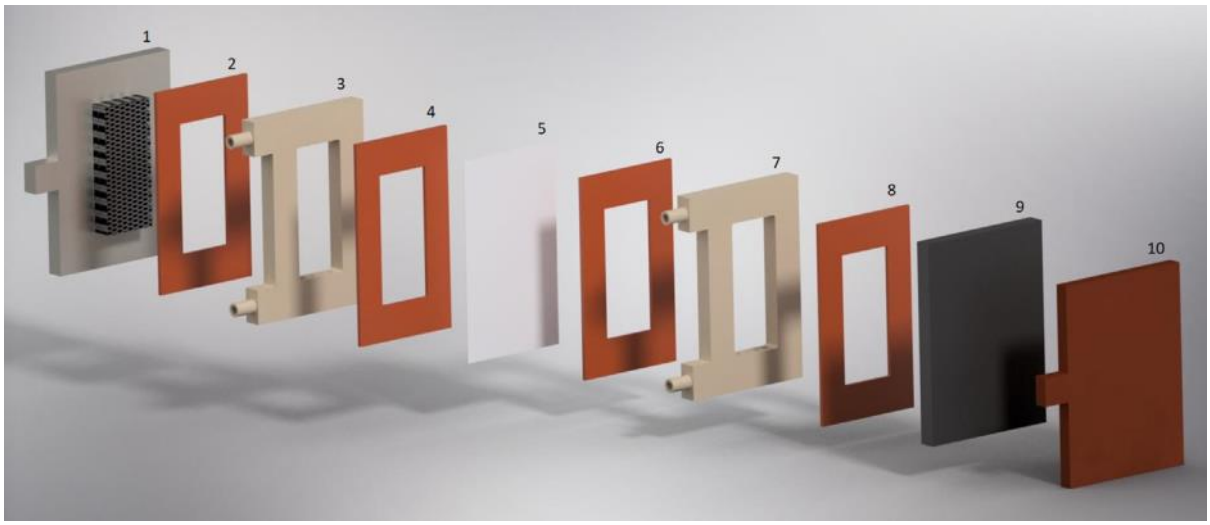


Figure 3.2. Components of bench-scale flow battery used in this study (reproduced with permission) [129]: Pt-Ti mesh positive electrode (1), silicone rubber gaskets (2, 4, 6, 8), acrylic flow channels (3, 7), ion exchange membrane (5), PVE negative electrode (9) and copper current collector (10).

Figure 3.3 shows the connection between the unit cell, electrolyte tanks, peristaltic pumps and reference electrode holder using Viton tubing. The negative and positive electrolytes are stored in separate external tanks and two peristaltic pumps are used to circulate the electrolytes into their respective cell compartment where the electrode reactions occur. A small amount of high-vacuum grease (Dow Corning) is applied to the surface of Viton tubing where it is in contact with the rollers inside the peristaltic pump (highlighted in blue) in order to reduce the friction between the rollers and the tubing that causes leakage of the electrolyte especially during long-term battery operation. Two T-shaped glass cells located between the pump and inlet of the battery are used to hold the reference electrodes used to monitor the negative and positive electrode potentials separately. On the negative side, the Ag/AgCl reference electrode is allowed to be in direct contact with the electrolyte. When this set-up was first installed, it was found that cerium ions would leak into the reference electrode placed on the positive side and irreversibly damage the reference electrode. To prevent this, the reference electrode on the positive side is placed in a glass tube and one end is sealed with a Nafion 117 membrane to prevent direct contact with the cerium ions in the positive electrolyte while still maintaining electrical contact. Previous measurements from our group

confirmed that the voltage drop across the Nafion membrane is negligible compared to the electrode potential measured from experiments.[38]

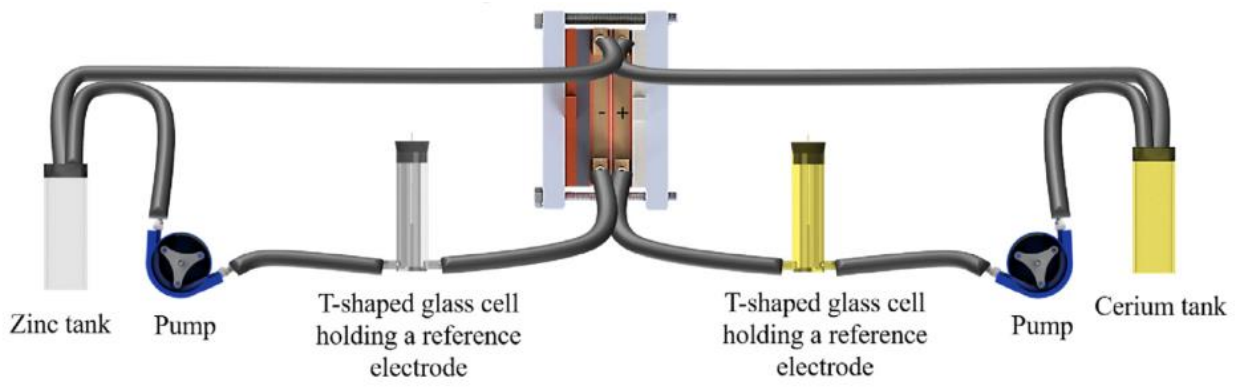


Figure 3.3. Diagram showing the connection between the RFB, external electrolyte reservoir tanks and reference electrodes inserted to monitor the positive and negative electrode potentials during battery operation (reproduced with permission).[38]

3.2 Electrochemical measurements

3.2.1 Half-cell measurement

A conventional 3-electrode system is used to study the kinetics of the electrode reactions, as shown in Figure 3.4. The working electrode is a Pt-disc electrode with an area of 3.14 mm^2, while a graphite rod (Alfa Aesar) is used as the counter electrode. An Ag/AgCl electrode (Pine Research) is used as the reference electrode. During three-electrode experiments, the current is measured between the counter electrode and the working electrode while the potential is measured with respect to the reference electrode. The electrochemical events of interest proceed on the working electrode, which ideally responds independently of any changes that might occur at the counter electrode. The reference electrode maintains a constant electrochemical potential, while the IR drop between the reference electrode and working electrode remains small since only a negligible small current is being passed through the part of circuit connecting the working electrode and reference electrode. Each scan begins at 0.5V vs. Ag/AgCl reference electrode and proceeds in the

positive direction to 2.1V at a scan rate of 50 mV/s before returning to the starting voltage. A Bio-logic EPP-4000 potentiostat is used to conduct the half-cell electrochemical experiments.

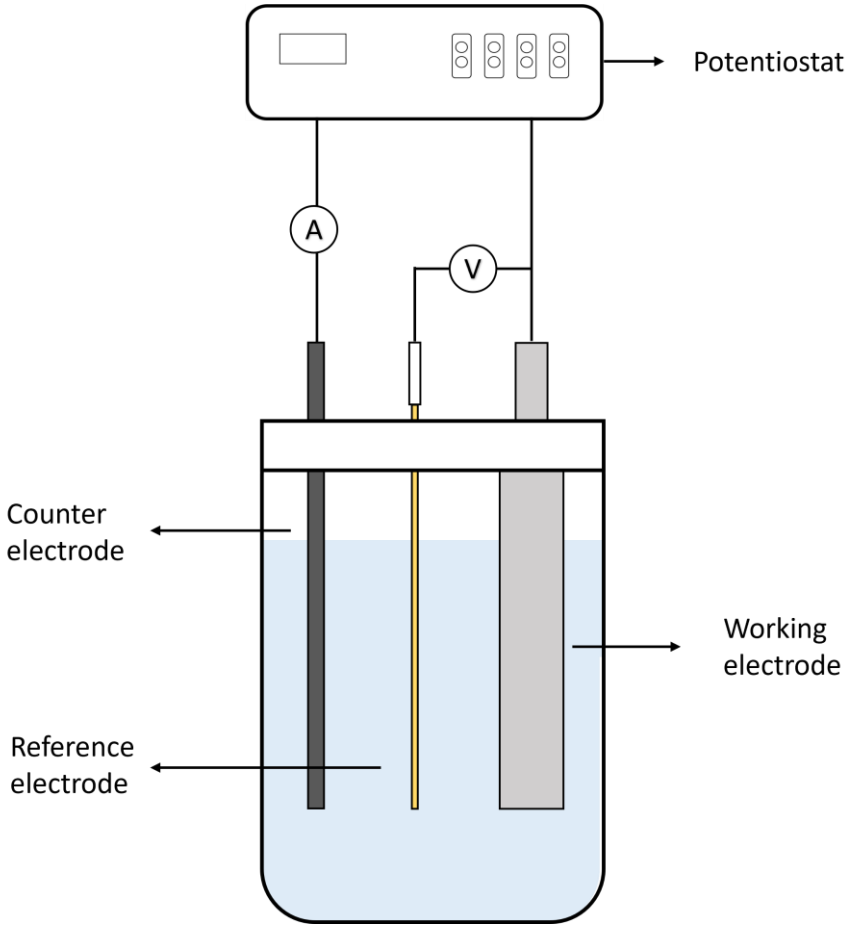


Figure 3.4. Schematic of three-electrode system used in this research.

3.2.2 Bench-scale full-cell system

Full-cell experiments are conducted in the bench-scale redox flow battery unit cell shown in Figure 3.3. The positive and negative electrolytes each with a volume of 30 mL are circulated from two external reservoirs through Viton tubing to their battery compartments using a 2-head Longer BT100-1L peristaltic pump. The flow rate of the electrolytes is controlled to be 60 mL/min on both

sides and the electrolyte tanks are immersed in a 50℃-water bath throughout the experiments. Prior to the experiments, the Nafion 117 membrane is activated by soaking in each of the following solutions for 1 hour at ~80℃ in the order: 3%(wt.) H_2O_2, ultrapure water, 0.5 mol/L H_2SO_4 solution and ultrapure water. The electrochemical measurements are conducted using Autolab PGSTAT 30 potentiostat connected to a computer controlled via Nova 2.1.5 software.

The battery efficiency is characterized by subjecting it to 30 galvanostatic charge-discharge cycles. Each cycle proceeds by charging the battery at a fixed current density of 25 mA/cm^2 for a duration of 1 hour followed by discharge at the same current density. Discharge is terminated when the battery cell voltage reaches a cut-off value of 0.5 V. The coulombic efficiency of the battery over each cycle is obtained from the ratio of discharge time to the charge time, while the voltage efficiency over each cycle is determined from the ratio of the average discharge cell voltage to charge cell voltage.

Discharge polarization experiments are conducted by first charging the battery at a current density of 50 mA/cm^2 for 90 minutes to reach a state-of-charge (SOC) of 50%. To ensure the SOC of the battery is maintained as close to 50% as possible throughout each polarization experiment, 60 mL of each positive and negative electrolytes are used for all the polarization experiments, which is twice as large as the volume of electrolytes used in the charge-discharge cycling tests. To check that the battery SOC remains at or very close to 50% throughout the experiment, the Ce(IV) concentration is measured immediately after the 90-minute battery charge and at the end of the polarization measurements. The results showed that the decrease of Ce(IV) concentration is small enough not to be a factor in the interpretation in the resulting polarization curves. Each polarization measurement involves discharging the battery for 20 seconds at a different current density within the range from 0 to 110 mA/cm^2 followed by a 20-second rest period before continuing to the next current density. The average cell voltage over each 20-second rest period obtained is then plotted versus the corresponding current density to yield the polarization curve.

3.3 Measurement of Ce(IV), H^+ and Zn(II) concentrations and electrolyte properties

The concentration of Ce(IV) in the positive electrolyte is measured by a colorimetric titration method using ferroin (1,10-phenanthroine iron (II) sulfate, Alfa Aesar) as an end-point indicator. 50 μL of positive electrolyte is collected and titrated by 0.05 mol/L ammonium iron (II) sulfate hexahydrate (99%, Sigma-Aldrich).[38,172] The ammonium iron(II) sulfate hexahydrate solution is added to the positive electrolyte sample drop by drop until the sample turns from yellow to red and maintains the colour for at least 5 minutes. The unknown concentration is then calculated by the following equation:

$$C_2 = \frac{C_1 \cdot V_1}{V_2} \tag{22}$$

In this equation, C_2 is the unknown Ce(IV) concentration in the sample electrolyte, C_1 is the Fe(II) concentration of the 0.05 mol/L ammonium iron (II) sulfate hexahydrate solution, V_1 is the cumulative volume of the titration solution when the end-point is reached and V_2 is the volume of the sample electrolyte.

To measure the concentration of Ce(III) in the positive electrolytes, another 50 μL sample is collected and then contacted with a certain amount of ammonium persulfate (thermo scientific, 98+%) and silver nitrate solution (Titripur, 0.1 mol/L) as catalyst to oxidize all Ce(III) present to Ce(IV).[173,174] This step is followed by colorimetric titration described above to determine the Ce(IV) content in this oxidized sample after the solution is cooled down to the room temperature. The Ce(III) concentration is then determined from the difference between the total Ce(IV) concentration after oxidation and the original Ce(IV) concentration prior to oxidation. The very small sample volumes required for these titrations ensure that the cumulative amount collected over the course of the experiments has no effect on battery operation.

The H^+ concentration in the negative electrolyte is determined by titration using 0.01 mol/L NaOH solution prepared by dissolving sodium hydroxide beads (VWR Analytical) in ultrapure water.[38,175] The end-point of this titration process as indicated by methyl red (Ricca Chemical) occurs when

the color of the solution changes from red to yellow. Unfortunately, this method cannot be used to determine the H^+ concentration in the positive electrolytes which appear yellow due to the presence of Ce(IV) ions, making it impossible to accurately determine the titration endpoint from a change in solution colour. Thus, the H^+ concentrations in the positive electrolyte are not measured in this study.

Inductively coupled plasma optical emission spectroscopy (ICP-OES, Teledyne Leeman Labs Prodigy) is used to measure the Zn(II) concentration in both positive and negative electrolytes. A certain amount of electrolyte is taken from the electrolyte tanks after each charge-discharge cycle and diluted to ~200 ppm level to ensure the concentrations of Zn(II) ions in the solutions are comparable to the standard solutions to achieve maximum accuracy. Due to the very low concentration of Ce(III) and Ce(IV) ions in the negative electrolytes, ICP-OES is also used to determine these concentrations since the titration method is no longer sensitive enough. The conductivity of different fresh positive electrolytes is measured with a Mettler-Toledo AG conductometer. The viscosity of the electrolytes at 50℃ is measured using a Brookfield DV2TLV digital rotational viscometer.

3.4 Battery performance evaluation metrics

Coulombic efficiency (CE): The coulombic efficiency (also termed current efficiency or Faradaic efficiency) is a measurement of the reversibility of the charge during each cycle and is the ratio of the discharge capacity over charge capacity calculated according to the following equation:

$$coulombic\ efficiency = \frac{\int_0^t I_d dt}{\int_0^t I_c dt} \times 100\% \tag{23}$$

In this equation, I_d is the current applied during discharge and I_c is the current applied during charge. In most cases, the charge current and discharge current are kept constant and equal to each other, in which case the coulombic efficiency is simply the ratio of the discharge time to the charge time. A 100% coulombic efficiency indicates that all the charge stored during the charge process is utilized for battery discharge. However, irreversible side reactions such as hydrogen and oxygen

evolution reaction are the main causes of coulombic efficiency loss in many RFBs. In addition, battery self-discharge also reduces the battery coulombic efficiency. In Zn-Ce RFBs, self-discharge can occur due to the undesired crossover of electroactive species across the membrane and corrosion of the zinc layer on the electrode surface in the acidic electrolyte. Corrosion reduces the amount of zinc available for battery discharge, but does not reduce the total amount of zinc in the battery system since the dissolved Zn(II) ions still remain in the electrolyte

A decrease in coulombic efficiency usually occurs at both high and low current densities. The coulombic efficiency drop at low current densities is associated with the extended charge and discharge periods when a fixed SOC is to be achieved. Longer charge and discharge periods lead to more self-discharge due to ion crossover and corrosion. On the other hand, the efficiency drop with an increase in current density usually arises since this disproportionally favours the irreversible side reactions. For redox flow battery stacks, further coulombic efficiency loss is associated with the shunt and bypass currents that flow through the common electrolytes between bipolar plates and are driven by the magnitude of the voltage difference across the stack.

Voltage efficiency (VE): The voltage efficiency measures the effects of cell polarization and the cell voltage losses across the battery. The following equation is used to calculate voltage efficiency:

$$voltage\ efficiency = \frac{V_{discharge}}{V_{charge}} \times 100\% \qquad (24)$$

In this equation, $V_{discharge}$ is the average discharge voltage and V_{charge} is the average charge voltage. Both the discharge and charged voltage are determined by the thermodynamic cell potential of the redox couple used in the battery as well as the ohmic drop and various overpotentials that arise when current flows through the cell.

The ohmic resistance of the battery system as well as the activation overpotentials and concentration overpotentials at the two electrodes combine to reduce the voltage efficiency of the battery. This voltage loss can be reduced by using electrode materials and electrolytes with high electrical conductivity.

Energy efficiency: The energy efficiency is used to quantify the actual amount of energy released during battery discharge relative to the amount of energy required to charge the battery and is simply the product of coulombic efficiency and voltage efficiency:

$$energy\ efficiency = CE \times VE \times 100\% \tag{25}$$

Energy efficiency is an overall battery performance indicator and is a reflection of the behavior of both coulombic and voltage efficiencies in combination. Therefore, the optimal operating current density of a redox flow battery to achieve maximum energy efficiency can be determined by monitoring the trends in coulombic and voltage efficiency.

Other battery attributes and performance metrics are summarized in Table 3.1.

Table 3.1. Quantities and descriptions used to evaluate battery attributes and performance.

Battery attributes and performance metrics	Definition	Description
Current density (mA/cm^2)	$J = \frac{I}{A_{electrode}}$	Current applied to the battery per negative electrode area.
Battery capacity (mA·h)	$C_{cell} = I \times t$	Battery capacity is the product of current and time.

Theoretical electrolyte capacity (mA·h)	$C_t = \frac{n \times c \times V \times F}{3600}$	n is number of electrons transferred per mole, c is concentration of electroactive species (mol/L), V is electrolyte volume (mL), F is the Faraday constant (C/mol).
SOC	$SOC = \frac{C_{cell}}{C_t} \times 100\%$	SOC is the ratio of battery capacity to theoretical capacity.
Volumetric capacity (mA·h/L)	$C_v = \frac{C_{cell}}{V}$	Battery capacity stored per unit volume electrolyte.
Capacity retention	$C_r = \frac{C_{battery}}{C_{battery,ini}}$	Battery capacity during certain cycle divided by the initial battery capacity
Energy density (Wh/L)	$E_{cell} = \frac{\int I \times t \times dV}{V}$	Energy output per unit volume of electrolyte.
Power density (W/cm^2)	$P_{cell} = \frac{I \times V_{cell}}{A_{membrane}}$	Battery power output per unit area of membrane at a specific SOC.

Chapter 4 Use of Mixed Methanesulfonic Acid/Sulfuric Acid as Positive Supporting Electrolyte in Zn-Ce Redox Flow Battery[1]

4.1 Introduction

Previous works showed that the optimum battery performance could be achieved using 0.8 mol/L cerous methanesulfonate in 4 mol/L methanesulfonic acid (MSA) as the positive electrolyte and 1.5 mol/L zinc methanesulfonate in 1 mol/L MSA as the negative electrolyte in the fully discharged state.[37,38] The use of MSA on the negative side has been shown to dramatically reduce the formation of zinc dendrites during battery charge, which can lead to membrane damage, mixing of the two electrolytes and a reduction in charge efficiency. Additionally, a high MSA concentration (4 mol/L) is required in the positive electrolyte to ensure high solubility of both Ce(III) and Ce(IV) ions, which is a key factor for the battery to achieve a high energy density. As reported in previous studies, the solubility of Ce(III) decreases as the concentration of MSA increases, whereas the opposite trend is observed for Ce(IV) ions.[127] Another advantage of using MSA as the supporting electrolyte is its high conductivity (0.30 S/cm), comparable to that of hydrochloric acid (0.35 S/cm) and sulfuric acid (0.44 S/cm), while being much less corrosive at the same time.[121]

However, the use of 4 mol/L MSA as the supporting electrolyte on the positive side has a major disadvantage over the course of repeated battery charge and discharge – the large net transfer of H^+ ions from the positive side to the negative side due to the large gradient in acid concentration. The continual rise in the acid concentration in the negative electrolyte over the course of operation leads to an ever-increasing extent of the undesired and irreversible hydrogen evolution side reaction during charge and a further decrease in the charge efficiency. At the same time, the accompanying decrease of acidity in the positive electrolyte reduces the solubility of Ce(IV) ions and eventually leads to the precipitation of CeO_2 in the positive electrolyte tank. The net transfer of H^+ ions to the negative side has another unfortunate effect. As more hydrogen evolution occurs at the negative electrode, less zinc is deposited during charge and available for oxidation during

[1] This chapter is adapted from my published work.[32]

the subsequent discharge step. This effect in turn limits the amount of Ce(IV) in the positive electrolyte that can be reduced back to Ce(III) during the same discharge cycle. In the worst case scenario, the positive electrolyte can become completely depleted of Ce(III) after a sufficient number of charge-discharge cycles with the result that it can no longer be re-charged through the oxidation of Ce(III) to Ce(IV) and the battery fails.

Thus, one approach to reduce this problem of H^+ transfer is to reduce the acid concentration in the positive electrolyte while maintaining high cerium solubility and Ce(III)/Ce(IV) reaction kinetics. It has previously been shown that the use of mixed acids or metal-binding additives in the positive electrolyte can enhance both the cerium solubility and Ce(III)/Ce(IV) reaction kinetics.[33,60] In this study, we explore the use of mixed acids as the supporting electrolyte on the positive side of a Zn-Ce RFB with the aim of capitalizing on their reported beneficial effects to reduce the acidity of the positive electrolyte. We focus particularly on the effectiveness of mixed acid positive electrolytes to improve long-term battery operation and reduce battery fade, which has not been studied by other research groups to the best of our knowledge. The following positive supporting electrolytes are evaluated: 2 mol/L MSA-1 mol/L HNO_3, 2 mol/L MSA-0.5 mol/L H_2SO_4, 3 mol/L MSA and the original 4 mol/L MSA. It should be noted that the total acidity in each of these mixed acids is lower than that of the 4 mol/L MSA. Half-cell experiments in a 3-electrode system are first conducted to compare the kinetics of the Ce(III)/Ce(IV) redox couple in the aforementioned supporting electrolytes. Next, the cell voltage and individual electrode potentials during operation of a bench-scale Zn-Ce redox flow battery are monitored over the course of ~40 charge-discharge cycles and the corresponding charge and voltage efficiencies determined to compare the performances when the various positive supporting electrolytes are used. In addition, the changes in the Ce(IV) concentration in the positive electrolyte and H^+ concentration in the negative electrolyte over the course of these cycles are measured to more closely track the cause of battery performance decay.

4.2 Experimental

4.2.1 Reagents

The negative electrolyte containing 1.5 mol/L zinc(II) methanesulfonate in 1 mol/L MSA was prepared by dissolving zinc oxide (Zochem Inc.) in an appropriate amount of 70% MSA (Alfa Aesar). 0.8 mol/L cerous methanesulfonate in 4 mol/L MSA in the positive half-cell was prepared by mixing 99% pure cerium carbonate (Treibacher Industrie AG) with the prescribed amount of 70% MSA. Ultra-pure water (~18 MΩ·cm) was used to prepare all electrolyte solutions in this work.

The changes in the Ce(IV) and H^+ concentrations at the end of each charge-discharge cycle over the course of long-term battery operation were determined using colorimetric titration methods. To do this, we collected 0.1 ml of each of the positive and negative electrolytes after each cycle. The concentration of H^+ in the negative electrolyte was determined by colorimetric titration using 0.1 mol/L NaOH solution prepared by dissolving sodium hydroxide beads (VWR Analytical) in ultra-pure water until the end-point was reached, as indicated by methyl red (Ricca Chemical). Although zinc(II) ions were also present in the negative electrolyte and could potentially interfere with the H^+ titration, it has been shown that this interference is negligible under the highly acidic conditions of the samples and does not change the end-point of titration.[176] To determine the Ce(IV) concentration in the positive electrolyte, 99% pure ammonium iron(II) sulfate hexahydrate (Sigma-Aldrich) was used for titration and ferroin (1,10-phenanthroine iron(II) sulfate, Alfa Aesar) was used as a colorimetric redox indicator. All the chemicals were used as received without any further pretreatment or purification.

4.2.2 Electrochemical Experiments

4.2.2.1 Half-cell system

A conventional 3-electrode system was used for half-cell experiments to study the kinetics of the Ce(III)/Ce(IV) redox couple in different supporting electrolytes. The following electrodes were used: a Pt-disc working electrode with an area of 3.14 mm^2, a graphite rod (Alfa Aesar) counter electrode and an Ag/AgCl reference electrode (Pine Research Instrumentation). A Bio-logic EPP-4000 potentiostat was used to conduct the half-cell electrochemical experiments.

4.2.2.2 Flow battery setup

As shown in Figure 3.3, the flow battery setup consisted of a Pt-Ti mesh with a Pt loading level of 7 mg/cm^2 (Metakem GmbH) as positive electrode, silicone rubber gaskets (CS Hyde Company) to prevent leakage, flow channels (acrylic sheets from CIP Wholesale) to distribute electrolyte, an ion exchange membrane (Nafion 117, Fuel Cell Store) to conduct ions, a polyvinyl ester (PVE) carbon sheet (TDM Fuel Cells) as negative electrode and a copper current collector (McMaster-Carr). 30 mL of the positive and negative electrolytes described previously were pumped from two external electrolyte tanks using a peristaltic pump (Longer Pump, BT100-1L) via Viton tubing (McMaster-Carr). The flow rate was controlled to be 60 mL/min and the temperature of electrolytes was maintained at 50˚C using a water bath (Neslab RTE-8) throughout the experiments. Before each full cell experiment, the Nafion 117 membrane was activated by soaking solutions at ~80˚C for 1 hour in the following sequence: 3%(wt.) H_2O_2, ultra-pure water, 0.5 mol/L H_2SO_4 solution and ultra-pure water. In addition to the total cell voltage, the positive and negative electrode potentials were also measured separately in our flow battery system by placing two Ag/AgCl reference electrodes into T-shaped glass cells located in the inlets of the battery. More details regarding these reference electrodes were provided in a previous work.[38] A data acquisition device (DATAQ Instruments, DI-1100) was used to monitor and record the two electrode voltages. The electrochemical measurements were conducted with an Autolab PGSTAT 30 connected to a computer controlled by Nova 2.1.5 software.

Discharge polarization experiments were conducted by first charging the battery at a current density of 50 mA/cm^2 for 45 min to achieve a state-of-charge (SOC) of 50%, followed by discharging the battery at different current densities for 30s. The battery was allowed to rest for 20s after discharge at each current density before continuing the next battery discharge. The 50% SOC was verified by the same titration procedure described previously to ensure that 0.4 mol/L Ce(IV) was present in the positive electrolyte after battery charge. The polarization curve was obtained by plotting the average cell voltage measured over each 30-s period of battery discharge versus the corresponding current density. During each polarization experiment, 50% SOC was maintained by regularly checking and adjusting (if necessary) the Ce(IV) concentration throughout the experiment.

4.3 Results and Discussion

4.3.1 Cyclic voltammetry

Half-cell cyclic voltammetry (CV) experiments were conducted to compare the kinetics of the Ce(III)/Ce(IV) redox couple in the 4 different electrolytes: 2 mol/L MSA-1 mol/L HNO_3, 2 mol/L MSA-0.5 mol/L H_2SO_4, 3 mol/L MSA and the original 4 mol/L MSA. In each case, the electrolyte originally contained 0.8 mol/L Ce(III) with no Ce(IV) ions present. Each scan began at 0.5 V vs. Ag/AgCl reference electrode and proceeded in the positive direction to 2.1 V at a scan rate of 50 mV/s before returning to the starting voltage. As shown in Figure 4.1, the Ce(III)/Ce(IV) redox couple shows better reaction kinetics when 2 mol/L MSA-0.5 mol/L H_2SO_4 mixed acid is used as the supporting electrolyte since the anodic current for Ce(III) oxidation starts to rise at a lower potential during the anodic scan than in the case of the other electrolytes. Importantly, the kinetics in this electrolyte appears significantly faster than that observed in the original 4 mol/L MSA, which is frequently used in Zn-Ce RFBs. So this meets the goal of reducing the acidity of the positive electrolyte, while actually enhancing the kinetics of the Ce(III)/Ce(IV) reaction.

Since the O_2 evolution reaction also occurs during the anodic scan, the total anodic charge passed during the CV cannot be used as a measure of the extent of the Ce(III) oxidation reaction. Perhaps a better approach is to compare the charge associated with Ce(IV) reduction (peak at ~1.25 V vs. Ag/AgCl) during the cathodic scan since the only source of Ce(IV) in the system comes from Ce(III) oxidation during the previous anodic scan. Based on this measure, the CVs in Figure 4.1 show that somewhat more Ce(III) oxidation has occurred in the 2 mol/L MSA-0.5 mol/L H_2SO_4 mixed acid than in the other electrolytes, slightly more than in 4 mol/L MSA. This agrees with the results in the previously mentioned studies that the Ce(III)/Ce(IV) redox couple in MSA/H_2SO_4 mixed acid shows better reaction kinetics and reversibility. Although the standard rate constant for the Ce(III)/Ce(IV) couple electrode reaction in HNO_3 media alone was reported in a previous study to be significantly larger than that in MSA and H_2SO_4 acid media, we have found that the least amount of Ce(III) oxidation occurs in the 2 mol/L MSA-1 mol/L HNO_3 mixed acid, indicating that MSA/ HNO_3 mixed acid is not a good option for a Zn-Ce RFB. This difference may be due to the fact that the HNO_3 concentration used in the earlier study was much higher than the level of 1 mol/L added here. Another commonly used measure is the separation between the anodic and

cathodic peaks for the Ce(III)/Ce(IV) redox couple as an indication of reversibility of the redox reactions. A comparison of the CVs shows that the peak separations are very similar (between ~0.64-0.69 V) when the reactions take place in 2 mol/L MSA-1 mol/L HNO_3, 2 mol/L MSA-0.5 mol/L H_2SO_4 and the original 4 mol/L MSA supporting electrolytes, reflecting comparable reaction reversibility. However, the peak separation in the case of 3 mol/L MSA is about 0.12 V larger, indicating slightly less reversibility. More detailed information of the CV curves is included in Table 4.1.

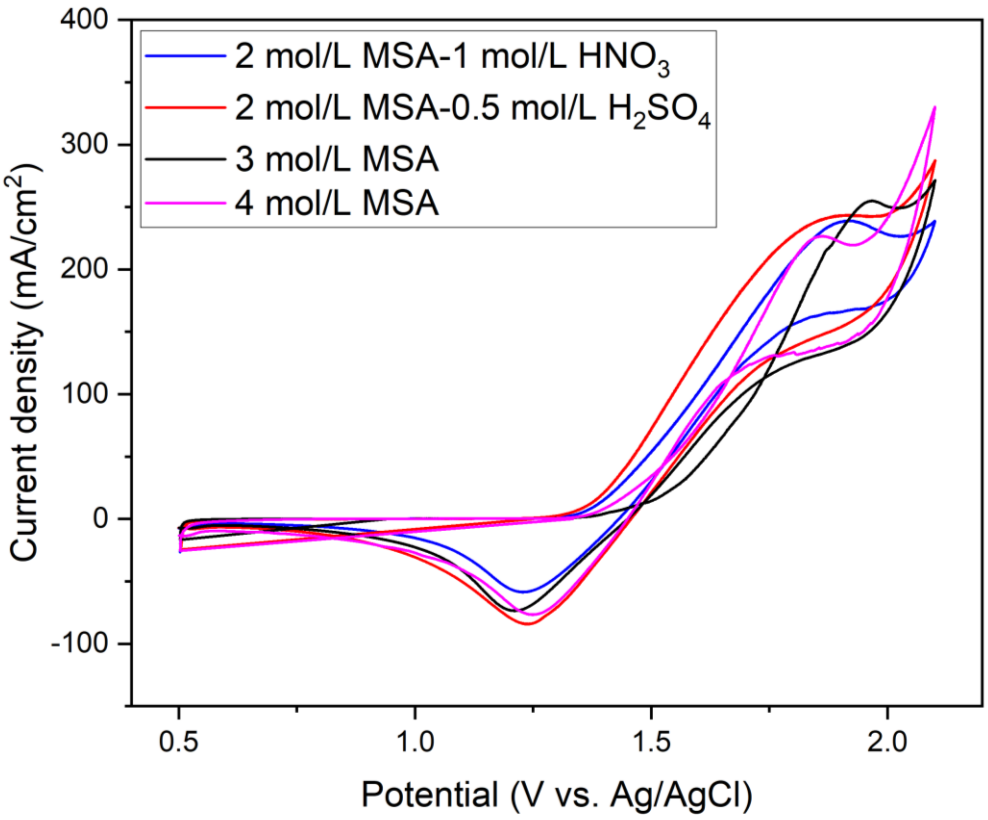


Figure 4.1. Cyclic voltammograms of the Ce(III)/Ce(IV) redox couple obtained in different supporting electrolytes at a scan rate of 50 mV/s. Each of the listed supporting electrolytes contains 0.8 mol/L Ce(III) in its initial state.

Table 4.1. Key information from CV curves.

Parameters	2 mol/L MSA-1 mol/L HNO_3	2 mol/L MSA-0.5 mol/L H_2SO_4	3 mol/L MSA	4 mol/L MSA
Anodic peak position (V vs Ag/AgCl)	1.91	1.90	1.97	1.87
Cathodic peak position (V vs Ag/AgCl)	1.22	1.23	1.20	1.23
Anodic–cathodic peak separation (V)	0.69	0.67	0.77	0.64

4.3.2 Battery cycling performance

Plots showing the variation in cell voltage over the 40 charge-discharge cycles using 4 mol/L MSA and 2 mol/L MSA-0.5 mol/L H_2SO_4 mixed acid as positive supporting electrolyte at 25 mA/cm^2 and 50 °C are shown in Figure 4.2 and Figure 4.3, respectively. The battery is charged for a duration of 1 hour for each cycle and battery discharge is terminated when the cut-off cell voltage of 0.5 V is reached. In both cases, the charge voltage remains at ~2.6 V for the first few cycles before it slowly rises to ~3.0 V at the end of charge process for the subsequent charge-discharge cycles. The gradual rise of charge voltage is attributed to the increase in the overpotential at the positive electrode caused by the drop in the Ce(III) concentration and rise in Ce(IV) concentration in the positive electrolyte over time. This is confirmed by the plots of the individual electrode potentials during charge in Figure 4.4 and Figure 4.5 which show an increase in the potential of the positive electrode (and cell potential) as cycling proceeds. In both cases, the positive electrode potential during battery charge remains at ~1.5 V vs. Ag/AgCl for the first few cycles before it slowly rises to ~1.7 V by the end of charge in the subsequent charge-discharge cycles. On the other hand, the negative electrode potential during charge remains unchanged throughout the entire

battery charge-discharge experiments. It is worth noting that a sharp drop or rise of an electrode potential at the end of each cycle is an indication that the electrolyte has become completely or nearly depleted of the reactant at that electrode during discharge. Thus, it is possible to determine which electrode becomes depleted of a reactant first and therefore identify the limiting half-cell reaction during discharge by observing the electrode potential that exhibits the largest change just before the end of a discharge cycle.

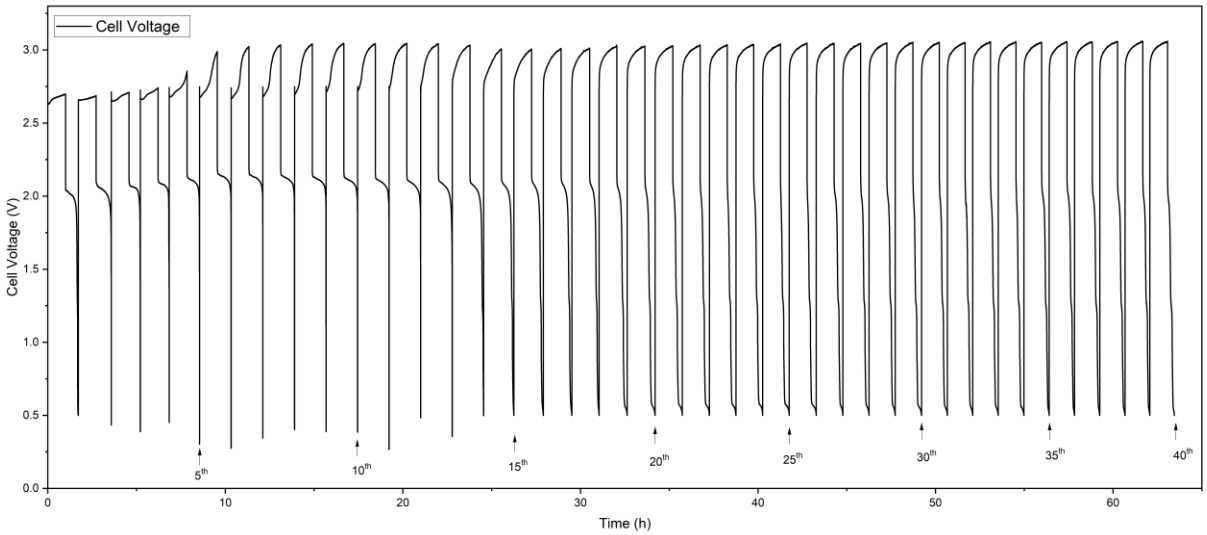


Figure 4.2. Cell voltage during 40 galvanostatic charge-discharge cycles at 25 mA/cm² and 50°C when 4 mol/L MSA is used as the positive supporting electrolyte.

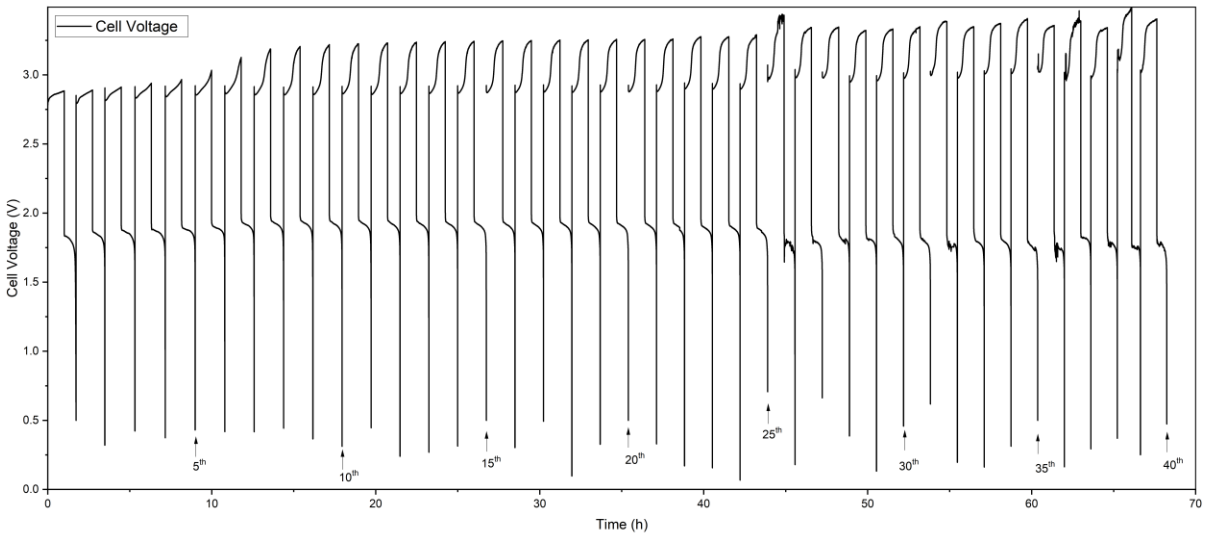


Figure 4.3. Cell voltage during 40 galvanostatic charge-discharge cycles at 25 mA/cm^2 and 50°C when 2 mol/L MSA-0.5 mol/L H_2SO_4 mixed acid is used as the positive supporting electrolyte.

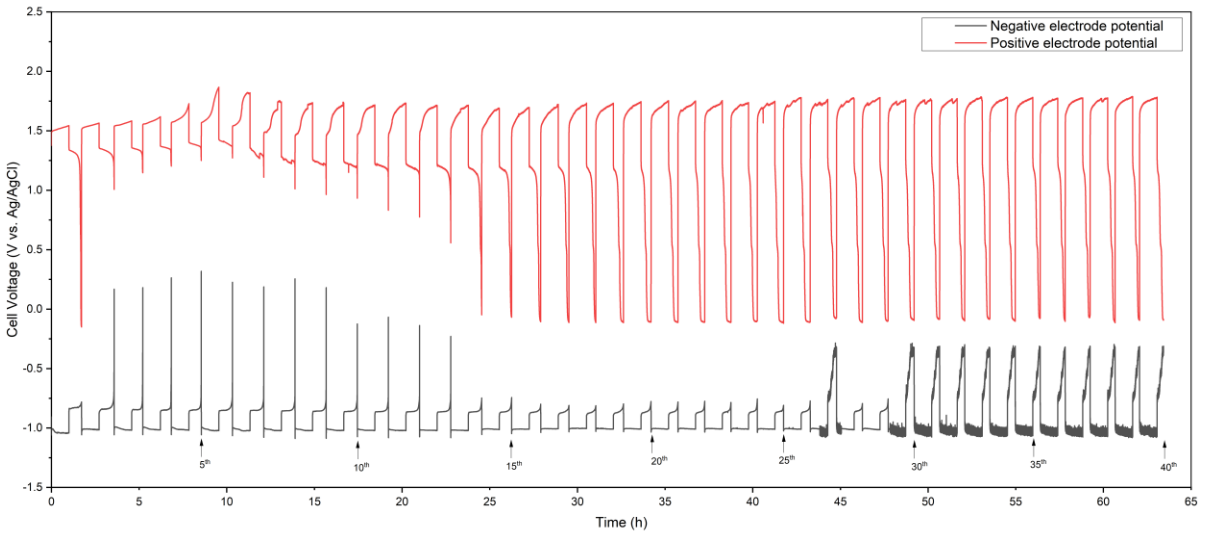


Figure 4.4. Negative and positive electrode potentials during 40 galvanostatic charge-discharge cycles at 25 mA/cm^2 and 50°C when 4 mol/L MSA is used as the positive supporting electrolyte.

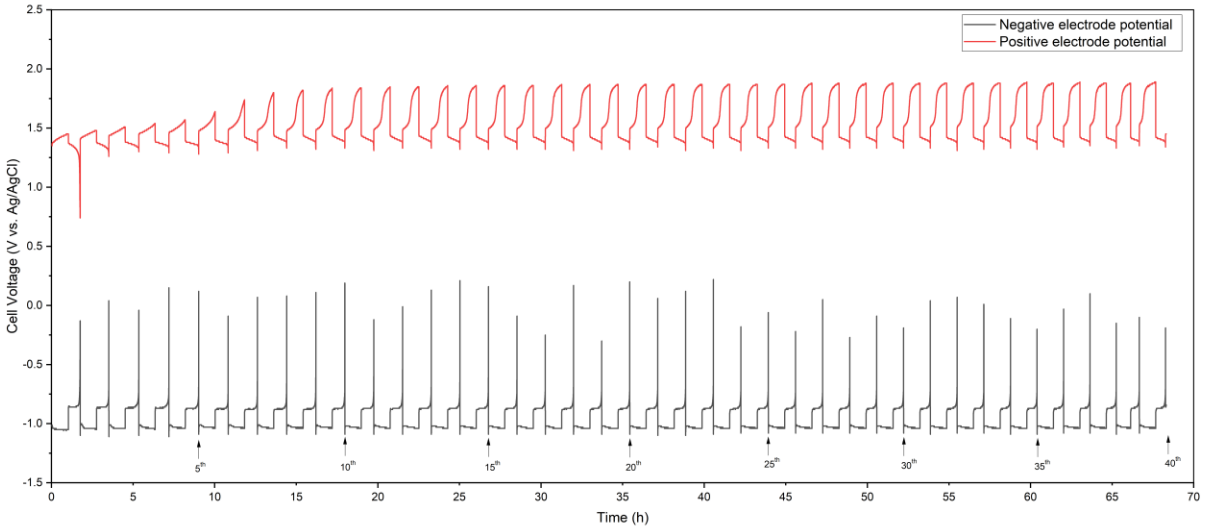


Figure 4.5. Negative and positive electrode potentials during 40 galvanostatic charge-discharge cycles at 25 mA/cm^2 and 50°C when 2 mol/L MSA-0.5 mol/L H_2SO_4 is used as the positive supporting electrolyte.

In the battery operating with the 4 mol/L MSA positive supporting electrolyte, the negative electrode reaction limits the efficiency of the battery during the early cycles (except during the first cycle) (Figure 4.4). Since hydrogen evolution at the negative electrode is not reversible, the amount of zinc available for anodic dissolution during discharge is less than the stoichiometric amount of Ce(IV) available for reduction on the positive side. As a result, the negative electrode becomes completely stripped of zinc before Ce(IV) is entirely consumed on the other side. This causes the negative electrode potential to rise sharply, triggering the termination of discharge. However, from the 14th cycle onward, the situation changes entirely and the limiting half-cell reaction during discharge switches to the Ce(III)/Ce(IV) couple at the positive electrode. As shown in Figure 4.4, the positive electrode potential now begins to drop very sharply during discharge and triggers the end of this part of the cycle. At the same time, the rise in the negative electrode potential begins to shrink and become insignificant. This dramatic change stems from another negative impact of the continual net transfer of H^+ ions into the negative compartment. As discussed previously, this leads to the ever-increasing extent of hydrogen evolution at the negative electrode during charge and the continual change in the positive electrolyte composition toward lower acidity, higher Ce(IV) and lower Ce(III) concentrations. This eventually leads to the

precipitation of CeO_2 in the positive electrolyte and a sudden drop in the total dissolved Ce concentration. Therefore, from the 14th cycle, the positive electrode reaction is limiting and the positive electrode potential drops more rapidly during discharge. Thus, the decay in the battery capacity when the positive electrolyte contains 4 mol/L MSA is accelerated by the reduction in the Ce(IV) solubility in the positive electrolyte after 14 cycles, although this entire chain of events is driven by the continual net transfer of H^+ ions from the positive side to the negative side.

It should be noted that some noise in the response of the negative electrode is observed from the 27th cycle to the 40th cycle when 4 mol/L MSA is present in the positive electrolyte (Figure 4.4). Such a response is not unusual in the case of metal electrodeposition accompanied by H_2 evolution. This is likely caused by fluctuations in the flow conditions (perhaps induced by gas bubbles) close to the T-shaped glass cell where the Ag/AgCl reference electrode is held. However, this phenomenon has no effect on the mean values of the electrode potential that are measured.

The electrode response of the battery operating with the 2 mol/L MSA-0.5 mol/L H_2SO_4 supporting electrolyte is similar to that observed when 4 mol/L MSA is used over the first 10 cycles (Figure 4.5). The cell voltage and the positive electrode potential during charge slowly increase over the first 10 cycles due to the accumulation of Ce(IV) ions and depletion of Ce(III) ions. However, thereafter the responses of the positive electrodes in the presence of the two positive electrolytes differ drastically. Unlike the situation with 4 mol/L MSA, only a small drop in the positive electrode potential occurs at the end of discharge when the positive electrolyte contains 2 mol/L MSA-0.5 mol/L H_2SO_4. Furthermore, the responses of both electrodes during both charge and discharge remain remarkably stable over the remainder of the experiment, which is a huge advantage for flow battery operation. The positive electrode remains much less polarized, reflecting faster electrode kinetics than that observed with the 4 mol/L MSA positive supporting electrolyte. Another noteworthy finding is that the negative electrode reaction remains the limiting process over the entire 40 cycles of the experiment based on the responses of the two electrodes. Similar to the case when 4 mol/L MSA is used, H_2 evolution occurs on the negative side. However, the Ce(III) and Ce(IV) solubilities remain high enough in the 2 mol/L MSA-0.5 mol/L H_2SO_4 supporting electrolyte that no precipitation of CeO_2 is observed to occur at any time during the 40 cycles. As will be shown later, this is due not only to the higher cerium solubility in the mixed acid but also because less H^+ transfers from the positive compartment to the negative compartment over

the course of battery operation. This allows the total dissolved cerium concentration in the positive electrolyte to remain high and constant throughout the experiment, leading to less polarization for the reduction of Ce(IV) to Ce(III) during discharge. Since the discharge voltage of the positive electrode is more stable and the duration for discharge is longer, both the average coulombic efficiency and voltage efficiency are higher from the 15th cycle onward. This is also the reason for the better overall performance and longer life-cycle of the battery operating with the mixed acid positive electrolyte.

Figure 4.6 presents a comparison of the coulombic efficiencies of the Zn-Ce redox flow battery over 40 charge-discharge cycles obtained in the 2 mol/L MSA-1 mol/L HNO_3, 2 mol/L MSA-0.5 mol/L H_2SO_4 and the original 4 mol/L MSA positive electrolytes. The efficiency data of the battery obtained when 3 mol/L MSA is used as the positive supporting electrolyte is not shown here since it is much lower than that obtained with the original 4 mol/L MSA electrolyte and drops below 60% very quickly. This is due to the lower Ce(IV) solubility in the 3 mol/L MSA and the precipitation of CeO_2 much earlier during the charge-discharge cycles. In all cases, a few cycles of conditioning are required in order for the system to exhibit more stable behaviour. The sudden drop in the current efficiency observed after the second charge-discharge cycle during the experiment in which 4 mol/L MSA is used is caused by a particular event that was observed only in this case. Near the end of the 2nd discharge, a small portion of zinc metal deposited on the negative electrode during the previous charge was observed to detach from the electrode, presumably due to poor attachment to the PVE substrate. Since this detached zinc was unavailable for battery discharge, this led to a lower coulombic efficiency than was otherwise possible. After the 3rd cycle, the adherence of the zinc deposit to the PVE substrate apparently improved (perhaps due to residual zinc left on the PVE from the previous cycles) and detachment of the zinc from the substrate during discharge was no longer observed and the current efficiency recovered. Since this phenomenon was not observed thereafter, it had no bearing on the long-term battery performance which is the focus of these experiments. This is supported by the recorded negative electrode potential during battery charge-discharge cycles, as has been shown previously. In comparison, no sudden decrease in coulombic efficiency is observed in the cases of the 2 mol/L MSA-0.5 mol/L H_2SO_4 and 2 mol/L MSA-1 mol/L HNO_3 positive electrolytes.

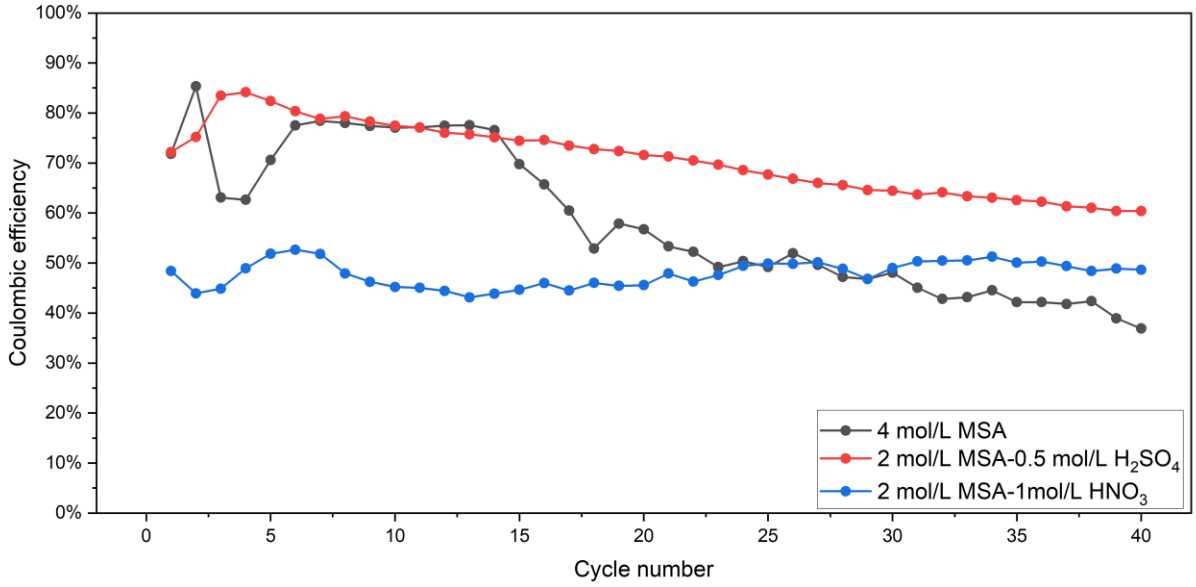


Figure 4.6. Coulombic efficiency of Zn-Ce redox flow battery operating with different positive electrolytes over 40 galvanostatic charge-discharge cycles. The current density during each charge-discharge cycle is 25 mA/cm^2 and the charge duration is 1 hour during each cycle.

The average coulombic efficiency of the battery over 40 cycles obtained in the 4 mol/L MSA supporting electrolyte is 58.3%, which is much lower than the level of 70.8% achieved in the 2 mol/L MSA-0.5 mol/L H_2SO_4 electrolyte. The average loss of coulombic efficiency of the battery per cycle when using 4 mol/L MSA is approximately 1.26%. Based on previous studies[38], this is believed to be caused by the net transfer of H^+ from the positive side to the negative side which leads to an ever-increasing amount of H_2 evolution occurring during charge. Since this reaction is not reversible and the charge passed during H_2 evolution reaction cannot be used for battery discharge, it causes a loss of current efficiency. As discussed previously, another factor leading to the lower coulombic efficiency when 4 mol/L MSA is used as the supporting positive electrolyte is the precipitation of Ce(IV) in the form of CeO_2 in the positive electrolyte. CeO_2 precipitation is observed after approximately the 10th charge-discharge cycle. Since this precipitation decreases the total Ce(IV) ion concentration available for battery discharge in the positive electrolyte, it causes both the positive potential during discharge and the coulombic efficiency to decrease significantly. The average loss of coulombic efficiency for the battery with 2 mol/L MSA-0.5

mol/L H_2SO_4 electrolyte is only 0.59% per charge-discharge cycle. Obviously, since CeO_2 precipitation is not observed to occur in this case, the capacity fade in this mixed acid is attributed entirely to the net transfer of H^+ from the positive side to the negative side. In summary, the replacement of 4 mol/L MSA with 2 mol/L MSA-0.5 mol/L H_2SO_4 mixed acid in the positive electrolyte leads to superior coulombic efficiency and slower capacity fade of the battery, both of which are especially beneficial for long-term operation.

In the case of 2 mol/L MSA-1 mol/L HNO_3 as the positive supporting electrolyte, the coulombic efficiency is more stable and almost no decrease of coulombic efficiency is observed over the course of 40 cycles. However, the coulombic efficiency is significantly lower than that of other two cases throughout the experiment. The average coulombic efficiency is only 47.9%, which differs significantly from the level of ~70% reported in a previous study.[177] However, it is important to note that the type of experiment and conditions in this earlier study were significantly different from those used here. The coulombic efficiency was not measured in an operating RFB undergoing numerous galvanostatic charge-discharge cycles and instead obtained in a flow-type electrolytic cell containing 6 mol/L HNO_3 by first oxidizing Ce(III) at an electrode potential of 1.5 V vs. Ag/AgCl for 155 min followed by cathodic reduction to reduce Ce(IV) back to Ce(III). It was also shown in another study that oxygen evolution is enhanced during anodic oxidation from an electrolyte containing nitric acid at concentrations above 0.5 mol/L since this causes the overpotential for oxygen evolution to drop below the onset potential for the Ce(III)/Ce(IV) redox couple.[33] Thus, if the positive electrode reaction is limiting during discharge, one would expect this effect to reduce the coulombic efficiency of a Zn-Ce RFB operating with the 2 mol/L MSA-1 mol/L HNO_3 supporting positive electrolyte. However, our experimental results (not included here) show that it is the negative potential that changes rapidly at the end of each charge-discharge cycle when 2 mol/L MSA-1 mol/L HNO_3 is used as the supporting positive electrolyte, which indicates that the negative electrode reaction is limiting during discharge throughout the 40 cycles. Thus, the cause for the low coulombic efficiency when the positive electrolyte contains 2 mol/L MSA-1 mol/L HNO_3 is more complicated and requires further investigation that is beyond the scope of the present study.

As noted previously, very poor results are achieved when a positive electrolyte containing 3 mol/L MSA at the start of operation is used and so are not shown here. The Ce(IV) solubility in this

solution is low enough that white CeO_2 precipitate particles start to appear in the positive electrolyte tank as early as the 4th charge-discharge cycle and the positive half-cell reaction becomes the limiting electrode reaction which accelerates battery performance decay.

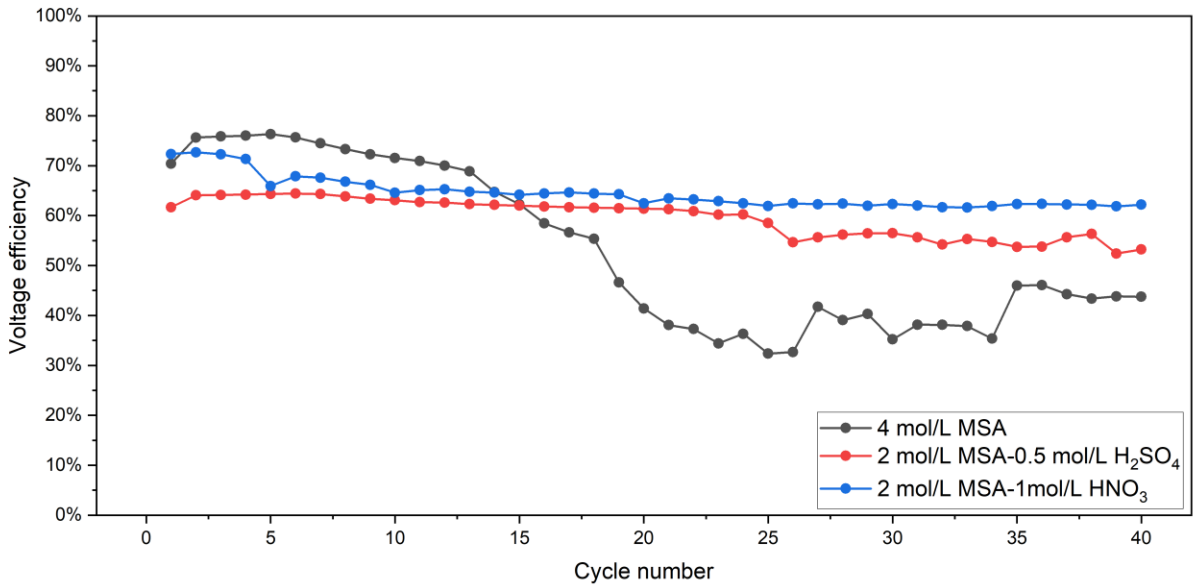


Figure 4.7. Voltage efficiency of Zn-Ce redox flow battery operating with different positive electrolytes over 40 galvanostatic charge-discharge cycles. The current density during each charge-discharge cycle is 25 mA/cm^2 and the charge duration is 1 hour during each cycle.

Figure 4.7 shows the corresponding voltage efficiencies obtained over the 40 charge-discharge cycles when the different positive electrolytes are used. The average voltage efficiency of the battery employing 4 mol/L MSA is 53.0%, whereas the voltage efficiencies are 59.6% and 64.4% in the cases of 2 mol/L MSA-0.5 mol/L H_2SO_4 and 2 mol/L MSA-1 mol/L HNO_3, respectively. Before the 15th cycle, the voltage efficiency of the battery using 4 mol/L MSA is the highest among the investigated positive electrolytes. However, it decreases rapidly after the 13th cycle and continues to drop until the end of 40 cycles. Since the total proton concentration in 4 mol/L MSA is higher than in the other positive electrolytes, a lower ohmic loss across the ion exchange membrane is expected, consistent with the higher voltage efficiency over the first few charge-discharge cycles. The sharper decrease of the voltage efficiency after the 13th cycle in the case of 4 mol/L MSA can be attributed to the precipitation of CeO_2, which reduces the total soluble Ce

concentration and increases the overpotential at the positive electrode during battery charge. This is confirmed by the gradual increase of the positive electrode potential during battery charge, as shown in Figure 4.4. The decrease in the total soluble Ce concentration should also increase the overpotential for Ce(IV) reduction during discharge. This is confirmed by the profile for the positive electrode potential in Figure 4.4 which shows a decrease in the average discharge potential after the first 6 charge-discharge cycles. This combination of effects of CeO_2 precipitation on the positive electrode potential during charge and discharge further lowers the voltage efficiency. The voltage efficiencies when 2 mol/L MSA-0.5 mol/L H_2SO_4 and 2 mol/L MSA-1 mol/L HNO_3 are used as positive supporting electrolyte remain relatively stable throughout the 40 charge-discharge cycles and decrease by only 0.27% and 0.26%, respectively, per charge-discharge cycle. In contrast, the voltage efficiency loss is 0.68% per cycle in the case of 4 mol/L MSA.

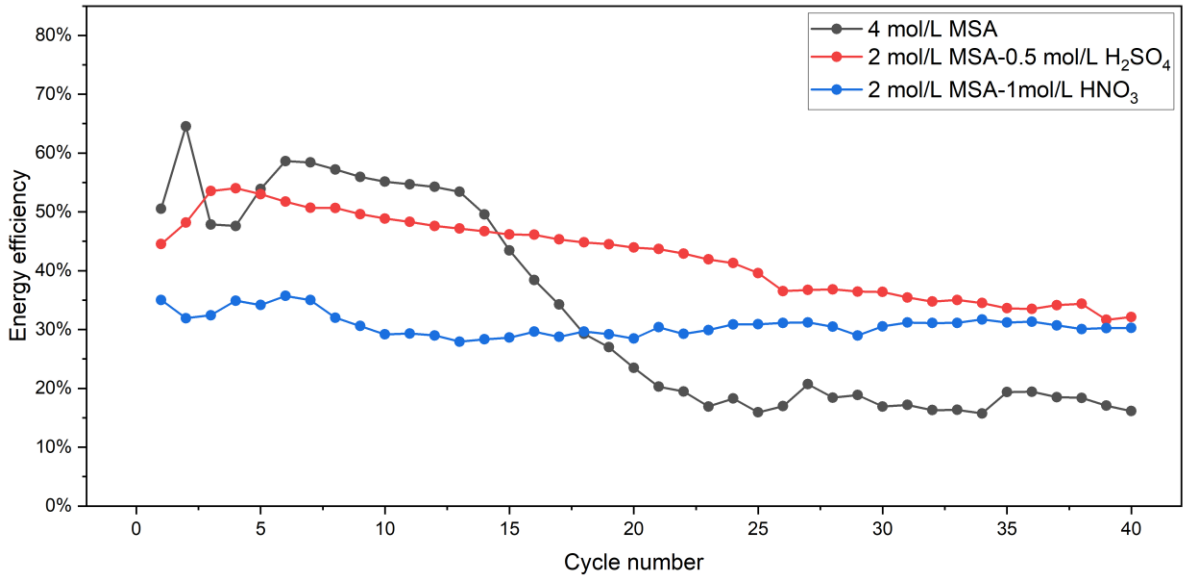


Figure 4.8. Energy efficiency of Zn-Ce redox flow battery operating with different positive electrolytes over 40 galvanostatic charge-discharge cycles. The current density during each charge-discharge cycle is 25 mA/cm^2 and the charge duration is 1 hour during each cycle.

The resulting change in the energy efficiency over time is shown in Figure 4.8. The battery employing 4 mol/L MSA exhibits higher energy efficiency (~75%) up to the 15th cycle, but then suffers a rapid drop to ~20% by the 23rd cycle until the end of 40 cycles. This sudden drop is a reflection of the sudden decrease of both the coulombic and voltage efficiencies during the 15th cycle. The average energy efficiency for 4 mol/L MSA over the entire experiment is 32.8%. After 40 charge-discharge cycles, the energy efficiency of the battery operating with 4 mol/L MSA as the positive supporting electrolyte is the lowest among the investigated electrolytes. For the batteries employing 2 mol/L MSA-0.5 mol/L H_2SO_4 and 2 mol/L MSA-1 mol/L HNO_3, the average energy efficiencies are 42.4% and 30.8%, respectively. Thus, for long-term battery operation, 2 mol/L MSA-0.5 mol/L H_2SO_4 exhibits better energy efficiency and higher stability than the original 4 mol/L MSA electrolyte.

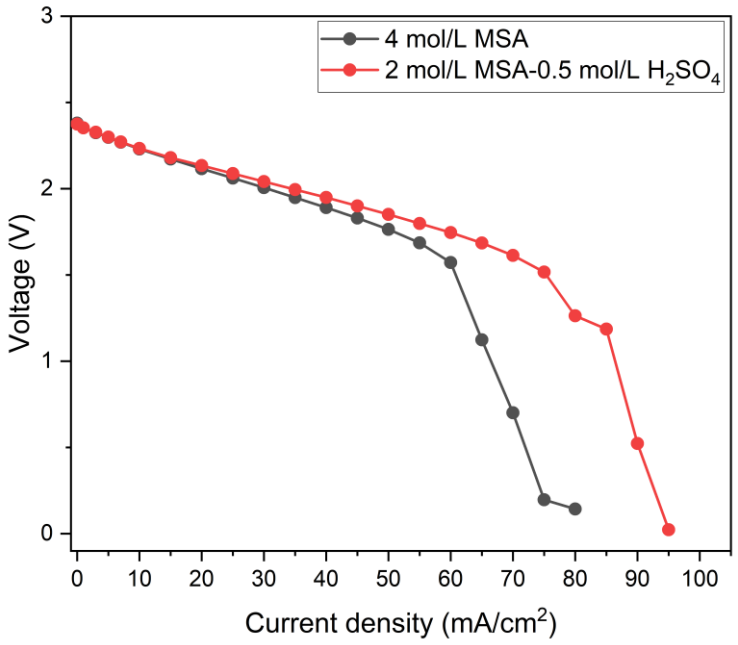


Figure 4.9. Polarization curve of Zn-Ce redox flow battery operating with 4 mol/L MSA and 2 mol/L MSA-0.5 mol/L H_2SO_4 mixed acid as positive supporting electrolyte.

Polarization experiments have been conducted to evaluate the battery performance operating with 4 mol/L MSA and 2 mol/L MSA-0.5 mol/L H_2SO_4 mixed acid as the positive supporting electrolytes. The polarization curve of the battery with 2 mol/L MSA-1 mol/L HNO_3 as the positive supporting electrolyte has not been obtained for comparison since this solution has already been shown to yield much lower coulombic and energy efficiencies. The two polarization curves shown in Figure 4.9 are very similar at low current densities (<10 mA/cm^2) where the battery operates under activation control, with an open-circuit voltage of ~2.38 V. Better battery performance is observed in the ohmic and mass transfer-limited regions when using 2 mol/L MSA-0.5 mol/L H_2SO_4 mixed acid electrolyte. The battery exhibits lower overpotential in the ohmic polarization and mass transfer-dominated regions. For the battery operating with 4 mol/L MSA, the battery becomes mass-transport controlled at a current density of ~60 mA/cm^2, whereas the sharp decrease in voltage due to mass transport limitations occurs at a higher current density of ~75 mA/cm^2 when 2 mol/L MSA-0.5 mol/L H_2SO_4 mixed acid is the positive supporting electrolyte. It will be shown later that H^+ ions continually transfer from the positive to the negative compartment and the Ce(III) and Ce(IV) concentrations in the positive electrolyte continually change during the course of battery operation. These phenomena complicate the interpretation of the differences in the polarization curves shown in Figure 4.9. To minimize these effects, the polarization experiments have been conducted so as to maintain the total elapsed time for completion as short as possible. Nevertheless, over the course of the ~ 1 hour to carry out each of the two polarization experiments shown in Figure 4.9, small changes in the H^+, Ce(III) and Ce(IV) concentrations have likely occurred. As will be shown, the Ce(IV) concentration in the positive electrolyte remains higher throughout operation when 2 mol/L MSA-0.5 mol/L H_2SO_4 mixed acid is present than when 4 mol/L MSA is used. This difference could contribute to faster Ce(IV) reduction, higher cell voltages and better battery performance during discharge at intermediate and high current densities evident in Figure 4.9 when the positive electrolyte contains 2 mol/L MSA-0.5 mol/L H_2SO_4 mixed acid. Another possible factor could be differences in the viscosities of the two positive electrolytes. The electrolyte containing 2 mol/L MSA-0.5 mol/L H_2SO_4 is less concentrated than the one containing 4 mol/L MSA and so likely has a lower viscosity which in turn could lead to a higher mass transfer coefficient and limiting current density for the reduction of Ce(IV) to Ce(III) in the positive electrolyte during discharge.

4.3.3 Evolution of H^+ concentration in negative electrolyte and Ce(IV) concentration in positive electrolyte

To gain further insight into the differences in the battery performance achieved using 2 mol/L MSA-0.5 mol/L H_2SO_4 mixed acid and 4 mol/L MSA, the variation of the H^+ concentration in the negative electrolyte and Ce(IV) concentration in the positive electrolyte during the charge-discharge cycles is shown in Figure 4.10 and Figure 4.11, respectively. The H^+ and Ce(IV) concentrations were not determined when 2 mol/L MSA-1 mol/L HNO_3 mixed acid was used as the supporting positive electrolyte since the corresponding battery performance was considerably poorer than that achieved using the other two positive supporting electrolytes.

When the battery operates with 4 mol/L MSA as the positive supporting electrolyte, the H^+ concentration in the negative electrolyte increases gradually from an initial value of 1 mol/L to 2.8 mol/L over 15 charge-discharge cycles (Figure 4.10). Thereafter, the H^+ concentration rises slowly and levels off at ~3.2 mol/L by the end of 40 cycles. Compared to the initial concentration on the negative side, the acidity has increased ~3 times, which undoubtedly accelerates the H_2 evolution side reaction. In addition, the decreased acidity in the positive electrolyte is the main factor that causes the precipitation of Ce(IV) ions as CeO_2. The data in Figure 4.10 show that the H^+ concentration in the negative electrolyte has already risen from 1 mol/L to ~ 1.6 mol/L over the 1st cycle alone, indicating that the initial transfer across the membrane is very rapid.

As expected, less H^+ is transferred from the positive to negative electrolyte when 2 mol/L MSA-0.5 mol/L H_2SO_4 mixed acid is used on the positive side due to the smaller H^+ concentration gradient across the membrane. Our results show that the H^+ concentration in the negative electrolyte has reached only ~ 1.2 mol/L by the end of the 1st cycle and eventually stabilizes at 2.2 mol/L by the 15th cycle with very little change over the following 25 cycles. A lower proton concentration in the negative electrolyte is beneficial to battery performance since less H_2 evolution side reaction should occur. While the coulombic efficiency of the full battery does not solely depend on the H^+ concentration on the negative side, the reduced H^+ concentration is likely to be one of the reasons that higher coulombic efficiency is achieved when the positive electrolyte consists of 2 mol/L MSA-0.5 mol/L H_2SO_4 mixed acid electrolyte on the positive side over long-term battery operation. Although H^+ crossover does occur in the case of the 2 mol/L MSA-0.5

mol/L H_2SO_4 mixed acid electrolyte and the acidity of the positive electrolyte decreases, importantly no precipitation of CeO_2 is ever observed due to the higher Ce(IV) solubility in the MSA-H_2SO_4 mixed acid electrolyte.

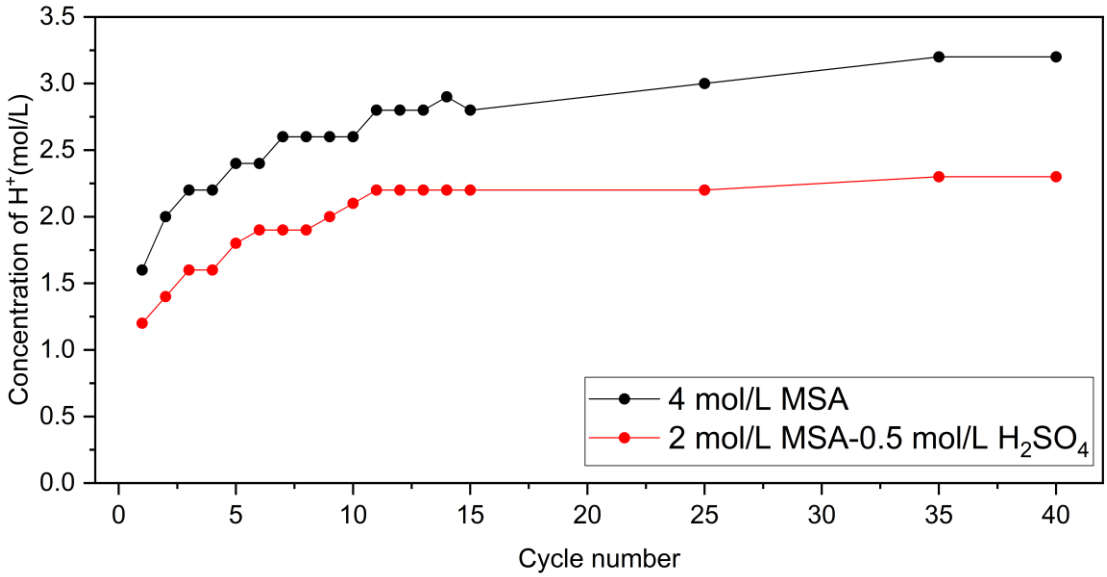


Figure 4.10. Variation of the H^+ concentration in the negative electrolyte over the course of 40 charge/discharge cycles when 4 mol/L MSA and 2 mol/L MSA-0.5 mol/L H_2SO_4 are used as the supporting positive electrolytes.

As noted previously, the Ce(IV) solubility in the positive electrolyte is one of the factors limiting the Zn-Ce RFB energy capacity. To understand the changes of composition in the positive electrolyte, we also have measured the Ce(IV) concentration at the end of each charge-discharge cycle. As shown in Figure 4.11, the gradual rise of Ce(IV) concentration in the positive electrolyte over the first 4 cycles confirms previous findings reported in the literature of the accumulation of Ce(IV) ions over time due to the limited amount of zinc deposit on the negative electrode available for discharge.[38] The Ce(IV) concentration reaches a maximum level of 0.38 mol/L when 4 mol/L MSA is used in the positive electrolyte. Ideally, the Ce(IV) concentration should drop to 0 mol/L

at the end of discharge if the battery operates at 100% coulombic efficiency since the positive electrolyte initially contains no Ce(IV). From the 5th cycle onward, the Ce(IV) concentration starts to decrease as CeO_2 precipitation occurs in the electrolyte and particles continue to form during the subsequent cycles. As shown in Figure 4.12b, a precipitate is visible in the yellow positive electrolyte collected after 40 cycles, as indicated by the arrows at the bottom of the electrolyte tank. The precipitation of Ce(IV) oxide has also been reported in several other studies.[125,130,178] Eventually, the Ce(IV) concentration stabilizes at ~0.3 mol/L by the end of 40 charge-discharge cycles. Previous work has shown that the solubility of both Ce(III) and Ce(IV) depends strongly on the concentration of MSA.[127] While the solubility of Ce(III) rises as the MSA concentration is lowered, the opposite trend is observed in the case of Ce(IV) ions.

When 2 mol/L MSA-0.5 mol/L H_2SO_4 mixed acid is used as the supporting positive electrolyte, no precipitate is observed to form even by the end of the 40 charge-discharge cycles. The electrolyte retains a clear orange colour, reflecting that it remains stable and the Ce(IV) solubility is higher than in the 4 mol/L MSA electrolyte (Figure 4.12c). Figure 4.12a shows a comparison of the colour of two electrolytes after 40 charge-discharge cycles. As shown in Figure 4.11, the Ce(IV) concentration remains significantly higher in the 2 mol/L MSA-0.5 mol/L H_2SO_4 mixed acid electrolyte than in 4 mol/L MSA throughout the experiment. Obviously, the decrease of the Ce(IV) concentration in the 2 mol/L MSA-0.5 mol/L H_2SO_4 mixed acid electrolyte from the 4th cycle onward cannot be attributed to Ce(IV) precipitation. The Ce(IV) concentration in the positive electrolyte can be determined by other factors – the relative extents of Zn(II) reduction and H_2 evolution at the negative electrode during charge and the possible transfer of Ce(IV) or Ce(III) across the membrane to the negative side. This second possibility is the subject of the investigation in the next chapter.

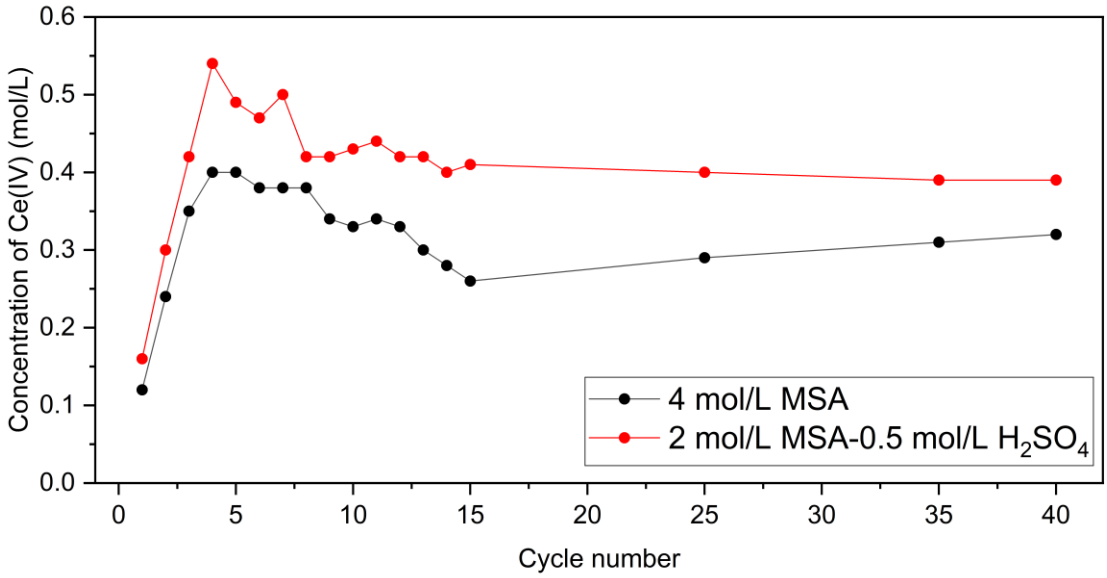


Figure 4.11. Variation in the Ce(IV) concentration in the positive electrolyte over the course of 40 charge/discharge cycles when 4 mol/L MSA and 2 mol/L MSA-0.5 mol/L H_2SO_4 are used as the supporting positive electrolytes.

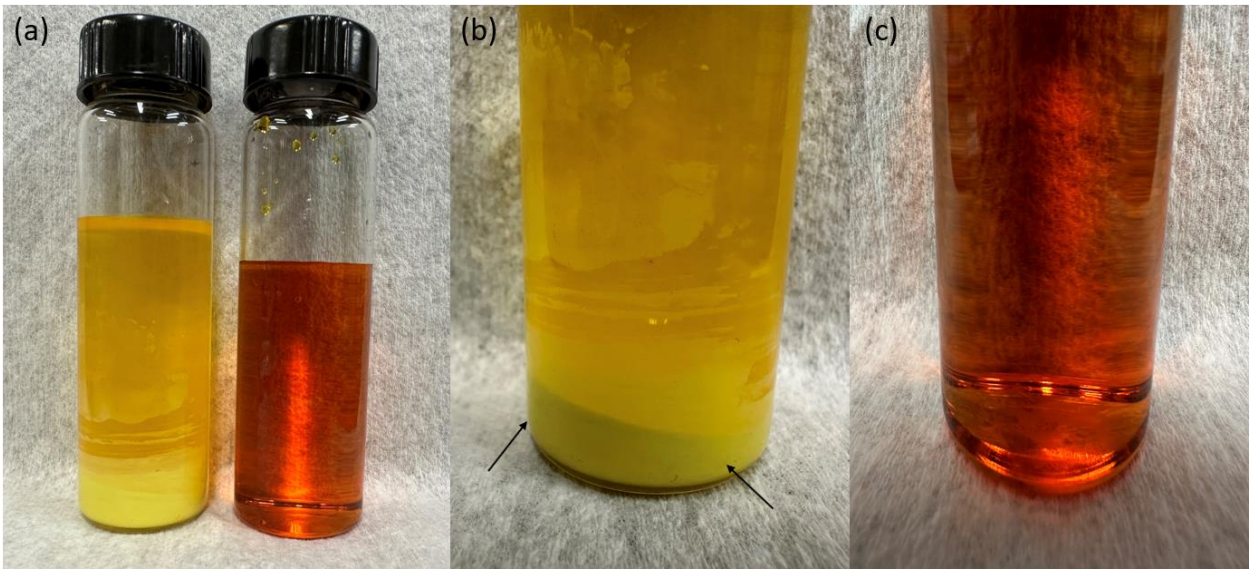


Figure 4.12. (a) Comparison of the positive electrolytes remaining after 40 charge-discharge cycles: 4 mol/L MSA (left) and 2 mol/L MSA-0.5 mol/L H_2SO_4 mixed acid (right) supporting electrolytes. (b) 4 mol/L MSA and (c) 2 mol/L MSA-0.5 mol/L H_2SO_4 mixed acid supporting electrolyte.

Chapter 5 Improving performance of hybrid Zn–Ce redox flow battery by controlling ion crossover and use of mixed acid positive electrolyte[2]

5.1 Introduction

A main focus of the study described herein is on measuring the ion crossover in Zn-Ce RFBs and reducing its detrimental effects on battery performance. However, it is first important to distinguish between transport of ions across the membrane that is necessary to just maintain the applied current flowing through the cell and additional transport driven by concentration gradients between the positive and negative electrolytes, but also can be due to pressure gradients and osmotic pressure differences.[168,170] The first type of transport can be termed as membrane exchange and the second type as crossover. Nafion-type membranes are very commonly used in Zn-Ce RFBs and many other systems due to their excellent proton conductivity and durability, but tend to be leaky and relatively non-selective. As a result, they typically allow a considerable amount of ion crossover during battery operation. The rate of ion crossover is generally time-dependent due to changes in ionic concentrations, electrical polarity, electrolyte viscosity and temperature.[180] An important difference between membrane exchange and crossover is the direction in which they act during battery charge-discharge cycles. The direction of membrane exchange which is governed by the electrical polarity of the cell reverses in direction when the battery switches from charge to discharge, while direction of crossover is governed entirely by the gradient that drives it regardless of the cell polarity. In most cases where ion crossover occurs due to concentration gradients across the membrane, it operates in the same direction throughout the charge-discharge cycles.

As noted above, perfluorinated cation exchange membranes such as Nafion 117 are widely used in redox flow batteries due to their high proton conductivity and excellent chemical and mechanical stability.[181–184] During battery charge, the reduction of Zn(II) and H^+ on the negative electrode reduces the amount of positive charge in the negative electrolyte, whereas the conversion of Ce(III) to Ce(IV) increases the positive charge on the positive side. Since the electrolytes must maintain electroneutrality, a net flow of positively charged ions occurs from the positive electrolyte to the

[2] This chapter is adapted from my published work.[179]

negative electrolyte through the membrane to balance the changes due to the electrode reactions and to conduct electricity. Ideally, a proton exchange membrane would allow only the transfer of H^+ from one side to another to prevent the mixing of the other electroactive species in the negative and positive electrolytes. During battery discharge, the deposited zinc metal layer on the negative electrode re-dissolves anodically into the negative electrolyte as Zn(II) ions and H^+ are transported from the negative electrolyte back to the positive electrolyte to complete the electrical circuit.

In our previous work, we showed that the continuous crossover of H^+ from the positive to the negative electrolyte increases the undesired H_2 evolution reaction and eventually causes the precipitation of CeO_2 in the positive electrolyte, which degrades battery performance even further.[32] The mitigation of these effects in a commercial RFB would require the periodic rebalancing of electrolyte compositions during long-term battery operation and therefore raise maintenance and operation costs.

One obvious approach to reducing H^+ crossover is to reduce the difference between its concentration on the positive side from that on the negative side. Typically, when MSA alone has been used as the supporting electrolyte on both sides, the acid concentration is 4 mol/L on the positive side and 1 mol/L on the negative side. In the previous chapter, we showed that the use of a novel 2 mol/L MSA–0.5 mol/L H_2SO_4 mixed acid (heretofore denoted as 2/0.5 MA) positive supporting electrolyte with an overall acid concentration of only 3 mol/L, while maintaining 1 mol/L MSA alone as the negative supporting electrolyte, led to a large improvement in the performance of a Zn-Ce RFB from that attained when the positive supporting electrolyte contained 4 mol/L MSA.[32] Another benefit of using this mixed acid positive electrolyte was that CeO_2 precipitation was not observed to occur even after many galvanostatic charge-discharge cycles, unlike what is always found in the case of the MSA-only electrolyte initially containing 4 mol/L.

In this work, we conduct a systematic study in which the H^+ concentration in the negative electrolyte and the Zn(II), Ce(III), and Ce(IV) concentrations in both electrolytes are monitored after each of 30 consecutive charge-discharge cycles, which has not been investigated in any previous reported study of Zn-Ce RFBs. The H^+ concentration in the positive electrolyte could not be measured since the colorimetric titration technique which was very successful for the negative electrolyte did not work in the case of the positive electrolyte due to its yellow color. The

information gained from these experiments was then used to modify the composition of the positive electrolyte in order to further improve battery performance. Although this work is concerned with the Zn-Ce hybrid flow battery, the general findings and strategies should be applicable to other similar flow battery systems where crossover of species between the electrode compartments contributes to poorer performance.

5.2 Experimental

5.2.1 Preparation of electrolyte

All chemicals were used as received without further purification. The negative electrolyte containing 1.5 mol/L zinc(II) methanesulfonate was prepared by dissolving zinc oxide (Zochem Inc.) in the appropriate amount of methanesulfonic acid (70%, Alfa Aesar). Extra methanesulfonic acid (MSA) was added to adjust the MSA concentration to be 1 mol/L. Similarly, the positive electrolytes with 0.8 mol/L cerous methanesulfonate and different amounts of zinc(II) methanesulfonate were prepared by dissolving mixtures of cerium carbonate (Treibacher Industrie AG, 99% pure) and zinc oxide with MSA. MSA and/or H_2SO_4 was then added to achieve 4 mol/L MSA or 2 mol/L MSA-0.5 mol/L H_2SO_4 mixed acid supporting electrolytes. Ultrapure water with a resistivity of ~18 MΩ cm was used to prepare all the solutions in this work.

5.2.2 Measurement of Ce(IV), H^+ and Zn(II) concentrations and electrolyte properties

The concentration of Ce(IV) in the positive electrolyte was measured by a colorimetric titration method using ferroin (1,10-phenanthroine iron (II) sulfate, Alfa Aesar) as an end-point indicator. 50 μL of positive electrolyte was collected and titrated by 0.05 mol/L ammonium iron (II) sulfate hexahydrate (99%, Sigma-Aldrich). To measure the concentration of Ce(III) in the positive electrolytes, another 50 μL sample was collected and then contacted with a certain amount of ammonium persulfate (thermo scientific, 98+%) and silver nitrate solution (Titripur, 0.1 mol/L) to oxidize all Ce(III) present to Ce(IV). This step was followed by colorimetric titration to determine the Ce(IV) content in this oxidized sample. The Ce(III) concentration could then be determined

from the difference between the total Ce(IV) concentration after oxidation and the original Ce(IV) concentration prior to oxidation. The very small sample volumes required for these titrations ensured that the cumulative amount collected over the course of the experiments had no effect on battery operation.

The H^+ concentration in the negative electrolyte was determined by colorimetric titration using a 0.01 mol/L NaOH solution, which was prepared by dissolving sodium hydroxide beads (VWR Analytical) in ultrapure water. The end-point of this titration process as indicated by methyl red (Ricca Chemical) occurred when the color of the solution changed from red to yellow. As noted previously, this technique could not be applied to the positive electrolyte due to it being colored (yellow) and so it was not possible to measure the H^+ concentration in the positive electrolyte. Inductively coupled plasma optical emission spectroscopy (ICP-OES, Teledyne Leeman Labs Prodigy) was used to measure the Zn(II) concentration in both positive and negative electrolytes. The conductivity of different fresh positive electrolytes was measured with a Mettler-Toledo AG conductometer. The viscosity of the electrolytes at 50 ℃ was measured using a Brookfield DV2TLV digital rotational viscometer.

5.2.2.1 Electrochemical measurements

Half-cell measurements

The kinetics of the Ce(III)/Ce(IV) redox couple at 50 ℃ in the different electrolytes was investigated by conducting cyclic voltammetry (CV) experiments using a conventional 3-electrode system. The working electrode was a Pt-disc electrode with an area of 3.14 mm^2, while a graphite rod (Alfa Aesar) was used as the counter electrode and an Ag/AgCl electrode (Pine Research Instrumentation) as the reference electrode. The CV experiments were conducted using a Bio-logic EPP-4000 potentiostat. The temperature of the solutions was maintained at 50 ℃ by immersing the electrochemical cell in a Neslab RTE-8 water bath.

Full-cell system

Full-cell experiments were conducted in a bench-scale redox flow battery consisting of a 6 mm-thick Pt-Ti mesh (Metakem GmbH) positive electrode with a Pt loading level of 7 mg/cm^2, a polyvinyl ester (PVE) carbon sheet (TDM Fuel Cells) negative electrode attached to a copper current collector (McMaster-Carr), two custom-made flow channels made from acrylic sheet (CIP Wholesale) to distribute electrolytes and an ion exchange membrane (Nafion 117, Fuel Cell Store) to separate the two compartments. Silicone rubber gaskets (CS Hyde Company) were used to prevent any electrolyte leakage. More details regarding the design and operation of this battery can be found in a previous study.[185]

The positive and negative electrolytes each with a volume of 30 mL were circulated from separate external reservoirs through Viton tubing (McMaster-Carr) to the battery compartments and back using a 2-head Longer BT100-1L peristaltic pump which enabled independent control of the two streams. The flow rate of the electrolytes was controlled to be 60 mL/min on both sides and the electrolyte tanks were immersed in a 50 ℃ water bath throughout the experiments. Prior to the experiments, the Nafion 117 membrane was activated by soaking in each of the following solutions for 1 hour at ~80 ℃ in the order: 3%(wt.) H_2O_2, ultrapure water, 0.5 mol/L H_2SO_4 solution and ultrapure water. The electrochemical measurements were conducted using Autolab PGSTAT 30 potentiostat connected to a computer controlled via Nova 2.1.5 software.

The battery efficiency was characterized by subjecting it to 30 galvanostatic charge-discharge cycles. Each cycle proceeded by charging the battery at a fixed current density of 25 mA/cm^2 for a duration of 1 hour followed by discharge at the same current density. Discharge was terminated when the battery cell voltage reached a cut-off value of 0.5 V. The coulombic efficiency of the battery over each cycle was obtained from the ratio of discharge time to the charge time, while the voltage efficiency over each cycle was determined from the ratio of the average discharge cell voltage to charge cell voltage. Discharge polarization experiments were conducted by first charging the battery at a current density of 50 mA/cm^2 for 90 minutes to reach a state-of-charge (SOC) of 50%. To ensure the SOC of the battery to be maintained as close to 50% as possible, 60 mL of each positive and negative electrolytes were used for all the polarization experiments, which was twice as large as the volume of electrolytes used in the charge-discharge cycling tests. To check that the battery SOC remained at or very close to 50% throughout the experiment, the Ce(IV) concentration was measured immediately after the 90-minute battery charge and at the end of the

polarization measurements. The results showed that the decrease of Ce(IV) concentration was small enough not to be a factor in the interpretation in the resulting polarization curves. Then the battery was discharged for 20 seconds at a different current density within the range from 0 to 110 mA/cm^2 followed by a 20-second rest period before continuing to the next current density. The average cell voltage over each 20-second period obtained was then plotted versus the corresponding current density to yield the polarization curve.

5.3 Results and Discussion

5.3.1 Crossover in battery operating with 4 mol/L MSA positive supporting electrolyte

In Chapter 4, we showed that the coulombic efficiency is limited by reactions at the negative electrode over the first 14 cycles when using 4 mol/L MSA as the positive electrolyte. This is reflected in the observation that the negative electrode potential rises abruptly and by a large amount at the end of battery discharge whereas the positive electrode potential changes very little, indicating the complete removal of the zinc deposit formed during battery charge. At the same time, unreacted Ce(IV) remains in the positive electrolyte at the end of discharge and so slowly accumulates from cycle to cycle. This imbalance arises because the irreversible HER side reaction occurring during battery charge at the negative electrode proceeds to a greater extent than does the irreversible OER side reaction at the positive electrode. As more H^+ is transferred from the positive to the negative side, the solubility of Ce(IV) decreases to the point that CeO_2 begins to precipitate out during the 6^{th} cycle and reduces the total amount of soluble cerium available for battery charge/discharge. As precipitation continues, the positive electrolyte becomes progressively more depleted of soluble cerium such that by the 14^{th} cycle the battery becomes limited by the Ce(III)/Ce(IV) reaction. In contrast, when the 2/0.5 MA is used as the positive supporting electrolyte, CeO_2 precipitation is not observed and the coulombic efficiency is always limited by the HER at the negative electrode.

As noted in the Introduction, the crossover of ions other than H^+ during operation of Zn-Ce RFBs has not been investigated to the best of our knowledge. To address this question, we measured the

concentrations of Zn(II), Ce(III) and Ce(IV) in both electrolytes and H^+ in the negative electrolyte at the end of each of 30 consecutive charge-discharge cycles operating at 25 mA/cm^2. The results obtained when the positive electrolyte contains 4 mol/L MSA are shown in Figure 5.1A-C. In the cases of H^+ and Zn(II), the observed changes in concentration can be attributed to ion crossover. The situation for Ce(III) and Ce(IV) is different, as will be discussed. As shown in Figure 5.1A, the Zn(II) concentration in the negative electrolyte decreases steadily from 1.5 to 0.96 mol/L by the end of 30 cycles, while it increases from 0 to ~0.66 mol/L over the same period in the positive electrolyte. This change is accompanied by a rise of the H^+ concentration in the negative electrolyte from 1.0 mol/L to ~2.7 mol/L due to transfer from the positive side (Figure 5.1B), similar to that reported previously.[32] Since these determinations are made at the end of discharge, the Zn(II) concentration measured in the negative electrolyte should ideally remain at 1.5 mol/L from cycle to cycle if no metal is lost from this side of the cell. Thus, the observed drop in the concentration represents a large and permanent loss of Zn(II) from the negative electrolyte due to leakage across the membrane, reaching ~36% of the initial amount present in the negative electrolyte at the start of operation by the end of 30 cycles. Obviously, this effect and the concomitant rise in the H^+ concentration in the negative electrolyte makes zinc deposition increasingly less competitive to H_2 evolution during battery charge as the cycles continue, which results in an ever lower coulombic efficiency. It is not surprising then that these trends can ultimately lead to the complete failure of the battery.[38]

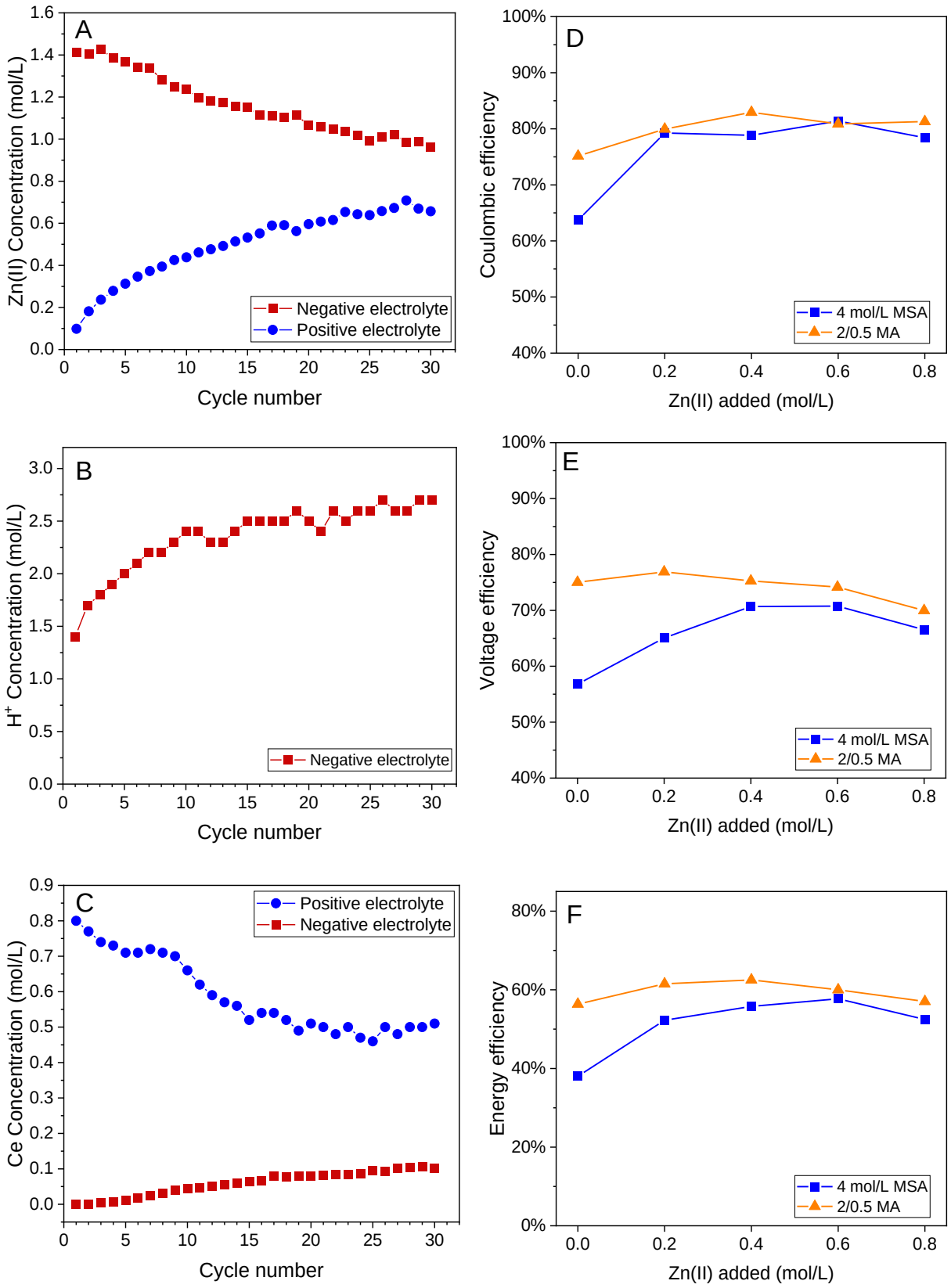

A
Zn(II) Concentration (mol/L)
Cycle number
Negative electrolyte
Positive electrolyte
B
H+ Concentration (mol/L)
Cycle number
Negative electrolyte
C
Ce Concentration (mol/L)
Cycle number
Positive electrolyte
Negative electrolyte
D
Coulombic efficiency
Zn(II) added (mol/L)
4 mol/L MSA
2/0.5 MA
E
Voltage efficiency
Zn(II) added (mol/L)
4 mol/L MSA
2/0.5 MA
F
Energy efficiency
Zn(II) added (mol/L)
4 mol/L MSA
2/0.5 MA

Figure 5.1. Variation of (A) Zn(II) concentration in the positive and negative electrolytes, (B) H^+ concentration in the negative electrolyte and (C) total soluble Ce(III)+Ce(IV) concentration in the positive and negative electrolytes obtained over 30 cycles at 25 mA/cm² using 4 mol/L MSA positive supporting electrolyte. Effect of Zn(II) concentration added to the positive electrolyte containing mixed acid (triangle) or MSA-only (square) on the resulting (D) average coulombic efficiency, (E) voltage efficiency and (F) energy efficiency of the battery over 30 cycles at 25 mA/cm².

As shown in Figure 5.1C, the total soluble Ce concentration in the positive compartment steadily drops over the first ~15 cycles while its level on the negative side rises due to the concentration difference driving Ce from the positive side to the negative side. When the positive electrolyte is based on MSA alone, Ce(IV) begins precipitating as CeO_2 by ~6^{th} cycle as the MSA concentration drops and the total Ce concentration in the positive electrolyte stabilizes at ~0.5 mol/L by the 15^{th} cycle. This drop is very substantial since only 62.5% of the initial Ce concentration remains on the positive side. This reflects another negative impact of the transfer of H^+ from the positive side to the negative side. Considering that ~0.1 mol/L of cerium has crossed the membrane into the negative electrolyte by the end of 30 cycles, the amount of Ce(IV) that has precipitated out corresponds to approximately 0.2 mol/L or 25% of the total amount of Ce in the system.

5.3.2 Effect of addition of Zn(II) to MSA and MSA-H_2SO_4 mixed acid positive supporting electrolytes on battery performance

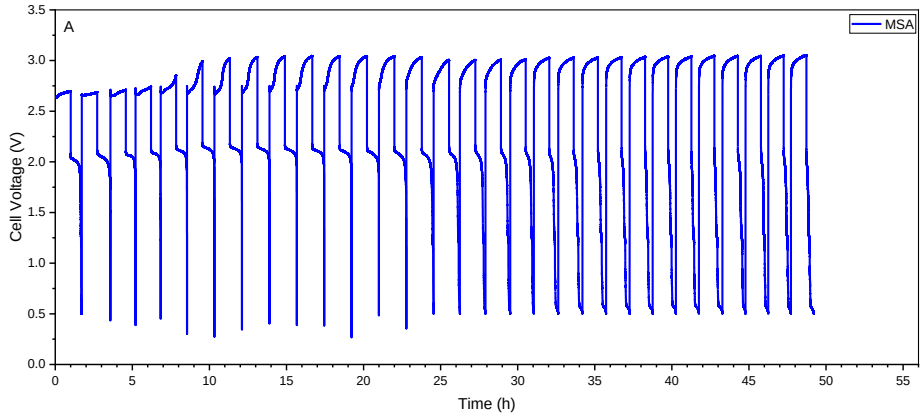
We showed previously that the replacement of 4 mol/L MSA with 2/0.5 MA as the positive supporting electrolyte has beneficial effects in reducing the extent of H^+ crossover by lowering the H^+ concentration gradient across the membrane and possibly providing higher cerium solubility.[32] Based on the findings above of substantial Zn(II) crossover, it is worthwhile to add different amounts of Zn(II) ions in the form of zinc(II) methanesulfonate to both the 2/0.5 MA and 4 mol/L MSA supporting positive electrolytes to reduce the Zn(II) concentration difference between the two sides and the loss of Zn(II) from the negative electrolyte. To this end, Zn(II) is added at concentrations of 0.2, 0.4, 0.6 and 0.8 mol/L to the positive electrolytes on battery performance. As shown in Figure 5.1D, when Zn(II) is not initially added to the positive side, the average

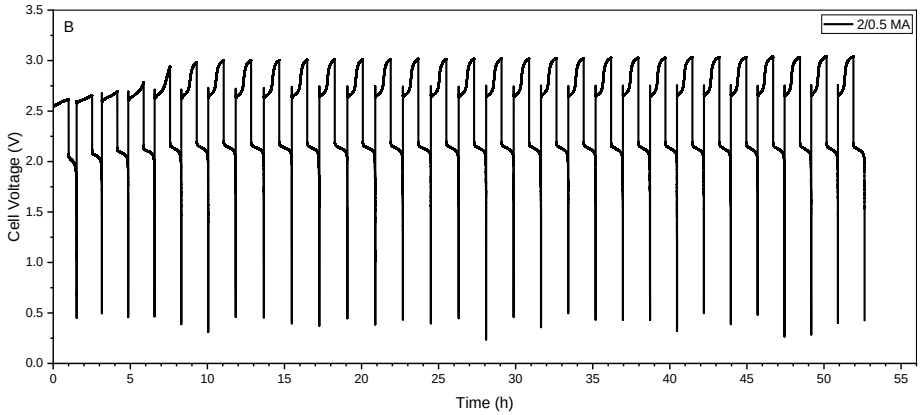
coulombic efficiency over 30 cycles of battery charge-discharge achieved using 2/0.5 MA supporting electrolyte is 75.2% compared to 63.7% attained with 4 mol/L MSA.

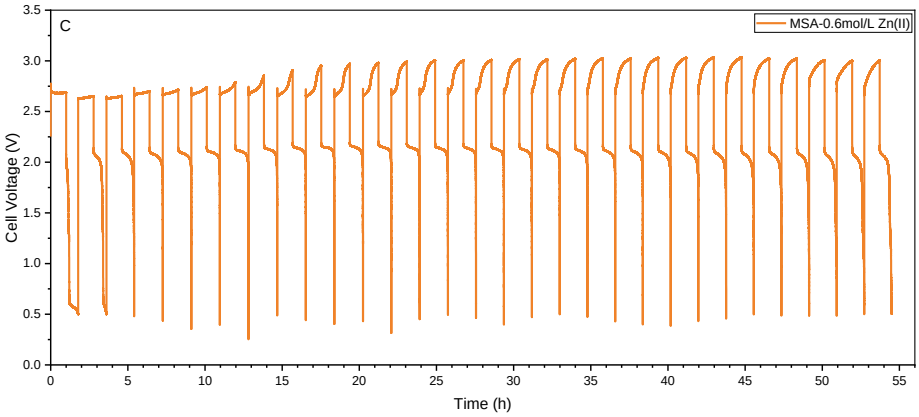
The variation in cell voltage over 30 cycles obtained with positive electrolytes containing 0 and 0.6 mol/L Zn(II) in 4 mol/L MSA and 0 and 0.4 mol/L Zn(II) in 2/0.5 MA is presented in Figure 5.2. The battery efficiencies are obtained by analyzing the recorded cell voltage profiles over 30 cycles. Examination of the cell voltage profiles in Figure 5.2 reveals two overall trends. Firstly, the response of the cell (particularly during discharge) over the course of the 30 cycles is much more stable and more efficient when the positive electrolyte contains 2/0.5 MA both in the absence and presence of Zn(II) than when the electrolyte is based on 4 mol/L MSA (compare Figure 5.2B and 2D with 2A and 2C. In fact, in the 2/0.5 MA electrolyte, the system is able to maintain a virtually repeatable response from cycle to cycle after ~ 5 cycles when no Zn(II) is present and after ~ 10 cycles when 0.4 mol/L Zn(II) is added until the end of each experiment. Secondly, the addition of Zn(II) to 4 mol/L MSA leads to a significant improvement (Figure 5.2C). In the absence of Zn(II), the cell is no longer able to hold its voltage during discharge after ~15 cycles when the positive electrolyte contains 4 mol/L MSA and no Zn(II), leading to a steep drop in discharge voltage throughout the entire half-cycle (Figure 5.2A) and a significant loss in efficiency. However, the battery performance particularly during discharge is stabilized when 0.6 mol/L Zn(II) is added, although it begins to degrade near the end of the 30-cycle experiment. In each of the four cases shown, the cell voltage during battery charge rises to ~3.0 V after a number of cycles due to the higher overpotential caused by the accumulation of Ce(IV) ions and the depletion of Ce(III) in the positive electrolyte. Interestingly, considerably more charge-discharge cycles are required for this rise in cell voltage during charge to occur when Zn(II) is added to both the 4 mol/L MSA and the 2/0.5 MA electrolytes. One difference in the responses during charge is that the cell voltages in the case of the 2/0.5 MA-based electrolytes remain close to 2.6 V during the first half of the cycle before rising to ~3.0 V only near the end of charge, whereas they tend to rise more quickly and remain close to 3.0 V during more of the cycle when operating the cell with the 4 mol/L MSA-based positive electrolytes, revealing another advantage of the use of the 2/0.5 MA electrolyte.

The variation of the H^+ concentration in the negative electrolyte over 30 cycles obtained with positive electrolytes containing 0.6 mol/L Zn(II) in 4 mol/L MSA and 0 and 0.4 mol/L Zn(II) in 2/0.5 MA (data obtained in the absence of Zn(II) was originally reported in our previous study [32])

is shown in Figure 5.3A. The higher coulombic efficiency achieved by switching from the 4 mol/L MSA to 2/0.5 MA supporting electrolyte can be attributed to the reduction in H^+ concentration difference between the two sides of the membrane, leading to less crossover of H^+ to the negative electrolyte and lower extent of the irreversible hydrogen evolution side reaction during charge.


A
MSA
Cell Voltage (V)
Time (h)


B
2/0.5 MA
Cell Voltage (V)
Time (h)


C
MSA-0.6mol/L Zn(II)
Cell Voltage (V)
Time (h)

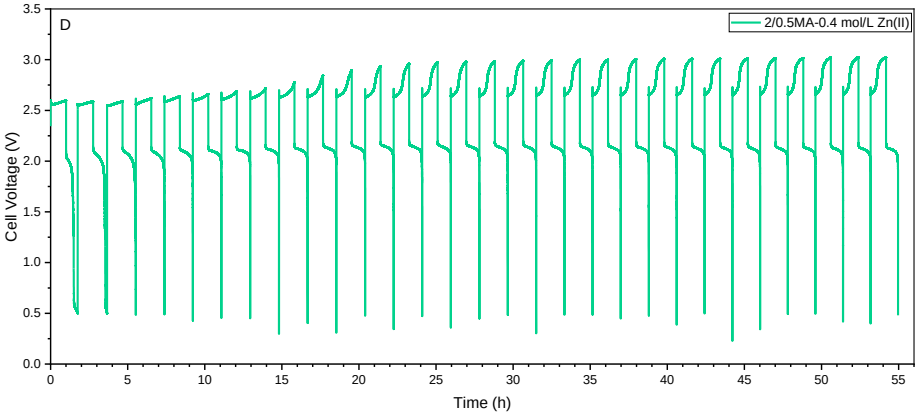
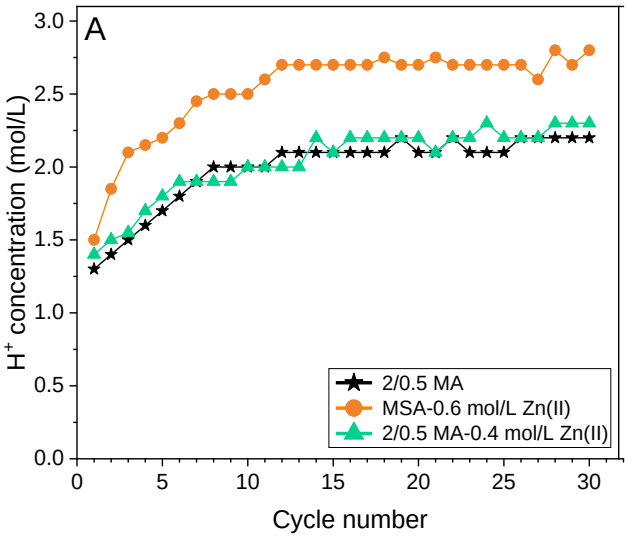
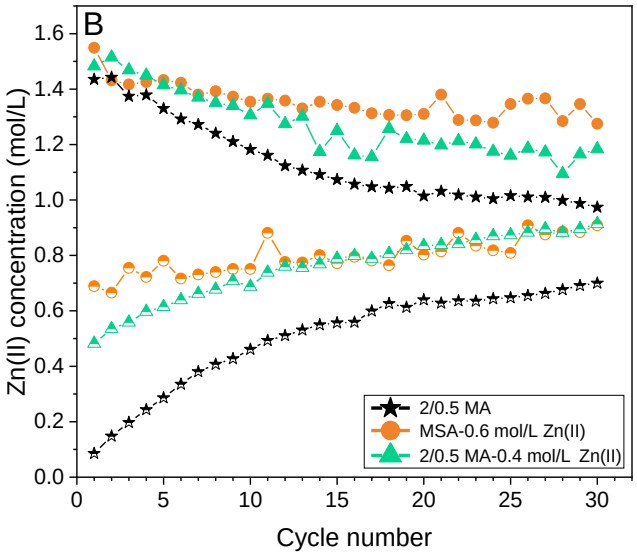

D
2/0.5MA-0.4 mol/L Zn(II)
Cell Voltage (V)
Time (h)

Figure 5.2. Cell voltage of the Zn-Ce redox flow battery over 30 cycles at 25 mA/cm^2 obtained when the fresh positive electrolyte contains 0.8 mol/L Ce(III) in 4 mol/L MSA(blue), 2/0.5 MA(black), 0.6 mol/L Zn(II) added to 4 mol/L MSA (orange) and 0.4 mol/L Zn(II) added to 2/0.5 MA (green). The fresh negative electrolyte contains 1.5 mol/L Zn(II) in 1 mol/L MSA.


A
H+ concentration (mol/L)
Cycle number
2/0.5 MA
MSA-0.6 mol/L Zn(II)
2/0.5 MA-0.4 mol/L Zn(II)


B
Zn(II) concentration (mol/L)
Cycle number
2/0.5 MA
MSA-0.6 mol/L Zn(II)
2/0.5 MA-0.4 mol/L Zn(II)

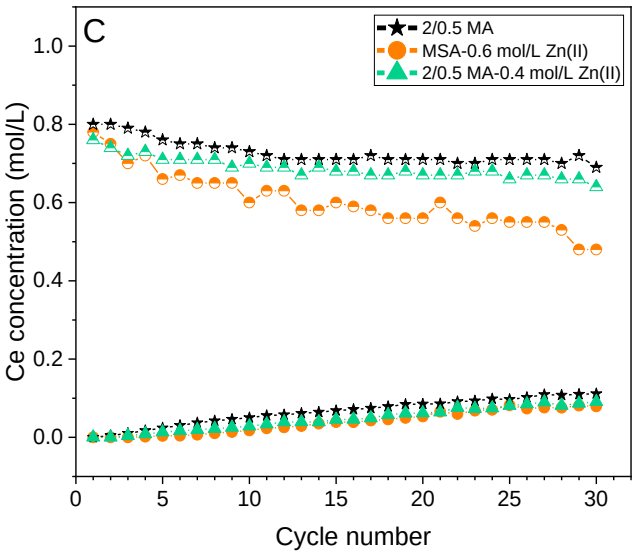

C
Ce concentration (mol/L)
Cycle number
2/0.5 MA
MSA-0.6 mol/L Zn(II)
2/0.5 MA-0.4 mol/L Zn(II)

Figure 5.3. Variation of (A) H^+ concentration in the negative electrolyte, (B) Zn(II) concentration in the positive (half-filled symbols) and negative electrolytes (fully-filled symbols) and (C) total soluble Ce(III) + Ce(IV) concentration in the positive (half-filled symbols) and negative (fully-filled symbols) electrolyte over 30 cycles at 25 mA/cm^2 obtained using the various positive electrolytes. The fresh positive electrolyte contains 0.8 mol/L Ce(III) in 4 mol/L MSA(blue), 2/0.5 MA(black), 0.6 mol/L Zn(II) added to 4 mol/L MSA (orange) and 0.4 mol/L Zn(II) added to 2/0.5 MA (green). The fresh negative electrolyte contains 1.5 mol/L Zn(II) in 1 mol/L MSA.

In all cases, the H^+ concentration increases more sharply over the first ~10 cycles and then stabilizes over the following 20 cycles. The final H^+ concentration in the negative electrolytes rises to ~2.8 mol/L when the 4 mol/L MSA electrolyte is used, whereas it reaches ~2.3 mol/L in the case of the mixed acid electrolyte. Similar to the case of cerium (Figure 5.3C), these results suggest that the transfer of H^+ across the membrane is mainly affected by its own concentration difference across the membrane and not by that of the other ions. Regardless of the positive supporting acid electrolyte used, the final H^+ concentration in the negative electrolyte at the end of 30 cycles remains essentially the same regardless of the amount of Zn(II) added to the positive electrolyte.

Another possible reason for better battery performance in the mixed acid supporting electrolyte is that CeO_2 is never observed to precipitate even at the end of 30 cycles. It is not clear whether the use of the mixed electrolyte has a direct effect by increasing the solubility of Ce(IV) or an indirect effect by enabling a higher acid concentration to be maintained in the positive electrolyte or both. Further investigation into this question is warranted. Regardless of the cause, this effect is clearly an advantage for the positive electrode reaction during battery charge and discharge. In the case of 4 mol/L MSA, Ce(IV) is observed to precipitate out as CeO_2 after ~6 cycles (~10 hours of battery operation) and cause the Ce(III)/Ce(IV) couple to be the limiting half-cell reaction and reduce the coulombic efficiency and capacity of the battery.

The addition of Zn(II) to the positive electrolytes causes the coulombic efficiency to increase for both 2/0.5 MA and 4 mol/L MSA supporting electrolytes (Figure 5.1D), particularly in the case of the latter. When 2/0.5 MA is used as the positive supporting electrolyte, the maximum coulombic efficiency achieved increases to 82.9% by adding 0.4 mol/L Zn(II), while the maximum coulombic efficiency for the 4 mol/L MSA supporting electrolyte rises to 81.4% when 0.6 mol/L Zn(II) is

present. Interestingly, the coulombic efficiency of the battery exhibits a dramatic increase from 63.7% to 80.0% when only 0.2 mol/L of Zn(II) is added to the original 4 mol/L MSA positive supporting electrolytes. As more Zn(II) is added to both positive supporting electrolytes, no further increase in the coulombic efficiency above ~80-82% is observed.

Figure 5.3B shows the Zn(II) concentration in both the positive and negative electrolytes over the course of 30 cycles at 25 mA/cm^2 for several supporting electrolyte compositions. For the battery operating with the mixed acid positive electrolyte and no Zn(II) added, the changes in Zn(II) concentration in both negative and positive electrolytes are similar to those observed when the 4 mol/L MSA positive electrolyte is used. The Zn(II) level in the negative electrolyte slowly drops from 1.5 mol/L to 0.97 mol/L and increases from 0 mol/L to 0.69 mol/L in the positive electrolyte over the course of 30 charge-discharge cycles. It should be noted that the sum of Zn(II) concentration in the negative and positive electrolyte is higher than the original Zn(II) concentration (1.5 mol/L) in the system. This is believed to be caused by the water transport from the negative to the positive electrolyte due to osmosis and the evaporation of water over the 30 cycles, as well as the error associated with the ICP-ODE measurements. When 0.4 mol/L Zn(II) is added to the mixed acid positive electrolyte (green curve), the Zn(II) concentration remains higher in the negative electrolyte compared to that measured when no Zn(II) is added (black curve). As expected, the purposeful addition of Zn(II) to the positive side reduces the concentration difference in the negative and positive electrolytes and the amount of Zn(II) that crosses the membrane from the negative side to the positive side. It is also evident from Figure 3B that the increase of the Zn(II) concentration on the positive side slows down as the charge/discharge cycling continues. This is due to the reduction of the concentration gradient of Zn(II) between the negative and positive electrolytes over time. This leaves more Zn(II) in the negative electrolyte that can be reduced to zinc metal during charge relative to the amount of H^+ available for H_2 evolution and to a higher coulombic efficiency. A similar effect is observed when 4 mol/L MSA is used as the supporting positive electrolyte.

Based on these results, it appears that it is not necessary to prevent all transport of Zn(II) from the negative to the positive electrolyte to have the maximum effect on the coulombic efficiency. The changes in Zn(II) concentration in the negative and positive electrolytes when only 0.2 mol/L Zn(II) is added to both positive electrolytes are not included here, but they show that the amount of Zn(II)

crossover has been decreased sufficiently. This decline in Zn(II) crossover appears to be enough to maintain the Zn(II) concentration on the negative side above a critical level to keep H_2 evolution much less competitive than Zn(II) reduction during charge.

As noted previously with regard to Figure 5.1, when the positive side contains 4 mol/L MSA or 2/0.5 MA with no Zn(II) added initially, as much as ~0.53 mol/L Zn(II) crosses the membrane and leaves the negative side by the end of 30 charge-discharge cycles, which represents ~35.3% of the total amount initially present. Obviously, this effect has a profound effect on the performance of the RFB and leads to a deterioration in battery performance and capacity fade over the course of operation. When 0.4 mol/L and 0.6 mol/L Zn(II) are added to 2/0.5 MA and 4 mol/L MSA positive electrolytes, respectively, notably more Zn(II) remains in the negative electrolyte at the end of 30 cycles. The amount of Zn(II) transferred from the negative electrolyte is found to be 0.32 mol/L and 0.22 mol/L respectively, which corresponds to 21.3% and 14.6% of the original amount of Zn(II) in the negative electrolytes. Not surprisingly, our results indicate that the amount of Zn(II) transferred after 30 cycles from the negative to positive electrolyte is governed primarily by the concentration difference across the membrane. The smaller the concentration difference, the less Zn(II) crossover occurs. Since a Zn(II) concentration difference between the negative and positive electrolytes always exists in these experiments, crossover of Zn(II) ions is only reduced but not eliminated. Obviously, one approach for preventing Zn(II) crossover is to add 1.5 mol/L Zn(II) to the positive side in order to match the concentration on the other side and completely eliminate any concentration difference. We have explored this idea, but unfortunately it does not work since the addition of Zn(II) methanesulfonate above ~0.6 mol/L yields very viscous solutions that are deleterious to mass transport and electric conductivity, resulting in poor battery performance. The electrical conductivity of the various electrolytes in this study is presented below in Figure 5.4A. The addition of Zn(II) to both positive electrolytes leads to large reductions in their conductivities. The decrease of electrolyte conductivity of concentrated solutions as the electrolyte concentration is further raised is a commonly observed phenomenon due to the formation of uncharged ion pairs arising from the association of oppositely charged ions.[186–188] We also observe that both the MSA-only and mixed acid solutions become noticeably more viscous as more Zn(II) is added (Figure 5.4B). The rise in solution viscosity and decrease in electrical conductivity as more Zn(II) is present are presumably the major factors preventing the further improvement in coulombic efficiency beyond what we were able to show here (Figure 5.1D).

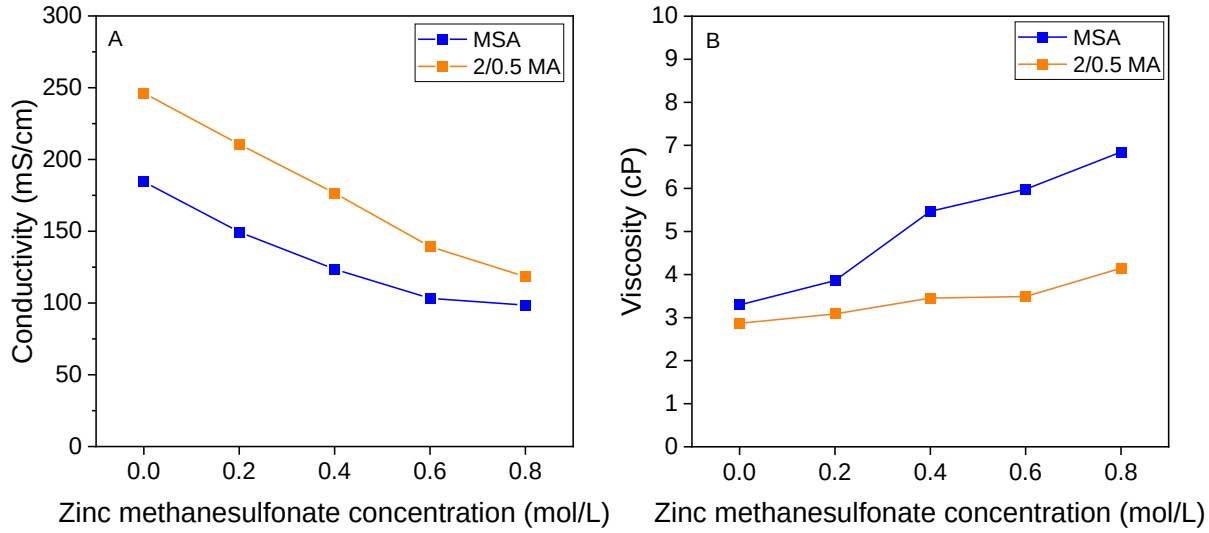


Figure 5.4. Effect of zinc(II) methanesulfonate concentration on the electrical conductivities (A) and viscosities (B) of the MSA (blue) and 2/0.5MA (orange) electrolytes in this study.

The addition of Zn to the positive side not only has a beneficial effect on the coulombic efficiency, but also on voltage efficiency. As shown in Figure 5.1E, the battery achieves a higher average voltage efficiency over the 30 cycles when the positive electrolyte contains 2/0.5 MA than when 4 mol/L MSA is used, particularly in the case when no Zn(II) is initially added to the positive side. A voltage efficiency of 56.8% is achieved with the 4 mol/L MSA positive supporting electrolyte, whereas it is 75% when 2/0.5 MA is used. As shown in Figure 5.2, our measurements of the cell voltage during operation show that the overpotential of the battery is smaller when the mixed acid supporting electrolyte is used, leading to a lower average charge voltage and higher discharge voltage than when 4 mol/L MSA is used. When 0.2 mol/L Zn(II) is added to the 2/0.5 MA electrolyte, the voltage efficiency increases slightly to 76.9% from 75%. The voltage efficiency then gradually decreases to 70% as the Zn(II) concentration is raised to 0.8 mol/L. For the 4 mol/L MSA positive electrolyte, a large increase in voltage efficiency from 56.8% to 70.7% is observed when 0.4 mol/L Zn(II) is added. The addition of 0.6 mol/L Zn(II) to the electrolyte only increases the voltage efficiency by a negligible amount. Similar to that observed in the case of mixed acid, the continued increase of Zn(II) concentration to 0.8 mol/L leads to a decrease in the voltage efficiency to 66.5%.

During the first few cycles, faster Ce(III)/Ce(IV) reaction kinetics in the mixed acid supporting electrolyte is the main reason for the lower overpotential during battery charge, as shown in the cyclic voltammetry curves in Chapter 4 and later in this study. We observed that the anodic current for the oxidation of Ce(III) to Ce(IV) in 2/0.5 MA in the absence of Zn(II) starts to rise at a lower potential during the anodic scan and the cathodic charge associated with the reduction of Ce(IV) back to Ce(III) is higher. Additionally, the effect of the total soluble Ce concentration in the positive electrolyte on the overpotential for the Ce(III)/Ce(IV) redox couple is another important factor that affects the voltage efficiency of the battery. The total soluble cerium (Ce(III) + Ce(IV)) concentration in the various positive electrolytes after each charge-discharge cycle is presented in Figure 5.3C. After ~6 cycles, CeO_2 precipitation occurs in the 4 mol/L MSA electrolyte due to the build-up of Ce(IV) ions and drop in acidity. This leads to a further decrease in the total soluble Ce(III) + Ce(IV) concentration. The crossover of Ce from the positive to the negative electrolyte also contributes to this gradual decrease. Approximately 37.5% of the original Ce(III) is lost due to both crossover and precipitation in the 4 mol/L MSA supporting electrolyte. This irreversible loss of Ce from the positive side leads to a larger overpotential for the Ce(III)/Ce(IV) redox couple at the positive electrode during both charge and discharge. After 30 cycles, the Ce concentration in the positive electrolyte is ~0.5 mol/L. The initial addition of 0.6 mol/L Zn(II) to the 4 mol/L MSA electrolyte does not help in this regard as the final Ce concentration is 0.48 mol/L (see orange curve). On the other hand, no CeO_2 precipitation occurs even after 30 cycles when 2/0.5 MA is used as the supporting electrolyte. As a result, the total cerium level in the positive electrolyte remains higher and drops only to 0.69 mol/L after 30 charge-discharge cycles in the 2/0.5MA case. Considering that ~0.1 mol/L of Ce is transported from the positive to the negative electrolyte due to its concentration gradient, this indicates that no Ce(IV) is lost from the positive electrolyte due to CeO_2 precipitation. When 0.4 mol/L Zn(II) is present in the mixed acid electrolyte, the final Ce concentration is 0.64 mol/L, which again is much higher than the final concentration in the 4 mol/L MSA electrolytes. The slight decrease in cerium concentration during the course of the cycles in the case of the mixed acid electrolytes observed in Figure 5.3C arises due to the crossover of cerium ions driven by the concentration differences in the positive and negative electrolytes. Approximately 0.1 mol/L of Ce is found to transfer from the positive to the negative electrolytes in all cases when the above mentioned 4 electrolytes are used in the battery. This indicates that the crossover of Ce ions to the negative side is largely determined by its own concentration gradient

and not affected by that of the supporting acid or Zn(II). On the whole, the total soluble Ce concentration remains higher throughout the experiment when mixed acid electrolytes are used, which enables the battery to operate with a smaller overpotential and achieve a better voltage efficiency than in the case of 4 mol/L MSA.

Another relevant observation comes from examination of the electrical conductivities of the various positive electrolytes (Figure 5.4A). It should be noted that all of these electrolytes also contain 0.8 mol/L Ce(III) methanesulfonate so that they are identical in composition to the positive electrolytes used during operation of the RFBs. The electrolytes based on 2/0.5 MA exhibit higher conductivities than the corresponding solutions containing 4 mol/L MSA. Given that the electrolyte resistance contributes to the overall ohmic drop in the RFB, this effect should also contribute to the higher voltage efficiency obtained in the case of the mixed acid positive electrolytes. As discussed previously, we also observed that both the MSA-only and mixed acid solutions become noticeably more viscous as more Zn(II) is added. This effect may contribute to the small drop in the voltage efficiency in both positive supporting electrolytes with increasing Zn(II) concentration once the Zn(II) level reaches ~0.4 mol/L (Figure 5.1E). Taken together, these results show that the addition of Zn(II) to the positive electrolyte has both beneficial and detrimental effects – less crossover of Zn(II) to the positive side and lower overpotential for the Ce(III)/Ce(IV) couple, but at the same time a more viscous and less conducting medium. The confluence of these opposing effects leads to the results shown in Figure 5.1E whereby the voltage (and coulombic) efficiencies reach their maximum levels at intermediate Zn(II) concentrations.

For the 4 mol/L MSA positive supporting electrolyte, the maximum coulombic and voltage efficiencies are achieved when 0.6 mol/L Zn(II) is added. In the case of the 2/0.5 MA positive supporting electrolyte, the highest coulombic efficiency is attained when 0.4 mol/L Zn(II) is added, whereas the highest voltage efficiency is achieved at 0.2 mol/L Zn(II). Overall, the highest energy efficiency is obtained when 0.4 mol/L Zn(II) is present in the mixed acid electrolyte. As shown in Figure 5.1F, the battery operating with 2/0.5 MA positive supporting electrolyte exhibits higher energy efficiency than that achieved with the 4 mol/L MSA particularly when 0 or 0.2 mol/L Zn(II) is present. The addition of Zn(II) ions is beneficial primarily for the 4 mol/L MSA electrolytes, while it has only a small effect on the mixed acid electrolytes. The maximum energy efficiency rises from 56.4% to 62.5% when 0.4 mol/L Zn(II) is added to the mixed acid supporting electrolyte,

while it increases from 38% to 57.7% when 0.6 mol/L Zn(II) is added to the mol/L MSA supporting electrolyte.

The energy efficiency of the battery when operated with 4 mol/L MSA positive supporting electrolytes is much lower and begins to drop drastically after the 13th cycle, whereas the energy efficiencies obtained when the other electrolytes are used on the positive side remain much higher and decline much more slowly over the course of the 30 cycles as shown in Figure 5.5. As a comparison, these efficiencies are higher than the levels of 46.8 and 42.9% reported by Leung et al based on experiments on a Zn-Ce flow battery at 20 and 50 mA/cm^2, respectively, in a positive electrolyte containing 0.8 mol/L Ce(III) in 4 mol/L MSA supporting electrolyte without any Zn(II) added and a negative electrolyte containing 1.5 mol/L Zn(II) in 1 mol/L MSA.[37]

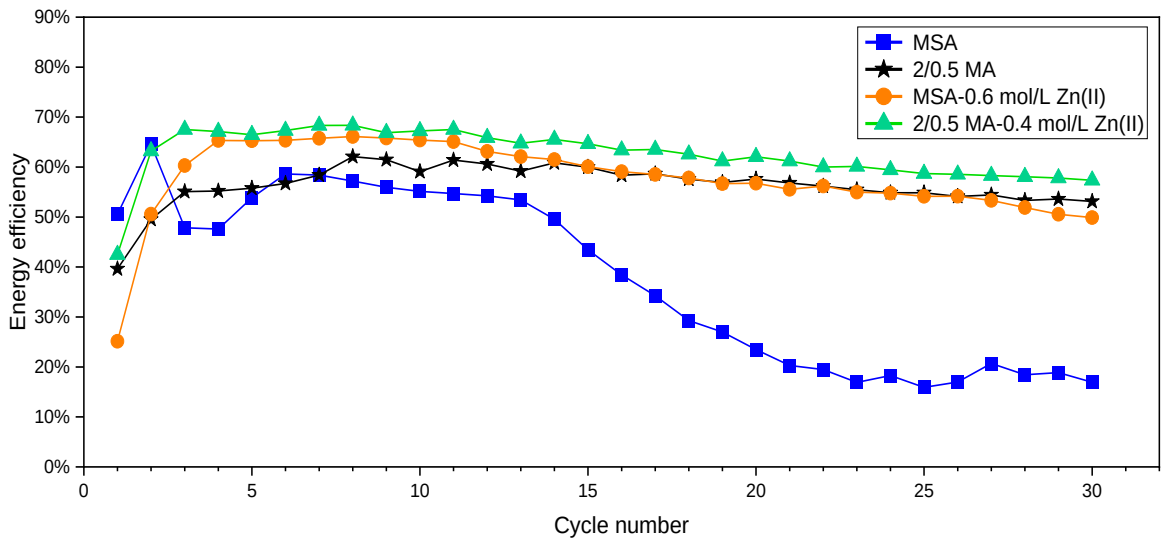
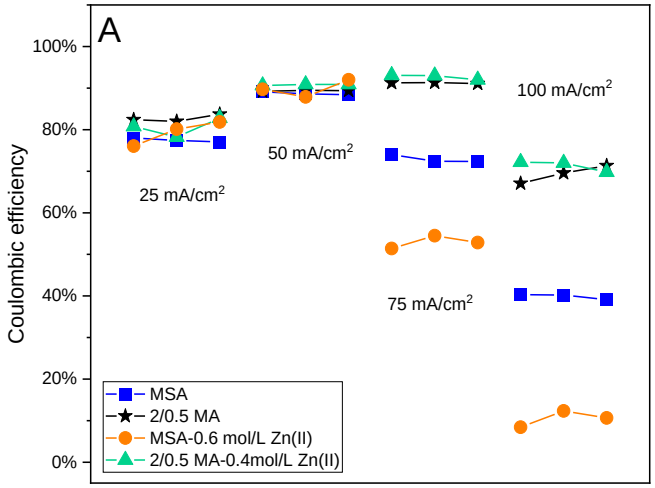
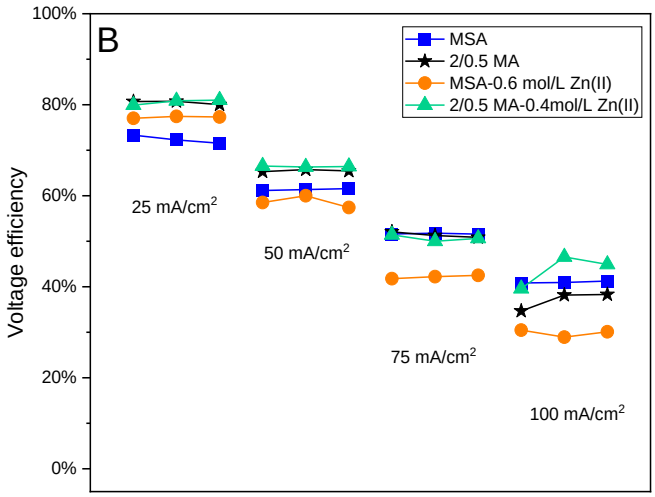


Figure 5.5. Energy efficiency of each charge-discharge cycle when the battery is operated for 30 cycles at 25 mA/cm^2. The fresh positive electrolyte contains 0.8 mol/L Ce(III) in 4 mol/L MSA(blue), 2/0.5 MA(black), 0.6 mol/L Zn(II) added to 4 mol/L MSA (orange) and 0.4 mol/L Zn(II) added to 2/0.5 MA (green). The fresh negative electrolyte contains 1.5 mol/L Zn(II) in 1 mol/L MSA

5.3.3 Effect of current density on battery efficiency

The coulombic, voltage and energy efficiencies of the battery obtained with the original positive supporting electrolytes as well as the best-performing solutions with Zn(II) present have been evaluated over 3 successive charge-discharge cycles at different current densities between 25 and 100 mA/cm^2, as shown in Figure 5.6. As evident in Figure 5.6A, the coulombic efficiency achieved with all 4 electrolytes is higher when the applied current density is increased from 25 to 50 mA/cm^2, presumably because higher current density favors Zn(II) reduction over hydrogen evolution during battery charge. Another possible reason is that the charge/discharge time required to achieve the same stage of charge is reduced at higher current densities. This should lead to less self-discharge of Zn at the negative electrode due to H^+ ions and fewer Ce(IV) ions that transfer from the positive to the negative electrolyte. As the current density increases to 75 mA/cm^2, the coulombic efficiency of the battery operating with the 2/0.5 MA supporting electrolytes continues to increase for the same reason, whereas it decreases drastically in the case of 4 mol/L MSA supporting electrolytes. This finding indicates that the mixed acid supporting electrolytes exhibit better performance when operating at higher current densities compared to the standard 4 mol/L MSA. At a current density of 100 mA/cm^2, a decrease in battery coulombic efficiency is observed in all cases. At such a high current density, the hydrogen/oxygen evolution reactions are likely enhanced more than Zn(II) reduction and Ce(III) oxidation during charge, leading to lower coulombic efficiency. It is worth mentioning that the coulombic efficiency drop is much smaller for the mixed acid electrolytes (green and black) than for the 4 mol/L MSA supporting electrolytes (orange). A steady decrease in voltage efficiency is observed with an increase of current density, as shown in Figure 5.6B. This can be attributed to a rise in the increased charge-discharge overpotential due to activation, concentration polarization and ohmic losses.


A
Coulombic efficiency
100%
80%
60%
40%
20%
0%
25 mA/cm2
50 mA/cm2
75 mA/cm2
100 mA/cm2
MSA
2/0.5 MA
MSA-0.6 mol/L Zn(II)
2/0.5 MA-0.4mol/L Zn(II)


B
Voltage efficiency
100%
80%
60%
40%
20%
0%
25 mA/cm2
50 mA/cm2
75 mA/cm2
100 mA/cm2
MSA
2/0.5 MA
MSA-0.6 mol/L Zn(II)
2/0.5 MA-0.4mol/L Zn(II)

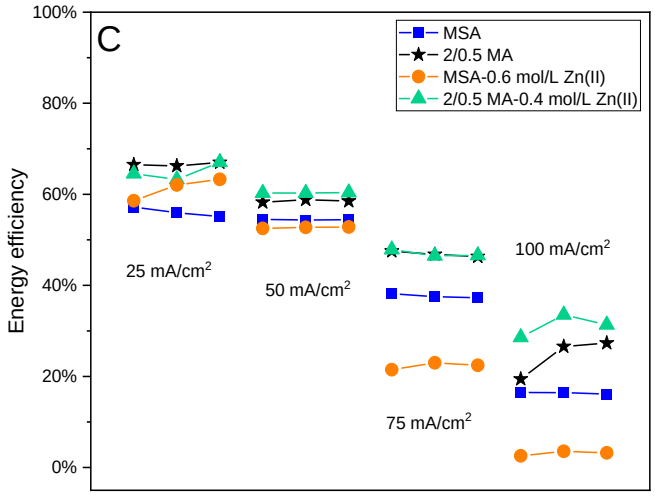

C
Energy efficiency
100%
80%
60%
40%
20%
0%
25 mA/cm2
50 mA/cm2
75 mA/cm2
100 mA/cm2
MSA
2/0.5 MA
MSA-0.6 mol/L Zn(II)
2/0.5 MA-0.4 mol/L Zn(II)

Figure 5.6. Effect of applied current density on the (A) coulombic, (B) voltage and (C) energy efficiencies of the Zn-Ce redox flow battery operating over 3 successive cycles. The fresh positive electrolyte contains 0.8 mol/L Ce(III) in 4 mol/L MSA(blue), 2/0.5 MA(black), 0.6 mol/L Zn(II) added to 4 mol/L MSA (orange) and 0.4 mol/L Zn(II) added to 2/0.5 MA (green). The fresh negative electrolyte contains 1.5 mol/L Zn(II) in 1 mol/L MSA

The positive electrolyte that contains 0.8 mol/L Ce(III) and 0.4 mol/L Zn(II) in 2/0.5 MA exhibits the highest energy efficiency at each of the applied current densities as shown in Figure 5.6C, indicating that this composition is the best among those that have been investigated. In general, the efficiency of the battery operating with mixed acid as positive electrolyte is higher compared to that obtained in 4 mol/L MSA in situations both when Zn(II) is initially present in the positive electrolyte and when it is not. This result again confirms that mixed acid supporting electrolyte is superior to the original 4 mol/L MSA supporting electrolyte. It is also observed that the energy efficiency decreases with the increase of current density in all cases. As just noted, this is likely caused by the enhancement of hydrogen and/or oxygen evolution at higher current densities that decreases the coulombic efficiency and the higher overpotential that decreases the voltage efficiency.

5.3.4 Effect of Zn(II) on Ce(III)/Ce(IV) redox couple and O_2 evolution

To study the effect of Zn(II) in the positive electrolyte on the reaction kinetics of the Ce(III)/Ce(IV) redox couple, cyclic voltammetry experiments have been conducted on a platinum electrode immersed in both the 4 mol/L MSA (Figure 5.7A) and mixed acid positive supporting electrolytes (Figure 5.7B) that initially contain 0.8 mol/L Ce(III). Each cyclic voltammetry scan starts at 0.5 V vs. Ag/AgCl reference electrode and proceeds in the positive direction to 2.1 V at a scan rate of 50 mV/s before returning to the initial potential.

The addition of Zn(II) to the 4 mol/L MSA supporting electrolyte leads to a slight reduction in the separation between the reduction and oxidation peaks for the Ce(III)/Ce(IV) redox couple. Although this effect could be interpreted as a sign of better reaction reversibility, it is complicated

by the fact that the position and height of the peak for Ce(III) oxidation during the anodic scan are strongly affected by the fact that oxygen evolution contributes to the overall current signal particularly at higher electrode potentials. The effect on Ce(III)/Ce(IV) reaction kinetics can be more clearly assessed by focusing on the total charge for the reduction of Ce(IV) during the cathodic scan since the only source of Ce(IV) in the system comes from the Ce(III) oxidation during the previous anodic scan. Since the scan rates are the same for all the CVs obtained in this study, the elapsed time during the anodic and cathodic scans remains unchanged from one experiment to experiment. Over this time, some of the Ce(IV) produced during the anodic scan diffuses away from the working electrode and is no longer available for reduction during the cathodic scan. In our analysis, we assume that the amount of Ce(IV) diffusing away from the working electrode during this time remains the same from experiment to experiment. With this assumption, comparison of the total charge for Ce(IV) reduction during the cathodic scans in the various CVs should provide a good measure of the relative amounts of Ce(III) oxidized during the anodic scans. For our purposes here, we determine the cathodic charge by integrating under the cathodic curves over the range from 0.6 V vs. Ag/AgCl up to the potential where the current crosses from positive to negative during the scan in each electrolyte. The integrated cathodic charges and other pertinent measures obtained from these CVs are listed in Table 5.1. The analysis shows that the maximum charge during the cathodic scan occurs when 0.6 mol/L Zn(II) are added, reflecting that more Ce(III) has been converted to Ce(IV) during the anodic portion of the scan. In addition, the addition of Zn(II) ions causes the anodic current to rise more steeply beginning at ~1.25 V vs. Ag/AgCl during the forward scan, which reflects faster kinetics for Ce(III) oxidation and wider separation from the oxygen evolution side reaction. Taken together, these results are consistent with a faster reaction rate and higher reversibility of the Ce(III)/Ce(IV) redox couple when 0.6 mol/L Zn(II) is present in 4 mol/L MSA, which is consistent with our previous findings of enhanced battery performance at this positive electrolyte composition. Although the peak separation becomes even smaller when 0.8 mol/L Zn(II) are added to the 4 mol/L MSA electrolyte, both the anodic and cathodic peak current become noticeably smaller probably due to the rise in the viscosity of the electrolyte which slows the entire process.

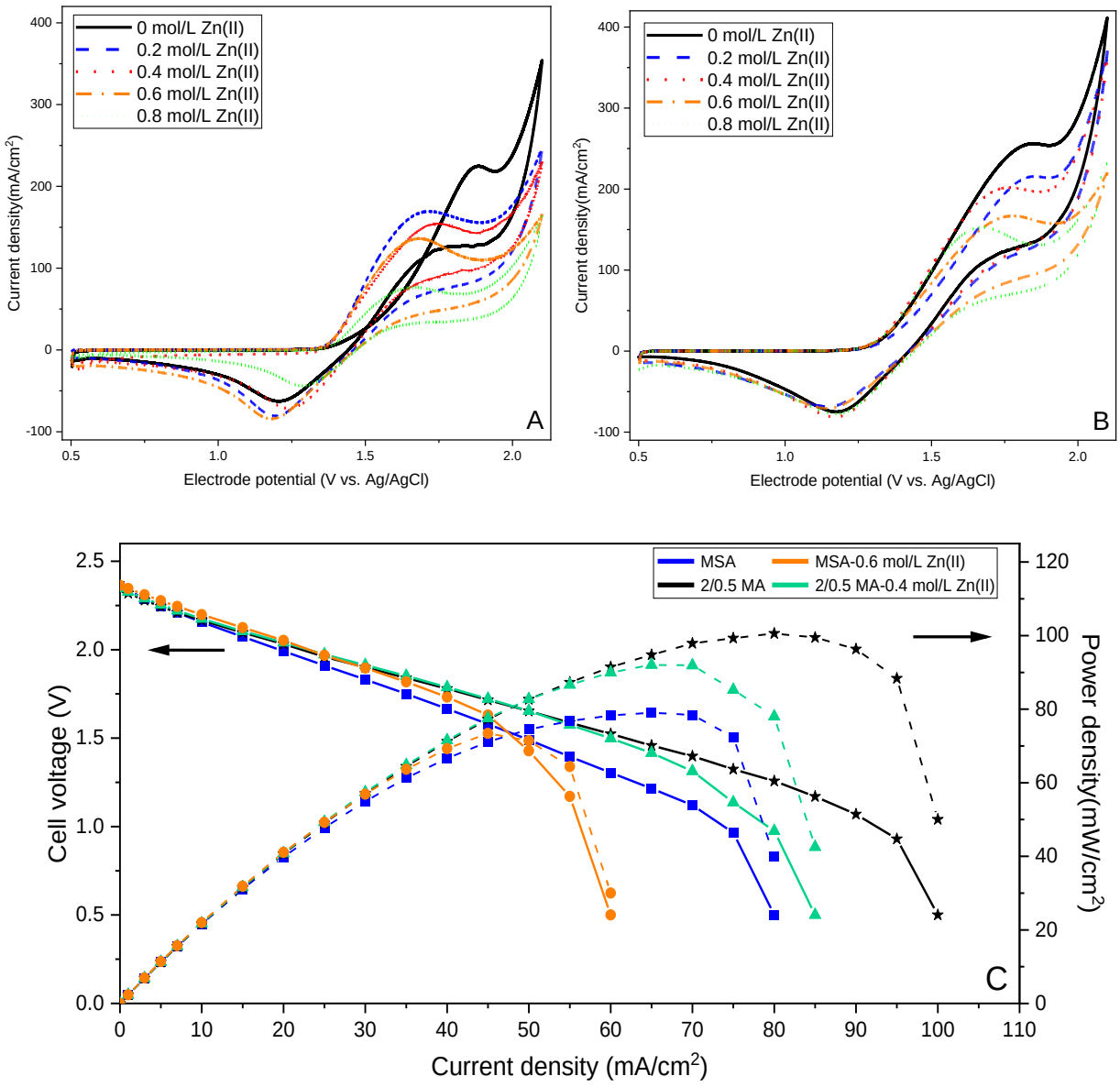


Figure 5.7. Effect of zinc(II) methanesulfonate concentration on the cyclic voltammograms for the Ce(III)/Ce(IV) redox couple in (A) 4 mol/L MSA and (B) 2/0.5 MA positive supporting electrolytes initially containing 0.8 mol/L Ce(III). Scan rate = 50 mV/s. (C) Discharge polarization (solid lines, square symbols) and power density (dashed lines, triangle symbols) curves of Zn-Ce redox flow battery operating with different positive electrolytes after being charged at 50 mA/cm^2 for 90 minutes to reach SOC of 50%. The battery is discharged for 20 s at each of the applied current densities followed by a 20 s rest period.

When 2/0.5 MA mixed acid is used as the supporting electrolyte, the addition of Zn(II) also reduces the reduction/oxidation peak separation, which again suggests that the reversibility of Ce(III)/Ce(IV) redox couple has been enhanced (Figure 5.7B). Again, we compare the cathodic charges for the various CVs to evaluate the reaction kinetics for the conversion of Ce(III) to Ce(IV) during the anodic scan. The results show that the addition of 0.4 mol/L Zn(II) leads to the highest total cathodic charge in this case, reflecting that the largest amount of Ce(IV) is produced under this condition. As in the case of 4 mol/L MSA, the trends obtained from these CVs are consistent with those observed during actual battery operation presented previously. However, although the electrode response during the anodic portion of the scan varies greatly depending on the amount of Zn(II) present in the mixed acid electrolyte, the cathodic portions of the response remain remarkably similar. This effect is very different from that observed for 4 mol/L MSA. The similarity of the cathodic responses in the mixed acid indicates that the conversion of Ce(III) to Ce(IV) during the anodic scan and conversion of Ce(IV) back to Ce(III) during the reverse scan are not notably affected by the amount of Zn(II) present. Also, the rise of the anodic current beginning at ~1.25 V vs. Ag/AgCl during the forward scan is similar in the various electrolytes, unlike that observed in 4 mol/L MSA. These effects indicate that the presence of Zn(II) has a relatively small impact on the Ce(III)/Ce(IV) redox couple in the mixed acid supporting electrolyte compared to that in the 4 mol/L MSA electrolyte. Again, these trends are consistent with the battery performance experiments presented earlier in this study which showed that Zn(II) has a smaller effect on the coulombic and voltage efficiencies in the mixed acid positive electrolyte than in the MSA-only solutions.

Another important observation from the CV curves is that the addition of Zn(II) ions to the positive electrolytes appears to inhibit the oxygen evolution reaction at higher electrode potentials (> 2.0 V vs. Ag/AgCl). In both 4 mol/L MSA and the mixed acid, the CVs clearly show that the current density at the positive end of the scan where oxygen evolution is dominant decreases as the Zn(II) concentration increases. For example, a current density of ~354 mA/cm^2 is reached at 2.1 V vs. Ag/AgCl in the absence of Zn(II) in the 4 mol/L MSA positive supporting electrolytes, whereas it drops drastically to 160 mA/cm^2 when the electrolyte contains 0.8 mol/L Zn(II). A similar trend is observed in the 2/0.5 MA. In this case, the current density at 2.1 V vs. Ag/AgCl decreases from 409 mA/cm^2 to 234 mA/cm^2 when 0.8 mol/L Zn(II) is added to the electrolyte. In order to more accurately analyze the effect of Zn(II) inhibition of oxygen evolution by eliminating complications

due to the Ce(III)/Ce(IV) redox couple, we conducted another set of CV experiments in which Ce is removed from the system. It was found that the addition of Zn(II) clearly inhibits the oxygen evolution reaction in both MSA and MSA-H_2SO_4 mixed acid positive supporting electrolytes, as shown in Figure S1 in the Appendix. For example, the current density for oxygen evolution which is 578 mA/cm^2 at 2.1 V vs. Ag/AgCl in 4 mol/L MSA decreases to 361 mA/cm^2 when 0.8 mol/L of Zn(II) is added. Similarly, the current density is 1009 mA/cm^2 at 2.1 V vs. Ag/AgCl in the MSA-H_2SO_4 mixed acid electrolyte and 672 mA/cm^2 when 0.8 mol/L of Zn(II) is added. These observations support the finding that the addition of Zn(II) ions not only benefits the Ce(III)/Ce(IV) redox couple, but also appears to inhibit the undesired irreversible oxygen evolution side reaction.

Table 5.1 Key information from CV curves

Zn(II) concentration (mol/L)	4 mol/L MSA					2 mol/L MSA-0.5 mol/L H_2SO_4				
	0	0.2	0.4	0.6	0.8	0	0.2	0.4	0.6	0.8
Oxidation peak (V)	1.87	1.71	1.74	1.68	1.65	1.84	1.85	1.75	1.78	1.67
Reduction peak (V)	1.21	1.19	1.24	1.18	1.29	1.17	1.15	1.17	1.15	1.17
Peak separation (V)	0.66	0.52	0.50	0.50	0.36	0.67	0.70	0.58	0.63	0.50
Cathodic charge $\times 10^{-2}$ (C)	0.87	1.08	0.76	1.26	0.48	1.10	1.16	1.33	1.16	1.30

5.3.5 Discharge polarization curves of batteries operating with various positive electrolytes

As shown in Figure 5.7C, discharge polarization experiments have been conducted to evaluate battery performance when operating with each of the following positive supporting electrolytes: 4 mol/L MSA, 2/0.5 MA , 0.6 mol/L Zn(II) in 4 mol/L MSA and 0.4 mol/L Zn(II) in 2/0.5 MA. The open-circuit voltage (OCV) in each case is measured to be ~2.36 V. In general, the polarization

curves show similar behavior at current densities smaller than 45 mA/cm^2 where activation and ohmic effects dominate battery operation, except when 4 mol/L MSA positive supporting electrolyte is used. This behavior is consistent with previous results in this study showing that 4 mol/L MSA has a lower conductivity than the MSA-H_2SO_4 mixed acid electrolyte (Figure 5.4A) and that the use of MSA-H_2SO_4 mixed acid electrolyte and the addition of Zn(II) ions improves the kinetics of the positive electrode reaction (Figure 5.7A and B).

The observation that the positive electrolyte composition has a relatively small effect on the cell voltage in the ohmic region implies that ionic transport through this portion of the battery is not limiting. Our measurements show that the conductivity of the negative electrolyte used in this study is 134.5 mS/cm, which is comparable to the values for the positive electrolytes. By contrast, the proton conductivity of the Nafion 117 membrane is reported to be ~33 mS/cm when measured in an electrochemical cell filled with sulfuric acid solution, which is smaller than that of the electrolytes.[189] Based on these values, one would expect the cell voltage in the ohmic region to be mainly affected by ionic transport through the membrane.

For the 4 mol/L MSA electrolyte, the sharp drop in cell voltage indicative of mass-transfer limiting control begins at a current density of ~70 mA/cm^2, which is lower than 90 mA/cm^2 obtained when the battery operates with the MSA-H_2SO_4 mixed acid electrolyte. This is an indication that the mixed acid-based electrolyte which is less concentrated than the 4 mol/L MSA-based one exhibits more favourable mass-transfer conditions for the battery. The addition of Zn(II) to both 4 mol/L MSA and H_2SO_4-MSA mixed acid leads to a decrease in the cell voltage at higher current densities, reflecting a poorer performance in the mass-transfer controlling region. When 0.6 mol/L of Zn(II) is added to the 4 mol/L MSA positive supporting electrolyte, mass-transfer limiting control begins at current densities as low as 45 mA/cm^2 compared to a current density of 70 mA/cm^2 when no Zn(II) is added, which suggests that the mass-transfer properties of the positive electrolyte have been negatively affected. Similar results are observed when Zn(II) is added to the H_2SO_4-MSA mixed acid positive supporting electrolyte. The battery becomes mass transfer-limited at a current density of 70 mA/cm^2 when 0.4 mol/L of Zn(II) is added to the H_2SO_4-MSA mixed acid electrolyte compared to the current density of 90 mA/cm^2 when no Zn(II) is added. Mass transfer of electroactive species to and from the electrode surface can be impeded when the electrolyte becomes too viscous. As shown in Figure 5.4B, the viscosity of both the 4 mol/L MSA- and 2/0.5

MA-based electrolytes (also containing 0.8 mol/L Ce(III)-MSA) increases as more Zn(II)-MSA is added. This effect is particularly strong in the case of the 4 mol/L MSA-based solutions. Also, the viscosities of the 4 mol/L MSA-based solutions are considerably higher than that of the 2/0.5 MA-based electrolytes for any given Zn(II)-MSA content. These effects no doubt are largely due to the fact that the 4 mol/L MSA-based solutions have significantly higher ionic strengths than the 2/0.5 MA-based ones. As shown in Figure 5.7C, the current density at which each of the polarization curves enters the mass-transfer limited region follows closely in the same order in which their viscosities decrease (see Figure 5.4B): 0.6 mol/L Zn(II) in 4 mol/L MSA > 4 mol/L MSA ≈ 0.4 mol/L Zn(II) in H_2SO_4-MSA mixed acid > H_2SO_4-MSA mixed acid. This correlation reinforces the conclusion that the viscosity of the electrolyte plays an important role in battery operation particularly at high current densities.

The peak power density of the Zn-Ce redox flow battery is higher when operating with 2/0.5 MA (black and green) as the positive supporting electrolyte than when 4 mol/L MSA is used. A maximum power density of 100.6 mW/cm^2 is achieved at a current density of 80 mA/cm^2 in the 2/0.5 MA positive supporting electrolyte (black symbols), whereas the maximum power density is 79 mW/cm^2 at a current density of 65 mA/cm^2 in the case of 4 mol/L MSA (blue symbols). For the battery in which 0.4 mol/L Zn(II) has been added to the 2/0.5 MA positive supporting electrolyte, the maximum power density is 92 mW/cm^2 at 65 mA/cm^2, whereas it drops to 73 mW/cm^2 at 45 mA/cm^2 when 0.6 mol/L Zn(II) is added to the 4 mol/L MSA positive supporting electrolyte.

Chapter 6 Regeneration of positive electrolyte using RuO_2 and H_2O_2

6.1 Introduction

Decreased battery efficiency over long-term operation is caused by the irreversible HER on the negative electrode during cell recharge. The current consumed at the negative electrode is split between Zn deposition and the HER, while the current at the positive electrode is used primarily for the Ce(III) oxidation to Ce(IV) and only a small amount for the OER. Since the HER consumes more of the current than the OER, the amount of Zn deposited is stoichiometrically less than the amount of Ce(IV) that is formed during each charge. On the other hand, during battery discharge, Zn oxidation and Ce(IV) reduction are the only reactions that occur. These differences in the current distribution during charge and discharge create an imbalance whereby the Zn deposit present at the start of discharge is completely stripped off from the negative electrode before all of the Ce(IV) has been reduced to Ce(III) at the positive electrode by the time that the criterion for termination of discharge is reached. It is important to note that this type of imbalance which originates due to the occurrence of side reactions is a problem that affects all RFB systems. In the case of Zn-Ce system, it leads to a continual build-up of Ce(IV) ions remaining in the positive electrolyte from cycle to cycle. After a sufficient number of cycles, the Ce(IV) concentration can exceed its solubility limit, resulting in the precipitation of Ce(IV) oxide, loss of available electroactive cerium for the Ce(III)/Ce(IV) reaction and therefore a reduced cell capacity. It is therefore of great importance to prevent this from occurring. As outlined in Chapter 2, efforts have been directed at impeding the HER. However, since this reaction cannot be eliminated entirely, the problem of Ce precipitation can only be postponed, but not avoided altogether

An alternative approach to extending the cycle-life is to intervene at the positive electrode and convert Ce(IV) back to Ce(III) before precipitation can occur. Such a periodic intervention to keep the cell in balance is commonly done with all-vanadium cells where electrolyte regeneration is necessary due to crossover of the various vanadium species.[35] In this study, we consider two methods to regenerate the positive electrolyte by converting the accumulated Ce(IV) ions back to Ce(III). The first method utilizes a catalytic reactor containing RuO_2 catalysts, which are known to reduce Ce(IV) to Ce(III). The second method involves the injection of H_2O_2 into the positive

electrolyte tank in order to drive the reduction of Ce(IV) to Ce(III), while leaving only water and O_2 bubbles as by-products. Each of these methods is explained in more detail below.

RuO_2 is an effective catalyst to oxidize water and thereby reduce Ce(IV) to Ce(III).[190] This mechanism was first employed in a V-Ce RFB to discharge the battery by converting Ce(IV) to Ce(III) as follows:[142]

$$4\,Ce(IV) + 2H_2O \xrightarrow{RuO_2} 4\,Ce(III) + 4H^+ + 0_2 \uparrow \quad (26)$$

The other method considered here involves the addition of a small amount of a H_2O_2 solution to the positive electrolyte tank. The presence of H_2O_2 drives the reduction of Ce(IV) back to Ce(III) as it is oxidized to oxygen gas. The reaction is shown below:

$$2\,Ce(IV) + H_2O_2 \rightarrow 2\,Ce(III) + 2H^+ + 0_2 \uparrow \quad (27)$$

The reaction kinetics of this reaction have been well-studied and shown to be very rapid since the H_2O_2 and Ce(IV) ions go to completion within a few seconds.[144] This method has several key advantages: Firstly, the H_2O_2 solution can be introduced easily and inexpensively to the positive electrolyte using a pipette; no external equipment is required; the expense of purchasing and replacing the RuO_2 catalyst is avoided; the amount of H_2O_2 needed can be easily determined by measuring the Ce(IV) concentration; and finally, no contaminants are introduced into the system.

These two approaches are explored and evaluated in detail in the remainder of this chapter.

6.2 Experimental

6.2.1.1 Preparation of electrolyte

The negative electrolyte containing 1.5 mol/L zinc(II) methanesulfonate was prepared by dissolving zinc oxide (Zochem Inc.) in the appropriate amount of methanesulfonic acid (70%, Alfa Aesar). Extra MSA was added to adjust the MSA concentration to be 1 mol/L. Similarly, the positive electrolytes with 0.8 mol/L cerous methanesulfonate and different amounts of zinc(II) methanesulfonate were prepared by dissolving mixtures of cerium carbonate (Treibacher Industrie AG, 99% pure) and zinc oxide with MSA. MSA was then added to achieve 4 mol/L MSA supporting electrolytes. All chemicals were used as received without further purification. Ultrapure water with a resistivity of ~18 MΩ cm was used to prepare all the solutions in this work.

6.2.1.2 Measurement of Ce(IV) concentration and electrolyte properties

The concentration of Ce(IV) in the positive electrolyte was measured by a colorimetric titration method using ferroin (1,10-phenanthroine iron (II) sulfate, Alfa Aesar) as the end-point indicator. 50 μL of positive electrolyte was collected and titrated by 0.05 mol/L ammonium iron (II) sulfate hexahydrate (99%, Sigma-Aldrich). The very small sample volumes required for these titrations ensured that the cumulative amount collected over the course of the experiments had no effect on battery operation.

6.2.1.3 Electrochemical measurements

Full-cell experiments were conducted in a bench-scale redox flow battery consisting of a 6 mm-thick Pt-Ti mesh (Metakem GmbH) positive electrode with a Pt loading level of 7 mg/cm^2, a polyvinyl ester (PVE) carbon sheet (TDM Fuel Cells) negative electrode attached to a copper current collector (McMaster-Carr), two custom-made flow channels made from acrylic sheet (CIP Wholesale) to distribute electrolytes and an ion exchange membrane (Nafion 117, Fuel Cell Store) to separate the two compartments. Silicone rubber gaskets (CS Hyde Company) were used to

prevent any electrolyte leakage. More details regarding the design and operation of this battery can be found in Chapter 4.

The positive and negative electrolytes each with a volume of 30 mL were circulated from separate external reservoirs through Viton tubing (McMaster-Carr) to the battery compartments and back using a 2-head Longer BT100-1L peristaltic pump which enabled independent control of the two streams. The flow rate of the electrolytes was controlled to be 66 mL/min on both sides and the electrolyte tanks were immersed in a 50℃-water bath throughout the experiments. Prior to the experiments, the Nafion 117 membrane was activated by soaking in each of the following solutions for 1 hour at ~80℃ in the order: 3%(wt.) H_2O_2, ultrapure water, 0.5 mol/L H_2SO_4 solution and ultrapure water. The electrochemical measurements were conducted using an Autolab PGSTAT 30 potentiostat connected to a computer controlled via Nova 2.1.5 software. The battery performance was characterized by subjecting it to 30 galvanostatic charge-discharge cycles. Each cycle proceeded by charging the battery at a fixed current density of 25 mA/cm^2 for a duration of 1 hour followed by discharge at the same current density. Discharge was terminated when the battery cell voltage reached a cut-off value of 0.5 V. The coulombic efficiency of the battery over each cycle was obtained from the ratio of discharge time to the charge time, while the voltage efficiency over each cycle was determined from the ratio of the average discharge cell voltage to the average charge cell voltage.

6.2.1.4 Regeneration of the positive electrolyte using RuO_2 catalyst

A custom-made catalytic bed as shown in Figure 6.1 was used for the regeneration of the positive electrolyte using RuO_2 (99.9%, Millipore Sigma) as catalyst. The pore size of the filter used in the catalytic bed was in the range of 11 to 16 μm. The RuO_2 catalyst was pretreated by heating it to 150℃ in an oven for 6 hours. Once pretreated, 0.02g RuO_2 was added to the catalytic bed. The regeneration process was initiated after the battery was completely discharged and the subsequent battery charge-discharge cycle was temporarily paused. During each regeneration, 10 mL of the positive electrolyte was pumped into the catalytic bed and allowed to remain for 30s in order for the reaction to occur. The electrolyte was then pumped back to the positive electrolyte tank and this procedure is repeated several times until all the content in the electrolyte tank appeared

colourless. Then, the subsequent battery charge-discharge cycle was re-initiated and continued until the next regeneration process. The total time that paused for the regeneration process is approximately 10 min. This regeneration process was repeated after every 5 charge-discharge cycles.

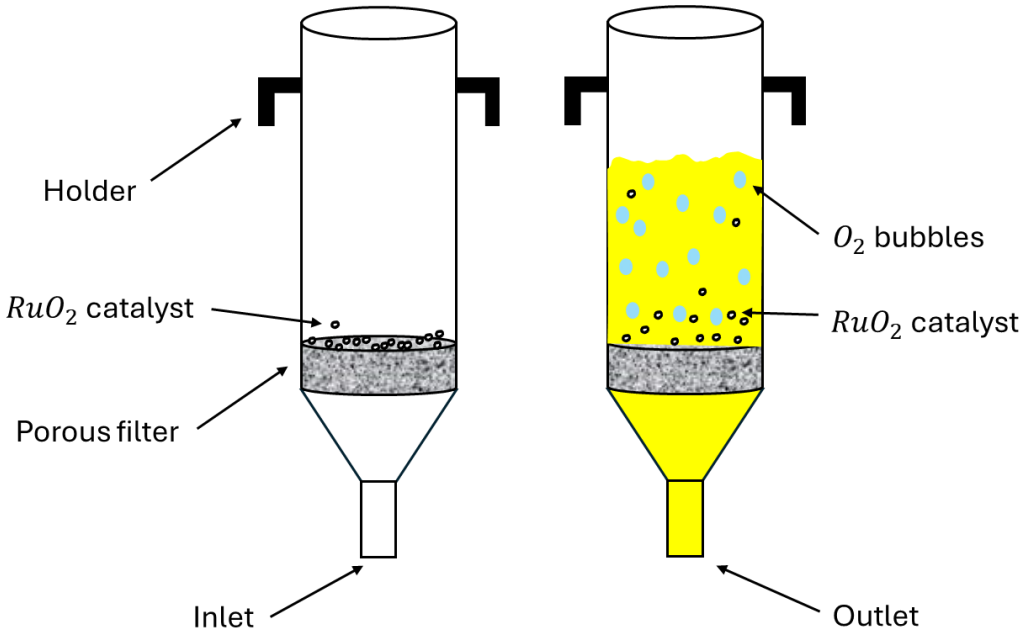


Figure 6.1. Schematic diagram of the custom-made catalytic bed used in this study for the electrolyte regeneration using RuO_2 as catalyst.

6.2.1.5 Regeneration of the positive electrolyte using H_2O_2

For the regeneration process using H_2O_2 solution (50wt.%, Millipore Sigma), H_2O_2 solution (~17.65 mol/L) was added directly to the positive electrolyte tank using a pipette. Battery operation was paused before electrolyte regeneration to ensure that the reaction was completed within the electrolyte tank. Otherwise, unreacted H_2O_2 would be pumped into the positive half-cell, react with Ce(IV) ions and produce a large amount of O_2 bubbles that might cover the surface of the positive electrode and cause an unstable voltage output. The volume of H_2O_2 solution was determined

according to the Ce(IV) concentration measured in the electrolyte and then the amount of H_2O_2 needed to convert 95% of the Ce(IV) back to Ce(III) was calculated. When the H_2O_2 solution was added to the electrolyte, 30s was allowed for the reaction to occur and another 50 μL of electrolyte sample was taken before the battery resumed for the next charge-discharge cycles. This 50 μL sample was then analyzed to confirm that Ce(IV) had been converted. The total time period of the regeneration process including the measurement of Ce(IV) ions and reaction time was about 5 min.

6.3 Results and Discussion

6.3.1 Catalytic regeneration of positive electrolyte using RuO_2

Experiments were first conducted to investigate the effectiveness of the positive electrolyte regeneration process using RuO_2 as catalyst. Figure 6.2 presents a comparison of the cell voltage and battery efficiency of 16 charge-discharge cycles when the battery was operated with and without the regeneration process. Each charge-discharge cycle was operated at a current density of 25 mA/cm^2, temperature of 323°K, electrolyte flow rate of 66 mL/min and charge duration of 1 hour. Both electrolytes were in their fully discharged states at the outset of these cycles, with the negative side containing 1.5 mol/L Zn(II) in 1 mol/L MSA and the positive one containing 0.8 mol/L Ce(III) in 4 mol/L MSA. The regeneration process was initiated at the end of each charge-discharge cycle if the maximum cell voltage reached 3V during charge, as indicated by the red arrows in Figure 6.2. As shown, this criterion was met and regeneration carried out three times over the course of the 16 charge-discharge cycles. The procedure lowers the average cell voltage during battery charge immediately after electrolyte regeneration at the 8th cycle (red arrows) by 0.24 V, which is beneficial for its voltage efficiency. The gradual increase of the charge voltage that tends to occur upon further cycling can be attributed to the accumulation of Ce(IV) in the positive electrolyte and the resulting increase of the positive electrode overpotential as previously discussed in Chapter 5 and our published work.[32] Regeneration converts Ce(IV) ions back to Ce(III) ions and thereby reduces the overpotential for Ce(III) oxidation during the subsequent charge. This conclusion is supported by the observation of the colour of the electrolyte changing from yellow to colourless upon regeneration, indicating that Ce(IV) has been reduced to Ce(III). The average

voltage efficiency of the battery over 16 charge-discharge cycles improves from 71.1% to 77.8% as a result of the three regenerations.

However, one critical problem of this method is that some RuO_2 catalyst particles are observed to escape through the filter into the positive electrolyte tank due to their very fine size. This leakage is very detrimental to battery performance since this causes the continual oxidation of water and conversion of Ce(IV) to Ce(III) in the positive electrolyte throughout both charge and discharge. Although Ce(IV) precipitation does not occur, the battery columbic efficiency is compromised since it reduces both the amount of Ce(IV) ions produced during battery charge and the available Ce(IV) ions for discharge. As a result, the average coulombic efficiency over the 16 charge-discharge cycles is lowered from of 74.1% to 57.8% when the regeneration process is applied. Overall, the energy efficiency is lowered from 52.7% to 45.0%, making this procedure infeasible. Consequently, the experiment has been terminated after 16 cycles. This method has other disadvantages: 1) inability to precisely control the amount of Ce(IV) being reduced, 2) requirement of an extra circulation system to divert the electrolyte from the tank to the catalytic bed, 3) need for a catalytic bed and 4) considerable complication of the RFB operating procedure.

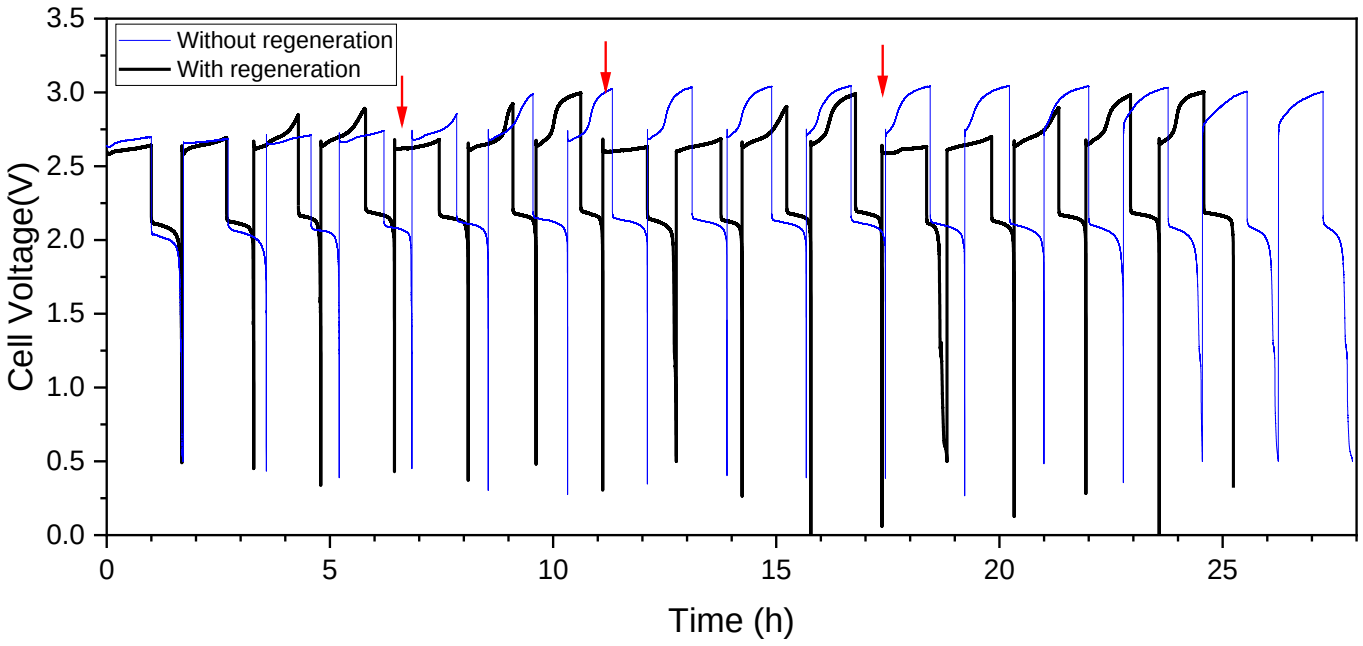


Figure 6.2. Cell voltage during 16 consecutive charge-discharge cycles of the Zn-Ce RFB operating at a current density of 25 mA/cm^2, temperature of 323°K, electrolyte flow rate of 66 mL/min and charge

duration of 1 hour with (black) and without (blue) regeneration using RuO_2 catalyst. The negative electrolyte contains 1.5 mol/L Zn(II) in 1 mol/L MSA and the positive electrolyte contains 0.8 mol/L Ce(III) in 4 mol/L MSA at the start of the cycles.

6.3.2 Regeneration of positive electrolyte using H_2O_2

Compared to the regeneration process using RuO_2 as catalyst, the reduction of Ce(IV) by the addition of a small volume of a H_2O_2 solution (~17.65 mol/L) is much simpler. Over the first 20 cycles, H_2O_2 is introduced to the electrolyte every 5 charge-discharge cycles and every 3 cycles after 20 cycles since the charge voltage increases more rapidly as cycling continues. A comparison of the cell voltage of the Zn-Ce RFB over 30 charge-discharge with and without the electrolyte regeneration process using H_2O_2 is presented in Figure 6.3. The regeneration process is conducted at the end of the 5^{th}, 10^{th}, 15^{th}, 20^{th}, 23^{rd}, 26^{th} and 29^{th} cycles, as indicated by the red arrows. Similar to the case when RuO_2 is used as catalyst to regenerate the positive electrolyte, the charge voltage of the battery is lowered drastically immediately after electrolyte regeneration. For example, the average charge voltage decreases by 0.2 V during the cycle immediately after electrolyte regeneration at the end of the 20^{th} cycle in comparison to the average charge voltage during the cycle prior to regeneration.

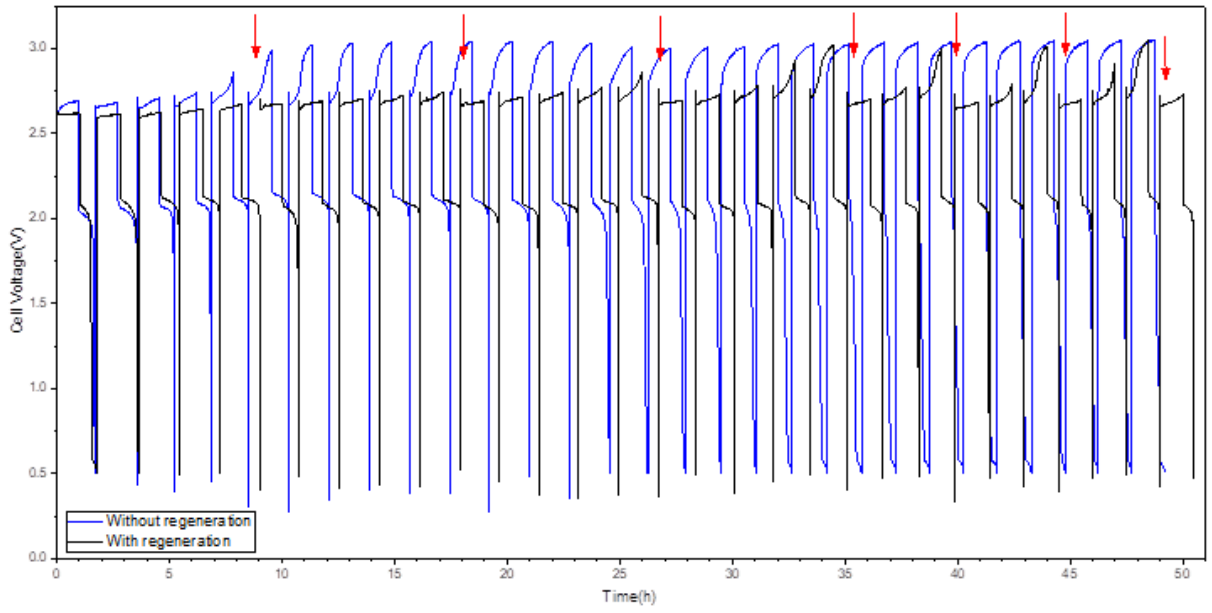


Figure 6.3. Cell voltage during 30 consecutive charge-discharge cycles of the Zn-Ce RFB operating at a current density of 25 mA/cm^2, temperature of 323°K, electrolyte flow rate of 66 mL/min and charge

duration of 1 hour with (black) and without (blue) regeneration by H_2O_2 addition. The negative electrolyte contains 1.5 mol/L Zn(II) in 1 mol/L MSA and the positive electrolyte contains 0.8 mol/L Ce(III) in 4 mol/L MSA at the start of the cycles.

Presumably, the lower charge voltage arises due to a decrease in the overpotential for Ce(III) oxidation at the positive electrode since the Ce(III) concentration is significantly increased and the Ce(IV) concentration reduced by the addition of H_2O_2. To confirm this, the positive and negative electrode potentials have also been monitored during these cycle experiments, as shown in Figure 6.4. Examination of Figure 6.3 and Figure 6.4 reveals that the gradual increase of the total cell voltage during each battery charge and from cycle to cycle is due to the rise in the potential of the positive electrode during charge (Figure 6.4A) since the change in the negative electrode potential from cycle to cycle is minimal (Figure 6.4B). The positive potential gradually increases due to the continual decline in Ce(III) concentration and accumulation of Ce(IV) ions. After electrolyte regeneration, the positive electrode potential during battery charge is reduced significantly, which causes a decrease in the cell charge voltage. For instance, the average positive electrode potential during the charge of the 6^{th} cycle is 1.71 V vs. Ag/AgCl when operated without regeneration, whereas the average positive electrode potential during charge of the 6^{th} cycle is only 1.48 V vs. Ag/AgCl after electrolyte regeneration. However, after regeneration, Ce(IV) ions again begin to slowly accumulate in the positive electrolyte and so the positive electrode potential during charge increases once again within a few cycles after electrolyte regeneration. This effect becomes more obvious especially after 20 charge-discharge cycles when the coulombic efficiency is lowered.

Another important finding is that the positive electrode reaction is no longer the limiting reaction except during the very first cycle, as reflected by the observation that it is the negative electrode potential that always rises sharply near the end of discharge, unlike the case when no regeneration is conducted (blue curve in Figure 6.4A). This is an indication that the performance of the positive electrode has improved to the point that the negative electrode reaction always limits the overall battery performance after the 1^{st} cycle. The positive electrode potentials during the first 5 cycles when the battery is operated with and without regeneration process are similar to each other. After the 5^{th} cycle, the positive electrode potential during battery discharge is much more stable and maintained at a higher level when the regeneration process is applied. For example, the average positive electrode potential during discharge is 1.35 V vs. Ag/AgCl when operated with

regeneration, whereas it is only 1.21 V when no regeneration is done. Some of this difference may be attributed to the Ce(IV) precipitation in the positive electrolyte which occurs only when no regeneration is carried out. The precipitation reduces the amount of Ce(IV) available for reduction during discharge and so would be expected to reduce the positive electrode potential. This effect is especially obvious after 15 cycles where the discharge voltage starts to drop almost at the beginning of battery discharge process. On the contrary, the discharge voltage is much more stable when the electrolyte regeneration process is applied.

The changes in the Ce(IV) concentration in the positive electrolyte after each charge-discharge cycle have also been measured and are plotted against cycle number in Figure 6.5. The blue curve represents the Ce(IV) concentration when the battery is operated under normal conditions without regeneration and was presented previously in Chapter 4. As was discussed, Ce(IV) begins to precipitate in the positive electrolyte after 6 cycles due to the accumulation of Ce(IV) ions and reduction in acidity. When regeneration by H_2O_2 addition is conducted, the Ce(IV) concentration immediately drops to very low levels after electrolyte regeneration at the end of the 5^{th}, 10^{th}, 15^{th}, 20^{th}, 23^{rd}, 26^{th} and 29^{th} cycles, as indicated by the red dots. It is worth noting that enough H_2O_2 is added each time to ensure that 95% of the Ce(IV) present in the electrolyte is reduced back to Ce(III) ions. From our experience, a bulk Ce(IV) concentration at the start of charge slightly higher than 0 mol/L (e.g., ~0.05 mol/L) is enough to ensure that the positive electrode reaction never becomes limiting and reduces battery efficiency. The success of the chemical regeneration is clearly evident in Figure 6.5 which shows that it is able to maintain the Ce(IV) concentration at levels considerably lower than otherwise would be the case during most of the battery operation. As expected, the potential of the positive electrode during charge is lowered after electrolyte regeneration due to the increase in the Ce(III) concentration in the positive electrolyte and the resulting decrease of the overpotential for Ce(III) oxidation. The positive electrode potential during battery charge again slowly increases over the following cycles due to the increase of Ce(IV) ions in the electrolyte until the next regeneration is conducted.

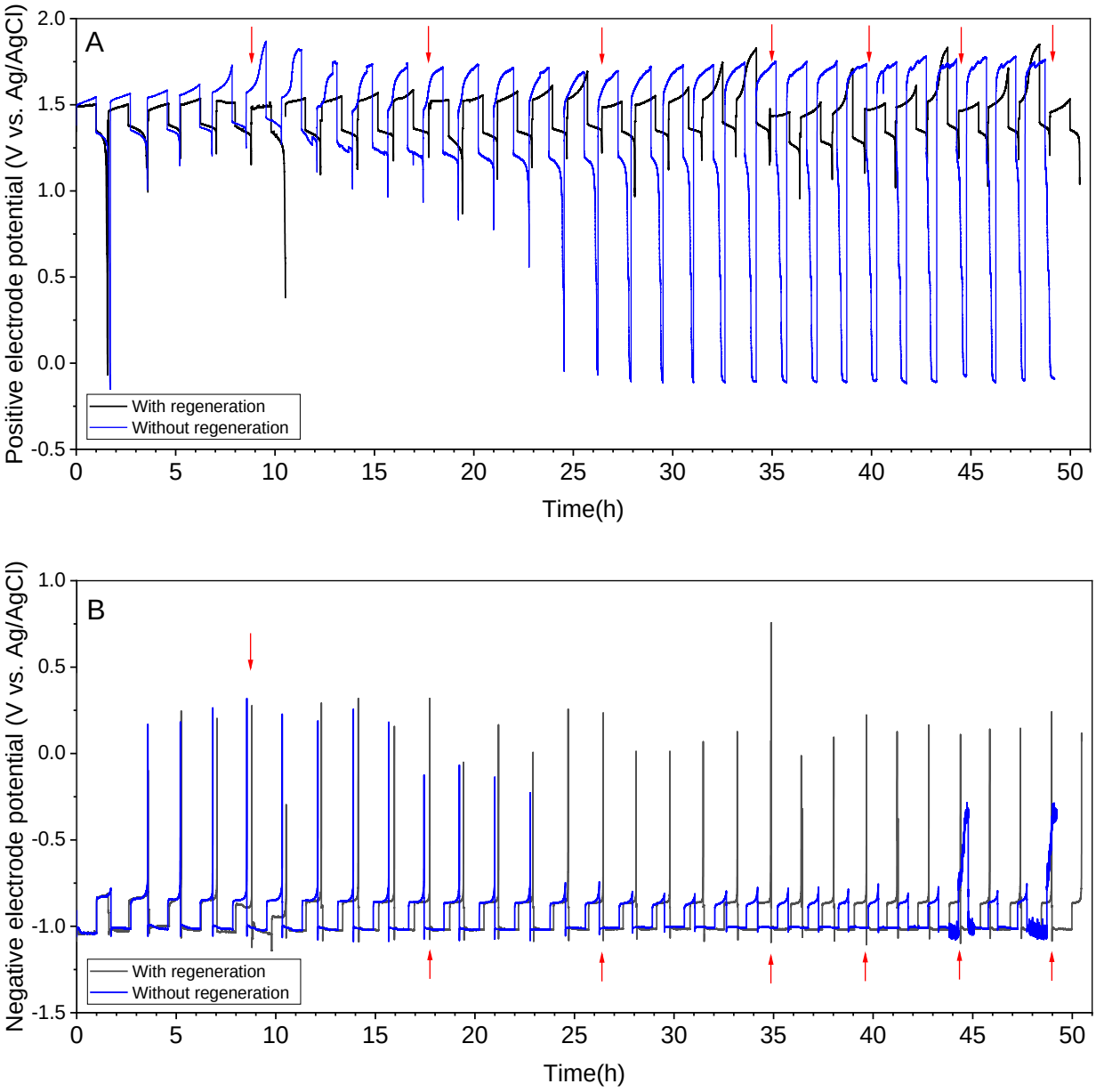


Figure 6.4. (A) Positive and (B) negative electrode potentials measured during 30 consecutive charge-discharge cycles of the Zn-Ce RFB operating at a current density of 25 mA/cm^2, temperature of 323°K, electrolyte flow rate of 66 mL/min and charge duration of 1 hour with (black) and without (blue) regeneration by H_2O_2 addition. The negative electrolyte contains 1.5 mol/L Zn(II) in 1 mol/L MSA and the positive electrolyte contains 0.8 mol/L Ce(III) in 4 mol/L MSA at the start of the cycles. Red arrows indicate the addition of H_2O_2 to the positive electrolyte.

The average coulombic efficiency, voltage efficiency and energy efficiency over 30 cycles when the battery is operated with and without regeneration are plotted in Figure 6.6. The average coulombic efficiency improves from 63.7% to 68.3% when H_2O_2 regeneration is carried out. The improvement occurs mainly after the first 15 cycles when the positive electrode reaction limits battery operation if the positive electrolyte is not regenerated. Although the improvement in coulombic efficiency is modest, it is certainly much more effective than RuO_2 catalysis. Closer evaluation of the negative electrode potentials in Figure 6.4B reveals that the battery coulombic efficiency is limited by the negative electrode from the 2nd cycle onward. Obviously, improvement of the positive electrode reaction cannot improve the overall battery performance when the battery is limited by the negative electrode reaction. Since the coulombic efficiency is limited by the negative electrode reaction and the regeneration process cannot prevent the transfer of H^+ ions into the negative electrolyte, further improvement in battery performance requires that attention be shifted to zinc deposition and the HER on the negative electrode, which is beyond the scope of the current study.

Interestingly, a decrease in the coulombic efficiency is observed during the cycles immediately after electrolyte regeneration (i.e. 6th, 11th, 16th, 21st, 24th and 27th cycles). This shows that the system has been negatively affected by the regeneration process to some extent, probably due to the pause in battery operation when conducting the electrolyte regeneration process. It is also interesting that the voltage efficiency is not similarly affected and, in fact, remains very stable throughout all the cycling and Ce(IV) concentration measurements. Fortunately, the effect is transient and the coulombic efficiency recovers by the next cycle. Nevertheless, it would be important to refine the regeneration procedure in future work so as to eliminate any negative effects on battery operation.

Compared to the coulombic efficiency, the voltage efficiency is greatly improved by the regeneration process (Figure 6.6B). The average voltage efficiency over 30 cycles improves from 56.8% to 76.1% and remains stable throughout the experiment. Since the potential of the negative electrode is relatively stable during either charge or discharge, the variation in voltage efficiency is mainly caused by changes in the positive electrode potential. Thus, the improvement in voltage efficiency can be attributed to the increase in the Ce(III) concentration in the positive electrolyte brought about by regeneration and the consequent reduction in the overpotential for Ce(III)

oxidation during charge at the positive electrode. This demonstrates the effectiveness of regeneration by H_2O_2 addition in improving the voltage efficiency of the Zn-Ce RFB system. When combined with the effect on the coulombic efficiency, this leads to an improvement from 38.1% to 51.2% in the average energy efficiency over 30 cycles, which indicates that this regeneration method should be useful for the Zn-Ce system and other RFB systems.

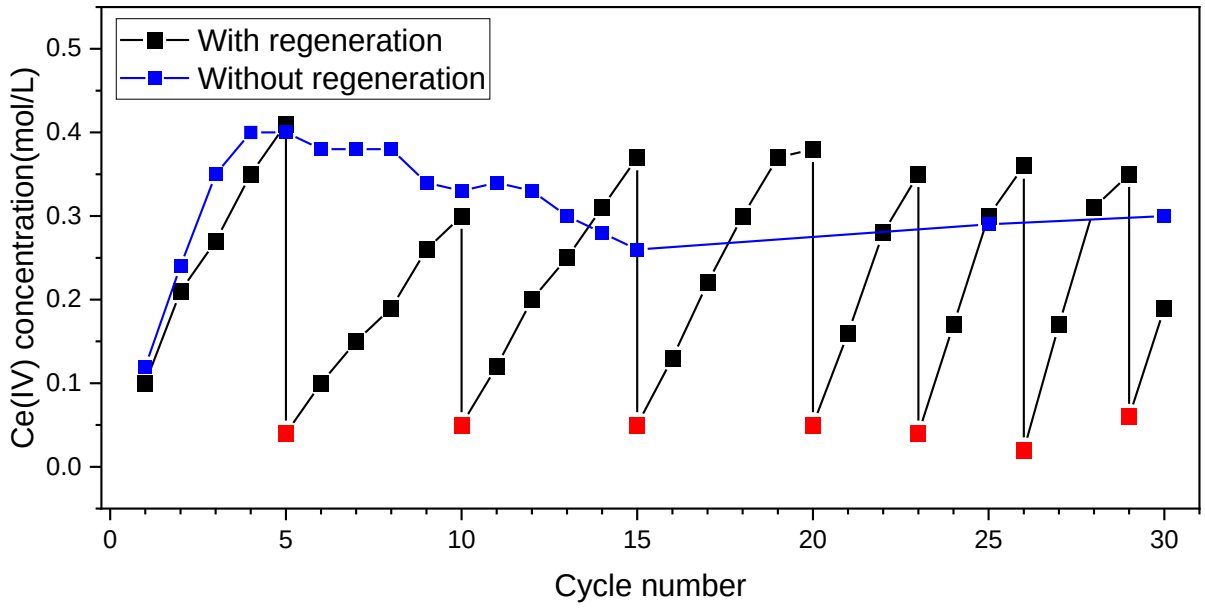
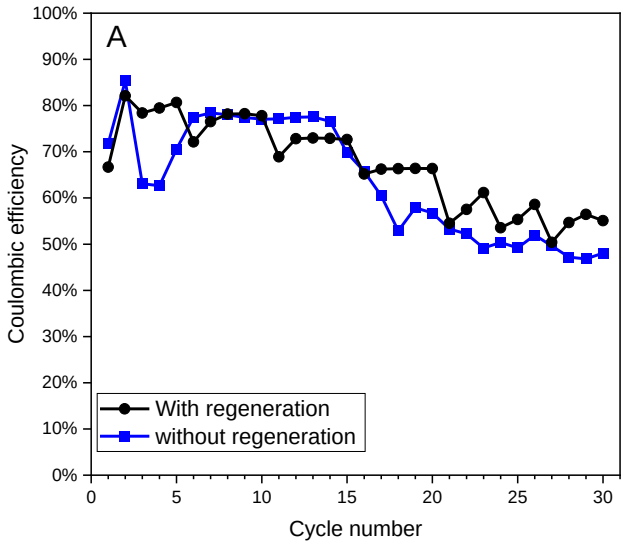
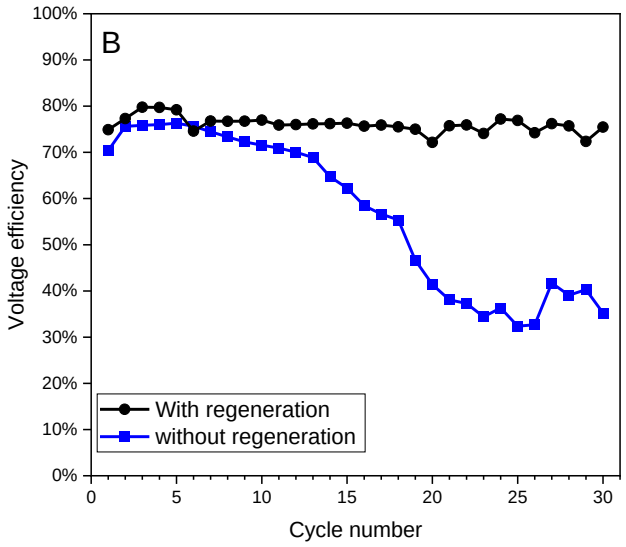


Figure 6.5. Ce(IV) concentration in the positive electrolyte measured during 30 consecutive charge-discharge cycles of the Zn-Ce RFB operating at a current density of 25 mA/cm^2, temperature of 323°K, electrolyte flow rate of 66 mL/min and charge duration of 1 hour with (black) and without (blue) regeneration by H_2O_2 addition. The negative electrolyte contains 1.5 mol/L Zn(II) in 1 mol/L MSA and the positive electrolyte contains 0.8 mol/L Ce(III) in 4 mol/L MSA at the start of the cycles. The red dots represent the Ce(IV) concentration immediately after electrolyte regeneration.


A
Coulombic efficiency
Cycle number
With regeneration
without regeneration


B
Voltage efficiency
Cycle number
With regeneration
without regeneration

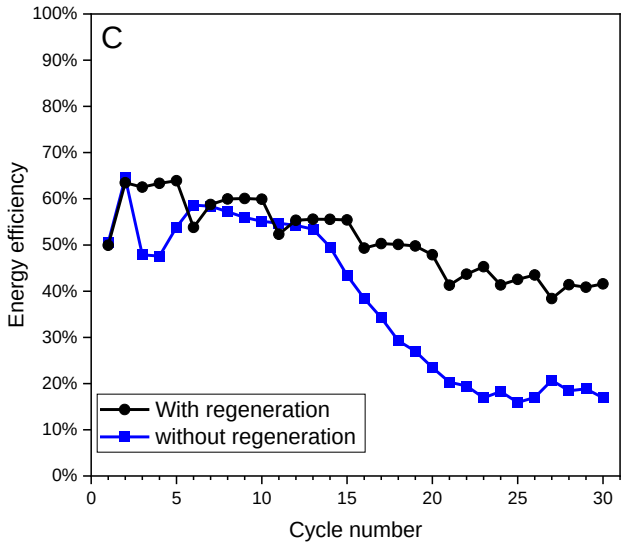

C
Energy efficiency
Cycle number
With regeneration
without regeneration

Figure 6.6. (A) Coulombic efficiency, (B) voltage efficiency and (C) energy efficiency during 30 consecutive charge-discharge cycles of the Zn-Ce RFB operating at a current density of 25 mA/cm^2, temperature of 323°K, electrolyte flow rate of 66 mL/min and charge duration of 1 hour with (black) and without (blue) regeneration by H_2O_2 addition. The negative electrolyte contains 1.5 mol/L Zn(II) in 1 mol/L MSA and the positive electrolyte contains 0.8 mol/L Ce(III) in 4 mol/L MSA at the start of the cycles.

Chapter 7 Two-Dimensional Transient Model of a Zn-Ce RFB Incorporating Ion Crossover

7.1 Introduction

Modeling the battery performance in cell level is important since it provides insights into the interplay of reaction kinetics, mass transport and electrolyte flow, which offer deeper understanding of RFB operation and might be difficult to obtain solely through experiments. The first 2D transient model of Zn-Ce RFB system was developed by Amini and Pritzker.[39] Their model combined all three modes of ion transport (migration, diffusion and convection) coupled with electrode kinetics and was validated against experimental data, which included full-cell voltage, separately measured positive and negative electrode potential and Ce(IV) concentration in the positive electrolyte. In this chapter, we present a more comprehensive model with the aim of further improving its accuracy and investigating battery performance under various operating conditions. Most importantly, the crossover of different ion species other than H^+ through the membrane is incorporated into the new model. This is accomplished by fitting the model against the actual measured concentrations of the different species in the positive and negative electrolytes that was already presented in Chapters 4 and 5. In addition, the performance of the Zn-Ce RFB operating with different positive electrode structures and under various conditions such as electrolyte flow rates and current density is investigated to provide valuable information for future improvement of Zn-Ce RFBs. To the best of our knowledge, the analysis presented here includes the most extensive comparison between experimental laboratory data and the calculated output from a RFB model that has been reported to date.

7.2 Experimental

The Zn-Ce redox flow battery experiments were conducted using a bench-scale single cell described in Chapter 4, composed of a copper current collector (McMaster-Carr), polyvinyl ester (PVE) carbon negative electrode (TDM Fuel Cells), two acrylic flow channels (CIP Wholesale), Nafion-117 proton exchange membrane (Fuel Cell Store), three-dimensional platinized titanium

mesh (7 mg/cm^2 Pt loading, Metakem GmbH) and four rubber silicone gaskets (CS Hyde Company). Both the negative and positive electrodes had dimensions of 2 cm × 4.5 cm exposed to the electrolyte. Unless otherwise stated, the battery charge-discharge cycles were conducted galvanostatically using an Autolab PGSTAT 30 potentiostat (Metrohm) at a current density of 25 mA/cm^2. A constant temperature of 50°C was maintained throughout the experiments using a Neslab RTE-8 water bath.

In their fully discharged states, the negative electrolyte contained 1.5 mol/L zinc methanesulfonate (ZnMSA) in 1 mol/L methanesulfonic acid (MSA), while the positive electrolyte contained 0.8 mol/L cerous methanesulfonate (CeMSA) in 4 mol/L MSA. The electrolytes were circulated through the battery at a flow rate of 60 mL/min from two external tanks containing 30 mL of negative and positive electrolyte. The potentials of the negative and positive electrodes during battery operation were measured using two Ag/AgCl reference electrodes (Pine Research Instrumentation) installed into the flow battery system, as described previously in Chapter 3. The H^+ concentration in the negative electrolyte was determined by titration using 0.01 mol/L NaOH solution, prepared by dissolving sodium hydroxide beads (VWR Analytical) into ultrapure water. The concentration of Ce(IV) in the positive electrolyte was measured by collecting 50 μL of positive electrolyte sample followed by titration using 0.05 mol/L ammonium iron (II) sulfate hexahydrate (99%, Sigma-Aldrich). The titration end-point was indicated by ferroin (1,10-phenanthroine iron (II) sulfate, Alfa Aesar) when the color of the solution changes from yellow to red. To measure the Ce(III) concentration in the positive electrolytes, another 50 μL sample was collected and then contacted with a certain amount of ammonium persulfate (thermo scientific, 98+%) and silver nitrate solution (Titripur, 0.1 mol/L) to oxidize all Ce(III) present to Ce(IV). This step was followed by colorimetric titration to determine the Ce(IV) content in this oxidized sample. The Ce(III) concentration was then determined from the difference between the total Ce(IV) concentration after oxidation and the original Ce(IV) concentration prior to oxidation. The total cerium concentration in the negative electrolyte and the Zn(II) concentration in both negative and positive electrolytes were also measured by inductively coupled plasma optical emission spectroscopy (ICP-OES, Teledyne Leeman Labs Prodigy). The total cerium concentration in the negative electrolyte was measured by ICP-OES and not by titration because the amount of cerium

that has crossed over after each charge-discharge cycle was too low to be reliably determined by the titration method.

7.3 Model Description

The geometry of the two-dimensional Zn-Ce flow battery described in the model is shown in Figure 7.1. A two-dimensional model has been chosen over one- and three-dimensional versions as a compromise between accuracy and computational effort. This is also consistent with the 2-dimensional Zn-Ce RFB model developed by Amini and Pritzker.[39] The direction perpendicular to the electrodes and membrane is denoted by the coordinate x, while the direction of electrolyte flow parallel to the electrode and membrane surfaces is given by the coordinate y. The battery consists of 3 domains: negative flow channel ($0 < x < x_1, 0 < \mathrm{y} < \mathrm{H}$), membrane ($x_1 < \mathrm{x} < x_2,\ 0 < \mathrm{y} < \mathrm{H}$) and platinized titanium mesh positive electrode ($x_2 < \mathrm{x} < x_3, 0 < \mathrm{y} < \mathrm{H}$) which was treated as a porous medium through which the electrolyte flowed. The coordinate system is defined so that the negative electrode (planar PVE carbon sheet) is located at $\mathrm{x} = 0$. The following assumptions are applied to the model during calculations:

1. Both electrolytes are incompressible liquids.
2. Laminar flow conditions are assumed in both electrolytes given that the Reynolds number is calculated to be less than 150.[39]
3. Transport and reaction chemistry in both electrolytes can be described using dilute solution theory.
4. The entire flow battery system is considered to be isothermal.
5. The effect of gas bubbles produced by the HER and OER side reactions on battery operation is not considered.
6. The effects of gravity are neglected.
7. The transport of ionic species current density, electrolyte potential and electrolyte velocity in the direction perpendicular to the x-y plane are not considered.

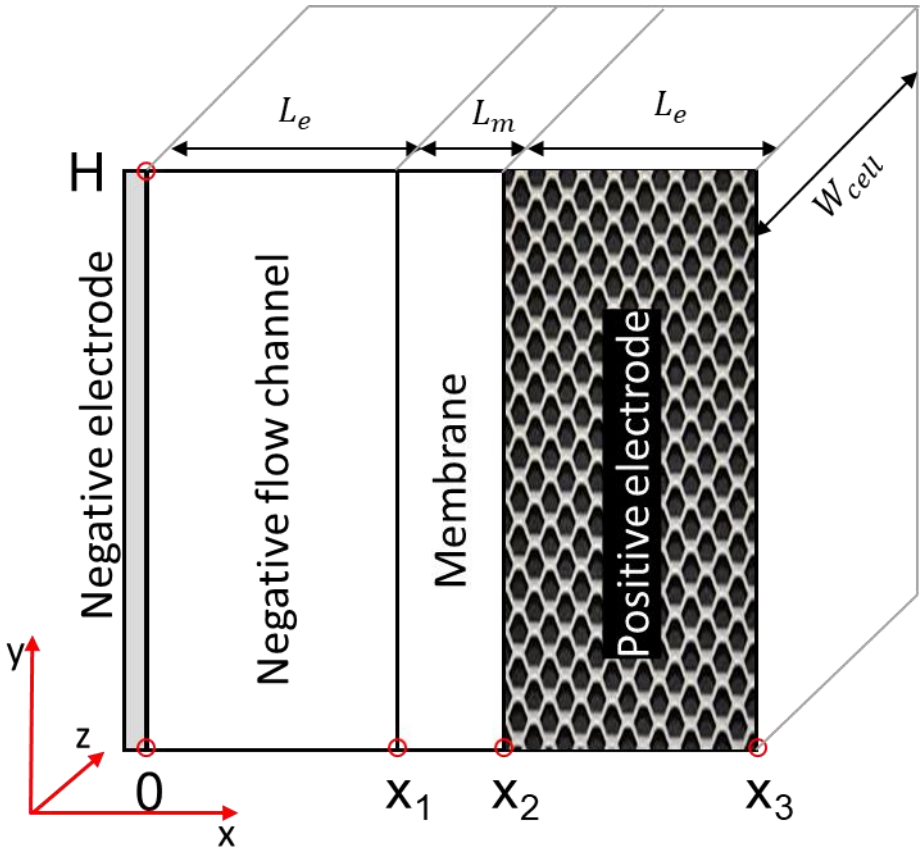


Figure 7.1. Schematic showing the geometry of the two-dimensional Zn-Ce redox flow battery described in the model.

Based on the known solution chemistry of zinc and cerium species for the conditions prevailing in Zn-Ce RFBs, the predominant Zn(II) species is Zn^{2+}, predominant Ce(III) species is Ce^{3+} and predominant Ce(IV) species is $CeOH^{3+}$.[191] Accordingly, the dissolved species considered in the model are H^+, Zn^{2+}, Ce^{3+}, $CeOH^{3+}$ and MSA^- (methanesulfonate). These species can be found in both negative and positive electrolytes due to ionic crossover. Metallic zinc is present only on the negative electrode surface located at $x = 0$ and was not treated as a moving boundary.

The primary electrode reactions in the Zn-Ce redox flow battery involving these species are as follows:

negative electrode: $$Zn^{2+} + 2e^- \underset{Discharge}{\overset{Charge}{\rightleftarrows}} Zn(s),\ E^0 = -0.959\ V\ vs.Ag|AgCl \quad (28)$$

positive electrode: $$Ce^{3+} + H_2O \underset{Discharge}{\overset{Charge}{\rightleftarrows}} CeOH^{3+} + e^- + H^+, E^0 = 1.28 - 1.72\ V\ vs.Ag|AgCl \quad (29)$$

During battery charge, the hydrogen and oxygen evolution side reactions also occur at the negative and positive electrodes, respectively, i.e.,

negative side reaction $$2H^+ + 2e^- \rightarrow H_2 \uparrow,\ E^0 = -0.197\ V\ vs.Ag|AgCl \quad (30)$$

positive side reaction $$2H_2O \rightarrow O_2 \uparrow + 4H^+ + 4e^-,\ E^0 = 1.03\ vs.Ag|AgCl \quad (31)$$

7.3.1 Electrolyte flow equations

The negative compartment is filled with flowing negative electrolyte whereas the positive compartment is filled with a porous platinized-titanium mesh electrode through which the positive electrolyte flows. Thus, the description of electrolyte flow through the negative compartment differs from that on the positive side. In the negative flow channel, the electrolyte flow velocity v_{neg} is calculated using the Navier-Stokes equation:

$$\rho_{neg}\left(\frac{\partial \vec{v}_{neg}}{\partial t} + \vec{v}_{neg} \cdot \nabla \vec{v}_{neg}\right) = -\nabla \vec{P}_{neg} + \mu_{neg} \nabla^2 \vec{v}_{neg} \tag{32}$$

where ρ_{neg} is the density of the negative electrolyte, $\vec{P}_{neg}$ is the pressure vector in the negative flow channel and μ_{neg} is the dynamic viscosity of the negative electrolyte.

Since the negative electrolyte is considered an incompressible fluid, the continuity expression applies, thus:

$$\nabla \cdot \vec{v}_{neg} = 0 \tag{33}$$

For the positive electrolyte flow, the velocity is calculated from Darcy's law:

$$\vec{v}_{pos} = -\frac{K}{\mu_{pos}} \nabla P_{pos} \tag{34}$$

where K is the intrinsic permeability of the platinized-titanium mesh positive electrode and μ_{pos} is the dynamic viscosity of the positive electrolyte. The continuity equation (Eqn.(33)) also applies to the positive electrolyte which is also taken to be incompressible.

7.3.2 Species transport equations in negative compartment

In the negative half-cell, the transport equation (Eqn. (35)) describes mass conservation of species i in the negative flow channel defined in the region $x_0 < x < x_1$ and $0 < y < H$, which is ultimately solved to yield the concentration $c_{i,neg}(x, y, t)$ of species i. No electrochemical reaction occurs within the flow channel and so the source term in the species balance equation below on

the right side is zero. The molar flux $\vec{N}_{i,neg}$ of species in the electrolyte is given by the Nernst-Planck equation, which includes species transport by diffusion, migration and convection:

$$\frac{\partial c_{i,neg}}{\partial t} + \nabla \cdot \vec{N}_{i,neg} = 0 \tag{35}$$

$$\vec{N}_{i,neg} = -D_{i,neg}\nabla c_{i,neg} - \frac{z_{i,neg}c_{i,neg}D_{i,neg}F}{RT}\nabla \phi_{e,neg} + \vec{v}_{neg}c_{i,neg} \tag{36}$$

In this expression, $D_{i,neg}$ and $z_{i,neg}$ are the diffusion coefficient and charge, respectively, of species i, $\phi_{e,neg}$ denotes the electric potential in the negative electrolyte and $\vec{v}_{neg}$ is the incompressible velocity of the negative electrolyte.

The electroneutrality condition is assumed to be valid everywhere within the negative half-cell domain, i.e.,

$$\sum_i z_{i,neg}c_{i,neg} = 0 \tag{37}$$

It should be mentioned that the concentration of MSA^- is not solved for because it is determined by the electroneutrality condition.

The current density flowing through the electrolyte is carried by all ionic species and is related to their concentrations by Faraday's law:

$$\vec{\imath}_{e,neg} = \sum_i z_{i,neg} F \vec{N}_{i,neg} \tag{38}$$

By incorporating the Nernst-Planck equation (Eqn.(36)) into Eqn.(38), the total current density flowing through the negative electrolyte can be related to the concentrations of the various species in this electrolyte by the following expression:

$$\vec{\imath}_{e,neg} = F \sum_i z_{i,neg} \left(-D_{i,neg} \nabla c_{i,neg}\right) - \frac{F^2}{RT} \sum_i z_{i,neg}^2 D_{i,neg} c_{i,neg} \nabla \phi_{e,neg} \tag{39}$$

7.3.3 Species transport equations in positive compartment

The species balances on the positive side differ from those on the negative side since the positive compartment is filled with a porous electrode located in the region defined by $x_2 < x < x_3$ and $0 < y < H$. Thus, a source term S_{ij} for species i due to electrode reaction j is added to the mass conservation equation for species i in the electrolyte, i.e.,

$$\frac{\partial\, \varepsilon_{pos} c_{i,pos}}{\partial t} + \nabla \cdot N_{i,pos} = \sum_j S_{ij} \tag{40}$$

The source term is related to the rates of the electrode reactions through Faraday's law:

$$S_{ij} \quad = \quad \sum_j \frac{a\, \nu_{ij} i_j}{n_j F} \tag{41}$$

where $c_{i,pos}$ is the concentration of species i, $N_{i,pos}$ is the molar flux of species i on the positive side and ε_{pos} is the porosity of the positive electrode. In the expression for the source term on the

right hand side of Eqn.(41), i_j is the current density due to reaction j, ν_{ij} and n_j are the stoichiometric coefficients of species i and electrons, respectively, in electrode reaction j written in the reduction direction and a is the specific area of the Pt-Ti mesh.

The molar flux of species in the electrolyte can be calculated by the Nernst-Planck equation, which includes species transport by diffusion, migration and convection:

$$\vec{N}_{i,pos} = -D_{i,pos}^{eff}\nabla c_{i,pos} - \frac{z_{i,pos}c_{i,pos}D_{i,pos}^{eff}F}{RT}\nabla\phi_{e,pos} + \vec{v}_{pos}\,c_{i,pos} \tag{42}$$

where D_i^{eff} and z_i are the effective diffusion coefficient and charge, respectively, of species i, $\phi_{e,pos}$ and $\vec{v}_{pos}$ denote the electrical potential and incompressible electrolyte flow velocity in the positive electrolyte. D_i^{eff} accounts for the porosity ε_{pos} of the positive electrode and is calculated using the Bruggemann correction, which is intended for overlapping cylinders so is well suited to the mesh used here:

$$D_{i,pos}^{eff} = {\varepsilon_{pos}}^{1.5} D_{i,pos} \tag{43}$$

The electroneutrality condition is also valid in the positive domain, i.e.,

$$\sum_i z_{i,pos}c_{i,pos} = 0 \tag{44}$$

Electrical current flows through both the liquid and solid phases in the positive compartment. Thus, the total current density at any point in the positive compartment is made up of the sum of the electronic current density flowing through the solid phase (i.e., $\vec{\imath}_{s,pos}$) and the ionic current density

(i.e., $\vec{\imath}_{e,pos}$) flowing through the electrolyte. Conservation of charge also requires that no accumulation of charge occurs at any position in the positive compartment. These conditions lead to the following:

$$\nabla \cdot \vec{\imath}_{pos} = \nabla \cdot \vec{\imath}_{s,pos} + \nabla \cdot \vec{\imath}_{e,pos} = 0 \tag{45}$$

Ohm's law is used to relate the relate the electrical potential $\phi_{s,pos}$ of the solid electrode to the ionic current density $\vec{\imath}_{s,pos}$:

$$\vec{\imath}_{s,pos} = -\sigma_s^{eff} \nabla \phi_{s,pos} \tag{46}$$

In Ohm's law, σ_s^{eff} is the effective electrical conductivity of the Pt-Ti mesh and is linked to the electrical conductivity σ_s of the bulk solid material using the Bruggeman correction:

$$\sigma_s^{eff} = (1 - \varepsilon_{pos})^{1.5} \sigma_s \tag{47}$$

Arguably a different exponent might be required on the Bruggeman correction than was used for the void phase, but 1.5 was used for lack of a more definitive value.

Two electrode reactions occur in the positive compartment and contribute to the source term in Eqn.(40): $Ce^{3+}/CeOH^{3+}$ and the OER. The current density i_{Ce} associated with the $Ce^{3+}/CeOH^{3+}$ reaction is given by the following Butler-Volmer equation:

$$i_{Ce} = i_{Ce,0}\left[\frac{c_{Ce^{3+},s}}{c_{Ce^{3+},bulk}}\exp\left(\frac{\alpha_{a,Ce}F}{RT}\eta_{Ce}\right) - \frac{c_{CeOH^{3+},s}}{c_{CeOH^{3+},bulk}}\exp\left(-\frac{\alpha_{c,Ce}F}{RT}\eta_{Ce}\right)\right] \quad (48)$$

$$i_{Ce,0} = Fk_{pos}^{0}{c_{Ce^{3+},s}}^{\alpha_{a,Ce}}{c_{CeOH^{3+},s}}^{\alpha_{c,Ce}} \quad (49)$$

In Eqn.(48), $c_{Ce^{3+},s}$ and $c_{CeOH^{3+},s}$ are the concentrations at the surface of the Pt-Ti mesh electrode, whereas $c_{Ce^{3+},bulk}$ and $c_{CeOH^{3+},bulk}$ are the corresponding bulk concentration. $\alpha_{a,Ce}$ and $\alpha_{c,Ce}$ denote the transfer coefficients in the anodic and cathodic directions of the electrode reaction. $i_{Ce,0}$ is the exchange current density cerium reaction expressed by Eqn.(49), where k_{pos}^{0} is the rate constant of the negative electrode reaction. η_{Ce} is the overpotential and is calculated using the following equation:

$$\eta_{Ce} = E_{pos} - E_{Ce}^{eq} = \phi_{s,pos} - \phi_{e,pos} - E_{Ce}^{eq} \quad (50)$$

where E_{Ce}^{eq} is the equilibrium potential of the $Ce^{3+}/CeOH^{3+}$ reaction determined by the Nernst equation:

$$E_{Ce}^{eq} = E_{Ce}^{0} + \frac{RT}{n_{Ce}F}\ln\left(\frac{c_{CeOH^{3+},bulk}\, c_{H^{+},bulk}}{c_{Ce^{3+},bulk}}\right) \quad (51)$$

E_{Ce}^{0} is the standard potential of the $Ce^{3+}/CeOH^{3+}$ reaction and n_{Ce} is the number of electrons transferred for each cerium converted by the redox reaction (i.e., $n_{Ce} = 1$) .

Because the Pt-Ti mesh is treated as a continua with effective properties, it is necessary to include expressions for the mass transfer resistance of Ce^{3+} and $CeOH^{3+}$ between the mesh surface and the bulk electrolyte flowing in the voids. This resistance is accounted for by the inclusion of the following expressions relating the surface and bulk concentrations of the electroactive species Ce^{3+} and $CeOH^{3+}$ to the rate of the electrode reactions, i.e.,

$$k_{m,Ce^{3+}}\left(c_{Ce^{3+},bulk} - c_{Ce^{3+},s}\right) = \frac{i_{Ce}}{F} \tag{52}$$

$$k_{m,Ce(OH)^{3+}}\left(c_{CeOH^{3+},bulk} - c_{CeOH^{3+},s}\right) = -\frac{i_{Ce}}{F} \tag{53}$$

where $k_{m,Ce^{3+}}$ and $k_{m,CeOH^{3+}}$ are the local mass transfer coefficients for Ce^{3+} and $CeOH^{3+}$respectively, at the interface between the Pt-Ti electrode and positive electrolyte. The mass transfer coefficients of the Ce^{3+} and $CeOH^{3+}$ ions can be determined using the following dimensionless relationship determined when the electrolyte flows through a porous material.[192]:

$$Sh = 0.906Re^{0.432}Sc^{0.432} \tag{54}$$

$$Re = \frac{vd_f}{u} \tag{55}$$

$$Sc = \frac{u}{D_i^{eff}} \tag{56}$$

$$Sh = \frac{k_m d_f}{D_i^{eff}} \tag{57}$$

where v is the velocity and u is the kinematic viscosity of the positive electrolyte. Re, Sc and Sh are the Reynolds, Schmidt and Sherwood number, respectively.

The second reaction occurring at the positive electrode during charge is the OER. The current density i_{O_2} due to this reaction is described by the Butler-Volmer equation:

$$i_{O_2} = i_{O_2,0}\left[\exp\left(\frac{\alpha_{O_2}F}{RT}\eta_{O_2}\right)\right] \tag{58}$$

where α_{O_2} and η_{O_2} are the transfer coefficient and overpotential, respectively, for the OER. The overpotential is given by:

$$\eta_{O_2} = \phi_{s,pos} - \phi_{e,pos} - E_{O_2}^{eq} \tag{59}$$

where $E_{O_2}^{eq}$ is the equilibrium potential of the OER given in Table 7.3. The OER is assumed to be kinetically controlled and the cathodic direction of the reaction is neglected in Eqn.(58) above due to the irreversible nature of this reaction.[193,194]

7.3.4 Species transport equations in membrane

The mass conservation equation also applies to species i in the membrane:

$$\frac{\partial \varepsilon_m c_{i,m}}{\partial t} + \nabla \cdot \vec{N}_{i,m} = 0 \tag{60}$$

where $c_{i,m}$ and $\vec{N}_{i,m}$ are the concentration and molar flux, respectively, of species i in the membrane. ε_m is the porosity of the membrane. Since no homogeneous reactions occur in this region, Eqn.(60) contains no source term. Unlike the situation in the electrolytes, the flux $\vec{N}_{i,m}$ is driven only be migration and diffusion since the flow velocity of the electrolyte (i.e., convection) through the membrane is negligible. The molar flux of species in the electrolyte can therefore be determined as follows:

$$\vec{N}_{i,m} = -D_{i,m}\nabla c_{i,m} - \frac{z_i c_{i,m} D_{i,m} F}{RT}\nabla \phi_m \tag{61}$$

where $D_{i,m}$ and $c_{i,m}$ are the diffusion coefficient and concentration, respectively, of species i in the membrane. ϕ_m denotes the electrical potential in the membrane.

The total current density flowing through the membrane arises from the flux of all ionic species across the membrane. At any time, the membrane contains both mobile ionic charge carriers and charged functional groups fixed into its structure (e.g., sulfonic acid groups in Nafion 117 ion exchange membranes). As is the case elsewhere in the system, local electroneutrality is assumed to hold at every location within the membrane. When these conditions are combined with the requirement that charge be conserved everywhere within the membrane, the following expressions are obtained:

$$\vec{\imath}_m = \sum_i z_i F \vec{N}_{i,m} \tag{62}$$

$$\nabla \cdot \vec{\imath}_m = 0 \tag{63}$$

$$z_f c_f + \sum_i z_i c_{i,m} = 0 \tag{64}$$

where z_f and c_f are the charge and concentration, respectively, of the fixed sulfonic acid groups present in the Nafion 117 ion exchange membrane.

7.3.5 Tank model

The negative and positive electrolyte tanks serve as reservoirs during the continuous operation of the Zn-Ce flow battery. These tanks are assumed to behave as CSTRs in which the electrolytes

become fully mixed immediately upon entry. Thus, the evolution of the concentration of species i in each tank can be described by the following ordinary differential equation:

$$V_{neg}\frac{dc_{i,neg}^{in}}{dt} = W_{cell}\left(\int_{outlet}(\vec{N}_{i,neg}\cdot\vec{n}_{neg})dL_e - \int_{intlet}(\vec{N}_{i,neg}\cdot\vec{n}_{neg})\,dL_e\right) \tag{65}$$

$$V_{pos}\frac{dc_{i,pos}^{in}}{dt} = W_{cell}\left(\int_{outlet}(\vec{N}_{i,pos}\cdot\vec{n}_{pos})dL_e - \int_{intlet}(\vec{N}_{i,pos}\cdot\vec{n}_{pos})\,dL_e\right) \tag{66}$$

where V_{neg} and V_{pos} are the volumes of the negative and positive electrolytes, respectively, $c_{i,neg}^{in}$ and $c_{i,pos}^{in}$ are the concentration of species i in the negative and positive electrolyte tanks, respectively, and W_{cell} is the out-of-plane thickness of the cell in the direction perpendicular to the *x-y* plane. L_e is the negative flow channel/positive electrode width, $\vec{N}_{i,neg}$ and $\vec{n}_{neg}$ are the molar flux of species i and normal vector at the boundary between the negative compartment and negative reservoir tank, respectively, and $\vec{N}_{i,pos}$ and $\vec{n}_{pos}$ are the molar flux of species i and normal vector at the boundary between the positive compartment and positive reservoir tank, respectively. The first and second terms of Eqn.(65) and (66) in the parenthesis on the right hand side correspond to the integration of the molar fluxes over the outlet and inlet boundary, respectively, of the negative and positive flow channels. It should be noted that Eqn.(65) and (66) are linked to the equations in the negative and positive compartment domains through the flux terms ($\vec{N}_{i,neg}$ and $\vec{N}_{i,pos}$) and concentration terms ($c_{i,neg}^{in}$ and $c_{i,pos}^{in}$) above that are evaluated at the boundaries between the compartments and reservoir tanks.

7.3.6 Initial and boundary conditions

The conditions at the various boundaries/interfaces in the system are shown schematically in Figure 7.2. The kinetics of the primary Zn/Zn^{2+} reaction at the negative electrode are given by the following Butler-Volmer equation:

$$i_{Zn} = i_{Zn,0}\left[\frac{c_{Zn}}{c_{Zn,ref}}\exp\left(\frac{\alpha_{a,Zn}n_{Zn}F}{RT}\eta_{Zn}\right) - \frac{c_{Zn^{2+},s}}{c_{Zn^{2+},bulk}}\exp\left(-\frac{\alpha_{c,Zn}n_{Zn}F}{RT}\eta_{Zn}\right)\right] \quad (67)$$

$$i_{Zn,0} = Fk_{neg}^{0}{c_{Zn}}^{\alpha_{a,Zn}}{c_{Zn^{2+},s}}^{\alpha_{c,Zn}} \quad (68)$$

In Eqn.(67), $c_{Zn^{2+},s}$ is the Zn^{2+} concentration at the negative electrode surface and $c_{Zn^{2+},bulk}$ is the bulk Zn^{2+} concentration in the negative electrolyte. c_{Zn} is the surface density of the zinc deposit on the negative electrode (in units of mol/m^2), $c_{Zn,ref}$ is the reference zinc surface density (set to be 1 mol/m^2) and n_{Zn} is the number of electrons transferred for each Zn converted by the Zn/Zn^{2+} reaction (i.e., $n_{Zn} = 2$). $\alpha_{a,Zn}$ and $\alpha_{c,Zn}$ are the transfer coefficients of the Zn/Zn^{2+} reaction in the anodic and cathodic directions, respectively. $i_{Zn,0}$ is the exchange current density of the Zn/Zn^{2+} reaction expressed by Eqn.(68). In this equation, F is the Faraday constant, R is the universal gas constant, T is the temperature of the system and k_{neg}^{0} is the rate constant of negative electrode reaction.[39] η_{Zn} and E_{Zn}^{eq} are the overpotential and equilibrium potential, respectively, of the Zn/Zn^{2+} reaction calculated by the following equations:

$$\eta_{Zn} = E_{neg} - E_{Zn}^{eq} = \phi_{s,neg} - \phi_{e,neg} - E_{Zn}^{eq} \quad (69)$$

$$E_{Zn}^{eq} = E_{Zn}^{0} + \frac{RT}{n_{Zn}F}\ln\left(\frac{c_{Zn^{2+},bulk}}{a_{Zn}}\right) \quad (70)$$

where E_{Zn}^{0} is the standard potential of the Zn/Zn(II) reaction. $\phi_{s,neg}$ and $\phi_{e,neg}$ are the negative electrode and electrolyte potential. a_{Zn} is the activity of zinc metal that has a value of 1 since it is a pure phase.

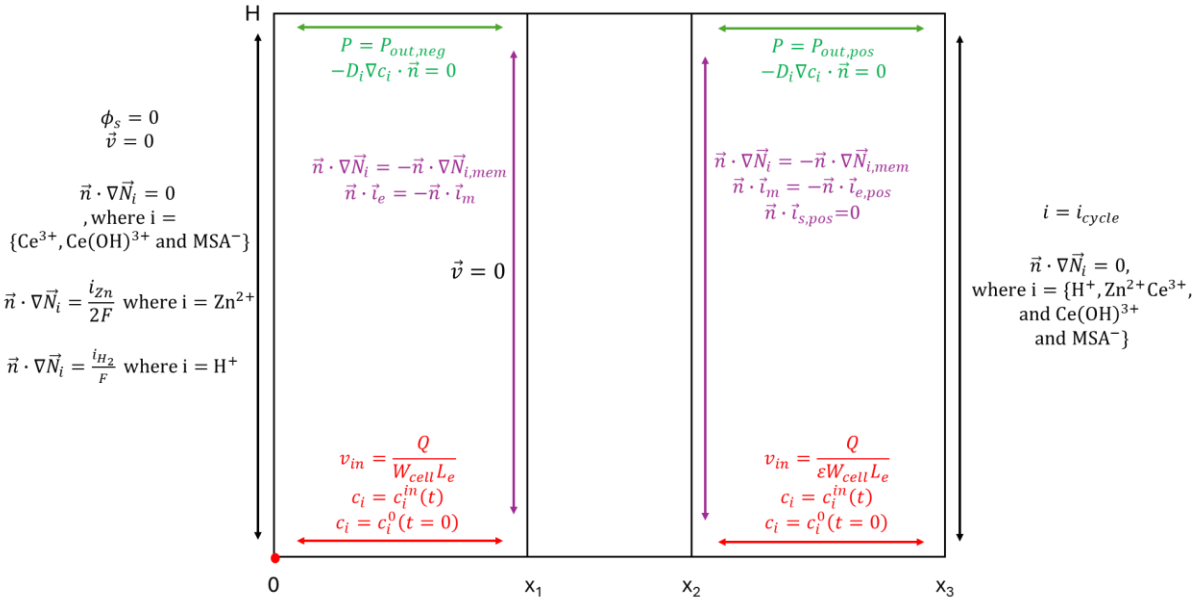


Figure 7.2. Boundary conditions applied to the Zn-Ce redox flow battery model.

The current density for the hydrogen evolution reaction at the surface of the negative electrode during battery charge is obtained as follows:

$$i_{H_2} = -i_{H_2,0}\left[\frac{c_{H^+,s}}{c_{H^+,bulk}}\exp\left(-\frac{\alpha_{H_2}F}{RT}\eta_{H_2}\right)\right] \tag{71}$$

where $c_{H^+,s}$ is the H^+ concentration at the surface of the negative electrode, $c_{H^+,bulk}$ is the bulk H^+ concentration in the negative electrolyte, α_{H_2} is the transfer coefficient for the HER and η_{H_2} is the overpotential for the HER calculated from:

$$\eta_{H_2} = \phi_{s,neg} - \phi_{e,neg} - E_{H_2}^{eq} \tag{72}$$

where $E_{H_2}^{eq}$ is the equilibrium potential for the HER given in Table 7.3. The anodic direction of the HER is neglected in Eqn.(71) above since this is an irreversible reaction. Similar to the OER on the positive electrode, the HER is also considered to be kinetically controlled.[193,194]

At the negative electrode ($x = 0$) and negative electrolyte/membrane interface ($x = x_1$), the no-slip condition is applied:

$$\vec{v} = 0 \tag{73}$$

Since the Zn^{2+} and H^+ react on the negative electrode surface at $x = 0$, the boundary conditions for Zn^{2+} and H^+ are:

$$\vec{n} \cdot \nabla \vec{N}_i = \frac{i_{Zn}}{2F}, for\ Zn^{2+} \tag{74}$$

$$\vec{n} \cdot \nabla \vec{N}_i = \frac{i_{H_2}}{F}, for\ H^+ \tag{75}$$

For species that do not participate in the electrode reactions (i.e. Ce^{3+}, $CeOH^{3+}$ and MSA^-) the molar flux on the negative electrode surface at $x = 0$ is given by

$$\vec{n} \cdot \vec{N}_i = 0 \tag{76}$$

Since the electrode reactions on the positive side occur in the whole domain rather than on the boundary, Eqn.(76) applies for all the species in the system at $x = x_3$.

During battery operation, a zero electric potential is specified at the negative current collector at $x = 0$ and a galvanostatic current condition is applied to the current collector of the positive electrode at $x = x_3$. Therefore, the following boundary condition is applied:

$$\phi_s(0, y, t) = 0 \tag{77}$$

The value of the potential $\phi_s(x_3, y, t)$ at the positive current collector is unknown and determined by numerical solution of the model equations.

At the inlets of the negative flow channel ($0 < x < x_1, y = 0$) and positive electrode ($x_2 < x < x_3, y = 0$), the flow rate of the electrolytes entering each half-cell and concentration of species i are given as follows:

$$v(x, 0, t) = v_{in,neg} = \frac{Q_{neg}}{W_{cell}L_e}, \qquad c_{i,neg}(x, 0, t) = c_{i,neg}^{in}(t) \tag{78}$$

$$v(x, 0, t) = v_{in,pos} = \frac{Q_{pos}}{\varepsilon_{pos}W_{cell}L_e}, \qquad c_{i,pos}(x, 0, t) = c_{i,pos}^{in}(t) \tag{79}$$

where Q_{neg} and Q_{pos} are the volumetric flow rates of the negative and positive electrolytes, respectively, $W_{cell}L_e$ is the cross-sectional area of the inlet perpendicular to the flow of the electrolytes, and $c_{i,pos}^{in}(t)$ and $c_{i,neg}^{in}(t)$ are the concentrations of species i in the inlet to the positive and negative half-cell domains, respectively.

The pressure is specified to have a constant value $P_{out,neg}$ and $P_{out,pos}$ at both outlets (($0 < x < x_1, y = H$) and ($x_2 < x < x_3, y = H$)). The concentration gradient of species i in the direction normal to the boundary to the cell outlet at $y = H$ is zero since the electrolyte is assumed to be

fully developed and no further change in concentration occurs in the direction of flow. This leads to the following boundary conditions:

$$P(x, H, t) = P_{out,neg} \; and \; \nabla c_{i,neg} \cdot \hat{n}|_{y=H} = 0 \tag{80}$$

$$P(x, H, t) = P_{out,pos} \; and \; \nabla c_{i,pos} \cdot \hat{n}|_{y=H} = 0 \tag{81}$$

At each electrode/membrane interface, the continuity of the molar flux of species i ensures that

$$\hat{n} \cdot \vec{N}_i = -\hat{n} \cdot \vec{N}_m \tag{82}$$

Furthermore, the membrane is an electronic insulator so that

$$\hat{n} \cdot \vec{\imath}_{s,pos}\big|_{x=x_2} = 0 \tag{83}$$

On the other hand, the membrane is an ionic conductor so that continuity of ionic current exists across the negative electrolyte/membrane interface at $x = x_1$ and across the positive electrode/membrane boundaries at $x = x_2$, i.e.,

$$\hat{n} \cdot \vec{\imath}_{e,neg}\big|_{x=x_1} = -\hat{n} \cdot \vec{\imath}_m|_{x=x_1} \tag{84}$$

$$\hat{n} \cdot \vec{\imath}_m|_{x=x_2} = -\hat{n} \cdot \vec{\imath}_{e,pos}\big|_{x=x_2} \tag{85}$$

where $\vec{\imath}_{e,neg}$, $\vec{\imath}_m$ and $\vec{\imath}_{e,pos}$ are the total current densities flowing through the negative compartment, membrane and positive compartment, which are equal to each other.

Finally, the Donnan effect can be applied to relate the potential drop to the ratio of the concentrations of permeating species on the two sides of the electrolyte/membrane interfaces at $x = x_1$ and $x = x_2$, i.e.,

$$\phi_m(x_1, y, t) = \phi_{e,neg}\big|_{x=x_1} + \frac{RT}{z_i F} \ln\left(\frac{c_{i,neg}}{c_{i,m}}\Big|_{x=x_1}\right) \tag{86}$$

$$\phi_m(x_2, y, t) = \phi_{e,pos}\big|_{x=x_2} + \frac{RT}{z_i F} \ln\left(\frac{c_{i,pos}}{c_{i,m}}\Big|_{x=x_2}\right) \tag{87}$$

where $c_{i,neg}$, $c_{i,m}$ and $c_{i,pos}$ are the concentrations of species i in the negative compartment, membrane and positive compartment, respectively.

7.3.7 initial conditions

The initial concentration c_i^0 of each species i in the electrolyte at $\mathrm{t} = 0$ corresponds to the composition of fully discharged positive and negative electrolytes at the start of battery operation. The initial $CeOH^{3+}$ concentration in the positive electrolyte is set to a very small value of 0.001

mol/L since a numerical problem preventing solution of the model is encountered when an initial value of 0 mol/L is used. The values are listed in Table 7.1.

Table 7.1. Initial concentrations of various species

Symbol	Parameter	c_i^0 (mol/L)
$c^0_{H^+,neg}$	H^+ initial concentration, negative electrolyte	1
$c^0_{Zn^{2+},neg}$	Zn^{2+} initial concentration, negative electrolyte	1.5
$c^0_{Ce^{3+},neg}$	Ce^{3+} initial concentration, negative electrolyte	0
$c^0_{CeOH^{3+},neg}$	$CeOH^{3+}$ initial concentration, negative electrolyte	0
$c^0_{MSA^-,neg}$	MSA^- initial concentration, negative electrolyte	4
$c^0_{H^+,mem}$	H^+ initial concentration, membrane	2.5
$c^0_{Zn^{2+},mem}$	Zn^{2+} initial concentration, membrane	0.75
$c^0_{Ce^{3+},mem}$	Ce^{3+} initial concentration, membrane	0.4
$c^0_{CeOH^{3+},mem}$	$CeOH^{3+}$ initial concentration, membrane	0
$c^0_{MSA^-,mem}$	MSA^- initial concentration, membrane	4
$c^0_{H^+,pos}$	H^+ initial concentration, positive electrolyte	4
$c^0_{Zn^{2+},pos}$	Zn^{2+} initial concentration, positive electrolyte	0
$c^0_{Ce^{3+},pos}$	Ce^{3+} initial concentration, positive electrolyte	0.8
$c^0_{CeOH^{3+},pos}$	$CeOH^{3+}$ initial concentration, positive electrolyte	0.001
$c^0_{MSA^-,pos}$	MSA^- initial concentration, positive electrolyte	6.4
$c_{Zn,ref}$	Zinc solid reference concentration	1

7.3.8 Details concerning numerical solution of model

The geometric features of the flow battery investigated in the experimental study and described by the model are listed below in Table 7.2. Table 7.3 provides the numerical values of the transport properties, kinetic parameters, electrochemical parameters and membrane properties defined in the model.

Table 7.2 Geometric features and operating conditions of the Zn-Ce flow battery in this study

Symbol	Geometric Feature	Value
H	cell height	45 mm
L_e	negative flow channel/positive electrode width	6 mm
L_{PVE}	thickness of the PVE negative electrode	6 mm
L_m	membrane width	180 μm
W_{cell}	out-of-plane thickness	20 mm
V	volume of each electrolyte	3.0×10^{-5} m^3
a	volumetric area of positive electrode	150 m^{-1} [39]
ε_{pos}	porosity of positive electrode	0.758[a]
ε_m	porosity of membrane	0.1

$P_{out,neg}$	negative flow channel outlet pressure	0 Pa
$P_{out,pos}$	positive electrode outlet pressure	100 Pa[195]
T	operating temperature	323.15°K
Q	flow rate	66 mL/min
c_f	fixed charge site concentration in the membrane	1200 mol/m³ [196]
σ_e	electrical conductivity of positive electrode	2.0×10^6 S/m [39]
σ_{PVE}	electrical conductivity of PVE negative electrode	15.58 S/m [measured in this study]
σ_m	ionic conductivity of membrane	14.23 S/m [calculated using Eqn.(88)]
K	permeability of platinized-titanium mesh	7.1×10^{-8} m² [195]

[a]Data from the supplier.

Table 7.3. Values of electrochemical and mass transport parameters used in the model.

Symbol	Parameter	Value
$D_{Zn^{2+}}$	Zn^{2+} diffusion coefficient	1.165×10^{-9} m^2/s [197]
$D_{Ce^{3+}}$	Ce^{3+} diffusion coefficient	1.52×10^{-10} m^2/s [198]
$D_{CeOH^{3+}}$	$CeOH^{3+}$ diffusion coefficient	1.075×10^{-10} m^2/s [199]
D_{H^+}	H^+ diffusion coefficient	1.23×10^{-8} m^2/s [200]
D_{MSA^-}	MSA^- diffusion coefficient	2.378×10^{-9} m^2/s [201]
E^0_{Ce}	standard electrode potential for $Ce^{3+}/CeOH^{3+}$ reaction	1.639 V vs. SHE [37]
E^0_{Zn}	standard electrode potential for Zn/Zn^{2+} reaction	-0.757 V vs. SHE [202]
$E^0_{O_2}$	standard electrode potential for oxygen	1.21 V vs. SHE [202]
$E^0_{H_2}$	standard electrode potential for hydrogen	0 V vs. SHE [202]
$k^{\ 0}_{pos}$	rate constant for $Ce^{3+}/CeOH^{3+}$ reaction	4.13×10^{-4} m/s [39]
k^0_{neg}	rate constant for Zn/Zn^{2+} reaction	9.9×10^{-6} m/s [39]

$\alpha_{c,Ce}$	transfer coefficient for reduction of $CeOH^{3+}$ to Ce^{3+}	0.27 [203]
$\alpha_{a,Ce}$	transfer coefficient for oxidation of Ce^{3+} to $CeOH^{3+}$	0.33 [203]
$\alpha_{c,Zn}$	transfer coefficient for reduction of Zn^{2+} to Zn	0.5 [204]
$\alpha_{a,Zn}$	transfer coefficient for oxidation of Zn to Zn^{2+}	0.5 [205]
β_{H_2}	transfer coefficient for HER	0.5 [206]
β_{O_2}	transfer coefficient for OER	0.52 [207]
i_{O_2}	exchange current density for OER	5.08×10^{-6} A/m^2 [172]
$k_{m,Ce^{3+}}$	mass transfer coefficient for Ce^{3+} at positive electrode	3.41×10^{-5} m/s [calculated using Eqn.(54)]
$k_{m,CeOH^{3+}}$	mass transfer coefficient for $CeOH^{3+}$ at positive electrode	2.8×10^{-5} m/s [calculated using Eqn.(54)]

Table 7.4. Charge numbers of dissolved species and stoichiometric coefficients for the electrode reactions.

Species	Charge number	Stoichiometric coefficient (written in reduction form)			
		Reaction (1)	Reaction (2)	Reaction (3)	Reaction (4)
Zn^{2+}	2	-1	0	0	0
Ce^{3+}	3	0	1	0	0
$CeOH^{3+}$	3	0	-1	0	0
H^{+}	1	0	-1	-2	-4
MSA^{-}	-1	0	0	0	0

The ionic conductivity of the Nafion 117 membrane used in this study is determined via the following equation developed by Zawodzinski et al.[208]:

$$S[S/m] = (0.5139\lambda - 0.326)\exp\left[1268\left(\frac{1}{303} - \frac{1}{T}\right)\right] \quad (88)$$

In this expression, λ is the water content (in atoms water per sulfonic acid group) in the membrane and has a value of 22 atom-H_2O/sulfonate at temperatures in the range from 298°K to 363°K, which is applicable to our case where the operating temperature is 323°K.

The cell voltage is calculated by the following equation:

$$V_{cell} = E_{pos} - E_{neg} \pm |IR_{total}| = (\phi_{s,pos} - \phi_{e,pos}) - (\phi_{s,neg} - \phi_{e,neg}) \pm |IR_{total}| \qquad (89)$$

where R_{total} corresponds to the total ohmic resistance of the system associated with the electrodes, electrolytes, Nafion 117 ion exchange membrane and contact points. The R_{total} value for our bench-scale flow battery was measured previously in our laboratory by electrochemical impedance spectroscopy.[172] In Eqn.(89), the $+$ sign applies when the battery is undergoing charge and the $-$ is used during discharge.

The battery is operated under galvanostatic conditions and so the current density to the current collector of the positive electrode is constant and specified as follows:

$$i = i_{cycle} = \begin{cases} i_{app}, (During\ charge) \\ -i_{app}, (During\ discharge) \end{cases} \qquad (90)$$

The specific area of the positive electrode was determined to be 150 m^{-1} in the previous modelling study on this Zn-Ce RFB by Amini and Pritzker.[39] This value was obtained by fitting the model to experimental data from the battery charge-discharge cycles when operated at a current density of 25 mA/cm^2 and 323°K and a charge duration of 1 hour. The fitted value of 150 m^{-1} is reasonable since the positive electrode is a 3D mesh substrate.

The system of equations given in section 7.3 defining the operation of the Zn-Ce redox flow battery has been numerically solved using the COMSOL 5.4 multi-physics software package which utilizes the finite-element method. Meshes with 2000 elements in each compartment and 150 elements in the membrane are used to ensure sufficient accuracy of the numerical solution. These rectangular-shaped elements are not equally sized and chosen to be smaller near the various boundaries and interfaces in the model to provide more resolution. The relative tolerance is set to 5×10^{-3} and the absolute tolerance to 10^{-3}. The total time to simulate 5 charge-discharge cycles (with

a charge duration of 1 hour each cycle) required approximately 0.5 hours on an AMD Ryzen 7 4800HS CPU with 16 GB RAM. The calculations were done by setting the total current density to a fixed value and then solving the model for quantities such as the fluid velocity, concentrations of the various species, electrolyte potential, membrane potential and molar fluxes at each position as well as the partial current densities, cell voltage, potential at the positive current collector and electrode potentials.

7.4 Results and Discussion

7.4.1 Model validation

The charge-discharge cycles have been conducted with a charge duration of 1 hour at a current density of 25 mA/cm^2 and 323°K, while both the positive and negative electrolytes are being circulated through the battery at a flow rate of 66 mL/min. At the outset of the cycles, the battery is in its fully discharged state in which the negative electrolyte contains 1.5 mol/L Zn^{2+} in 1 mol/L MSA and positive electrolyte contains 0.8 mol/L Ce^{3+} in 4 mol/L MSA. It should be noted that only the first 5 charge-discharge cycles are used to fit the model to the measured data because $CeOH^{3+}$ began to precipitate beginning during the 6th cycle and effectively reduced the total amount of Ce available for the positive reaction when 4 mol/L MSA was used as the positive supporting electrolyte. Since the model does not account for the precipitation of $CeOH^{3+}$ in the positive electrolyte, it is obviously not appropriate to include cycles beyond the 5th one in the data set used to fit the model.

The model is fitted to experimental data obtained in this study using a manual procedure outlined below and used to obtain numerical values of the $i_{H_2,0}$ and the diffusion coefficients of the 5 species in the membrane. The numerical values of these quantities obtained by fitting the model to the experimental data are presented in Table 7.5 shown below. The initial guesses of the $i_{H_2,0}$ are based on the work by Amini and Pritzker and the initial guesses of the diffusion coefficients in the membrane are set to be the same as the corresponding values in free electrolyte.[39] An estimate for $i_{H_2,0}$ is first determined using the experimental data of the evolution of the cell voltage and electrode potentials during the 5 charge-discharge cycles without adjusting the values of the

diffusion coefficients. When an approximate $i_{H_2,0}$ value is obtained, the model is then fitted to the measured values of the concentrations of the various ions in both the positive and negative electrolytes obtained at the end of each of the 5 charge-discharge cycles to determine the diffusion coefficients. The estimate of $i_{H_2,0}$ is readjusted to a new value (which turns out to be very similar to the original fitted value) so that the computed cell voltages and electrode potentials over the course of the 5 charge-discharge cycles are still in agreement with the experimental data.

A comparison of the model-fitted cell voltage and negative and positive electrode potentials (blue) during 5 consecutive charge-discharge cycles with the experimental data (red and black) under the same operating conditions is shown in Figure 7.3. These results show excellent agreement between the model and experimental data over the majority of the experimental run.

Table 7.5. Model parameters obtained in this study by fitting model to the experimental data

Symbol	Parameter	Value
i_{H_2}	exchange current density for HER	1.79×10^{-5} A/m^2 [Fitted]
$D^m_{Zn^{2+}}$	Zn^{2+} diffusion coefficient in membrane	6.45×10^{-11} m^2/s [Fitted]
$D^m_{Ce^{3+}}$	Ce^{3+} diffusion coefficient in membrane	3.60×10^{-12} m^2/s [Fitted]
$D^m_{CeOH^{3+}}$	$CeOH^{3+}$ diffusion coefficient in membrane	2.55×10^{-12} m^2/s [Fitted]
$D^m_{H^+}$	H^+ diffusion coefficient in membrane	2.33×10^{-10} m^2/s [Fitted]
$D^m_{MSA^-}$	MSA^- diffusion coefficient in membrane	7.52×10^{-11} m^2/s [Fitted]

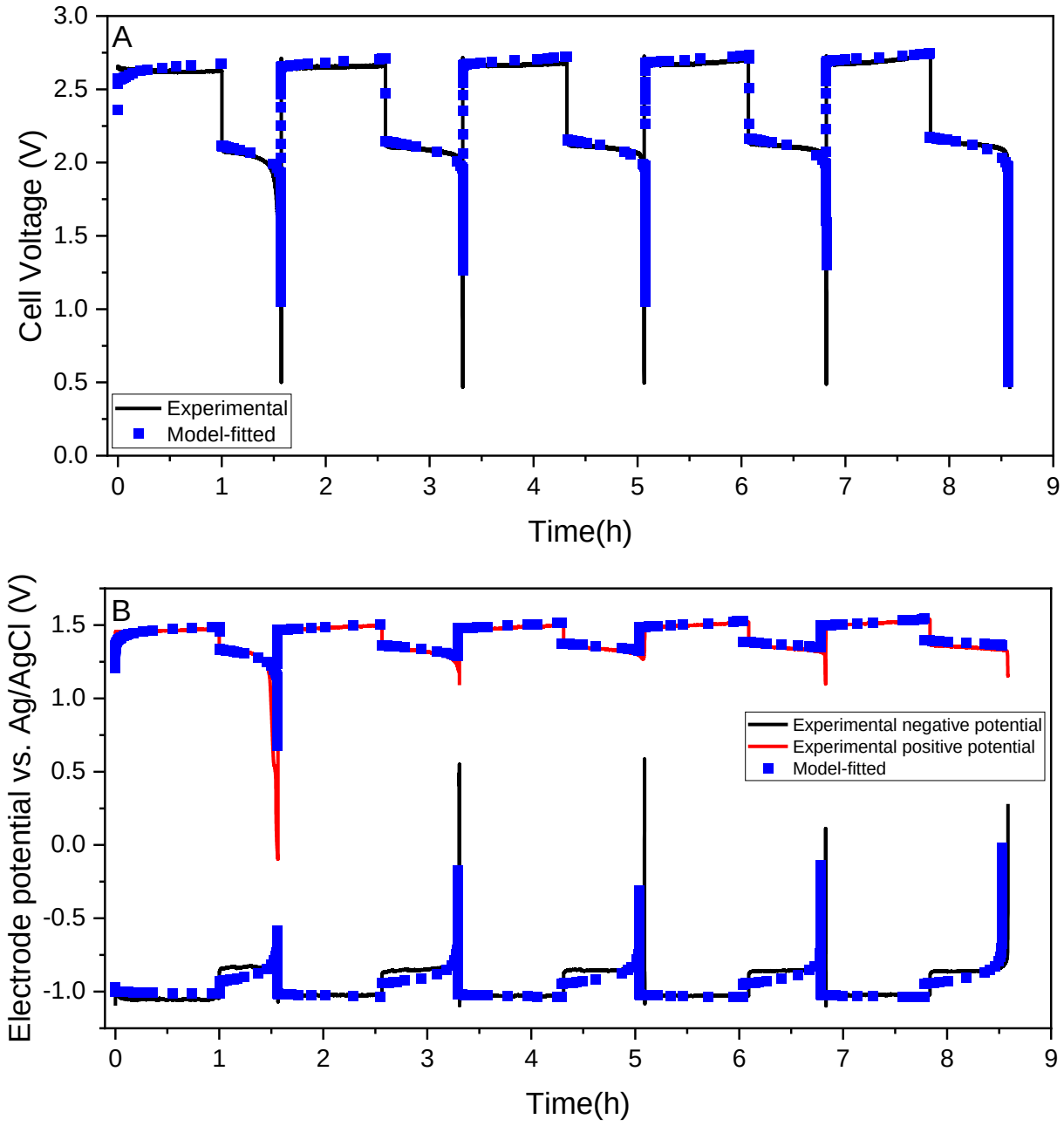


Figure 7.3. Comparison of model-fitted values of cell voltage (A) and electrode potential (B) with experimental measurements over 5 consecutive charge-discharge cycles operating at a current density of 25 mA/cm^2, 323°K temperature, negative and positive electrolyte flow rates of 66 mL/min and charge duration of 1 hour. The negative electrolyte initially contains 1.5 mol/L Zn^{2+} in 1 mol/L MSA and the positive electrolyte contains 0.8 mol/L Ce^{3+} in 4 mol/L MSA.

The exchange current density for HER is found to be 4.20×10^{-5} A/m^2 when the model is fitted for only the first charge-discharge cycle, which is higher than the value of 1.79×10^{-5} A/m^2 obtained when fitted to the experimental data over the subsequent 4 cycles. For comparison, a similar value of 2.21×10^{-5} A/m^2 for $i_{H_2,0}$ was obtained by Amini and Pritzker in their modeling study.[39] The first cycle serves as a preconditioning step that increases the roughness of the negative electrode surface and tends to exhibit a lower columbic efficiency compared to the following cycles, as discussed previously.[38,197] The higher $i_{H_2,0}$ during the first cycle compared to the subsequent cycles has also been reported in other modeling studies of zinc-based batteries.[209] Therefore, the $i_{H_2,0}$ determined from the first cycle should not be used when describing the battery overall performance during later cycles.

As discussed in Chapter 5, we measured the concentrations of the various species in the two compartments during battery operation. Due to its high concentration in both electrolytes, H^+ should be the primary ionic charge carrier in the system and move to the negative side during battery charge and back to the positive side during battery discharge. However, due to the fact that the Nafion membrane is not perfectly selective to H^+ ions, concentration gradients and the requirement to maintain electroneutrality drive both a larger amount of H^+ beyond the minimum just to meet the demand from the applied current as well as crossover by Zn^{2+}, Ce^{3+}, $CeOH^{3+}$ and MSA^- through the membrane. These phenomena are detrimental to the efficiency of Zn-Ce RFB, which leads to the imbalance of electroltyes and capacity fade over repeated cycling. As discussed in Chapter 5, the net crossover of H^+ from the positive electrolyte enhances the HER on the negative side and eventually results in the precipitation of $CeOH^{3+}$ on the positive side due to the reduction in the H^+ concentration when 4 mol/L MSA is used as the supporting electrolyte.[32] Moreover, the decrease of the Zn^{2+} and Ce^{3+}/$CeOH^{3+}$concentrations in their respective compartments caused by this crossover reduces the overall battery efficiency.

As shown in Figure 7.4A – E, comparison of the experimental and model-fitted Zn^{2+} and total Ce concentrations in the positive and negative electrolytes and the H^+ concentration in the negative electrolyte after each charge-discharge cycle shows good agreement. Since the colometric titration method described in the Experimental section could not be used to measure the H^+ concentration in the positive electrolyte due to its yellowish colour, only a comparison of the H^+ concentration in the negative electrolyte is included in Figure 7.4E. Figure 7.4F shows the H^+ concentration in

the positive electrolyte determined from the model. It should be noted that experimental data for the total Ce concentration in the negative electrolyte at the end of the first 2 cycles are not shown in the plot simply because the concentration of Ce in the negative electrolyte is too low and below the detectable limit of the ICP-OES method. Some discrepancy between the model-fitted and experimental values of the total Ce concentration in the negative electrolyte at the end of cycles 3 and 4 might be due to errors associated with the ICP-OES measurements since the Ce levels are very low and close to the detection limit. In addition, the model does not account for the osmosis of a small amount of water across the membrane during battery operation. This would not affect the accuracy of the model in the case of the relatively high Zn^{2+} concentrations in the negative and positive electrolytes, Ce concentration in the positive electrolyte and H^{+} concentration in the negative electrolyte, but could affect the accuracy of the very low Ce concentrations on the positive side.

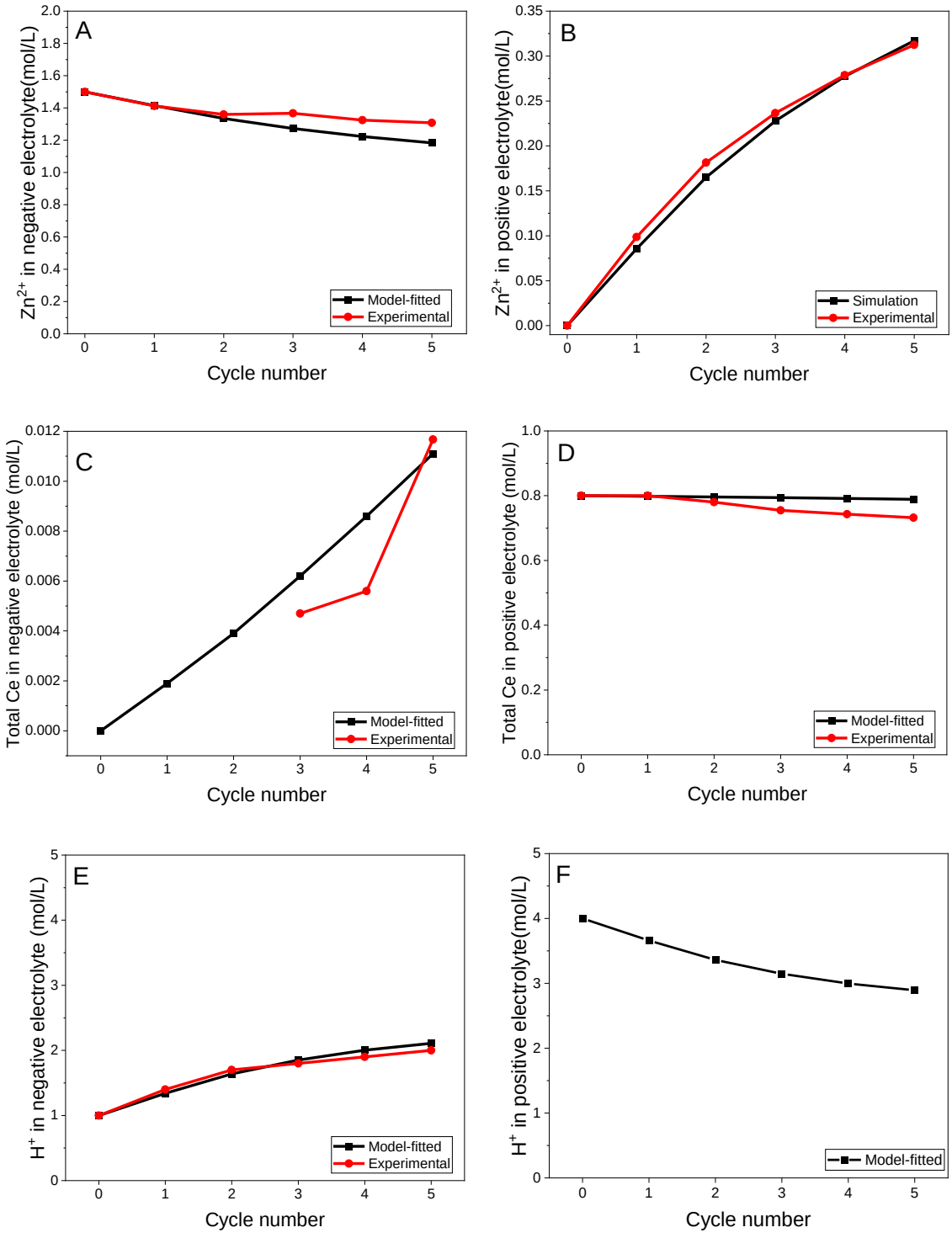


Figure 7.4. Comparison of experimental and model-fitted concentrations of (A) Zn^{2+} in the negative electrolyte, (B) Zn^{2+} in the positive electrolyte, (C) total Ce in the negative electrolyte, (D) total Ce in the positive electrolyte, (E) H^+ in the negative electrolyte. The H^+ concentration in the positive electrolyte as determined by the model is shown in (F).

The excellent agreement between the experimental and model-fitted data presented here indicates that the model can reliably compute the cell voltage, positive and negative electrode potentials and concentrations of the various species in the two compartments of the Zn-Ce battery during charge-discharge cycling. Based on this result, we can use the validated model to provide insight into various phenomena occurring in the Zn-Ce system that cannot be directly measured and to predict the behaviour of this battery under different operating conditions.

7.4.2 Use of validated model to investigate battery behaviour

With the model now validated, it can be used to investigate the battery behaviour in more detail and provide further insight into phenomena that cannot be directly observed or measured during operation.

The model is able to successfully capture the observation that the battery operation is limited by the positive half-cell reaction during the 1st cycle, but shifts to control by the negative half-cell reaction from the 2nd to the 5th cycle. As shown in Figure 7.3B, the positive electrode potential drops rapidly near the end of battery discharge in the 1st cycle, indicating the depletion of reactant $CeOH^{3+}$ ions near the surface of the positive electrode. During the subsequent cycles, an abrupt rise of the negative electrode potential is observed near the end of discharge, indicating that the zinc layer deposited during battery charge has been completely removed by the end of battery discharge and that some $CeOH^{3+}$ still remains unreacted in the positive electrolyte. This finding is supported by Figure 7.5A and B which show the surface density of the deposited zinc layer on the negative electrode and surface concentrations of Ce^{3+} and $CeOH^{3+}$ ions over time during the 5 cycles. During battery charge, Zn^{2+} in the negative electrolyte is reduced to zinc metal on the negative electrode surface, whereas the Ce^{3+} ions are oxidized to $CeOH^{3+}$ ions at the positive electrode surface. A surface density of ~ 0.16 mol/m^2 zinc metal remains on the negative electrode at the end of the 1st discharge (Figure 7.5A), whereas the surface $CeOH^{3+}$ concentration has dropped to 0 mol/L (Figure 7.5B), although the bulk $CeOH^{3+}$ concentration still remains at ~0.1 mol/L in the positive electrolyte (Figure 7.5C). At this point, it is the complete depletion of $CeOH^{3+}$ at the electrode surface that causes the positive electrode potential to abruptly drop (Figure 7.3B) and the criterion for termination of discharge (cell voltage < 0.5 V) to be reached. This is an

indication that mass transfer of $CeOH^{3+}$ from the bulk to the electrode surface is the limiting step during the first discharge cycle and that improvement of its mass transfer could potentially boost battery performance. However, this situation soon changes. Both the HER and OER side reactions occur during charge, but HER occurs to a much greater extent, as shown in Figure 7.5E and F. Since these reactions are irreversible, this generates an imbalance in which the stoichiometric amount of Zn deposited on the negative electrode during charge is less than the amount of Ce^{3+} converted to $CeOH^{3+}$ at the positive electrode. The negative electrode was stripped of Zn before the concentration of $CeOH^{3+}$ on the positive side was sufficiently reduced to cause mass transfer limitation, which eventually leads to the negative reaction being the limiting reaction during discharge. In fact, by the 2^{nd} cycle, it has become more dominant than $CeOH^{3+}$ mass transfer to the positive electrode so that all of the zinc deposit has been removed and the surface $CeOH^{3+}$ concentration at the positive electrode no longer drops to zero during discharge (Figure 7.5A and B). This trend holds as the operation proceeds through the subsequent cycles, leading to a gradual (and essentially linear) rise in both the bulk and surface $CeOH^{3+}$ concentrations and concomitant drop in the Ce^{3+} concentration at the end of each cycle. This finding from the model mirrors experimental observations reported in Chapter 4. The changes in the H^+ concentrations in both the negative and positive electrolytes obtained from the model are also plotted in Figure 7.5D. These show the steady decrease of the H^+ concentration in the positive electrolyte and rise in the negative electrolyte.

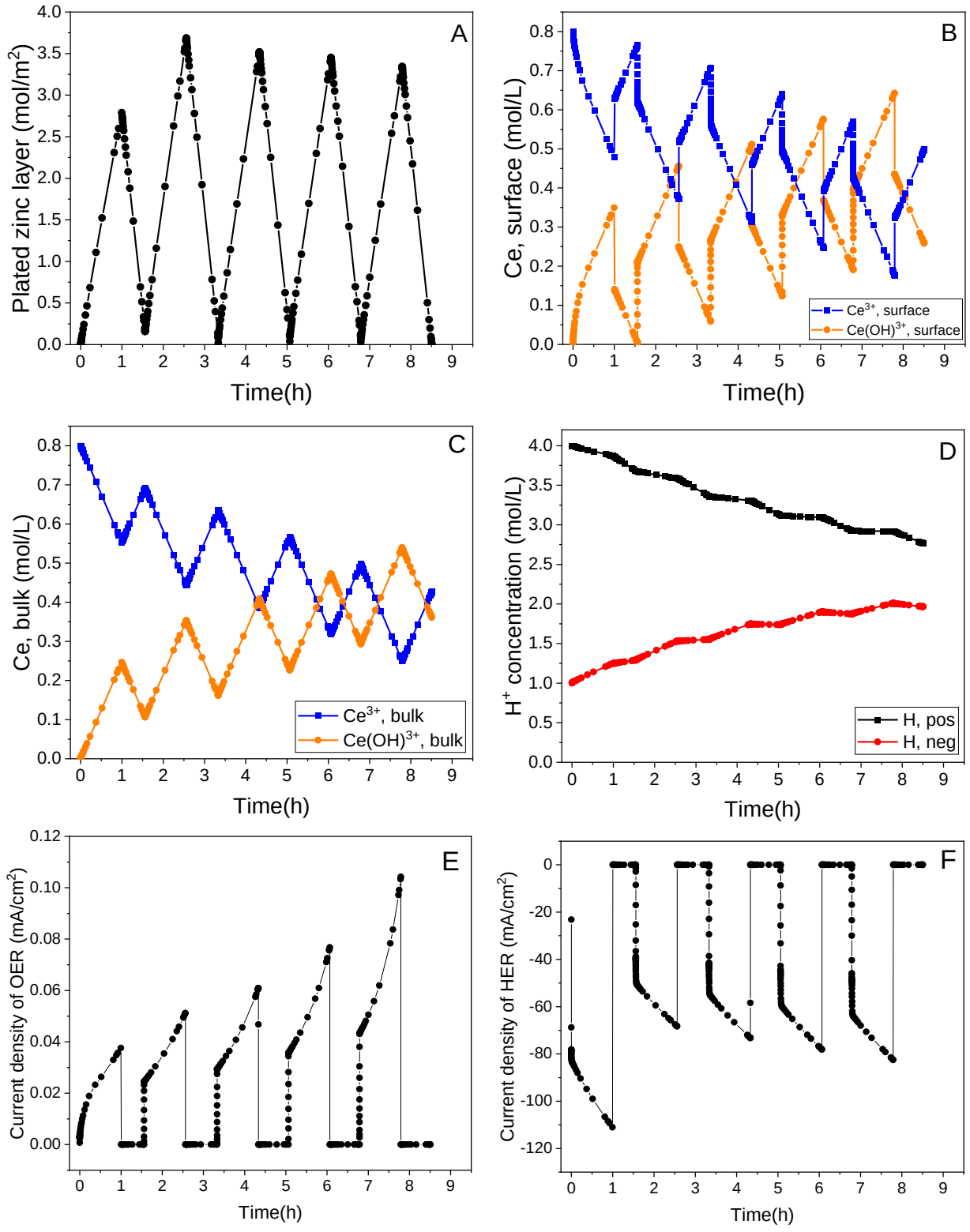


Figure 7.5. Variation of the (A) surface density of zinc deposit on the negative electrode, (B) surface Ce^{3+} and $CeOH^{3+}$ concentrations in the positive electrolyte, (C) bulk Ce^{3+} and $CeOH^{3+}$ concentrations in the

positive electrolyte, (D) H^+ concentrations in the positive and negative electrolytes, (E) current density of OER and (F) current density of HER over the 5 consecutive charge-discharge cycles. The charge-discharge cycles were conducted at a current density of 25 mA/cm^2, temperature of 323°K and charge duration of 1 hour and positive and negative electrolyte flowrates of 66 mL/min. The negative electrolyte contains 1.5 mol/L Zn^{2+} in 1 mol/L MSA and the positive electrolyte contains 0.8 mol/L Ce^{3+} in 4 mol/L MSA at the start of the 1st cycle.

7.4.3 Effect of applied current density on molar fluxes

The model has been used to investigate the behaviour of the Zn-Ce RFB during charge-discharge cycles at different current densities ranging between 5 and 70 mA/cm^2. The simulations are carried out such that the charge duration is kept fixed at 1 hour for all current densities. To better understand the effect of current density on the mechanisms driving the transport of each species across the membrane, the breakdown of the average overall molar flux of each species across the membrane according to diffusion and migration during the 3rd charge-discharge cycle is plotted in Figure 7.6. No contribution to the flux across the membrane comes from convection due to the assumption that the velocity of the electrolyte at the electrolyte/membrane interfaces is zero. Note that a positive molar flux signifies that ions are transported from the negative to the positive half-cell through the membrane, whereas a negative flux indicates transport in the reverse direction. For our purposes here, the fluxes at a single instant during charge (i.e., 30 minutes after the start of charge during the 3rd cycle) and a single instant during discharge (i.e., 30 minutes after the start of discharge during the 3rd cycle) are shown here. Similar results are obtained if the analysis is based on the average molar fluxes calculated over the entire 3rd cycle.

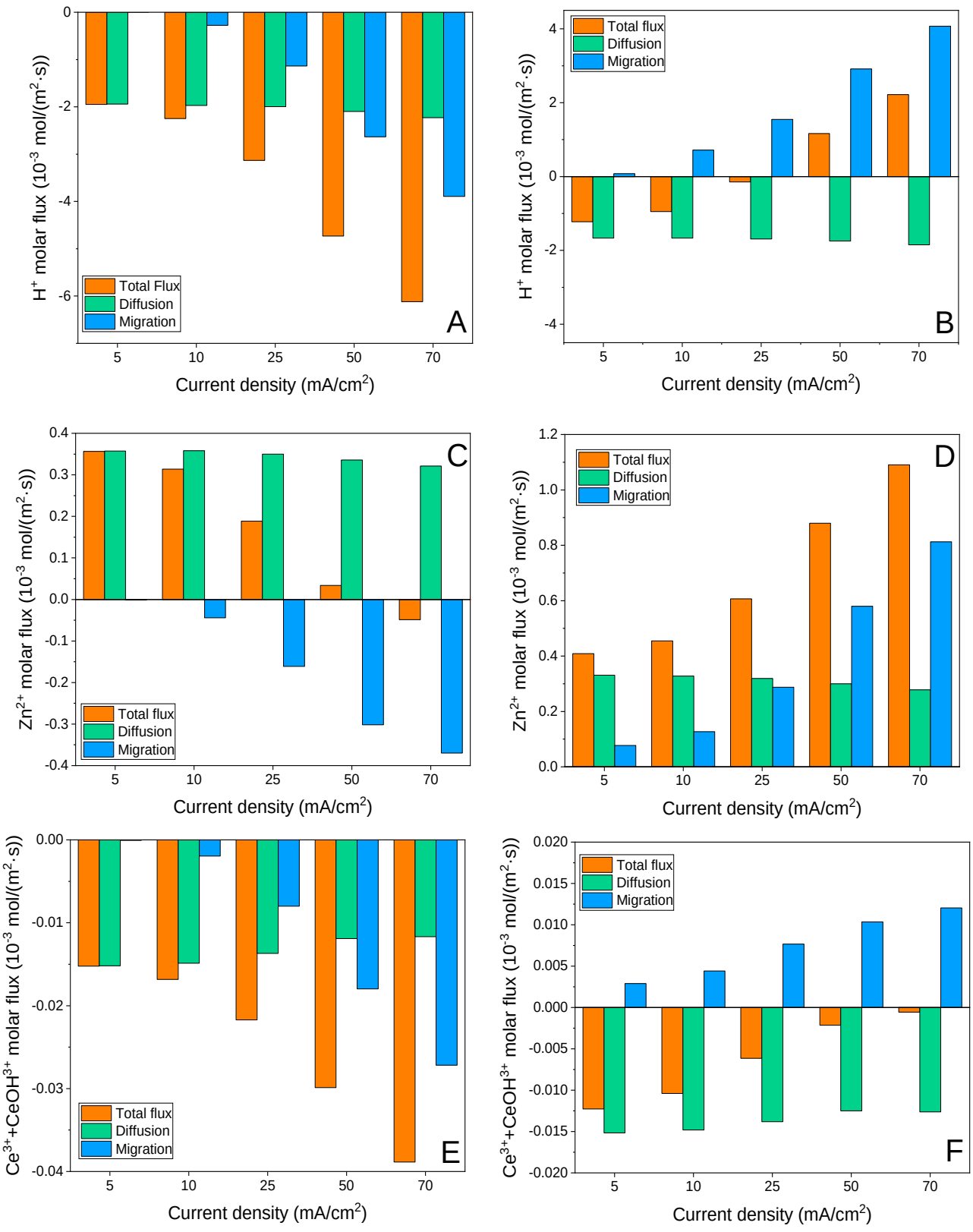

A
B
C
D
E
F
Total Flux
Total flux
Diffusion
Migration
H+ molar flux (10-3 mol/(m2·s))
Zn2+ molar flux (10-3 mol/(m2·s))
Ce3++CeOH3+ molar flux (10-3 mol/(m2·s))
Current density (mA/cm2)
5
10
25
50
70

Figure 7.6. Breakdown of computed diffusional and migrational molar fluxes of each species across the membrane obtained at t = 30 min during charge (A, C and E) and t = 30 min during discharge (B, D and F) of the 3rd cycle computed using the model for battery operation at 323°K, charge duration of 1 hour and positive and negative electrolyte flowrates of 66 mL/min. The negative electrolyte contains 1.5 mol/L Zn^{2+} in 1 mol/L MSA and the positive electrolyte contains 0.8 mol/L Ce^{3+} in 4 mol/L MSA at the start of the 1st cycle.

As expected, the net flux of H^+ is in the direction of the negative electrode during battery charge regardless of the current density applied (Figure 7.6A). The diffusional flux of H^+ across the membrane remains almost constant regardless of the current density because the concentration gradient driving diffusion and the composition of the electrolytes at the start of battery operation are the same. Although the bulk composition of the electrolytes changes during subsequent cycles, it is small enough not to significantly affect the diffusion flux. Migration drives H^+ in the same direction as diffusion during charge, although its magnitude increases more strongly with the applied current density than does diffusion since it is proportional to the electric field. As a result, the overall flux of H^+ from the positive to the negative electrolyte during battery charge increases more than three-fold as the current density is raised from 5 mA/cm^2 to 70 mA/cm^2. When the battery operation shifts to discharge and the cell polarity changes, the effect of the current density on the overall flux of H^+ becomes more complicated since diffusion and migration of H^+ now operate in opposite directions (Figure 7.6B). Diffusion still drives H^+ from the positive electrolyte to the negative electrolyte, as it does during charge, since the concentration gradient is not affected by the change in polarity. On the other hand, the migrational flux changes with the cell polarity to drive H^+ from the negative side to the positive side. As during charge, the magnitude of the current density has little effect on the diffusional flux, but a large effect on the migrational flux. The combination of these effects results in diffusional flux dominating at low current densities and the net flux of H^+ being directed toward the negative side and the migrational flux being dominant at high current densities so that the net direction of H^+ is reversed toward the positive side. The change in the direction of the flux occurs when the applied current density becomes slightly larger than 25 mA/cm^2. It is important to note that at high current densities the magnitude of the net flux of H^+ toward the positive side during battery discharge remains smaller than the net flux toward

the negative side during battery charge, leading to the gradual increase of the H^+ concentration in the negative electrolyte and the negative impacts discussed previously.

When the battery is operated at higher current density, the final H^+ concentration in the negative electrolyte at the end of the 5 cycles becomes lower, as shown in Figure 7.7. For example, the final concentration of H^+ is 1.84 mol/L when the battery is operated at a current density of 70 mA/cm^2, which is lower than 2.01 mol/L when the applied current density is 5 mA/cm^2. Since the net direction of the H^+ flux during charge is opposite from that during discharge, the difference of the H^+ concentration at the end of each charge and discharge becomes more obvious when the battery is operated at higher current densities (i.e., 50 and 70 mA/cm^2 shown in blue and red in Figure 7.7). Compared to the magnitude of the Zn^{2+} and Ce fluxes across the membrane, the H^+ flux is much larger due to its much higher diffusivity and concentration in the cell. It should be noted that the charge duration instead of the state-of-charge of the battery are kept the same when operated at different current densities. Therefore, the number of Coulombs that pass through the battery is larger at higher current densities and smaller at lower current densities, which leads to different amounts of H^+ transferring across the membrane to maintain the electroneutrality of the system. This could potentially affect the composition of the electrolytes and the diffusion flux that driven by concentration gradient, although this effect is shown to be very small as shown in Figure 7.6.

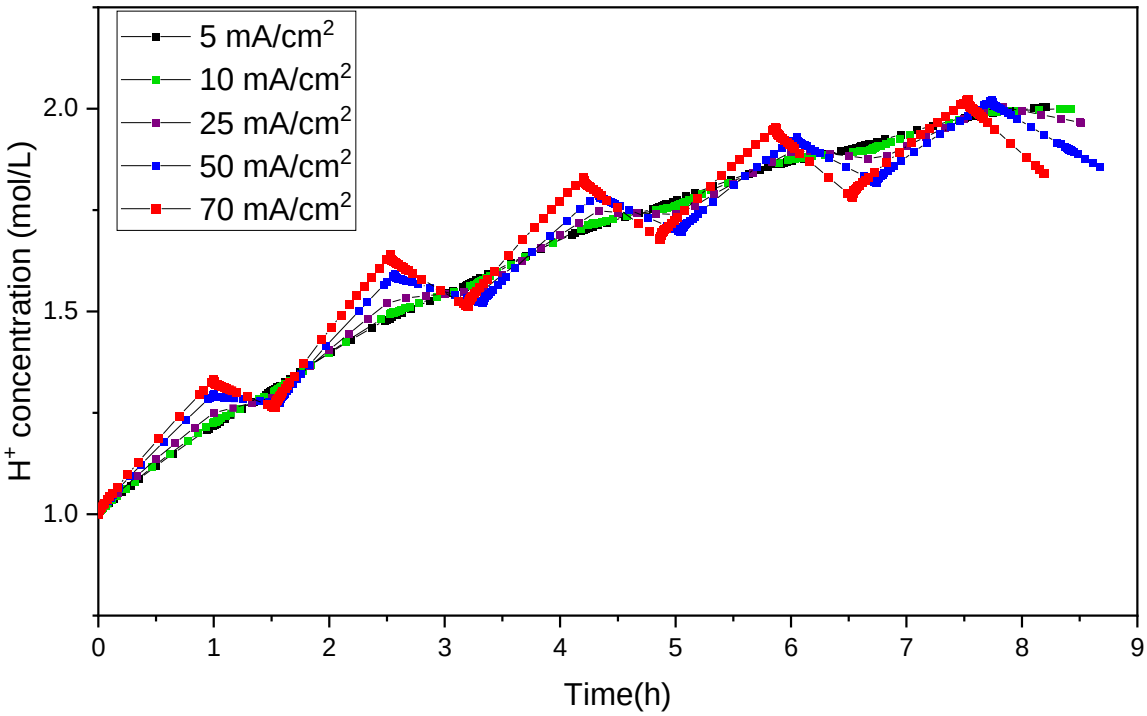


Figure 7.7. Variation of H^+ concentration in the negative electrolyte over 5 consecutive charge-discharge cycles when the Zn-Ce RFB is operated at different current densities.

As shown in Figure 7.6C and D, diffusion moves Zn^{2+} toward the positive electrode during both charge and discharge since the initial concentrations of Zn^{2+} in the negative and positive electrolytes are 1.5 mol/L and 0 mol/L, respectively. As is the case with the H^+ ions, migration moves Zn^{2+} ions toward the negative electrode during charge at a rate that increases with current density. Therefore, the net flux of Zn^{2+} during charge is toward the positive electrolyte until the current density reaches ~70 mA/cm^2 whereupon the migrational flux exceeds the diffusional flux and the direction of Zn^{2+} is reversed. During battery discharge, the situation is more straightforward since diffusion and migration operate in the same direction and transport Zn^{2+} toward the positive side. The initial concentration of Ce^{3+} is 0.8 mol/L in the positive electrolyte and 0 mol/L in the negative electrolyte. Subsequently, diffusion drives both Ce species toward the negative electrolyte during both battery charge and discharge (Figure 7.6E and F). Migration also moves both Ce^{3+} and $CeOH^{3+}$ in the same direction during battery charge, but in the opposite direction during discharge. Consequently, these species are driven to the negative side during

charge regardless of the applied current density. During battery discharge at current densities up to 70 mA/cm^2, the magnitude of the migrational flux always remains less than that of diffusion so that these species always move from the positive side to the negative side.

Taken together, these results show that the applied current density affects the magnitude of the net flux of the various species differently. In cases where diffusion and migration operate in the same direction (i.e., H^+ during charge, Zn^{2+} during discharge and Ce^{3+} and $CeOH^{3+}$ during charge), the magnitude of the overall flux increases with current density. On the other hand, when diffusion and migration oppose each other (i.e., H^+ during discharge, Zn^{2+} during charge and Ce^{3+} and $CeOH^{3+}$ during discharge), increasing the current density tends to reduce the magnitude of the overall flux until high values are reached whereupon the flux reverses in direction and begins to rise in magnitude.

7.4.4 Effect of flow rate

The flow rates of the two electrolytes through the battery are important factors influencing its performance since they affect the concentration polarization by controlling the supply and removal of electroactive species between the electrode surface and bulk electrolyte. It should be noted that a change in the electrolyte flowrate affects the model in several ways. Obviously, it affects fluid flow directly through the Navier-Stokes equations and the Darcy's law (Eqns.(32) and (34)). Secondly, it influences the Nernst-Planck transport equations Eqn.(35) and (42) for the various species in the negative and positive electrolyte. Finally, the mass transfer of Ce^{3+} and $CeOH^{3+}$ to and from the Pt-Ti positive electrode depends on the electrolyte flowrate through Eqns.(54) – (57). Accordingly, we have used the validated model to investigate the effect of the electrolyte flowrate on the performance of the Zn-Ce RFB. Figure 7.8A shows the variation of the cell voltage during the 1st charge-discharge cycle when the battery is operating at 33 mL/min, 66 mL/min, 132 mL/min and 330 mL/min at an applied current density of 25 mA/cm^2. The experiments were conducted at 66 mL/min, so these flow rates correspond to 0.5f, f, 2f and 5f where f corresponds to the original flowrate. The volumetric flow rates of the positive and negative electrolytes were the same in both experiments and simulations. As shown in Figure 7.8A, the discharge time is reduced from 35.0 min to 26.1 min when the flow rate is decreased to half of the original value, corresponding to a

drop in the coulombic efficiency from 58.3% to 43.6%. Examination of the variation of the concentrations of the electroactive species during charge and discharge (Figure 7.8B and C) reveals that the reduction in the discharge time at the lowest flowrate is caused by complete depletion of $CeOH^{3+}$ at the positive electrode surface much earlier during discharge than at the other flowrates (compare the blue curve with the others in Figure 7.8C). A reduction in the flow rate leads to slower mass transfer of $CeOH^{3+}$ from the bulk to the electrode surface and therefore a lower surface concentration throughout the entire battery discharge. On the other hand, the amount of zinc deposited on the negative electrode surface is still abundant and available for battery discharge at the end of the cycle as shown in Figure 7.8D, indicating that the positive electrode reaction limits discharge during this 1st cycle. Although not shown here, it should be noted that a significant amount of $CeOH^{3+}$ (0.14 mol/L) remains in the bulk positive electrolyte at the end of discharge, indicating that the available capacity on the positive side has not been fully utilized at this low flowrate. The discharge capacity can be increased and higher efficiency attained if mass transfer of $CeOH^{3+}$ to the electrode surface is improved such as by raising the electrolyte flowrate. This is clearly shown when the flowrate is raised from 0.5f to f, 2f and 5f (compare black, red and green curves with blue curve in Figure 7.8A). As shown in Figure 7.8C, the $CeOH^{3+}$ surface concentration drops to zero by the end of discharge when the flowrate is 0.5f and f, but becomes non-zero when the flowrate reaches 2f and 5f, reflecting that the positive reaction no longer limits the discharge capacity. This effect is further confirmed by examination of the effect of the flowrate on the surface density of the zinc deposit on the negative electrode in Figure 7.8D. Some zinc deposit remains at the end of discharge at flowrates of 0.5f and f, but not at 2f and 5f, which signifies that the negative reaction now limits discharge at the higher flowrates. However, examination of Figure 7.8A shows that the improvement in the columbic efficiency when the flowrate is raised from f to 2f is relatively small and negligible with a further increase to 5f, reflecting that the reactions at the negative electrode are kinetically controlled and not limited by mass transfer.

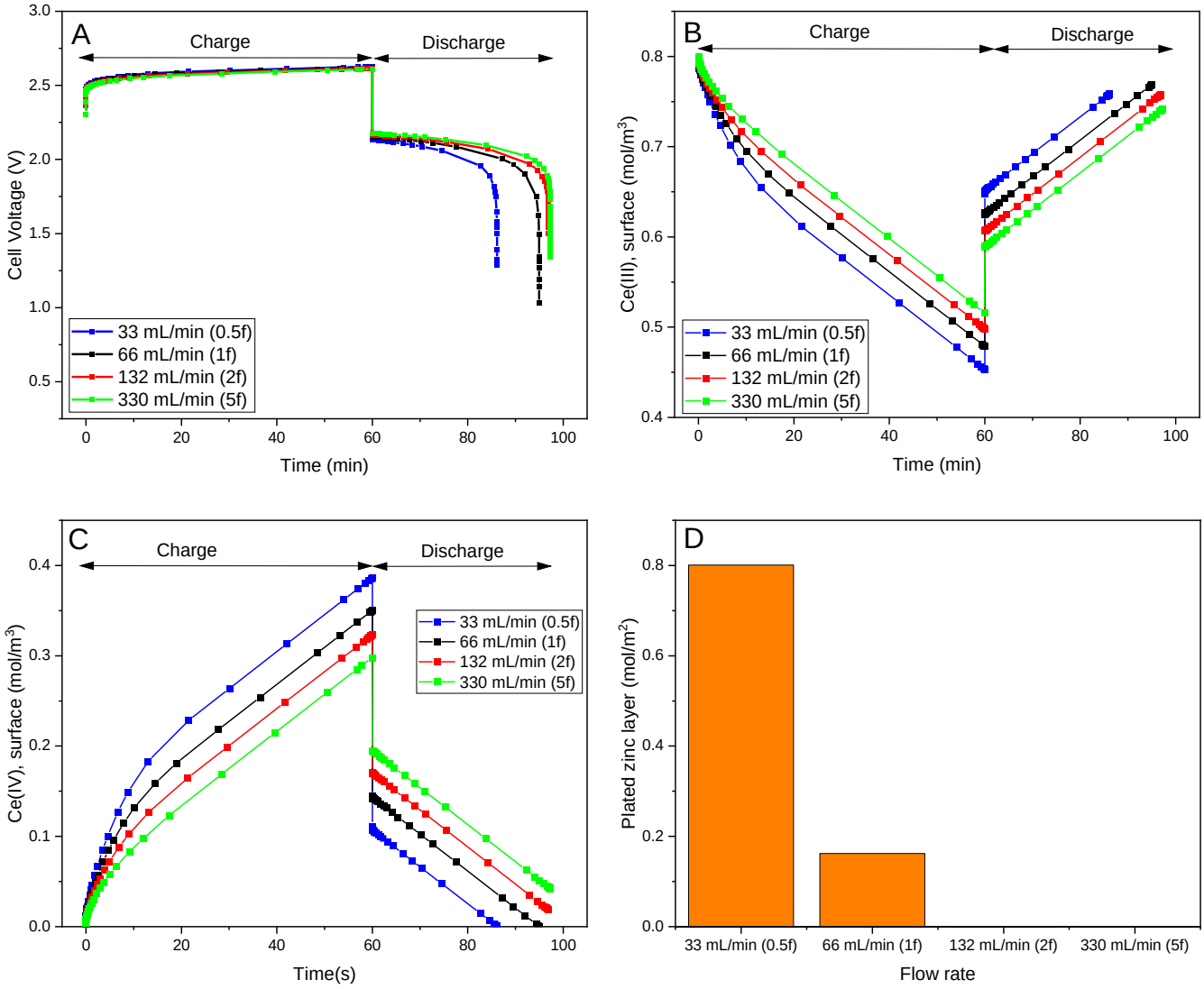


Figure 7.8. Effect of electrolyte flowrate on (A) cell voltage, surface concentration of (B) Ce^{3+} and (C) $CeOH^{3+}$ during the 1st charge-discharge cycle and (D) surface density of the zinc deposit at the end of the 1st discharge cycle. The charge-discharge cycles are conducted at a current density of 25 mA/cm², temperature of 323°K, charge duration of 1 hour and at various flow rates of the positive and negative electrolytes. The negative electrolyte contains 1.5 mol/L Zn^{2+} in 1 mol/L MSA and positive electrolyte contains 0.8 mol/L Ce^{3+} in 4 mol/L MSA at the start of the cycle.

When higher flow rates are used, the charge voltage decreases very slightly, whereas the discharge voltage increases to a larger extent as shown in Figure 7.8A. This is beneficial since this means that a lower voltage is required to charge the battery at the applied current and the battery can generate a higher voltage when it is being discharged, which corresponds to a higher voltage efficiency. Ce^{3+} is the principal reactant for the positive electrode reaction during battery charge, whereas $CeOH^{3+}$ is the reactant for the positive electrode reaction during discharge. The increase in voltage efficiency as flowrate is increased can be attributed to the lower overpotential during battery charge arising from the rise in the Ce^{3+} surface concentration (Figure 7.8B) and the lower overpotential during discharge arising from the rise in the $CeOH^{3+}$ surface concentration (Figure 7.8C) due to enhanced mass transfer of both Ce^{3+} and $CeOH^{3+}$. As shown in Figure 7.9, the decrease in overpotential with flowrate is only very small during charge, but very significant during discharge.

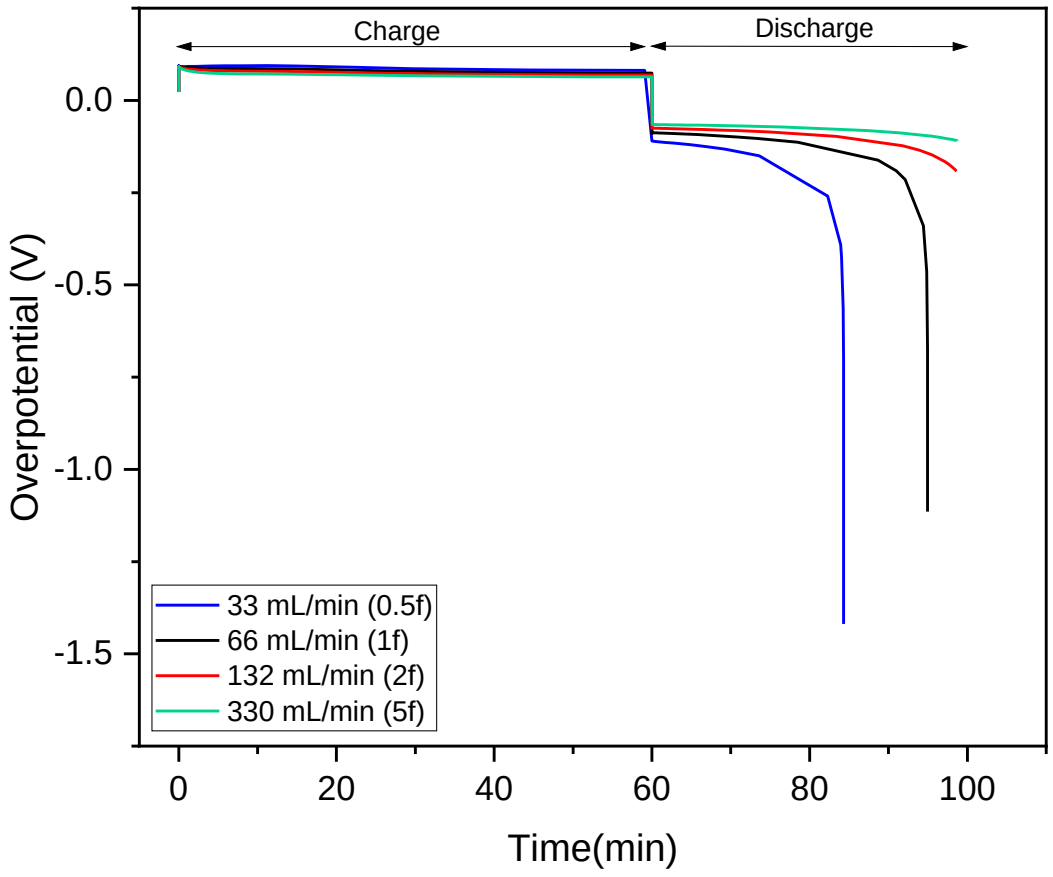


Figure 7.9. Effect of positive and negative electrolyte flowrates on the overpotential of $Ce^{3+}/CeOH^{3+}$ reaction. Charge-discharge cycle is conducted at current density of 25 mA/cm², temperature of 323°K and charge duration of 1 hour. The negative electrolyte contains 1.5 mol/L Zn^{2+} in 1 mol/L MSA and positive electrolyte contains 0.8 mol/L Ce^{3+} in 4 mol/L MSA at the start of the cycle.

The mass transfer of Zn^{2+} on the negative side is also improved by raising the flowrate. As shown in Figure 7.10A, the profiles of the Zn^{2+} concentration at the half-cell height (H/2) are plotted across the negative compartment at different flow rates after 30 minutes of battery charge (solid lines) and 30 minutes of discharge (dash lines). During battery charge, Zn^{2+} ions are deposited as metallic zinc at the negative electrode, which results in a decrease of the Zn^{2+} concentration near the electrode. Conversely, the zinc deposit re-dissolves into the electrolyte as Zn^{2+} ions during battery discharge, leading to a higher Zn^{2+} concentration at the surface than in the bulk due to mass transfer limitations. The concentration gradients across the boundary layer close to the electrode

surface ($x = 0$) are reduced by a small amount during both charge and discharge when the flow rate is increased from 0.5f to 5f. A higher surface concentration is beneficial for the battery coulombic efficiency since it improves the reaction rate of the Zn/Zn^{2+} redox couple (see Eqn.(67)). To confirm this, the effect of the flowrate on the amount of zinc deposited during battery charge is plotted in Figure 7.10B. Although the total amount of the deposited zinc for each case is similar, an increase of the flowrate from 0.5f to f leads to a small increase (3.1%) in the amount of deposited zinc from 2.89 mol/m^2 to 2.98 mol/m^2, which confirms the improved mass transfer at the higher flow rate. A further increase in the flowrate causes only a minimal increase (0.65%) in the amount of zinc deposited on the electrode surface. This is an indication that zinc deposition is largely kinetically controlled rather than mass-transport controlled. During battery discharge, higher flow rates enable a more efficient removal of Zn^{2+} ions from the electrode surface as they are generated by the dissolution of the zinc deposit, leading to a reduction in the concentration gradient as shown by the dash lines in Figure 7.10A. Further examination of the current density for zinc deposition and the HER obtained from the model in Figure 7.11 confirms that the zinc deposition reaction is benefited by the increased flow rates. As shown in Figure 7.11A, the current density due to zinc deposition increases while the current density due to the HER decreases as the flowrate rises, although the effect is quite small.

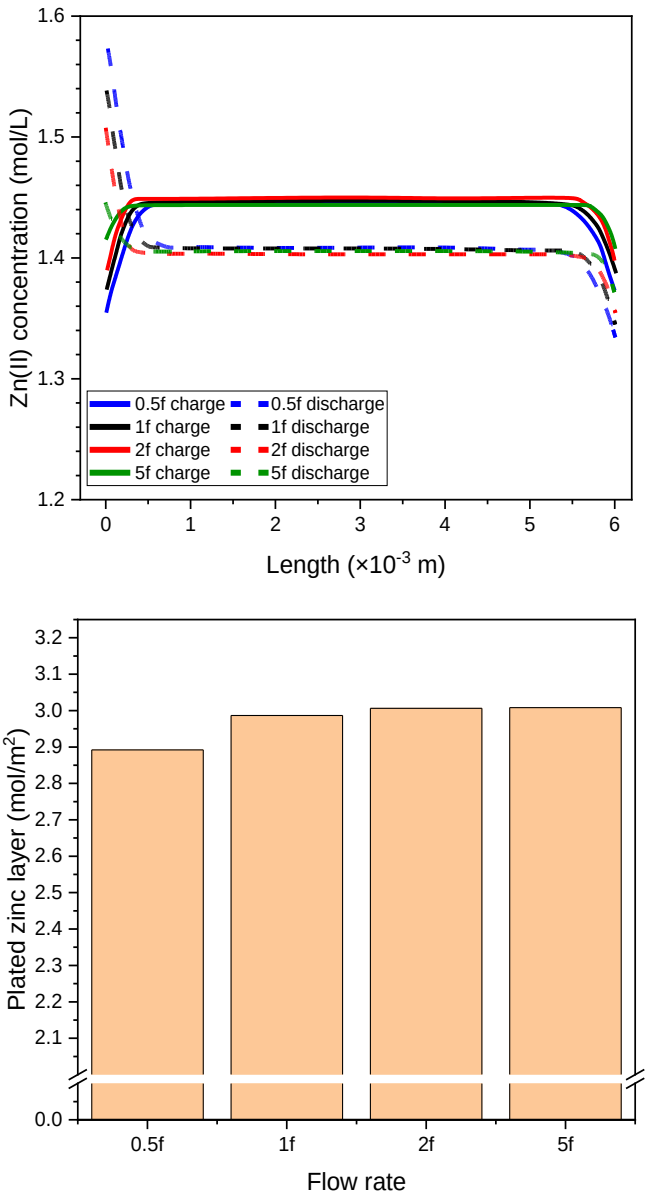


Figure 7.10. (A) Effect of electrolyte flowrate on the Zn^{2+} concentration profiles across the negative compartment at a height of H/2. The solid lines correspond to the profiles during charge and dash lines to the profiles during discharge. The data is taken at the 30 min from the start of battery charge and 30 min from battery discharge. (B) Effect of electrolyte flowrate on the surface density of the zinc metal deposit on the negative electrode surface after charge. Charge-discharge cycle is conducted at current density of 25 mA/cm^2, temperature of 323°K and charge duration of 1 hour. The negative electrolyte contains 1.5 mol/L Zn^{2+} in 1 mol/L MSA and positive electrolyte contains 0.8 mol/L Ce(III) in 4 mol/L MSA at the start of the cycle.

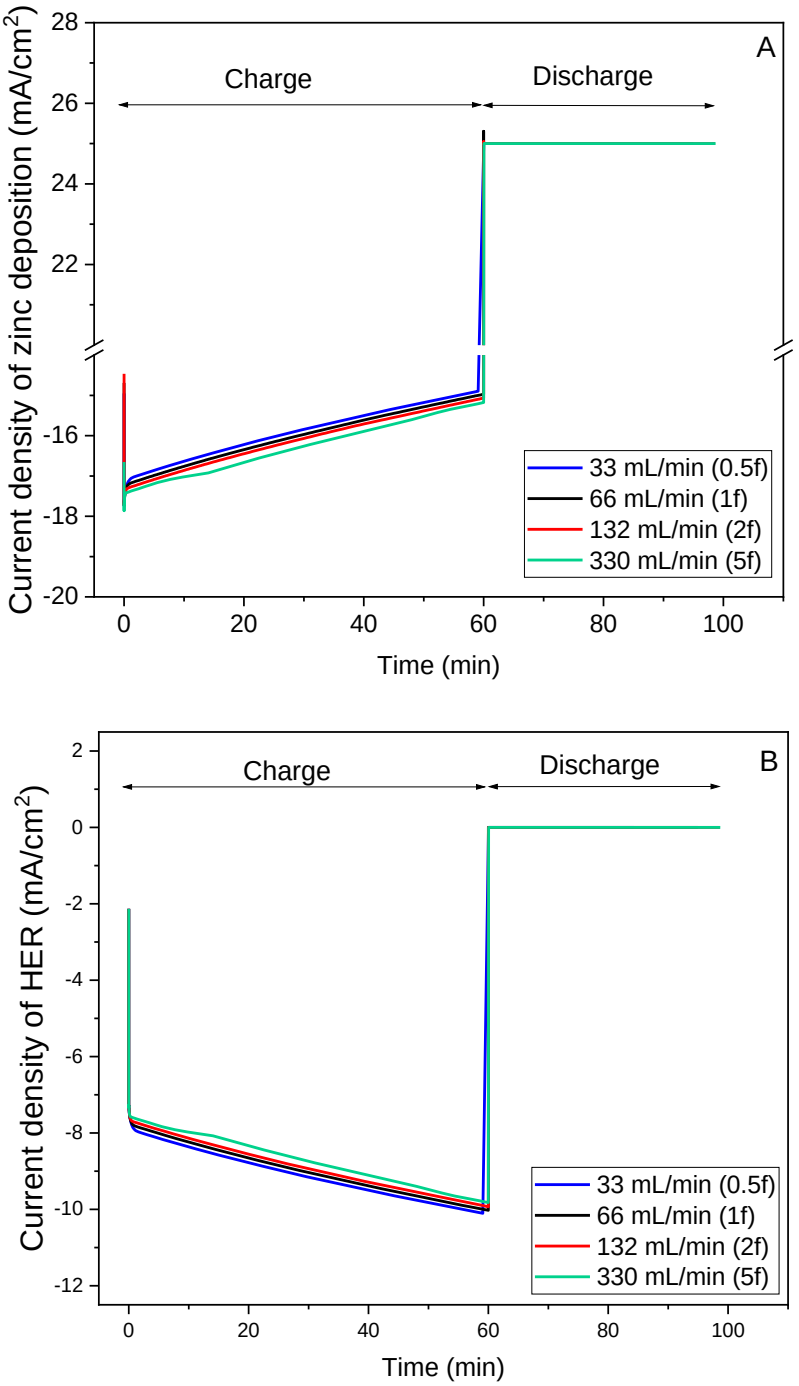


Figure 7.11. Effect of electrolyte flowrate on current density for (A) zinc deposition and (B) HER. Charge-discharge cycle is conducted at current density of 25 mA/cm^2, temperature of 323°K and charge duration of 1 hour. The negative electrolyte contains 1.5 mol/L Zn^{2+} in 1 mol/L MSA and positive electrolyte contains 0.8 mol/L Ce^{3+} in 4 mol/L MSA at the start of the cycle.

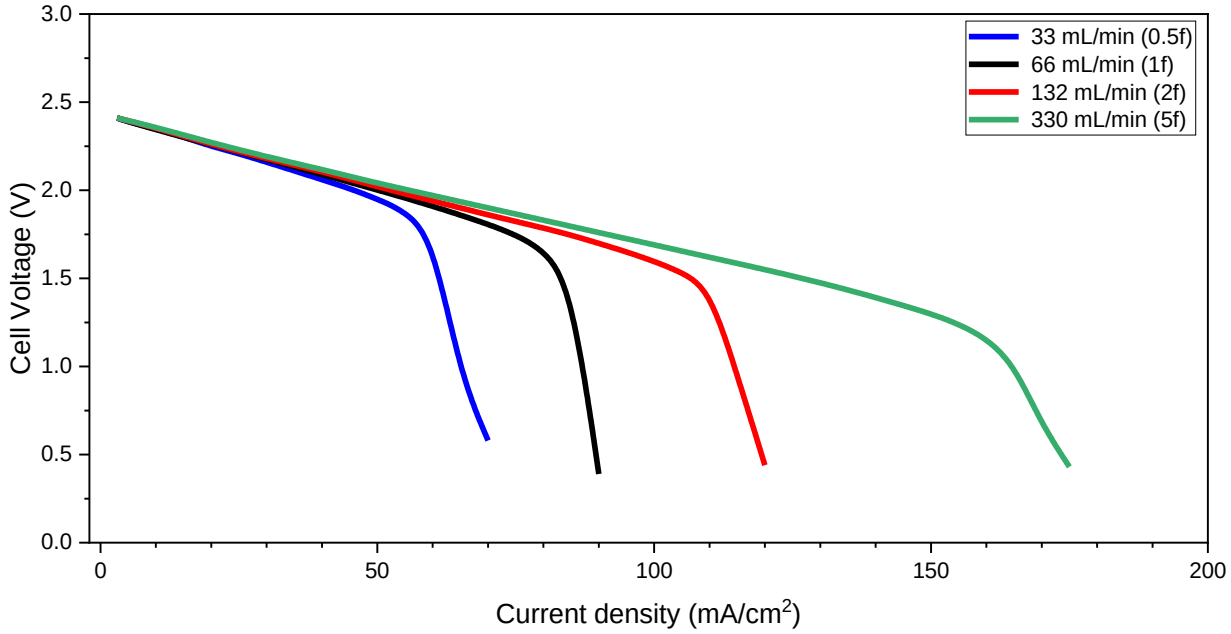


Figure 7.12. Effect of the electrolyte flowrates on the discharge polarization curves of the Zn-Ce RFB. These polarization simulations are conducted by first charging the battery at 50 mA/cm² for 45 minutes to reach an SOC of 50%, followed by battery discharge for 20s at different current densities ranging from 1 to 175 mA/cm² until a point is reached where cell voltage drops to the discharge termination criterion of 0.5 V.

Polarization curves of the Zn-Ce system obtained from the model for different flowrates are plotted in Figure 7.12. These polarization simulations are conducted by first charging the battery at 50 mA/cm^2 for 45 minutes to reach an SOC of 50%, followed by battery discharge for 20s at different current densities ranging from 3 to 175 mA/cm^2 until a point is reached where cell voltage drops to the discharge termination criterion of 0.5 V. The cell voltages plotted in Figure 7.12 are the specific values obtained at the end of the 20s discharge and the polarization curve is generated by discharging first at the lowest current density of 3 mA/cm^2, then at 5 mA/cm^2 and then by increasing at intervals of 5 mA/cm^2 thereafter.

When the Zn-Ce RFB is operated at a flow rate of f, its discharge is limited by mass transfer of $CeOH^{3+}$ to the positive electrode at a current density of ~80 mA/cm^2 (Figure 7.12). When the flow rate is reduced to 0.5f, the mass transfer of $CeOH^{3+}$ begins to limit discharge at a lower current

density of ~ 50 mA/cm^2. An increase in flowrate to 2f and 5f facilitates mass transfer so that current densities up to ~110 mA/cm^2 and ~160 mA/cm^2, respectively, can be applied before battery operation becomes limited. It is worth noting that the portions of the polarization curves in Figure 7.12 at low current density are virtually identical to each other due to the fact that the total resistance is the same in all cases and unaffected by the electrolyte flowrate.

7.4.5 Effect of positive electrode geometry and specific surface area

In this section, the model is used to investigate the effect of the geometry and specific surface area of the Pt-Ti positive electrode on battery performance at an applied current density of 25 mA/cm^2. The geometry of the electrode is an important lever when designing the battery because it directly affects the mass transfer of the electroactive species from the bulk to the electrode surface and determines the number of electrochemically active sites for the redox reactions to occur. For this reason, Arenas et al conducted experimental studies on Zn-Ce RFBs operating with Pt-Ti positive electrodes spanning a wide range of porosities and specific surface areas.[195,210] Photographs of these electrodes are shown in Figure 7.13, while their geometrical dimensions obtained from these studies are listed in the table below. A photograph of the Pt-Ti electrode used in this work to obtain the experimental data is shown in Figure 3.1 (Chapter 3). The properties of these electrodes are used in the model to simulate the charge-discharge cycles of the Zn-Ce RFB obtained with each of these positive electrodes.

Table 7.6. Properties of the different positive electrode evaluated in the model simulations.

	Fibre diameter (mm)	Porosity	Specific surface area (m^{-1})
Pt-Ti original[a]	1.5	0.745	150
Pt-Ti mesh	3	0.71	386.67
Pt-Ti micromesh	0.2	0.53	9400.00
Pt-Ti felt	0.067	0.8	12012.01

[a]Positive electrode used in the experiments throughout the work.

The specific surface area of the electrodes can be calculated from knowledge of the fibre diameter d_f and porosity ε using the following equation[211]:

$$a = \frac{4(1-\varepsilon)}{d_f} \tag{91}$$

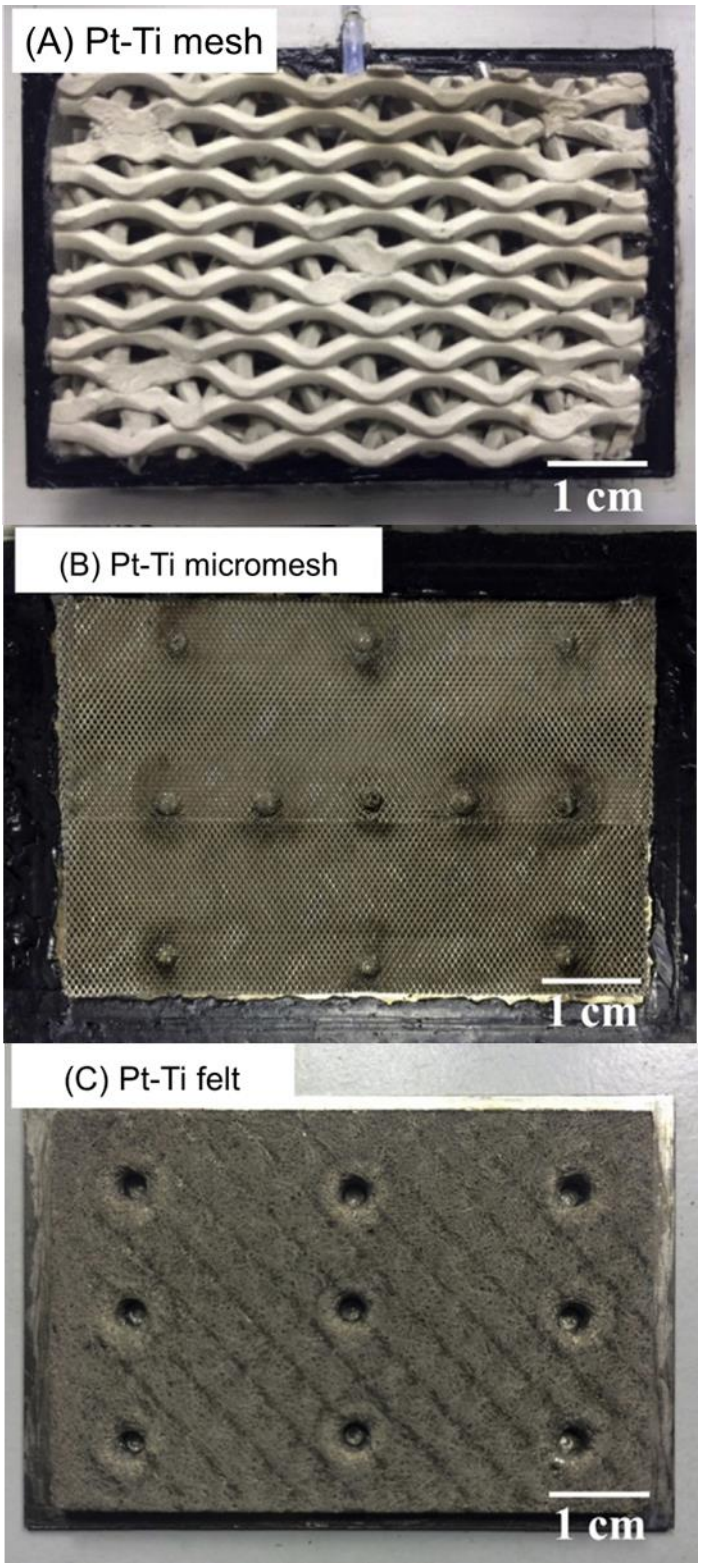


Figure 7.13. Optical photographs of (A) Pt-Ti mesh, (B), Pt-Ti micromesh, and (C) Pt-Ti felt (reproduced with permission).[195,210]

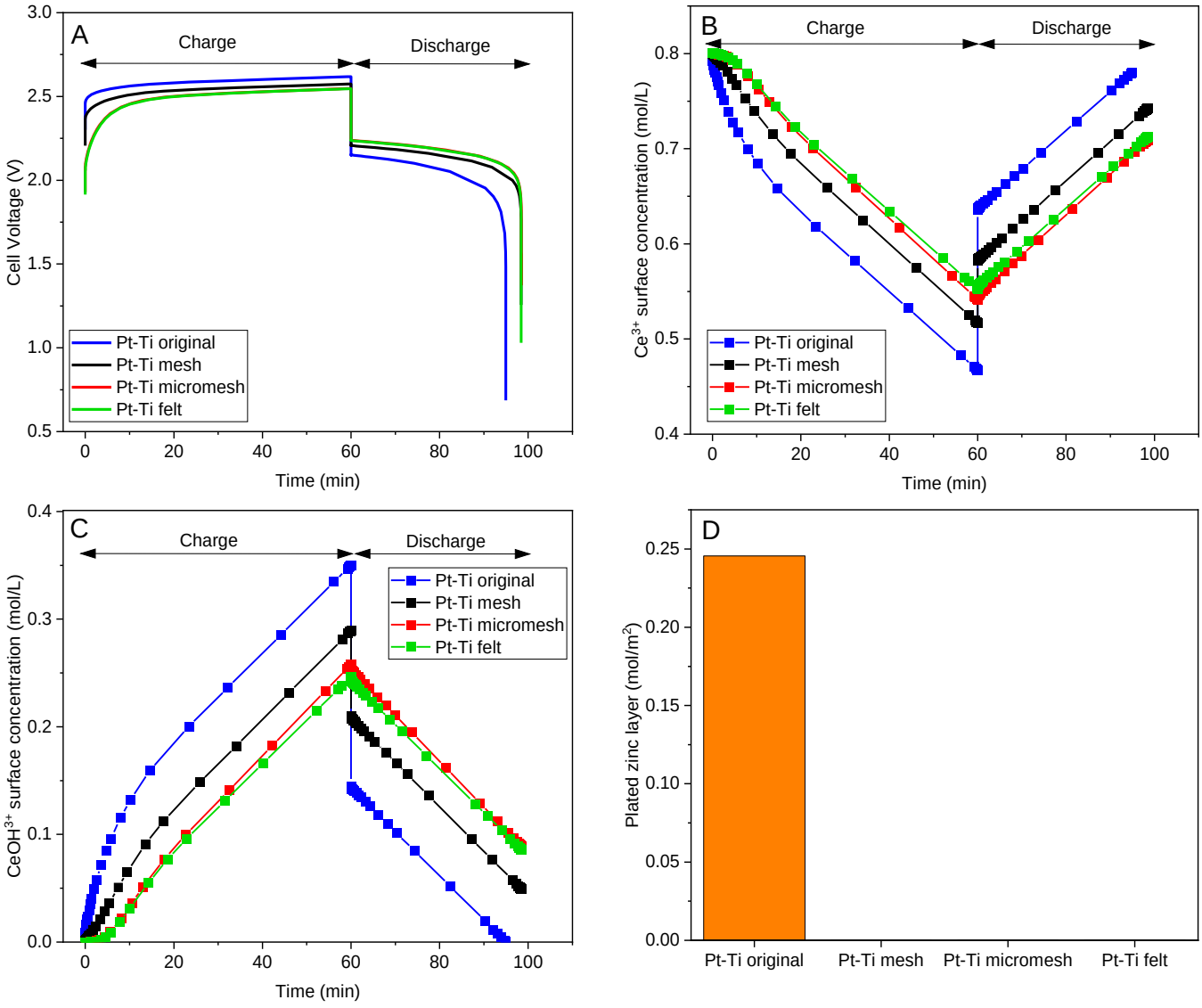


Figure 7.14. (A) Cell voltage, (B) Ce^{3+} surface concentration, (C) $CeOH^{3+}$ surface concentration and (D) zinc deposit remaining on the negative electrode at the end of 1st charge-discharge cycle using the different positive electrodes.

It can be seen from Figure 7.14A that both the coulombic and voltage efficiencies are improved when the Zn-Ce RFB is operated with positive electrodes that have higher specific surface area. The voltage efficiency of the battery using the original Pt-Ti positive electrode is 79.3%, whereas it increases to 84.3% when operated with the Pt-Ti mesh electrode that has a specific surface area

~2.5 times larger. Since the only changes are the specific area of the electrode and porosity that affects the electrolyte flow rate, this increase in voltage efficiency can be attributed to the enhanced mass transfer of the Ce^{3+} and $CeOH^{3+}$ ions. As shown in Figure 7.14B, the surface concentration of Ce^{3+} is much higher during battery charge when electrodes with larger specific surface area are used, which reduces the concentration overpotential of the electrode reaction and therefore enables a lower cell voltage over the 60 minutes of charge. For example, the overpotential of the Ce reaction is 0.078 V after 30 min of battery charge when using the original positive electrode, whereas it decreases to 0.034 V when using Pt-Ti mesh electrode. The use of the Pt-Ti micromesh and Pt-Ti felt electrodes that have even higher surface area further reduces the overpotential to ~0.001 V. During battery discharge, a much higher $CeOH^{3+}$ surface concentration is obtained using the Pt-Ti mesh electrode compared to the originally used electrode (Figure 7.14C). This higher $CeOH^{3+}$ surface concentration again reduces the concentration overpotential and enables the battery to be discharged at a higher voltage and achieve a higher voltage efficiency. The overpotential of the Ce reaction after 30 min of discharge is -0.178 V and decreases to -0.044 V when the positive electrode is changed from the original to Pt-Ti mesh electrode. A further increase of the positive electrode surface area by using the Pt-Ti micromesh leads to an even higher voltage efficiency. As before, this improvement is due to the higher surface concentrations of Ce^{3+} and $CeOH^{3+}$ ions during battery charge and discharge, which lead to lower overpotentials. The overpotentials again are reduced to -0.001 V when using Pt-Ti micromesh and Pt-Ti felt as positive electrodes. However, although the specific surface area of the Pt-Ti micromesh electrode is ~24 times higher than the Pt-Ti mesh electrode, the improvement on the voltage efficiency is not proportional to the rise in the specific surface area. The voltage efficiency only improves from 84.3% to 87.3% when the Pt-Ti mesh is replaced by the Pi-Ti micromesh. This is an indication that the surface area of the positive electrode is becoming less important for improvement of the battery voltage efficiency. In other words, mass transfer of Ce^{3+} and $CeOH^{3+}$ ions from the bulk to the surface is becoming fast enough to keep up with the rate of consumption by the electrode reactions at the surface. Therefore, the concentration gradients of the Ce^{3+} and $CeOH^{3+}$ ions close to the surface of the positive electrode disappear and can be considered equal to each other, as shown in Figure S2 and Figure S3 in the Apendix. Unsurprisingly, the even higher surface area provided by the Pt-Ti felt positive electrode does not improve the battery performance any further and the cell voltage profile coincides entirely with the curve obtained when the Pi-Ti micromesh is used

(Figure 7.14A). In addition, the surface concentrations of Ce^{3+} and $CeOH^{3+}$ ions are almost identical to those when Pi-Ti micromesh is used as the positive electrode. However, it should be noted that pumping cost is expected to increase when using electrodes with finer mesh to achieve the same flow rate, although the analysis of pumping cost is outside the scope of this present work.[212]

The coulombic efficiency improves from 58.3% to 64.1% when the original Pt-Ti positive electrode is replaced with the Pt-Ti mesh electrode having larger surface area. When the battery is operated using the original Pt-Ti electrode, the $Ce^{3+}/CeOH^{3+}$ reaction is the limiting reaction since ~0.25 mol/m^2 of the zinc deposit still remains on the negative electrode surface at the end of discharge (Figure 7.14D). As discussed previously, this is attributed to the slow mass transfer of the $CeOH^{3+}$ from the bulk to the surface, which results in its complete depletion at the positive electrode surface during discharge. It should be noted that the bulk concentration of $CeOH^{3+}$ is still ~0.2 mol/L, which is not available for battery discharge. When the battery is operated with the Pt-Ti mesh electrode, a much higher $CeOH^{3+}$ ion concentration can be maintained at the electrode surface during battery discharge and therefore enables the battery to discharge for a longer time. As shown in Figure 7.14C and Figure 7.14D, the $CeOH^{3+}$ concentration is ~0.05 mol/L whereas the zinc deposit on the negative electrode has been completely removed by the end of battery discharge. Therefore, the negative electrode reaction becomes the limiting half-cell reaction at this point. Any further increase of the positive electrode surface area and $CeOH^{3+}$ surface concentration resulting from the use of the Pt-Ti micromesh and felt electrodes has no effect on the coulombic efficiency since the battery is now controlled by the negative electrode reaction.

Figure 7.15 shows the discharge polarization curves of the Zn-Ce RFB using the different positive electrodes operated at 50°C and a flow rate of 66 mL/min. The open-circuit voltage of the battery when using the different positive electrodes remains the same at 2.42 V in all cases. For the battery operating with the original Pt-Ti electrode, the battery becomes mass transfer-limited at a current density of ~80 mA/cm^2. When the Pt-Ti mesh electrode is used, a much higher current density of ~200 mA/cm^2 can be applied during discharge before the battery becomes mass transfer-limited. This improved mass transfer can be attributed to the increase of the positive electrode surface area since it is the only parameter that has been changed. When the battery is operated with the Pt-Ti micromesh and Pt-Ti felt electrodes that have an even larger electrode surface area, the mass-

transfer limiting region of the polarization curve disappears entirely. The surface areas of these positive electrodes are high enough that mass transfer-limiting conditions are not reached even at a current density as high as ~380 mA/cm^2. In these cases, the decrease in the cell voltage as the applied current density increases is mainly caused by the ohmic losses. High current density-operation (>300 mA/cm^2) is a critical feature for a RFB to be technically feasible for commercial-scale applications, as shown in a report by Reed et al. of the Pacific Northwest National Laboratory.[213] Thus, the results shown in these polarization curves reveal the great promise and need for the use of an electrode such as Pt-Ti micromesh or felt in a commercial-scale RFB.

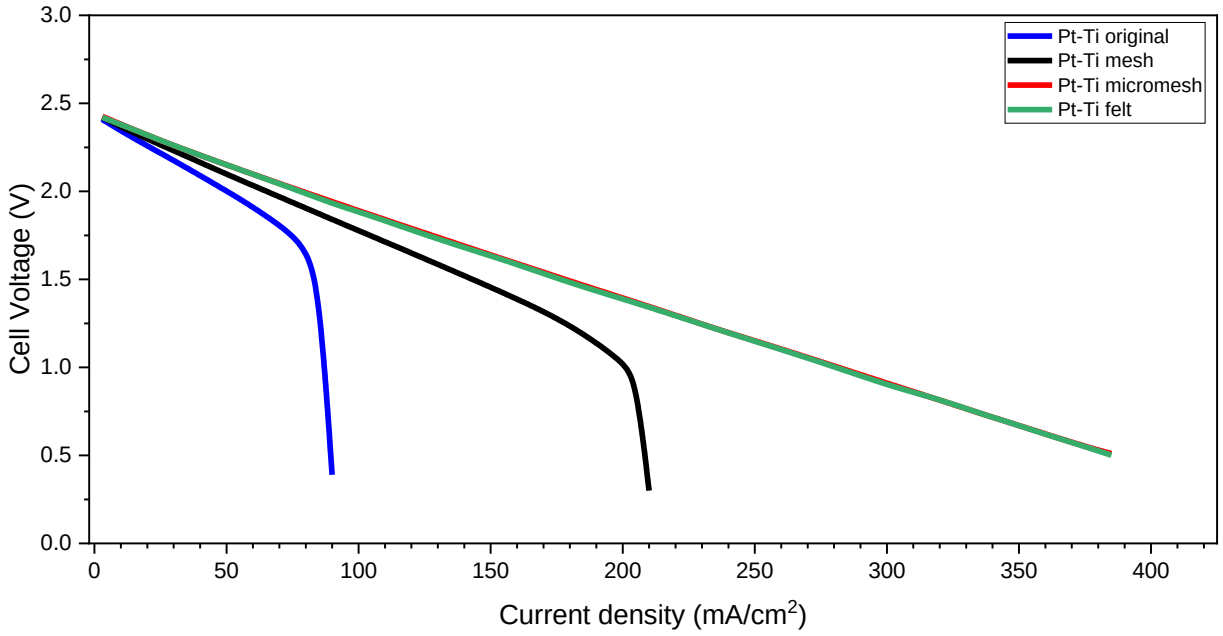


Figure 7.15. Polarization curves of the Zn-Ce RFB obtained at 323°K and a flow rate of 66 mL/min when operated using the original Pt-Ti, Pt-Ti mesh, Pt-Ti micromesh and Pt-Ti felt electrodes. The polarization simulation was conducted by first charging the battery at 50 mA/cm^2 for 45 minutes to reach an SOC of 50%, followed by battery discharge for 20s at each of the applied current densities.

7.4.6 Effect of negative electrode thickness

In the course of our investigation into flow battery performance, we found that the internal electrical resistance of the system plays an important role in the efficiency of the battery. For

example, a higher resistance increases the required voltage for battery charge and reduces the output voltage during battery discharge, which reduces the voltage efficiency. Another consideration is that a higher internal resistance leads to a higher energy loss in the form of joule heating which is proportional to the resistance. Although our model is developed under the assumption that the battery operates under isothermal conditions and the effect of heat generation is neglected, the temperature rise during the operation of large-scale RFBs is an important consideration that requires the use of a thermal management module to prevent overheating and accelerated degradation of the battery components.[214] Therefore, minimization of the battery internal resistance is beneficial for improving its overall efficiency, power output and battery life-cycle, all of which are essential for cost-effective energy storage systems. Accordingly, we have used the model to investigate approaches to reducing the internal resistance of the system. In order to do so, a slight modification to the model is required. As the model has been defined to this point, the ohmic resistance in the battery is lumped together as a single term R_{total} in Eqn.(89). The value of this overall resistance was taken from the work of Amini and Pritzker.[39] In order to investigate the various contributions to the overall ohmic resistance, it is necessary to break it down into its components: PVE negative electrode, negative electrolyte, membrane, combined positive Pt-Ti electrode/electrolyte and other miscellaneous contact points, connections and current collector. The ohmic resistance of the PVE negative is given as

$$R_{PVE} = \frac{L_{PVE}}{\sigma_{PVE}} \tag{92}$$

where L_{PVE} and σ_{PVE} are the thickness (m) and electrical conductivity (S/m) of the PVE electrode, respectively.

Of these quantities, we have measured the resistances of the PVE negative electrode, negative electrolyte and combined positive electrode/electrolyte directly while the value for the membrane is available in the literature. The ohmic resistance of the miscellaneous contact points and connections is obtained from the difference between the overall resistance as measured by Amini and Pritzker[39] and the sum of the other components above.

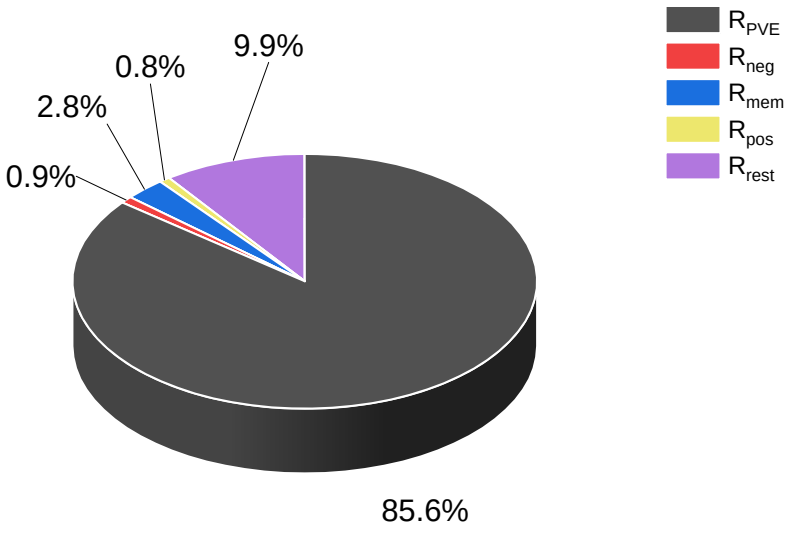


Figure 7.16. Breakdown of the contribution of the different components in the Zn-Ce RFB to its total ohmic resistance based on measurements and the model.

Table 7.7. Ohmic resistances of the different components of the Zn-Ce RFB based on measurements and the model.

Symbol	Component	Area resistance (ohm-m^2)
R_{total}	Total	4.50×10^{-4}
R_{PVE}	PVE negative electrode	3.85×10^{-4}

R_{neg}	Negative electrolyte	3.87×10^{-6}
R_{mem}	Membrane	1.27×10^{-5}
R_{pos}	Combined positive electrode + positive electrolyte	3.45×10^{-6}
R_{rest}	Miscellaneous components, contact points, current collectors	4.47×10^{-5}

As shown in Figure 7.16, the PVE negative electrode is by far the largest contributor to the overall resistance of the Zn-Ce RFB used in our experiments by accounting for 86% of the total. This stems from its relatively low electrical conductivity and its thickness of 6 mm. The ohmic resistances of the negative electrolyte, Nafion 117 membrane and combined positive electrode/electrolyte listed in Table 7.7 combine for only ~ 4.4% of the total battery resistance. The resistance R_{rest} from other sources such as the connecting wires, contact resistance between electrodes and current collectors make up ~ 10% of the total.

The purpose of the PVE negative electrode is to conduct electricity and provide a substrate for zinc deposition to occur. Therefore, an ideal negative electrode should have proper mechanical strength with superior conductivity to minimize undesired voltage loss. Based on Figure 7.16, the simplest and most effective way to minimize the overall resistance of the Zn-Ce RFB would be to reduce the resistance of the PVE electrode. Given that the original PVE electrode is unnecessarily thick (6 mm), a lower electrode resistance can be easily achieved by using a thinner PVE electrode. The cell voltage of a single charge-discharge cycle of the Zn-Ce RFB has been determined using the model for the cases when the battery is operated with PVE electrodes having the original 6 mm-thickness, a thickness that is a factor of 0.5 of that of the original and a thickness that is a factor of 0.1 of the original electrode. The resistance of the PVE negative electrodes with different thickness

is calculated according to Eqn.(92). The variation of the cell voltage for a battery operated with PVE electrode having different thicknesses (denoted as Original PVE, 0.5 PVE and 0.1 PVE) are plotted in Figure 7.17.

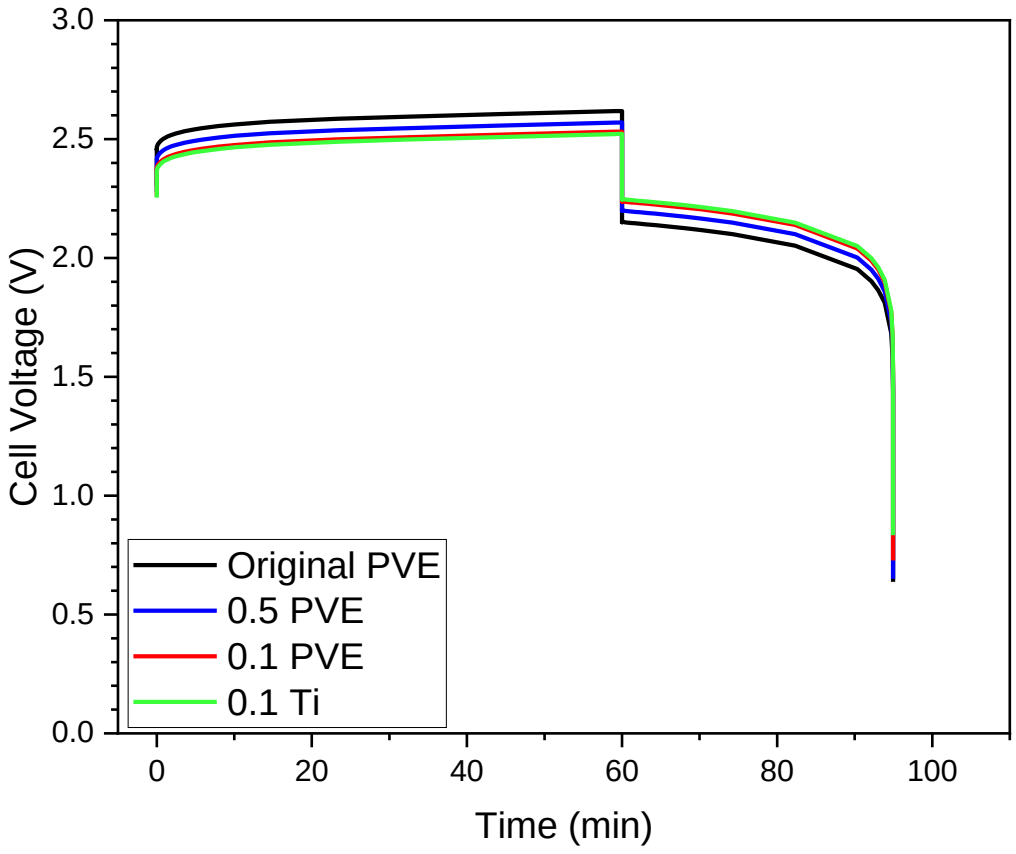


Figure 7.17. Effect of the thickness of the negative PVE electrode on the cell voltage obtained during charge and discharge of the Zn-Ce RFB. The charge-discharge cycles are conducted at a current density of 25 mA/cm^2, temperature of 323°K, charge duration of 1 hour, electrolyte flow rate of 66 mL/min. The negative electrolyte contains 1.5 mol/L Zn^{2+} in 1 mol/L MSA and the positive electrolyte contains 0.8 mol/L Ce^{3+} in 4 mol/L MSA at the start of the cycle.

Not surprisingly, the results in Figure 7.17 show that the charge voltage of the battery is the highest and the discharge voltage is the lowest when the original PVE electrode is used. As the thickness of the PVE electrode decreases from the original to ×0.1 thickness, the charge voltage decreases

by 0.082 V to a value of 2.498 V. At the same time, the average discharge voltage obtained when the thinnest PVE electrode is used is found to be 2.138V, which is 0.087 V higher than when the original PVE is used in the battery. The voltage efficiencies of the battery operating with the PVE negative electrode that is 0.5× and 0.1× of the original thickness are 82.7% and 85.6% respectively, compared to 79.3% with the original thick PVE electrode. This improvement in voltage efficiency by simply reducing the thickness of the PVE negative electrode is viable and cost-effective. Since PVE is sufficiently sturdy, the use of a thin PVE electrode that is 0.6 mm thick would be strong enough to withstand the compression when assembling the Zn-Ce RFB. Since the only change of the battery is the thickness of the PVE electrode and the associated resistance, this improvement in battery voltage efficiency could solely be attributed to the improved PVE electrode design that has lower electrical resistance. As expected, the results of the simulations in Figure 7.17 show that the coulombic efficiency of the battery is not affected by the thickness of the PVE electrodes that has no influence on factors such as electrode reaction kinetics or mass transport.

The polarization curves of the Zn-Ce RFB when the PVE negative electrodes with the different thicknesses are used have been simulated and plotted in Figure 7.18. Not surprisingly, the battery becomes mass transfer-limited at ~80 mA/cm^2 in all cases since mass transfer of species within the cell is unaffected by the thickness of the negative electrode. However, it is clearly seen that the ohmic loss is reduced when thinner PVE with lower resistance is used as the negative electrode. When the Zn-Ce RFB is operated at a current density of 50 mA/cm^2, the discharge cell voltage is 2.18V when using PVE with ×0.1 of the original thickness, which is higher than 2.10V and 2.00V achieved using PVE with ×0.5 and the original thickness, respectively. This is beneficial to battery performance since a higher cell voltage, lower energy loss and larger power output can be achieved during discharge at the same applied current density.

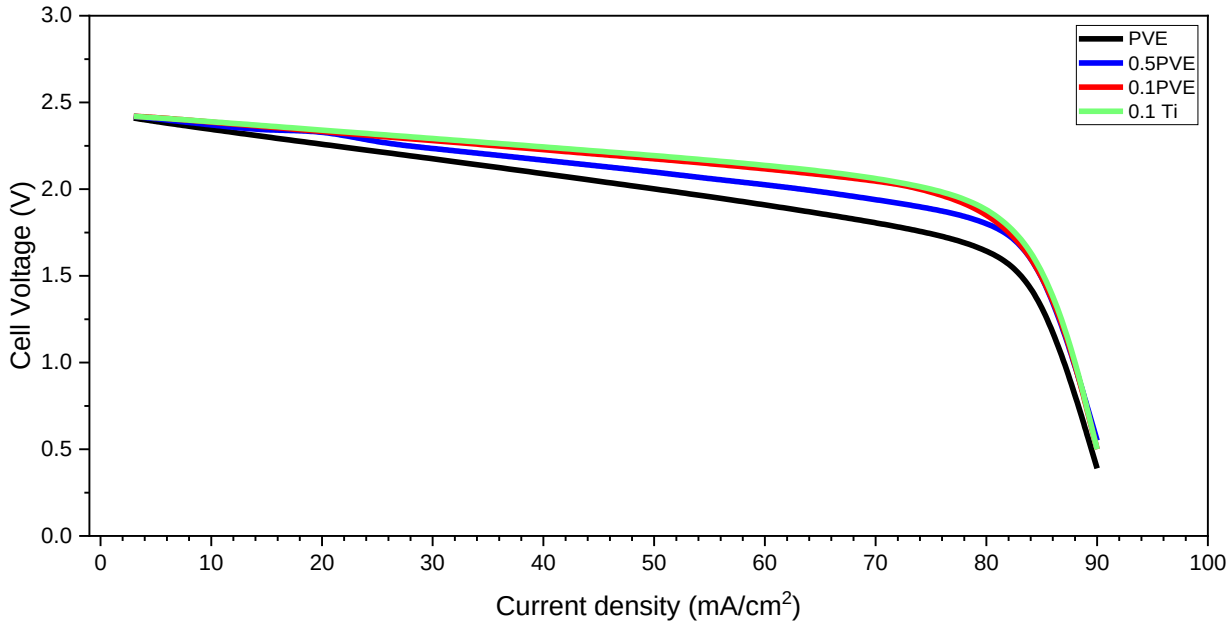


Figure 7.18. Effect of negative PVE electrode thickness on the discharge polarization curves of the Zn-Ce RFB operating at 323°K. The polarization simulation is done by first charging the battery at 50 mA/cm^2 for 45 minutes to reach an SOC of 50%, followed by battery discharge for 20s at each of the applied current densities.

The use of another material that is inexpensive and has high chemical and mechanical stability, electroactivity and conductivity as the negative electrode is obviously also worth investigating. For instance, the cell voltage of the Zn-Ce RFB when using Ti sheet as the negative electrode material with a thickness equivalent to that of 0.1 PVE (denoted as 0.1 Ti) has been modeled under the otherwise identical conditions to those used to generate the plots shown in Figure 7.17 and Figure 7.18. The evolution of the cell voltage during the 1st charge-discharge cycle and polarization curves obtained for RFBs containing the original PVE and 0.1 PVE are determined under the assumption that all other properties of the battery such as electrode kinetics and flow rate remain the same. As shown in Figure 7.19, the overall battery resistance is the lowest when the Ti sheet is used as the negative electrode and any further decrease of the resistance can come only from other components such as the membrane and wire connections. The model calculations show that the voltage efficiency is further increased to 86.3% compared to 85.6% achieved using PVE with ×0.1 of the original thickness. This is only a small improvement despite the fact that the conductivity

of Ti (2.0×10^6 S/m) is much higher than that of PVE (15.58 S/m). Examination of the data from the model simulations provides an explanation for this small effect. The ohmic resistance of the negative PVE electrode is a significant contributor to the overall ohmic resistance and voltage losses when its thickness is 6 mm, but not when it is 0.6 mm. Thus, the shift from PVE to Ti as the negative electrode when both have a thickness of 0.6 mm has only a small effect on the overall performance of the battery. Other factors such as the activation and concentration overpotentials at the two electrodes would have to be addressed in order to achieve significantly higher voltage efficiency. For the same reason as above, the polarization curve of the battery that employs a Ti negative electrode is virtually identical to the one obtained when 0.1PVE is used (Figure 7.18).

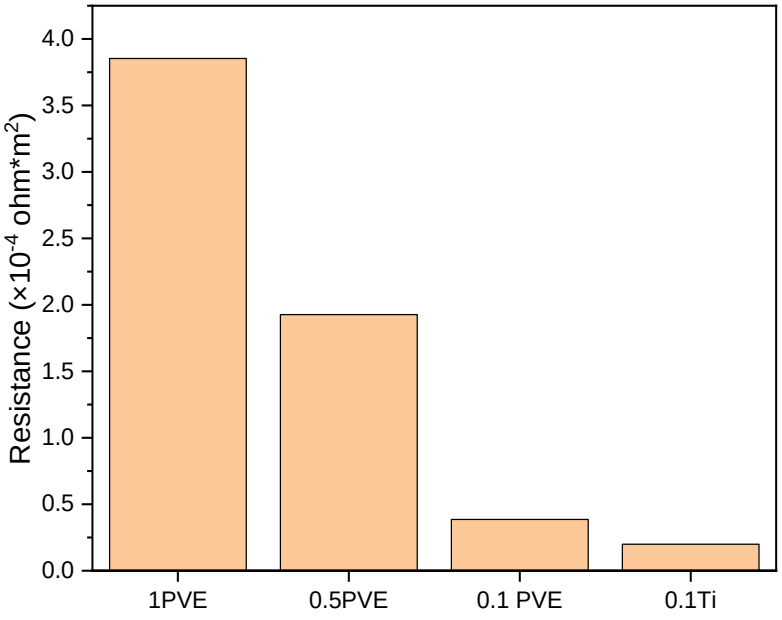


Figure 7.19. Resistance of different negative electrodes.

Chapter 8 Conclusions and Recommendations for Future Work

8.1 Conclusions

This work focused on the improvement of the performance of redox flow batteries that are based on Zn(0)/Zn(II) and Ce(III)/Ce(IV) chemistries. The thesis contains 8 chapters in total. Chapter 1 is an overview of the flow battery technology and the research objectives of this work. In Chapter 2, a comprehensive literature review of the development of redox flow batteries are presented and redox flow batteries that utilize different redox couples have been introduced. Particular attention has been focused on the evaluation of the kinetics of negative and positive electrode reactions and the overall performance of Zn-Ce RFBs. In addition, the challenges that the Zn-Ce system is currently facing have been identified, which need to be satisfactorily addressed for further battery performance improvement. The previous research on the modeling of redox flow batteries at different levels such as market-level, stack-and-system level, cell-level and material-level is reviewed. Chapter 3 described the details of the full-cell and half-cell experiments used in this study and the battery performance metrics used in this work.

In Chapter 4, we show that the use of 2 mol/L MSA-0.5 mol/L H_2SO_4 mixed acid as the supporting positive electrolyte has good promise for improving the long-term operation of Zn-Ce RFBs. This can be attributed to the fact that less H^+ is transported from the positive side to the negative side due to a smaller H^+ concentration gradient, which leads to less of the undesired H_2 evolution side reaction at the negative electrode and a higher acidity in the positive electrolyte throughout battery operation. Furthermore, the higher Ce(IV) solubility in 2 mol/L MSA-0.5 mol/L H_2SO_4 mixed acid enables a higher Ce(IV) concentration to exist in the positive electrolyte for battery discharge. This also explains the observation the positive electrode reaction is no longer the limiting half-cell reaction during discharge when 2 mol/L MSA-0.5 mol/L H_2SO_4 mixed acid is used as the positive supporting electrolyte. This leads to much less polarization during charge and discharge, particularly at the positive electrode. In addition, battery performance remains much more stable over the course of 40 charge-discharge cycles with much less capacity fade than in the case when the cell is operated with 4 mol/L MSA in the positive electrolyte. Therefore, a Zn-Ce RFB operating with 2 mol/L MSA-0.5 mol/L H_2SO_4 mixed acid positive supporting electrolyte would

be expected to outperform a Zn-Ce battery operating with the original 4 mol/L MSA in a commercial grid-scale energy storage cell.

In Chapter 5, the crossover of different electroactive species across the Nafion 117 membrane in a Zn-Ce redox flow battery operated with 4 mol/L MSA and 2/0.5 MA mixed acid supporting electrolytes at 25 mA/cm^2 is monitored for the first time over 30 consecutive charge-discharge cycles. These measurements reveal that the gradual battery capacity decay is caused by the crossover of Zn(II) from the negative to the positive electrolyte and H^+ from the positive to the negative electrolyte. Therefore, we intentionally add Zn(II) to both positive supporting electrolytes at the outset of battery operation with the intention of reducing ion crossover. The crossover of Ce(III), Ce(IV) and Zn(II) and H^+ has been studied in detail during the course of 30 consecutive charge-discharge cycles at 25 mA/cm^2 when the Zn-Ce redox flow battery was operating with positive electrolytes containing 0.8 mol/L Ce and each of the following supporting components: 4 mol/L MSA, with 0.6 mol/L Zn(II) in 4 mol/L MSA, 2/0.5 MA and 0.4 mol/L Zn(II) in 2/0.5 MA. Our results show that the net transfer of each ion over the cycle is mainly determined by its own concentration gradient across the membrane and not affected by the flux of other ions. The addition of Zn(II) ions is found to be beneficial for both MSA and MSA-H_2SO_4 mixed acid supporting electrolytes by reducing the extent of Zn(II) crossover from the negative side to the positive side and enabling the Zn(II) concentration in the negative electrolyte to remain at higher levels. This makes Zn(II) reduction more competitive relative to H_2 evolution during charge than otherwise possible and leads to higher columbic and voltage efficiency during battery operation and a considerably slower degradation in battery performance over successive charge-discharge cycles. Furthermore, CV experiments reveal that the addition of Zn(II) ions improves the reaction kinetics of the Ce(III)/Ce(IV) redox couple and suppresses O_2 evolution on the positive electrode. The maximum energy efficiency of 62.5% is achieved at 25 mA/cm^2 by adding 0.4 mol/L Zn(II) to the 2/0.5 MA positive electrolyte, compared to 56.4% when no Zn(II) is added. In the case of 4 mol/L MSA positive supporting electrolyte, the energy efficiency of the battery increases from 38% to 57.7% when 0.6 mol/L Zn(II) is added to the electrolyte. The use of this simple and effective method to reduce undesired ion crossover can also be applied to other systems to mitigate the non-ideal behaviour of the ion exchange membranes. Although the addition of Zn(II) to both MSA and MSA-H_2SO_4 mixed acid leads to higher battery efficiency at lower current densities based on the efficiencies obtained over 30 cycles, polarization experiments reveal that the advantage of the use

of these Zn(II)-containing positive electrolytes disappears at high currents when the battery operates under mass-transfer conditions likely due to their high viscosities.

In Chapter 6, we investigate two methods to regenerate the positive electrolyte by converting Ce(IV) that accumulates in the positive electrolyte to Ce(III) with the goal of improving the overall battery efficiency. The first regeneration method utilizing RuO_2 as a catalyst improves the voltage efficiency from 71.1% to 77.8% over 16 charge-discharge cycles. However, the coulombic efficiency declines from 74.1% to 57.8% due to the leakage of RuO_2 catalyst through the porous filter into the positive electrolyte. On the other hand, the use of H_2O_2 to regenerate the positive electrolyte shows excellent promise for the Zn-Ce RFB system. The H_2O_2 is introduced simply to the positive electrolyte using a pipette, which is much easier to operate and control compared to the complications associated with the additional catalytic bed and electrolyte circulation system required for the RuO_2 method. Charge-discharge cycle experiments show that the coulombic efficiency improves from 63.7% to 68.3%, due to the implementation of this regeneration method. This improvement mainly occurs over the last 15 charge-discharge cycles when the positive reaction is the limiting reaction. Compared to coulombic efficiency, the voltage efficiency due to regeneration is improved even more from 56.8% to 76.1%, with no apparent drop in voltage efficiency over the course of the 30 charge-discharge cycles. It is worth noting that these two positive electrolyte regeneration methods can also be seamlessly applied to other Ce-based RFBs such as V-Ce and Br-Ce RFBs. In addition, due to the simplicity and efficient nature of the regeneration method that use H_2O_2, this method should be very promising for extending the lifespan of the positive electrolyte in real-life applications and reducing the overall operating costs.

In Chapter 7, a transient 2-D model accounting for the crossover of different electroactive species through the membrane is developed. This model includes all three modes of transport (migration, diffusion and convection) coupled with the electrode kinetics of the Zn/Zn(II) and Ce(III)/Ce(IV) redox couples as well as the HER and OER side reactions. An extensive set of experimental data consisting of the evolution of the cell voltage, negative electrode potential, positive electrode potential and the concentrations of the various dissolved species in the two compartments over the course of 5 consecutive charge-discharge cycles of the RFB obtained in our laboratory is used to validate the model. The validated model is then used to simulate the battery behaviour over 5 charge-discharge cycles and provide detailed information such as the evolution of the electrode

overpotential and the concentrations of the dissolved species over time and the molar flux of each species through the membrane at different current densities. In addition, the performance of a Zn-Ce battery operating with positive electrodes that have higher surface area and finer pore structure, thinner negative electrodes and various electrolyte flow rates has been investigated. It is found that higher flow rates enable a more efficient supply of reactants and removal of products between the bulk electrolyte and electrode surface, which reduces electrode overpotential and improves voltage efficiency. The voltage efficiency increases from 79.3% to 87.3% when the positive electrode is changed from the original Pt-Ti mesh to a Pt-Ti felt that has larger surface area due to the reduction in the overpotential in both the anodic and cathodic directions of the Ce(III)/Ce(IV) reaction. More importantly, the model calculations show that a high surface area positive electrode such as a micromesh or felt material is required in order for the battery to operate at the high current densities required for commercial-scale energy storage applications. The use of a highly conducting and mechanically strong material such as stainless steel or a titanium sheet as the negative electrode is a simple and effective method to improve battery performance. To the best of our knowledge, the comparison between experimental data and model calculations carried out in this study is the most extensive one for a RFB system that has been reported to date. The model should serve as a useful basis for the future design of Zn- or Ce-based RFBs with the aim of further improving their performance.

8.2 Future work

8.2.1 Inhibition of HER

As shown in Chapter 4, the parasitic HER occurring on the negative electrode surface during battery charge is detrimental to battery performance by reducing the coulombic efficiency and accelerating the accumulation of Ce(IV) in the positive electrolyte that leads to capacity decay. Therefore, inhibition of the HER is one of the most critical challenges that must be addressed to ensure the success for Zn-Ce RFBs. A promising method is the modification of the negative electrode itself by coating the high conductivity electrode bulk material with a surface that have low catalytic activity for HER. For example, Tian et al. found that the HER in acidic electrolyte media could be inhibited by coating stainless steel with polypyrrole.[215] Also, the addition of soluble

organic reagents such as sodium dodecyl sulfate (SDS), dimethyl sulfoxide (DMSO) and 1,2-dimenthoxyethane (DME) to aqueous electrolyte was also found to effectively suppress the HER.[216] Therefore, studies on the addition of HER inhibitors to the negative electrolyte and the modification of negative electrode surface are highly recommended for improving overall battery performance.

8.2.2 Optimization of positive electrolyte composition

Further experiments aimed at optimizing the positive electrolyte composition are warranted. This includes the determination of the actual solubility of Ce(III) and Ce(IV) in the 2 mol/L MSA-0.5 mol/L H_2SO_4 mixed acid electrolyte and changes in Ce(III) and Ce(IV) concentrations during the course of long-term battery operation. In addition, future experiments can be conducted to investigate the use of other MSA-H_2SO_4 mixed acid compositions as positive supporting electrolyte that exhibit even higher Ce(III)/Ce(IV) solubility and lead to faster Ce(III)/Ce(IV) reaction kinetics with lower acidity. The possibility of other acid choices such as phosphoric acid and hydrochloric acid should also be considered and evaluated via half-cell and full-cell experiments. It would also be helpful to measure the exchange current density and standard rate constant for the Ce(III)/Ce(IV) redox couple in the above mentioned electrolytes to obtain more quantitative knowledge of the electrochemical reaction properties.

8.2.3 Minimization of undesired ion crossover

Our focus in Chapter 5 was on the positive electrolyte composition and so we made no effort to modify and/or optimize the other components of the battery such as the electrodes, membrane or negative electrolyte composition. Given the success of adding Zn(II) to the positive electrolyte, future work should focus on the addition of Ce(III) to the negative electrolyte to reduce its crossover from the positive electrolyte and maintain the total soluble Ce concentration in the positive electrolyte at higher levels.

The results of Chapter 5 also point to the critical role that ion crossover plays in battery operation and underscores the need to develop highly selective membranes. Currently, Nafion membranes are the most popular membrane used in RFBs for their superior mechanical and electrochemical durability in highly acidic and oxidizing conditions, although the selectivity of Nafion membranes is moderate. Therefore, the development of durable cation exchange membranes with better ion selectivity would be very beneficial for the improvement of battery efficiency and reduce battery capacity decay, especially over long-term operation. In addition, the use of anion exchange membrane to replace cation exchange membranes could also benefit the battery efficiency by reducing the transfer of H^+ from the concentration electrolyte to the diluted one. Our preliminary results as well as the work published by Amini and Pritzker showed that the use of anion exchange membrane can reduce the transfer of H^+ from the positive to the negative electrolyte and therefore improve coulombic efficiency of the battery.[38] However, these anion exchange membranes were not designed to be operated in such highly acidic and oxidizing conditions as in the positive electrolyte and so they were permanently damaged early during operation. Therefore, the fabrication of durable anion exchange membranes would also be critical to achieve better performance and slower capacity decay.

8.2.4 Further improvement of multi-physics model

In Chapter 7, the crossover of electroactive species such as Zn(II), Ce(III) and Ce(IV) was incorporated into the model, which provided more information regarding the performance of Zn-Ce RFB. However, the model was fitted to data for only the first 5 of the 30 charge-discharge cycles conducted in our experiments using 4 mol/L MSA in the positive electrolyte due to the precipitation of Ce(IV) which began to occur during the 6^{th} cycle. It would obviously be desirable to validate the model against a larger experimental data set obtained over many more cycles so that it can be used to simulate long-term battery performance. In addition, the phenomena of osmotic and electro-osmotic transfer of water across the membrane and Ce(IV) precipitation in the electrolyte should be incorporated into the model particularly since their effects on battery performance become increasingly more important as the duration of battery operation is further extended. It would also be useful to validate the model against other experimental data collected

in this study such as when 2 mol/L MSA-0.5 mol/L H_2SO_4 mixed acid was used in the positive electrolyte and Ce(IV) precipitation did not occur.

8.2.5 Regeneration of positive electrolyte

Charge-discharge cycle experiments showed that the coulombic efficiency was improved from 63.7% to 68.3% due to the implementation of positive electrolyte regeneration using H_2O_2. The voltage efficiency has improved from 56.8% to 76.1% and no apparent decrease in voltage efficiency was found throughout the 30 charge-discharge cycles. However, a decrease in the coulombic efficiency was observed during the cycles immediately after electrolyte regeneration. This shows that the system was negatively affected when the battery operation was paused in order to measure the Ce(IV) concentration and regenerate the positive electrolyte.

Therefore, the development of an electrolyte regeneration method that can be implemented without pausing battery operation is desirable. One solution to solve this problem is to use another electrolyte reservoir for the electrolyte regeneration reaction to occur without the requirement to pause the charge-discharge cycle. The Ce(IV) concentration would first be measured and the required volume of H_2O_2 estimated based on the Ce(IV) concentration near the end of battery discharge. Then the battery would proceed to the next charge cycle without pause. During the subsequent battery charge, a certain portion of the positive electrolyte in the electrolyte tank could be transferred to the regeneration reservoir and a small amount of H_2O_2 added to reduce Ce(IV) back to Ce(III). The addition of H_2O_2 would be immediately stopped when the electrolyte in the reservoir becomes colourless to prevent the addition of any excess amount of H_2O_2 to the reservoir. Then the electrolyte in the reservoir would be transferred back to the electrolyte tank, followed by the transfer of a new portion of untreated positive electrolyte from the tank. This process would be repeated several times until the total required volume of H_2O_2 is completely added. In this way, the regeneration process could be operated without the need to pause the battery, while ensuring that H_2O_2 is introduced into the positive electrolyte. Another possible method to avoid the need of pausing for electrolyte regeneration relies on the use of equipment that enables the real-time measurements of Ce(IV) ions in the electrolyte, such as ion-selective electrodes and portable spectrophotometry-based devices. Once the Ce(IV) concentration in the electrolyte can be

determined at short time intervals (i.e. every 10 mins) regardless of battery charging or discharging, the amount of H_2O_2 solution needed to rebalance the electrolyte could be estimated accordingly and added to the electrolyte after each measurement. As such, the Ce(IV) concentration in the positive electrolyte can be precisely controlled throughout the battery operation to make sure no precipitation occur and the oxygen bubbles will not be likely to enter the cell and disturb electrode reaction due to small volume of H_2O_2 to be added.

In our studies, battery operation was also paused prior to positive electrolyte regeneration to ensure that the reaction was completed within the electrolyte tank and that O_2 bubbles generated during regeneration did not accumulate in the positive electrolyte and inhibit transfer of reactants and products to and from the positive electrode surface. This problem was exacerbated by the relatively small volumes of the negative and positive electrolyte (30 mL each) in our RFB, which were used partly for convenience to reduce the total number of charge-discharge cycles before changes in its capacity would become evident. Fortunately, this will not be a concern in a commercial-scale operation where the battery is operated with a high electrolyte volume-to-electrode surface area ratio. When a commercial-scale battery with a large electrolyte volume is operated, the Ce(IV) concentration will still be measured and the volume of H_2O_2 solution needed estimated near the end of battery discharge prior to regeneration, as was done in the current study. However, regeneration of the electrolyte in the positive reservoir tank could now be conducted during the charge step of the subsequent cycle without the need to pause the battery operation. Since the regeneration reaction is extremely fast and the total volume of the electrolyte is large, the reaction will be completed and the added H_2O_2 will be totally consumed before the electrolyte reaches the positive compartment of the battery. In this way, any disruption due to electrolyte regeneration would be avoided.

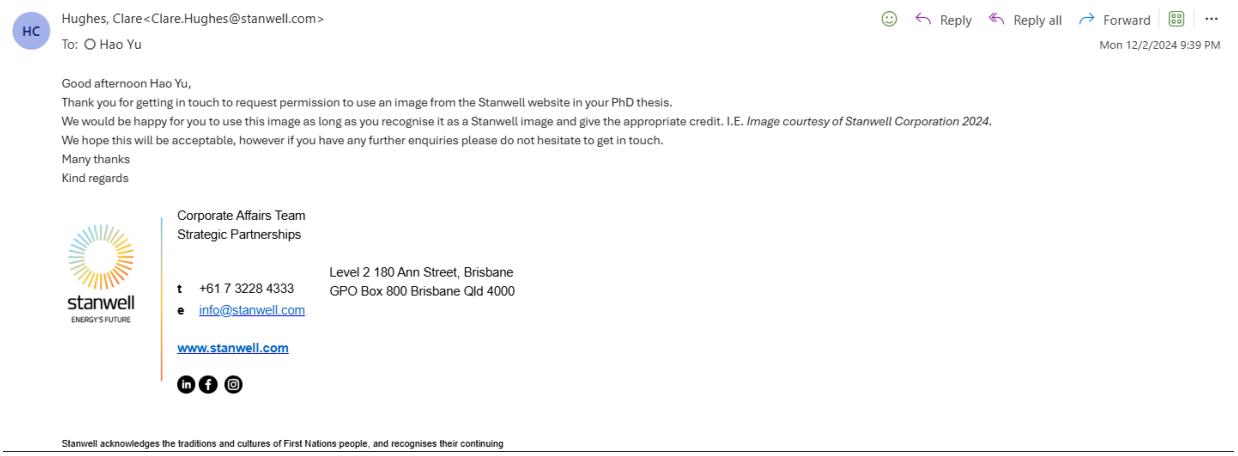
8.2.6 Low-cost positive electrode material

The Ce(III)/Ce(IV) redox couple exhibits good kinetics on Pt-Ti mesh and carbon felt electrodes. However, the high cost of platinum and low stability of carbon felt are major challenges for their use in commercial-scale applications. Therefore, the development of positive electrode materials that have both high electrochemical activity for the Ce(III)/Ce(IV) redox couple and excellent

stability in a highly acidic and oxidizing environment would be very beneficial for the commercial application of Ce-based RFBs. The commercially available material termed Ebonex® with the general formula of Ti_nO_{2n-1} ($3<n<10$) has been shown to exhibit high conductivity, chemical stability and catalytic activity.[118] It has also been shown that Ebonex® coated with only 2 mg/cm^2 of Pt can achieve similar electrochemical activity for a number of redox couples as does a pure Pt electrode.[120] Consequently, a 3-D mesh electrode made with pure Ebonex® or Ebonex® coated with only a minimal amount of Pt could be very promising to replace the Pt-Ti mesh electrodes with a Pt loading of 7 mg/cm^2 to reduce the total cost when used for large-scale applications. In addition, since Ebonex® is a mechanically strong and hard material similar to a ceramic material, it can be manufactured into a micromesh structure with very high specific surface area, which is promising for use as positive electrode in Ce-based RFBs.

Letters of Copyright Permission

Letter of permission for Figure 1.1



Hughes, Clare<Clare.Hughes@stanwell.com>
To: Hao Yu

Reply Reply all Forward
Mon 12/2/2024 9:39 PM

Good afternoon Hao Yu,
Thank you for getting in touch to request permission to use an image from the Stanwell website in your PhD thesis.
We would be happy for you to use this image as long as you recognise it as a Stanwell image and give the appropriate credit. I.E. *Image courtesy of Stanwell Corporation 2024.*
We hope this will be acceptable, however if you have any further enquiries please do not hesitate to get in touch.
Many thanks
Kind regards

Corporate Affairs Team
Strategic Partnerships

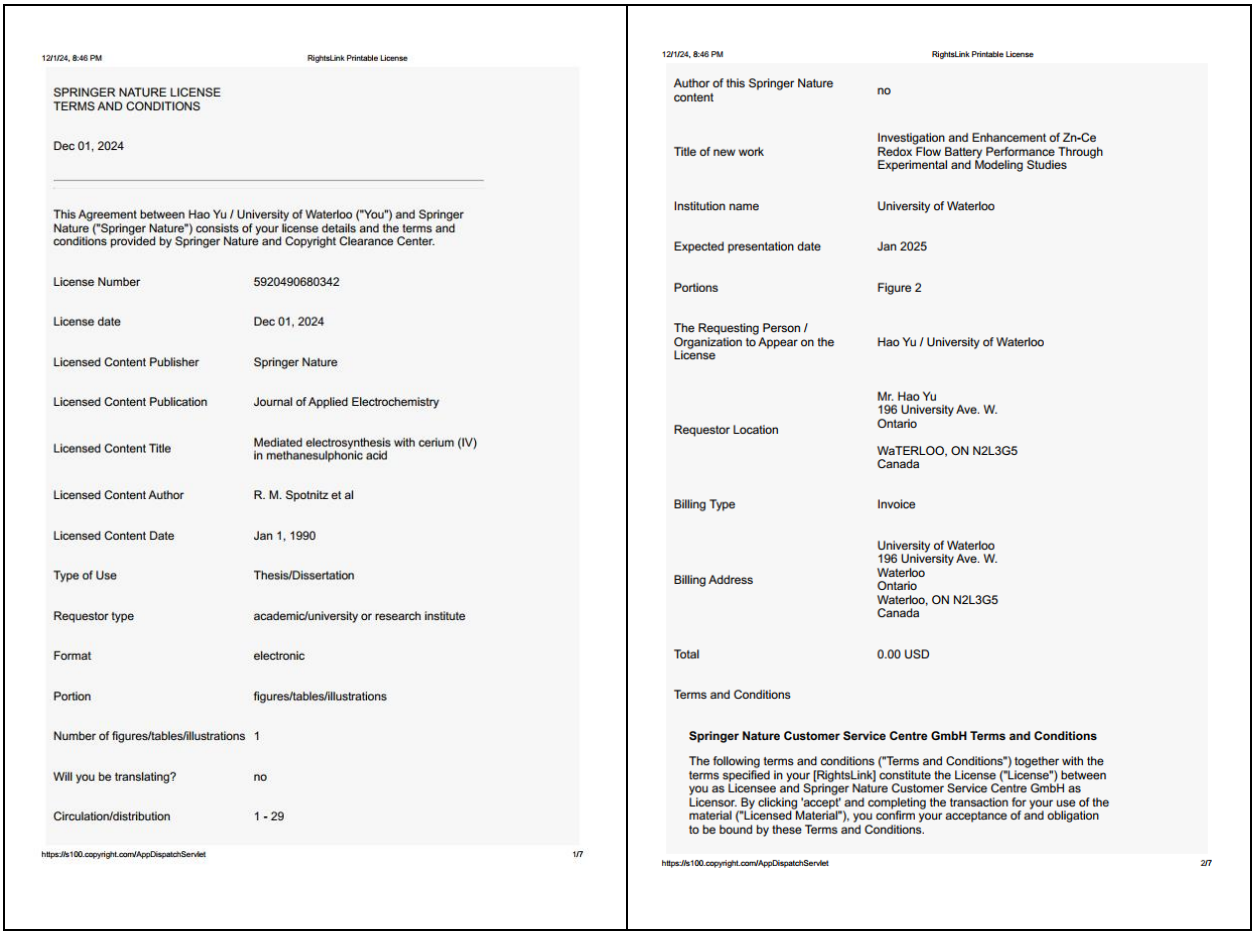
t +61 7 3228 4333
e info@stanwell.com

Level 2 180 Ann Street, Brisbane
GPO Box 800 Brisbane Qld 4000

www.stanwell.com

Stanwell acknowledges the traditions and cultures of First Nations people, and recognises their continuing

Letter of permission for Figure 2.2



12/1/24, 8:46 PM RightsLink Printable License

SPRINGER NATURE LICENSE
TERMS AND CONDITIONS

Dec 01, 2024

This Agreement between Hao Yu / University of Waterloo ("You") and Springer Nature ("Springer Nature") consists of your license details and the terms and conditions provided by Springer Nature and Copyright Clearance Center.

License Number	5920490680342
License date	Dec 01, 2024
Licensed Content Publisher	Springer Nature
Licensed Content Publication	Journal of Applied Electrochemistry
Licensed Content Title	Mediated electrosynthesis with cerium (IV) in methanesulphonic acid
Licensed Content Author	R. M. Spotnitz et al
Licensed Content Date	Jan 1, 1990
Type of Use	Thesis/Dissertation
Requestor type	academic/university or research institute
Format	electronic
Portion	figures/tables/illustrations
Number of figures/tables/illustrations	1
Will you be translating?	no
Circulation/distribution	1 - 29

https://s100.copyright.com/AppDispatchServlet 1/7

12/1/24, 8:46 PM RightsLink Printable License

Author of this Springer Nature content	no
Title of new work	Investigation and Enhancement of Zn-Ce Redox Flow Battery Performance Through Experimental and Modeling Studies
Institution name	University of Waterloo
Expected presentation date	Jan 2025
Portions	Figure 2
The Requesting Person / Organization to Appear on the License	Hao Yu / University of Waterloo
Requestor Location	Mr. Hao Yu 196 University Ave. W. Ontario WaTERLOO, ON N2L3G5 Canada
Billing Type	Invoice
Billing Address	University of Waterloo 196 University Ave. W. Waterloo Ontario Waterloo, ON N2L3G5 Canada
Total	0.00 USD

Terms and Conditions

Springer Nature Customer Service Centre GmbH Terms and Conditions

The following terms and conditions ("Terms and Conditions") together with the terms specified in your [RightsLink] constitute the License ("License") between you as Licensee and Springer Nature Customer Service Centre GmbH as Licensor. By clicking 'accept' and completing the transaction for your use of the material ("Licensed Material"), you confirm your acceptance of and obligation to be bound by these Terms and Conditions.

https://s100.copyright.com/AppDispatchServlet 2/7

Letter of permission for Figure 3.2

Order Completed

Thank you for your order.

This Agreement between Hao Yu ("You") and Elsevier ("Elsevier") consists of your license details and the terms and conditions provided by Elsevier and Copyright Clearance Center.

Your confirmation email will contain your order number for future reference.

Printable Details

License Number	5951461390992
License date	Jan 17, 2025

Licensed Content

Licensed Content Publisher	Elsevier
Licensed Content Publication	Applied Energy
Licensed Content Title	Improvement of zinc-cerium redox flow batteries using mixed methanesulfonate-chloride negative electrolyte
Licensed Content Author	Kiana Amini,Mark D. Pritzker
Licensed Content Date	Dec 1, 2019
Licensed Content Volume	255
Licensed Content Issue	n/a
Licensed Content Pages	1

Order Details

Type of Use	reuse in a thesis/dissertation
Portion	figures/tables/illustrations
Number of figures/tables/illustrations	1
Format	both print and electronic
Are you the author of this Elsevier article?	No
Will you be translating?	No

About Your Work

Title of new work	Investigation and Enhancement of Zn-Ce Redox Flow Battery Performance Through Experimental and Modeling Studies
Institution name	University of Waterloo
Expected presentation date	Jan 2025

Additional Data

Portions	Figure 1.
The Requesting Person / Organization to Appear on the License	Hao Yu

Requestor Location

Requestor Location	Mr. Hao Yu 200 University Ave. W Waterloo, ON N2L 3G1 Canada

Tax Details

Publisher Tax ID	GB 494 6272 12

Letter of permission for Figure 3.3

Order Completed

Thank you for your order.

This Agreement between Hao Yu ("You") and Elsevier ("Elsevier") consists of your license details and the terms and conditions provided by Elsevier and Copyright Clearance Center.

Your confirmation email will contain your order number for future reference.

Printable Details

License Number	5951470206019
License date	Jan 17, 2025

Licensed Content

Licensed Content Publisher	Elsevier
Licensed Content Publication	Electrochimica Acta
Licensed Content Title	Life-cycle analysis of zinc-cerium redox flow batteries
Licensed Content Author	Kiana Amini,Mark D. Pritzker
Licensed Content Date	Oct 1, 2020
Licensed Content Volume	356
Licensed Content Issue	n/a
Licensed Content Pages	1

Order Details

Type of Use	reuse in a thesis/dissertation
Portion	figures/tables/illustrations
Number of figures/tables/illustrations	1
Format	both print and electronic
Are you the author of this Elsevier article?	No
Will you be translating?	No

About Your Work

Title of new work	Investigation and Enhancement of Zn-Ce Redox Flow Battery Performance Through Experimental and Modeling Studies
Institution name	University of Waterloo
Expected presentation date	Jan 2025

Additional Data

Portions	Figure 1.
The Requesting Person / Organization to Appear on the License	Hao Yu

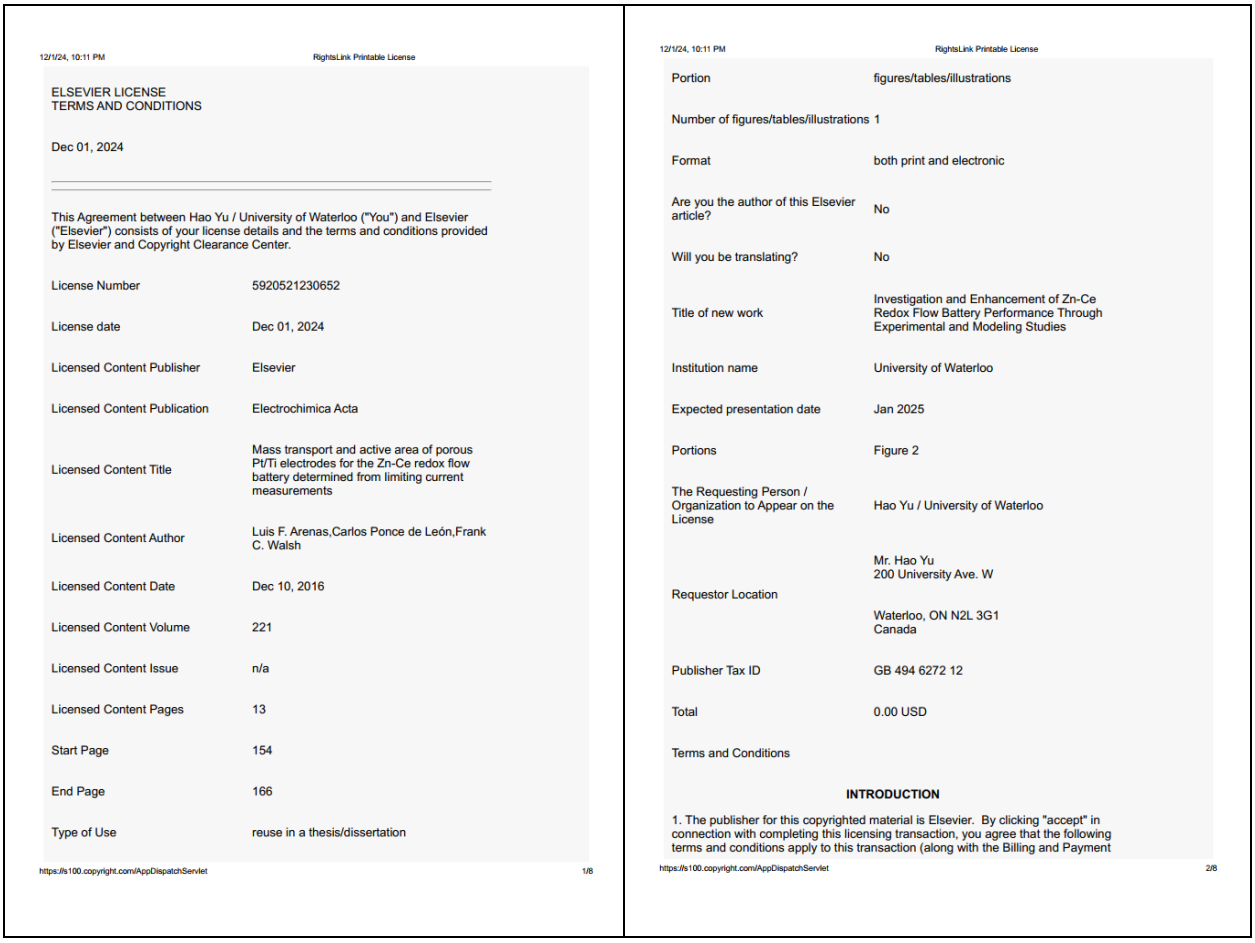
Requestor Location

Requestor Location	Mr. Hao Yu 200 University Ave. W Waterloo, ON N2L 3G1 Canada

Tax Details

Publisher Tax ID	GB 494 6272 12

Letter of permission for Figure 7.13



12/1/24, 10:11 PM RightsLink Printable License

ELSEVIER LICENSE
TERMS AND CONDITIONS

Dec 01, 2024

This Agreement between Hao Yu / University of Waterloo ("You") and Elsevier ("Elsevier") consists of your license details and the terms and conditions provided by Elsevier and Copyright Clearance Center.

License Number	5920521230652
License date	Dec 01, 2024
Licensed Content Publisher	Elsevier
Licensed Content Publication	Electrochimica Acta
Licensed Content Title	Mass transport and active area of porous Pt/Ti electrodes for the Zn-Ce redox flow battery determined from limiting current measurements
Licensed Content Author	Luis F. Arenas,Carlos Ponce de León,Frank C. Walsh
Licensed Content Date	Dec 10, 2016
Licensed Content Volume	221
Licensed Content Issue	n/a
Licensed Content Pages	13
Start Page	154
End Page	166
Type of Use	reuse in a thesis/dissertation

https://s100.copyright.com/AppDispatchServlet 1/8

12/1/24, 10:11 PM RightsLink Printable License

Portion	figures/tables/illustrations
Number of figures/tables/illustrations	1
Format	both print and electronic
Are you the author of this Elsevier article?	No
Will you be translating?	No
Title of new work	Investigation and Enhancement of Zn-Ce Redox Flow Battery Performance Through Experimental and Modeling Studies
Institution name	University of Waterloo
Expected presentation date	Jan 2025
Portions	Figure 2
The Requesting Person / Organization to Appear on the License	Hao Yu / University of Waterloo
Requestor Location	Mr. Hao Yu 200 University Ave. W Waterloo, ON N2L 3G1 Canada
Publisher Tax ID	GB 494 6272 12
Total	0.00 USD

Terms and Conditions

INTRODUCTION

1. The publisher for this copyrighted material is Elsevier. By clicking "accept" in connection with completing this licensing transaction, you agree that the following terms and conditions apply to this transaction (along with the Billing and Payment

https://s100.copyright.com/AppDispatchServlet 2/8

References

(1) Ritchie, H.; Rosado, P.; Roser, M. Breakdown of Carbon Dioxide, Methane and Nitrous Oxide Emissions by Sector. *Our World in Data* **2024**.

(2) *Data point: renewable energy use is on the rise*. https://impact.economist.com/sustainability/net-zero-and-energy/data-point-renewable-energy-use-is-on-the-rise (accessed 2024-06-05).

(3) *World renewable energy cities - CDP*. https://www.cdp.net/en/cities/world-renewable-energy-cities (accessed 2024-06-05).

(4) Canada, N. R. *About renewable energy in Canada*. https://natural-resources.canada.ca/our-natural-resources/energy-sources-distribution/renewable-energy/about-renewable-energy-canada/7295 (accessed 2024-06-05).

(5) Sánchez-Díez, E.; Ventosa, E.; Guarnieri, M.; Trovò, A.; Flox, C.; Marcilla, R.; Soavi, F.; Mazur, P.; Aranzabe, E.; Ferret, R. Redox Flow Batteries: Status and Perspective towards Sustainable Stationary Energy Storage. *Journal of Power Sources* **2021**, *481*, 228804. https://doi.org/10.1016/j.jpowsour.2020.228804.

(6) *The National Academies Summit on America's Energy Future: Summary of a Meeting*; National Academies Press, 2008.

(7) Chen, H.; Cong, T. N.; Yang, W.; Tan, C.; Li, Y.; Ding, Y. Progress in Electrical Energy Storage System: A Critical Review. *Progress in Natural Science* **2009**, *19* (3), 291–312. https://doi.org/10.1016/j.pnsc.2008.07.014.

(8) Poli, N.; Schäffer, M.; Trovò, A.; Noack, J.; Guarnieri, M.; Fischer, P. Novel Electrolyte Rebalancing Method for Vanadium Redox Flow Batteries. *Chemical Engineering Journal* **2021**, *405*, 126583. https://doi.org/10.1016/j.cej.2020.126583.

(9) Bai, J.; Liu, F.; Xue, X.; Wei, W.; Chen, L.; Wang, G.; Mei, S. Modelling and Control of Advanced Adiabatic Compressed Air Energy Storage under Power Tracking Mode Considering Off-Design Generating Conditions. *Energy* **2021**, *218*, 119525. https://doi.org/10.1016/j.energy.2020.119525.

(10) Zobaa, A. F. *Energy Storage: Technologies and Applications*; BoD – Books on Demand, 2013.

(11) Deane, J. P.; Ó Gallachóir, B. P.; McKeogh, E. J. Techno-Economic Review of Existing and New Pumped Hydro Energy Storage Plant. *Renewable and Sustainable Energy Reviews* **2010**, *14* (4), 1293–1302. https://doi.org/10.1016/j.rser.2009.11.015.

(12) Weber, A. Z.; Mench, M. M.; Meyers, J. P.; Ross, P. N.; Gostick, J. T.; Liu, Q. Redox Flow Batteries: A Review. *J Appl Electrochem* **2011**, *41* (10), 1137–1164. https://doi.org/10.1007/s10800-011-0348-2.

(13) A. Shah, A.; Leung, P.; Xu, Q.; Sui, P.-C.; Xing, W. Electrochemical Theory and Overview of Redox Flow Batteries. In *New Paradigms in Flow Battery Modelling*; A. Shah, A., Leung, P., Xu, Q., Sui, P.-C., Xing, W., Eds.; Springer Nature: Singapore, 2023; pp 19–64. https://doi.org/10.1007/978-981-99-2524-7_2.

(14) Dreghorn, B. *Go with the flow: What are flow batteries, and how do they work?*. What's Watt. https://whatswatt.com.au/go-with-the-flow-what-are-flow-batteries-and-how-do-they-work/ (accessed 2024-06-06).

(15) Piro, N. A.; Robinson, J. R.; Walsh, P. J.; Schelter, E. J. The Electrochemical Behavior of Cerium(III/IV) Complexes: Thermodynamics, Kinetics and Applications in Synthesis. *Coordination Chemistry Reviews* **2014**, *260*, 21–36. https://doi.org/10.1016/j.ccr.2013.08.034.

(16) Brown, M. A.; Paulenova, A.; Gelis, A. V. Aqueous Complexation of Thorium(IV), Uranium(IV), Neptunium(IV), Plutonium(III/IV), and Cerium(III/IV) with DTPA. *Inorg. Chem.* **2012**, *51* (14), 7741–7748. https://doi.org/10.1021/ic300757k.

(17) Paulenova, A.; Creager, S. E.; Navratil, J. D.; Wei, Y. Redox Potentials and Kinetics of the Ce3+/Ce4+ Redox Reaction and Solubility of Cerium Sulfates in Sulfuric Acid Solutions. *Journal of Power Sources* **2002**, *109* (2), 431–438. https://doi.org/10.1016/S0378-7753(02)00109-X.

(18) Haynes, W. M. *CRC Handbook of Chemistry and Physics*, 97th ed.; CRC Press: Boca Raton, 2016. https://doi.org/10.1201/9781315380476.

(19) Binnemans, K. Chapter 229 Applications of Tetravalent Cerium Compounds. In *Handbook on the Physics and Chemistry of Rare Earths*; Gschneidner, K. A., Bunzli, J.-C. G., Pecharsky, V. K., Eds.; Elsevier, 2006; Vol. 36, pp 281–392. https://doi.org/10.1016/S0168-1273(06)36003-5.

(20) Li, Y.; Geysens, P.; Zhang, X.; Sniekers, J.; Fransaer, J.; Binnemans, K.; Vankelecom, I. F. J. Cerium-Containing Complexes for Low-Cost, Non-Aqueous Redox Flow Batteries (RFBs). *Journal of Power Sources* **2020**, *450*, 227634. https://doi.org/10.1016/j.jpowsour.2019.227634.

(21) Ebner, S.; Spirk, S.; Stern, T.; Mair-Bauernfeind, C. How Green Are Redox Flow Batteries? *ChemSusChem* **2023**, *16* (8), e202201818. https://doi.org/10.1002/cssc.202201818.

(22) Arenas, L. F.; Walsh, F. C.; León, C. P. de. The Importance of Cell Geometry and Electrolyte Properties to the Cell Potential of Zn-Ce Hybrid Flow Batteries. *J. Electrochem. Soc.* **2015**, *163* (1), A5170. https://doi.org/10.1149/2.0261601jes.

(23) Wen, Y.; Neville, T. P.; Jorge Sobrido, A.; Shearing, P. R.; Brett, D. J. L.; Jervis, R. Bismuth Concentration Influenced Competition between Electrochemical Reactions in the All-Vanadium Redox Flow Battery. *Journal of Power Sources* **2023**, *566*, 232861. https://doi.org/10.1016/j.jpowsour.2023.232861.

(24) Wei, L.; Zhao, T. S.; Xu, Q.; Zhou, X. L.; Zhang, Z. H. In-Situ Investigation of Hydrogen Evolution Behavior in Vanadium Redox Flow Batteries. *Applied Energy* **2017**, *190*, 1112–1118. https://doi.org/10.1016/j.apenergy.2017.01.039.

(25) Jayathilake, B. S.; Plichta, E. J.; Hendrickson, M. A.; Narayanan, S. R. Improvements to the Coulombic Efficiency of the Iron Electrode for an All-Iron Redox-Flow Battery. *J. Electrochem. Soc.* **2018**, *165* (9), A1630. https://doi.org/10.1149/2.0451809jes.

(26) Banik, S. J.; Akolkar, R. Suppressing Dendrite Growth during Zinc Electrodeposition by PEG-200 Additive. *J. Electrochem. Soc.* **2013**, *160* (11), D519. https://doi.org/10.1149/2.040311jes.

(27) Wilcox, G. D.; Mitchell, P. J. Electrolyte Additives for Zinc-Anoded Secondary Cells I. Brighteners, Levellers and Complexants. *Journal of Power Sources* **1989**, *28* (4), 345–359. https://doi.org/10.1016/0378-7753(89)80064-3.

(28) Ein-Eli, Y.; Auinat, M.; Starosvetsky, D. Electrochemical and Surface Studies of Zinc in Alkaline Solutions Containing Organic Corrosion Inhibitors. *Journal of Power Sources* **2003**, *114* (2), 330–337. https://doi.org/10.1016/S0378-7753(02)00598-0.

(29) Wang, J. M.; Zhang, L.; Zhang, C.; Zhang, J. Q. Effects of Bismuth Ion and Tetrabutylammonium Bromide on the Dendritic Growth of Zinc in Alkaline Zincate Solutions. *Journal of Power Sources* **2001**, *102* (1), 139–143. https://doi.org/10.1016/S0378-7753(01)00789-3.

(30) Mansfeld, F.; Gilman, S. The Effect of Lead Ions on the Dissolution and Deposition Characteristics of a Zinc Single Crystal in 6 N KOH. *J. Electrochem. Soc.* **1970**, *117* (5), 588. https://doi.org/10.1149/1.2407584.

(31) Arenas, L. F.; Walsh, F. C.; Ponce de León, C. Zinc–Cerium and Related Cerium-Based Flow Batteries: Progress and Challenges. In *Flow Batteries*; John Wiley & Sons, Ltd, 2023; pp 819–835. https://doi.org/10.1002/9783527832767.ch36.

(32) Yu, H.; Pritzker, M.; Gostick, J. Use of Mixed Methanesulfonic Acid/Sulfuric Acid as Positive Supporting Electrolyte in Zn-Ce Redox Flow Battery. *J. Electrochem. Soc.* **2023**, *170* (2), 020536. https://doi.org/10.1149/1945-7111/acb8dd.

(33) Nikiforidis, G.; Daoud, W. A. Effect of Mixed Acid Media on the Positive Side of the Hybrid Zinc-Cerium Redox Flow Battery. *Electrochimica Acta* **2014**, *141*, 255–262. https://doi.org/10.1016/j.electacta.2014.06.142.

(34) Xie, Z.; Liu, Q.; Chang, Z.; Zhang, X. The Developments and Challenges of Cerium Half-Cell in Zinc–Cerium Redox Flow Battery for Energy Storage. *Electrochimica Acta* **2013**, *90*, 695–704. https://doi.org/10.1016/j.electacta.2012.12.066.

(35) Jirabovornwisut, T.; Arpornwichanop, A. A Review on the Electrolyte Imbalance in Vanadium Redox Flow Batteries. *International Journal of Hydrogen Energy* **2019**, *44* (45), 24485–24509. https://doi.org/10.1016/j.ijhydene.2019.07.106.

(36) Wang, B.; Zhao, L.; Ge, K.; Xu, W.; Chen, R.; Deng, S. A Novel High-Efficiency Integrated System Combining a Thermally Regenerative Electrochemical Cycle and a Flow Battery. *Journal of Materials Chemistry A* **2024**. https://doi.org/10.1039/D4TA03715D.

(37) Leung, P. K.; Ponce-de-León, C.; Low, C. T. J.; Shah, A. A.; Walsh, F. C. Characterization of a Zinc–Cerium Flow Battery. *Journal of Power Sources* **2011**, *196* (11), 5174–5185. https://doi.org/10.1016/j.jpowsour.2011.01.095.

(38) Amini, K.; Pritzker, M. D. Life-Cycle Analysis of Zinc-Cerium Redox Flow Batteries. *Electrochimica Acta* **2020**, *356*, 136785.

(39) Amini, K.; Pritzker, M. D. A Two-Dimensional Transient Model for a Zinc-Cerium Redox Flow Battery Validated by Extensive Experimental Data. *Journal of Power Sources* **2021**, *506*, 230237.

(40) Amini, K. Experimental and Modeling Study of Zinc-Cerium Redox Flow Batteries. **2021**.

(41) Kangro, D. W. Method for Storing Electrical Energy. DE914264C, June 28, 1949. https://patents.google.com/patent/DE914264C/en (accessed 2024-07-31).

(42) Posner, A. M. Redox Fuel Cell. *Fuel; (United Kingdom)* **1955**, *34:3*.

(43) Pieper, H. Zur Frage Der Speicherung von Elektrischer Energie in Flüssigkeiten. PhD Thesis, 1958.

(44) Thaller, L. H. *Electrically Rechargeable Redox Flow Cells*; 1974; pp 924–928.

(45) Lim, H. S.; Lackner, A. M.; Knechtli, R. C. Zinc-Bromine Secondary Battery. *J. Electrochem. Soc.* **1977**, *124* (8), 1154. https://doi.org/10.1149/1.2133517.

(46) Sum, E.; Skyllas-Kazacos, M. A Study of the V(II)/V(III) Redox Couple for Redox Flow Cell Applications. *Journal of Power Sources* **1985**, *15* (2), 179–190. https://doi.org/10.1016/0378-7753(85)80071-9.

(47) Jing, M.; Wei, Z.; Su, W.; He, H.; Fan, X.; Qin, Y.; Liu, J.; Yan, C. Improved Electrochemical Performance for Vanadium Flow Battery by Optimizing the Concentration of the Electrolyte. *Journal of Power Sources* **2016**, *324*, 215–223. https://doi.org/10.1016/j.jpowsour.2016.05.099.

(48) Liao, J. B.; Lu, M. Z.; Chu, Y. Q.; Wang, J. L. Ultra-Low Vanadium Ion Diffusion Amphoteric Ion-Exchange Membranes for All-Vanadium Redox Flow Batteries. *Journal of Power Sources* **2015**, *282*, 241–247. https://doi.org/10.1016/j.jpowsour.2015.02.025.

(49) Hwang, G.-J.; Kim, S.-W.; In, D.-M.; Lee, D.-Y.; Ryu, C.-H. Application of the Commercial Ion Exchange Membranes in the All-Vanadium Redox Flow Battery. *Journal of Industrial and Engineering Chemistry* **2018**, *60*, 360–365. https://doi.org/10.1016/j.jiec.2017.11.023.

(50) Wu, Y.; Holze, R. Electrocatalysis at Electrodes for Vanadium Redox Flow Batteries. *Batteries* **2018**, *4* (3), 47. https://doi.org/10.3390/batteries4030047.

(51) Park, S.-K.; Shim, J.; Yang, J. H.; Jin, C.-S.; Lee, B. S.; Lee, Y.-S.; Shin, K.-H.; Jeon, J.-D. The Influence of Compressed Carbon Felt Electrodes on the Performance of a Vanadium Redox Flow Battery. *Electrochimica Acta* **2014**, *116*, 447–452. https://doi.org/10.1016/j.electacta.2013.11.073.

(52) Al-Yasiri, M.; Park, J. A Novel Cell Design of Vanadium Redox Flow Batteries for Enhancing Energy and Power Performance. *Applied Energy* **2018**, *222*, 530–539. https://doi.org/10.1016/j.apenergy.2018.04.025.

(53) Hruska, L. W.; Savinell, R. F. Investigation of Factors Affecting Performance of the Iron-Redox Battery. *J. Electrochem. Soc.* **1981**, *128* (1), 18. https://doi.org/10.1149/1.2127366.

(54) Matsuda, Y.; Tanaka, K.; Okada, M.; Takasu, Y.; Morita, M.; Matsumura-Inoue, T. A Rechargeable Redox Battery Utilizing Ruthenium Complexes with Non-Aqueous Organic Electrolyte. *J Appl Electrochem* **1988**, *18* (6), 909–914. https://doi.org/10.1007/BF01016050.

(55) Wen, Y. H.; Cheng, J.; Ma, P. H.; Yang, Y. S. Bifunctional Redox Flow Battery-1 V(III)/V(II)–Glyoxal(O2) System. *Electrochimica Acta* **2008**, *53* (9), 3514–3522. https://doi.org/10.1016/j.electacta.2007.11.073.

(56) Wen, Y. H.; Cheng, J.; Xun, Y.; Ma, P. H.; Yang, Y. S. Bifunctional Redox Flow Battery: 2. V(III)/V(II)–l-Cystine(O2) System. *Electrochimica Acta* **2008**, *53* (20), 6018–6023. https://doi.org/10.1016/j.electacta.2008.03.026.

(57) Liu, Q.; Sleightholme, A. E. S.; Shinkle, A. A.; Li, Y.; Thompson, L. T. Non-Aqueous Vanadium Acetylacetonate Electrolyte for Redox Flow Batteries. *Electrochemistry Communications* **2009**, *11* (12), 2312–2315. https://doi.org/10.1016/j.elecom.2009.10.006.

(58) Hazza, A.; Pletcher, D.; Wills, R. A Novel Flow Battery: A Lead Acid Battery Based on an Electrolyte with Soluble Lead(Ii) Part I. Preliminary Studies. *Physical Chemistry Chemical Physics* **2004**, *6* (8), 1773–1778. https://doi.org/10.1039/B401115E.

(59) Clarke, R.; Dougherty, B.; Harrison, S.; Millington, P.; Mohanta, S. Cerium Batteries. US20040202925A1, October 14, 2004. https://patents.google.com/patent/US20040202925A1/en (accessed 2024-10-09).

(60) Walsh, F. C.; Ponce de Léon, C.; Berlouis, L.; Nikiforidis, G.; Arenas-Martínez, L. F.; Hodgson, D.; Hall, D. The Development of Zn–Ce Hybrid Redox Flow Batteries for Energy Storage and Their Continuing Challenges. *ChemPlusChem* **2015**, *80* (2), 288–311. https://doi.org/10.1002/cplu.201402103.

(61) Nikiforidis, G.; Cartwright, R.; Hodgson, D.; Hall, D.; Berlouis, L. Factors Affecting the Performance of the Zn-Ce Redox Flow Battery. *Electrochimica Acta* **2014**, *140*, 139–144. https://doi.org/10.1016/j.electacta.2014.04.150.

(62) Xie, X.; Mushtaq, F.; Wang, Q.; Daoud, W. A. The Renaissance of the Zn-Ce Flow Battery: Dual-Membrane Configuration Enables Unprecedentedly High Efficiency. *ACS Energy Lett.* **2022**, *7* (10), 3484–3491. https://doi.org/10.1021/acsenergylett.2c01646.

(63) Berlouis, L.; Nikiforidis, G. Performance Characteristics of the Zn-Ce Hybrid Redox Flow Battery. *Meet. Abstr.* **2015**, *MA2015-03* (3), 666. https://doi.org/10.1149/MA2015-03/3/666.

(64) Huskinson, B.; Marshak, M. P.; Suh, C.; Er, S.; Gerhardt, M. R.; Galvin, C. J.; Chen, X.; Aspuru-Guzik, A.; Gordon, R. G.; Aziz, M. J. A Metal-Free Organic–Inorganic Aqueous Flow Battery. *Nature* **2014**, *505* (7482), 195–198. https://doi.org/10.1038/nature12909.

(65) Wei, Z.; Liu, D.; Hsu, C.; Liu, F. All-Vanadium Redox Photoelectrochemical Cell: An Approach to Store Solar Energy. *Electrochemistry Communications* **2014**, *45*, 79–82. https://doi.org/10.1016/j.elecom.2014.05.018.

(66) Peljo, P.; Lloyd, D.; Doan, N.; Majaneva, M.; Kontturi, K. Towards a Thermally Regenerative All-Copper Redox Flow Battery. *Physical Chemistry Chemical Physics* **2014**, *16* (7), 2831–2835. https://doi.org/10.1039/C3CP54585G.

(67) Maye, S.; H. Girault, H.; Peljo, P. Thermally Regenerative Copper Nanoslurry Flow Batteries for Heat-to-Power Conversion with Low-Grade Thermal Energy. *Energy & Environmental Science* **2020**, *13* (7), 2191–2199. https://doi.org/10.1039/D0EE01590C.

(68) Santos, M. S. S.; Peixoto, L.; Azevedo, J.; Monteiro, R. A. R.; Dias-Ferreira, C.; Alves, M. M.; Mendes, A. Microbially-Charged Electrochemical Fuel for Energy Storage in a Redox Flow Cell. *Journal of Power Sources* **2020**, *445*, 227307. https://doi.org/10.1016/j.jpowsour.2019.227307.

(69) Rychcik, M.; Skyllas-Kazacos, M. Characteristics of a New All-Vanadium Redox Flow Battery. *Journal of Power Sources* **1988**, *22* (1), 59–67. https://doi.org/10.1016/0378-7753(88)80005-3.

(70) Lourenssen, K.; Williams, J.; Ahmadpour, F.; Clemmer, R.; Tasnim, S. Vanadium Redox Flow Batteries: A Comprehensive Review. *Journal of Energy Storage* **2019**, *25*, 100844. https://doi.org/10.1016/j.est.2019.100844.

(71) Zhao, P.; Zhang, H.; Zhou, H.; Chen, J.; Gao, S.; Yi, B. Characteristics and Performance of 10 kW Class All-Vanadium Redox-Flow Battery Stack. *Journal of Power Sources* **2006**, *162* (2), 1416–1420. https://doi.org/10.1016/j.jpowsour.2006.08.016.

(72) Rahman, F.; Skyllas-Kazacos, M. Solubility of Vanadyl Sulfate in Concentrated Sulfuric Acid Solutions. *Journal of Power Sources* **1998**, *72* (2), 105–110. https://doi.org/10.1016/S0378-7753(97)02692-X.

(73) Zhang, Y.; Xi, J.; Liu, L.; Wu, Z. Boosting the Thermal Stability of Electrolytes in Vanadium Redox Flow Batteries via 1-Hydroxyethane-1,1-Diphosphonic Acid. *J Appl Electrochem* **2020**, *50* (2), 255–264. https://doi.org/10.1007/s10800-019-01384-1.

(74) Li, L.; Kim, S.; Wang, W.; Vijayakumar, M.; Nie, Z.; Chen, B.; Zhang, J.; Xia, G.; Hu, J.; Graff, G.; Liu, J.; Yang, Z. A Stable Vanadium Redox-Flow Battery with High Energy Density for Large-Scale Energy Storage. *Advanced Energy Materials* **2011**, *1* (3), 394–400. https://doi.org/10.1002/aenm.201100008.

(75) Hagedorn, N. *NASA Redox Storage System Development Project.*; DOE/NASA/12726-24, NASA-TM-83677, 6472995; 1984; p DOE/NASA/12726-24, NASA-TM-83677, 6472995. https://doi.org/10.2172/6472995.

(76) *US Geological Survey & Orienteering S: Mineral commodity... - Google Scholar*. https://scholar.google.com/scholar_lookup?title=Mineral%20Commodity%20Summaries%202020&publication_year=2020&author=US%20Geological%20Survey (accessed 2024-06-17).

(77) Schulte, R. F.; Bryden, B. N. Mineral Industry Surveys. **2016**.

(78) *Review of the Development of First-Generation Redox Flow Batteries: Iron-Chromium System - Sun - 2022 - ChemSusChem - Wiley Online Library*. https://chemistry-europe.onlinelibrary.wiley.com/doi/full/10.1002/cssc.202101798 (accessed 2024-06-18).

(79) Lopez-Atalaya, M.; Codina, G.; Perez, J. R.; Vazquez, J. L.; Aldaz, A. Optimization Studies on a Fe/Cr Redox Flow Battery. *Journal of Power Sources* **1992**, *39* (2), 147–154. https://doi.org/10.1016/0378-7753(92)80133-V.

(80) Bae, C.-H.; Roberts, E. P. L.; Dryfe, R. A. W. Chromium Redox Couples for Application to Redox Flow Batteries. *Electrochimica Acta* **2002**, *48* (3), 279–287. https://doi.org/10.1016/S0013-4686(02)00649-7.

(81) Zeng, Y. K.; Zhou, X. L.; Zeng, L.; Yan, X. H.; Zhao, T. S. Performance Enhancement of Iron-Chromium Redox Flow Batteries by Employing Interdigitated Flow Fields. *Journal of Power Sources* **2016**, *327*, 258–264. https://doi.org/10.1016/j.jpowsour.2016.07.066.

(82) Su, L.; Kowalski, J. A.; Carroll, K. J.; Brushett, F. R. Recent Developments and Trends in Redox Flow Batteries. In *Rechargeable Batteries: Materials, Technologies and New Trends*;

Zhang, Z., Zhang, S. S., Eds.; Springer International Publishing: Cham, 2015; pp 673–712. https://doi.org/10.1007/978-3-319-15458-9_24.

(83) Huskinson, B.; Marshak, M. P.; Gerhardt, M. R.; Aziz, M. J. Cycling of a Quinone-Bromide Flow Battery for Large-Scale Electrochemical Energy Storage. *ECS Trans.* **2014**, *61* (37), 27. https://doi.org/10.1149/06137.0027ecst.

(84) Li, Z.; Pan, M. S.; Su, L.; Tsai, P.-C.; Badel, A. F.; Valle, J. M.; Eiler, S. L.; Xiang, K.; Brushett, F. R.; Chiang, Y.-M. Air-Breathing Aqueous Sulfur Flow Battery for Ultralow-Cost Long-Duration Electrical Storage. *Joule* **2017**, *1* (2), 306–327. https://doi.org/10.1016/j.joule.2017.08.007.

(85) Shin, K.; Lee, J.-H.; Heo, J.; Kim, H.-T. Current Status and Challenges for Practical Flowless Zn–Br Batteries. *Current Opinion in Electrochemistry* **2022**, *32*, 100898. https://doi.org/10.1016/j.coelec.2021.100898.

(86) Bonaldo, C.; Poli, N. Vanadium Redox Flow Batteries: Characteristics and Economic Value. In *New Metropolitan Perspectives*; Calabrò, F., Della Spina, L., Piñeira Mantiñán, M. J., Eds.; Springer International Publishing: Cham, 2022; pp 1721–1731. https://doi.org/10.1007/978-3-031-06825-6_166.

(87) Passerini, S.; Bresser, D.; Moretti, A.; Varzi, A. *Batteries: Present and Future Energy Storage Challenges*; John Wiley & Sons, 2020.

(88) Exchange, T. L. M. *LME Zinc | London Metal Exchange*. Lme. https://www.lme.com/Metals/Non-ferrous/LME-Zinc (accessed 2024-10-24).

(89) Crotty, D. Zinc Alloy Plating for the Automotive Industry. *Metal Finishing* **1996**, *94* (9), 54–58. https://doi.org/10.1016/0026-0576(96)82103-9.

(90) Gong, K.; Fang, Q.; Gu, S.; Yau Li, S. F.; Yan, Y. Nonaqueous Redox-Flow Batteries: Organic Solvents, Supporting Electrolytes, and Redox Pairs. *Energy & Environmental Science* **2015**, *8* (12), 3515–3530. https://doi.org/10.1039/C5EE02341F.

(91) Lowenheim, F. A.; Society, A. E. *Electroplating*; McGraw-Hill, 1978.

(92) Díaz-Arista, P.; Meas, Y.; Ortega, R.; Trejo, G. Electrochemical and AFM Study of Zn Electrodeposition in the Presence of Benzylideneacetone in a Chloride-Based Acidic Bath. *J Appl Electrochem* **2005**, *35* (2), 217–227. https://doi.org/10.1007/s10800-004-6304-7.

(93) Trejo, G.; B, R. O.; Meas, Y.; Ozil, P.; Chainet, E.; Nguyen, B. Nucleation and Growth of Zinc from Chloride Concentrated Solutions. *J. Electrochem. Soc.* **1998**, *145* (12), 4090. https://doi.org/10.1149/1.1838919.

(94) Hull, R. O.; Wernlund, C. J. Cyanide Zinc Plating Baths. *Trans. Electrochem. Soc.* **1941**, *80* (1), 407. https://doi.org/10.1149/1.3071347.

(95) Graham, A. K. A Study of Cyanide Zinc Plating Baths Using the Aluminum Mercury Zinc Anode. *Trans. Electrochem. Soc.* **1933**, *63* (1), 121. https://doi.org/10.1149/1.3493801.

(96) Zheng, X.; Ahmad, T.; Chen, W. Challenges and Strategies on Zn Electrodeposition for Stable Zn-Ion Batteries. *Energy Storage Materials* **2021**, *39*, 365–394. https://doi.org/10.1016/j.ensm.2021.04.027.

(97) Zuo, Y.; Wang, K.; Pei, P.; Wei, M.; Liu, X.; Xiao, Y.; Zhang, P. Zinc Dendrite Growth and Inhibition Strategies. *Materials Today Energy* **2021**, *20*, 100692. https://doi.org/10.1016/j.mtener.2021.100692.

(98) Despić, A. R.; Jovanović, Dj.; Rakić, T. Kinetics and Mechanism of Deposition of Zinc from Zincate in Concentrated Alkali Hydroxide Solutions. *Electrochimica Acta* **1976**, *21* (1), 63–77. https://doi.org/10.1016/0013-4686(76)85111-0.

(99) Kim, J. T.; Jorné, J. The Kinetics and Mass Transfer of Zinc Electrode in Acidic Zinc-Chloride Solution. *J. Electrochem. Soc.* **1980**, *127* (1), 8. https://doi.org/10.1149/1.2129646.

(100) Sorour, N.; Zhang, W.; Ghali, E.; Houlachi, G. A Review of Organic Additives in Zinc Electrodeposition Process (Performance and Evaluation). *Hydrometallurgy* **2017**, *171*, 320–332. https://doi.org/10.1016/j.hydromet.2017.06.004.

(101) Boto, K. Organic Additives in Zinc Electroplating. *Electrodeposition and Surface Treatment* **1975**, *3* (2), 77–95. https://doi.org/10.1016/0300-9416(75)90048-6.

(102) Wang, N.; Wan, H.; Duan, J.; Wang, X.; Tao, L.; Zhang, J.; Wang, H. A Review of Zinc-Based Battery from Alkaline to Acid. *Materials Today Advances* **2021**, *11*, 100149. https://doi.org/10.1016/j.mtadv.2021.100149.

(103) Suzuki, Y.; Nankawa, T.; Francis, A. J.; Ohnuki, T. Redox Behavior of Ce(IV)/Ce(III) in the Presence of Nitrilotriacetic Acid: A Surrogate Study for An(IV)/An(III) Redox Behavior. *Radiochimica Acta* **2010**, *98* (7), 397–402. https://doi.org/10.1524/ract.2010.1735.

(104) Xu, J.; Radkov, E.; Ziegler, M.; Raymond, K. N. Plutonium(IV) Sequestration: Structural and Thermodynamic Evaluation of the Extraordinarily Stable Cerium(IV) Hydroxypyridinonate Complexes. *Inorganic Chemistry* **2000**, *39* (18), 4156–4164. https://doi.org/10.1021/ic000063i.

(105) Smith, G. F.; Getz, C. A. Cerate Oxidimetry. *Ind. Eng. Chem. Anal. Ed.* **1938**, *10* (4), 191–195. https://doi.org/10.1021/ac50120a006.

(106) Sroor, F.; Edelmann, F. T. Tetravalent Chemistry Inorganic; 2012.

(107) Fang, B.; Iwasa, S.; Wei, Y.; Arai, T.; Kumagai, M. A Study of the Ce(III)/Ce(IV) Redox Couple for Redox Flow Battery Application. *Electrochimica Acta* **2002**, *47* (24), 3971–3976. https://doi.org/10.1016/S0013-4686(02)00370-5.

(108) Xiong, F.; Zhou, D.; Xie, Z.; Chen, Y. A Study of the Ce3+/Ce4+ Redox Couple in Sulfamic Acid for Redox Battery Application. *Applied Energy* **2012**, *99*, 291–296. https://doi.org/10.1016/j.apenergy.2012.05.021.

(109) Schmickler, W.; Nazmutdinov, R. R.; Wang, Q.; Daoud, W. A. Electrochemistry of Ce(IV)/Ce(III) Redox Couples in Mixed Solutions for Aqueous Flow Battery: Experimental and Molecular Modelling Study. *Electrochimica Acta* **2021**, *368*, 137601. https://doi.org/10.1016/j.electacta.2020.137601.

(110) Buchanan, C. A.; Herrera, D.; Balasubramanian, M.; Goldsmith, B. R.; Singh, N. Unveiling the Cerium(III)/(IV) Structures and Charge-Transfer Mechanism in Sulfuric Acid. *JACS Au* **2022**, *2* (12), 2742–2757. https://doi.org/10.1021/jacsau.2c00484.

(111) H. Randle, T.; T. Kuhn, A. Kinetics and Mechanism of the Cerium(IV)/Cerium(III) Redox Reaction on a Platinum Electrode. *Journal of the Chemical Society, Faraday Transactions 1: Physical Chemistry in Condensed Phases* **1983**, *79* (8), 1741–1756. https://doi.org/10.1039/F19837901741.

(112) Tong, J. Y.-P.; King, E. L. The Kinetics and Mechanism of the Reaction of Cerium (IV) and Chromium (III) [1,2]. *J. Am. Chem. Soc.* **1960**, *82* (15), 3805–3809. https://doi.org/10.1021/ja01500a001.

(113) Mackinnon, D. J.; Morrison, R. M.; Mouland, J. E.; Warren, P. E. The Effects of Antimony and Glue on Zinc Electrowinning from Kidd Creek Electrolyte. *J Appl Electrochem* **1990**, *20* (5), 728–736. https://doi.org/10.1007/BF01094298.

(114) Xu, M.; Ivey, D. G.; Xie, Z.; Qu, W. Rechargeable Zn-Air Batteries: Progress in Electrolyte Development and Cell Configuration Advancement. *Journal of Power Sources* **2015**, *283*, 358–371. https://doi.org/10.1016/j.jpowsour.2015.02.114.

(115) *Zinc Price Monthly Insights: Commodity Markets Review | YCharts*. https://ycharts.com/indicators/zinc_price_cmr (accessed 2024-11-17).

(116) *Cerium price today | Historical Cerium Price Charts | SMM Metal Market*. https://www.metal.com/Rare-Earth-Metals/201102250153 (accessed 2024-11-17).

(117) Leung, P. K.; Ponce de León, C.; Walsh, F. C. An Undivided Zinc–Cerium Redox Flow Battery Operating at Room Temperature (295 K). *Electrochemistry Communications* **2011**, *13* (8), 770–773. https://doi.org/10.1016/j.elecom.2011.04.011.

(118) Smith, J. R.; Walsh, F. C.; Clarke, R. L. Electrodes Based on Magnéli Phase Titanium Oxides: The Properties and Applications of Ebonex® Materials. *Journal of Applied Electrochemistry* **1998**, *28* (10), 1021–1033. https://doi.org/10.1023/A:1003469427858.

(119) Walsh, F. C.; Wills, R. G. A. The Continuing Development of Magnéli Phase Titanium Sub-Oxides and Ebonex® Electrodes. *Electrochimica Acta* **2010**, *55* (22), 6342–6351. https://doi.org/10.1016/j.electacta.2010.05.011.

(120) Farndon, E. E.; Pletcher, D. Studies of Platinized Ebonex® Electrodes. *Electrochimica Acta* **1997**, *42* (8), 1281–1285. https://doi.org/10.1016/S0013-4686(96)00299-X.

(121) Gernon, M. D.; Wu, M.; Buszta, T.; Janney, P. Environmental Benefits of Methanesulfonic Acid . Comparative Properties and Advantages. *Green Chemistry* **1999**, *1* (3), 127–140. https://doi.org/10.1039/A900157C.

(122) Leung, P. K.; Ponce-de-León, C.; Low, C. T. J.; Walsh, F. C. Zinc Deposition and Dissolution in Methanesulfonic Acid onto a Carbon Composite Electrode as the Negative Electrode Reactions in a Hybrid Redox Flow Battery. *Electrochimica Acta* **2011**, *56* (18), 6536–6546. https://doi.org/10.1016/j.electacta.2011.04.111.

(123) Baker, S. C.; Kelly, D. P.; Murrell, J. C. Microbial Degradation of Methanesulphonic Acid: A Missing Link in the Biogeochemical Sulphur Cycle. *Nature* **1991**, *350* (6319), 627–628. https://doi.org/10.1038/350627a0.

(124) Kelly, D. P.; Murrell, J. C. Microbial Metabolism of Methanesulfonic Acid. *Arch Microbiol* **1999**, *172* (6), 341–348. https://doi.org/10.1007/s002030050770.

(125) Kreh, R. P.; Spotnitz, R. M.; Lundquist, J. T. Mediated Electrochemical Synthesis of Aromatic Aldehydes, Ketones, and Quinones Using Ceric Methanesulfonate. *J. Org. Chem.* **1989**, *54* (7), 1526–1531. https://doi.org/10.1021/jo00268a010.

(126) Raju, T.; Basha, C. A. Process Parameters and Kinetics for the Electrochemical Generation of Cerium(IV) Methanesulphonate from Cerium(III) Methanesulphonate. *Ind. Eng. Chem. Res.* **2008**, *47* (22), 8947–8952. https://doi.org/10.1021/ie701727x.

(127) Spotnitz, R. M.; Kreh, R. P.; Lundquist, J. T.; Press, P. J. Mediated Electrosynthesis with Cerium (IV) in Methanesulphonic Acid. *J Appl Electrochem* **1990**, *20* (2), 209–215. https://doi.org/10.1007/BF01033596.

(128) Chen, R.; Hempelmann, R. Ionic Liquid-Mediated Aqueous Redox Flow Batteries for High Voltage Applications. *Electrochemistry Communications* **2016**, *70*, 56–59. https://doi.org/10.1016/j.elecom.2016.07.003.

(129) Amini, K.; Pritzker, M. D. Improvement of Zinc-Cerium Redox Flow Batteries Using Mixed Methanesulfonate-Chloride Negative Electrolyte. *Applied energy* **2019**, *255*, 113894.

(130) Amini, K.; Pritzker, M. D. Electrodeposition and Electrodissolution of Zinc in Mixed Methanesulfonate-Based Electrolytes. *Electrochimica Acta* **2018**, *268*, 448–461. https://doi.org/10.1016/j.electacta.2018.02.087.

(131) Wada, T.; Hirashima, T. Progress in Polyethylene Separators for Lead–Acid Batteries. *Journal of Power Sources* **2002**, *107* (2), 201–210. https://doi.org/10.1016/S0378-7753(01)01006-0.

(132) Zhao, W.; Pan, Z.; Zhang, Y.; Liu, Y.; Dou, H.; Shi, Y.; Zuo, Z.; Zhang, B.; Chen, J.; Zhao, X.; Yang, X. Tailoring Coordination in Conventional Ether-Based Electrolytes for Reversible Magnesium-Metal Anodes. *Angewandte Chemie International Edition* **2022**, *61* (30), e202205187. https://doi.org/10.1002/anie.202205187.

(133) Dong, Y.; Miao, L.; Ma, G.; Di, S.; Wang, Y.; Wang, L.; Xu, J.; Zhang, N. Non-Concentrated Aqueous Electrolytes with Organic Solvent Additives for Stable Zinc Batteries. *Chem. Sci.* **2021**, *12* (16), 5843–5852. https://doi.org/10.1039/D0SC06734B.

(134) Kao-ian, W.; Nguyen, M. T.; Yonezawa, T.; Pornprasertsuk, R.; Qin, J.; Siwamogsatham, S.; Kheawhom, S. Highly Stable Rechargeable Zinc-Ion Battery Using Dimethyl Sulfoxide Electrolyte. *Materials Today Energy* **2021**, *21*, 100738. https://doi.org/10.1016/j.mtener.2021.100738.

(135) Dou, Q.; Lei, S.; Wang, D.-W.; Zhang, Q.; Xiao, D.; Guo, H.; Wang, A.; Yang, H.; Li, Y.; Shi, S.; Yan, X. Safe and High-Rate Supercapacitors Based on an "Acetonitrile/Water in Salt" Hybrid Electrolyte. *Energy Environ. Sci.* **2018**, *11* (11), 3212–3219. https://doi.org/10.1039/C8EE01040D.

(136) Ma, G.; Miao, L.; Dong, Y.; Yuan, W.; Nie, X.; Di, S.; Wang, Y.; Wang, L.; Zhang, N. Reshaping the Electrolyte Structure and Interface Chemistry for Stable Aqueous Zinc Batteries. *Energy Storage Materials* **2022**, *47*, 203–210. https://doi.org/10.1016/j.ensm.2022.02.019.

(137) Chen, J.; Zhao, W.; Jiang, J.; Zhao, X.; Zheng, S.; Pan, Z.; Yang, X. Challenges and Perspectives of Hydrogen Evolution-Free Aqueous Zn-Ion Batteries. *Energy Storage Materials* **2023**, *59*, 102767. https://doi.org/10.1016/j.ensm.2023.04.006.

(138) Zhao, L.; Chen, B.; Wu, J.; Wang, D. Study of Electrochemically Active Carbon, Ga2O3 and Bi2O3 as Negative Additives for Valve-Regulated Lead-Acid Batteries Working under High-Rate, Partial-State-of-Charge Conditions. *Journal of Power Sources* **2014**, *248*, 1–5. https://doi.org/10.1016/j.jpowsour.2013.09.056.

(139) Chen, D.; Wang, S.; Xiao, M.; Meng, Y. Synthesis and Characterization of Novel Sulfonated Poly(Arylene Thioether) Ionomers for Vanadium Redox Flow Battery Applications. *Energy Environ. Sci.* **2010**, *3* (5), 622–628. https://doi.org/10.1039/B917117G.

(140) Yun, S.; Parrondo, J.; Ramani, V. A Vanadium–Cerium Redox Flow Battery with an Anion-Exchange Membrane Separator. *ChemPlusChem* **2015**, *80* (2), 412–421. https://doi.org/10.1002/cplu.201402096.

(141) Gu, S.; Gong, K.; Z. Yan, E.; Yan, Y. A Multiple Ion-Exchange Membrane Design for Redox Flow Batteries. *Energy & Environmental Science* **2014**, *7* (9), 2986–2998. https://doi.org/10.1039/C4EE00165F.

(142) Amstutz, V.; E. Toghill, K.; Powlesland, F.; Vrubel, H.; Comninellis, C.; Hu, X.; H. Girault, H. Renewable Hydrogen Generation from a Dual-Circuit Redox Flow Battery. *Energy & Environmental Science* **2014**, *7* (7), 2350–2358. https://doi.org/10.1039/C4EE00098F.

(143) Sigler, P. B.; Master, B. J. THE HYDROGEN PEROXIDE-INDUCED Ce*(III)-Ce(IV) EXCHANGE SYSTEM. *Journal of the American Chemical Society (U.S.)* **1957**, *Vol: 79*. https://doi.org/10.1021/ja01581a003.

(144) Sworski, T. J.; Mahlman, H. A.; Matthews, R. W. Reduction of Cerium(IV) by Hydrogen Peroxide. Dependence of Reaction Rate on Hammett's Acidity Function. *J. Phys. Chem.* **1971**, *75* (2), 250–255. https://doi.org/10.1021/j100672a012.

(145) Czapski, G.; Bielski, B. H. J.; Sutin, N. THE KINETICS OF THE OXIDATION OF HYDROGEN PEROXIDE BY CERIUM(IV)[1]. *J. Phys. Chem.* **1963**, *67* (1), 201–203. https://doi.org/10.1021/j100795a503.

(146) Zhang, M.; Moore, M.; Watson, J. S.; Zawodzinski, T. A.; Counce, R. M. Capital Cost Sensitivity Analysis of an All-Vanadium Redox-Flow Battery. *J. Electrochem. Soc.* **2012**, *159* (8), A1183. https://doi.org/10.1149/2.041208jes.

(147) Viswanathan, V.; Crawford, A.; Stephenson, D.; Kim, S.; Wang, W.; Li, B.; Coffey, G.; Thomsen, E.; Graff, G.; Balducci, P.; Kintner-Meyer, M.; Sprenkle, V. Cost and Performance Model for Redox Flow Batteries. *Journal of Power Sources* **2014**, *247*, 1040–1051. https://doi.org/10.1016/j.jpowsour.2012.12.023.

(148) Noack, J.; Wietschel, L.; Roznyatovskaya, N.; Pinkwart, K.; Tübke, J. Techno-Economic Modeling and Analysis of Redox Flow Battery Systems. *Energies* **2016**, *9* (8), 627. https://doi.org/10.3390/en9080627.

(149) Al-Fetlawi, H.; Shah, A. A.; Walsh, F. C. Non-Isothermal Modelling of the All-Vanadium Redox Flow Battery. *Electrochimica Acta* **2009**, *55* (1), 78–89. https://doi.org/10.1016/j.electacta.2009.08.009.

(150) Shah, A. A.; Tangirala, R.; Singh, R.; Wills, R. G. A.; Walsh, F. C. A Dynamic Unit Cell Model for the All-Vanadium Flow Battery. *J. Electrochem. Soc.* **2011**, *158* (6), A671. https://doi.org/10.1149/1.3561426.

(151) Tang, A.; Ting, S.; Bao, J.; Skyllas-Kazacos, M. Thermal Modelling and Simulation of the All-Vanadium Redox Flow Battery. *Journal of Power Sources* **2012**, *203*, 165–176. https://doi.org/10.1016/j.jpowsour.2011.11.079.

(152) Scamman, D. P.; Reade, G. W.; Roberts, E. P. L. Numerical Modelling of a Bromide-Polysulphide Redox Flow Battery. Part 2: Evaluation of a Utility-Scale System. *Journal of Power Sources* **2009**, *189* (2), 1231–1239. https://doi.org/10.1016/j.jpowsour.2009.01.076.

(153) Xing, F.; Zhang, H.; Ma, X. Shunt Current Loss of the Vanadium Redox Flow Battery. *Journal of Power Sources* **2011**, *196* (24), 10753–10757. https://doi.org/10.1016/j.jpowsour.2011.08.033.

(154) Fedkiw, P. S.; Watts, R. W. A Mathematical Model for the Iron/Chromium Redox Battery. *J. Electrochem. Soc.* **1984**, *131* (4), 701. https://doi.org/10.1149/1.2115676.

(155) Evans, T. I.; White, R. E. A Review of Mathematical Modeling of the Zinc/Bromine Flow Cell and Battery. *J. Electrochem. Soc.* **1987**, *134* (11), 2725. https://doi.org/10.1149/1.2100277.

(156) Lee, J.; Selman, J. R. Effects of Separator and Terminal on the Current Distribution in Parallel-Plate Electrochemical Flow Reactors. *J. Electrochem. Soc.* **1982**, *129* (8), 1670. https://doi.org/10.1149/1.2124247.

(157) Shah, A. A.; Watt-Smith, M. J.; Walsh, F. C. A Dynamic Performance Model for Redox-Flow Batteries Involving Soluble Species. *Electrochimica Acta* **2008**, *53* (27), 8087–8100. https://doi.org/10.1016/j.electacta.2008.05.067.

(158) You, D.; Zhang, H.; Chen, J. A Simple Model for the Vanadium Redox Battery. *Electrochimica Acta* **2009**, *54* (27), 6827–6836. https://doi.org/10.1016/j.electacta.2009.06.086.

(159) Ma, X.; Zhang, H.; Xing, F. A Three-Dimensional Model for Negative Half Cell of the Vanadium Redox Flow Battery. *Electrochimica Acta* **2011**, *58*, 238–246. https://doi.org/10.1016/j.electacta.2011.09.042.

(160) Knehr, K. W.; Agar, E.; Dennison, C. R.; Kalidindi, A. R.; Kumbur, E. C. A Transient Vanadium Flow Battery Model Incorporating Vanadium Crossover and Water Transport through the Membrane. *J. Electrochem. Soc.* **2012**, *159* (9), A1446–A1459. https://doi.org/10.1149/2.017209jes.

(161) König, S.; Suriyah, M. R.; Leibfried, T. Model Based Examination on Influence of Stack Series Connection and Pipe Diameters on Efficiency of Vanadium Redox Flow Batteries under Consideration of Shunt Currents. *Journal of Power Sources* **2015**, *281*, 272–284. https://doi.org/10.1016/j.jpowsour.2015.01.119.

(162) König, S.; Suriyah, M. R.; Leibfried, T. Innovative Model-Based Flow Rate Optimization for Vanadium Redox Flow Batteries. *Journal of Power Sources* **2016**, *333*, 134–144. https://doi.org/10.1016/j.jpowsour.2016.09.147.

(163) Tsushima, S.; Suzuki, T. Modeling and Simulation of Vanadium Redox Flow Battery with Interdigitated Flow Field for Optimizing Electrode Architecture. *J. Electrochem. Soc.* **2020**, *167* (2), 020553. https://doi.org/10.1149/1945-7111/ab6dd0.

(164) Qiu, G.; Joshi, A. S.; Dennison, C. R.; Knehr, K. W.; Kumbur, E. C.; Sun, Y. 3-D Pore-Scale Resolved Model for Coupled Species/Charge/Fluid Transport in a Vanadium Redox Flow

Battery. *Electrochimica Acta* **2012**, *64*, 46–64. https://doi.org/10.1016/j.electacta.2011.12.065.

(165) Qiu, G.; Dennison, C. R.; Knehr, K. W.; Kumbur, E. C.; Sun, Y. Pore-Scale Analysis of Effects of Electrode Morphology and Electrolyte Flow Conditions on Performance of Vanadium Redox Flow Batteries. *Journal of Power Sources* **2012**, *219*, 223–234. https://doi.org/10.1016/j.jpowsour.2012.07.042.

(166) Vijayakumar, M.; Li, L.; Graff, G.; Liu, J.; Zhang, H.; Yang, Z.; Hu, J. Z. Towards Understanding the Poor Thermal Stability of V5+ Electrolyte Solution in Vanadium Redox Flow Batteries. *Journal of Power Sources* **2011**, *196* (7), 3669–3672. https://doi.org/10.1016/j.jpowsour.2010.11.126.

(167) Vijayakumar, M.; Li, L.; Nie, Z.; Yang, Z.; Hu, J. Structure and Stability of Hexa-Aqua V(III) Cations in Vanadium Redox Flow Battery Electrolytes. *Phys. Chem. Chem. Phys.* **2012**, *14* (29), 10233–10242. https://doi.org/10.1039/C2CP40707H.

(168) Perry, M. L.; Saraidaridis, J. D.; Darling, R. M. Crossover Mitigation Strategies for Redox-Flow Batteries. *Current Opinion in Electrochemistry* **2020**, *21*, 311–318. https://doi.org/10.1016/j.coelec.2020.03.024.

(169) Chou, Y.-S.; Yen, S.-C.; Arpornwichanop, A.; Singh, B.; Chen, Y.-S. Mathematical Model to Study Vanadium Ion Crossover in an All-Vanadium Redox Flow Battery. *ACS Sustainable Chem. Eng.* **2021**, *9* (15), 5377–5387. https://doi.org/10.1021/acssuschemeng.1c00233.

(170) Darling, R. M.; Weber, A. Z.; Tucker, M. C.; Perry, M. L. The Influence of Electric Field on Crossover in Redox-Flow Batteries. *J. Electrochem. Soc.* **2015**, *163* (1), A5014. https://doi.org/10.1149/2.0031601jes.

(171) Yang, X.-G.; Ye, Q.; Cheng, P.; Zhao, T. S. Effects of the Electric Field on Ion Crossover in Vanadium Redox Flow Batteries. *Applied Energy* **2015**, *145*, 306–319. https://doi.org/10.1016/j.apenergy.2015.02.038.

(172) Amini, K.; Pritzker, M. D. In Situ Polarization Study of Zinc–Cerium Redox Flow Batteries. *Journal of Power Sources* **2020**, *471*, 228463.

(173) Banks, C. V.; O'Laughlin, J. W. Determination of Cerium and Chromium in Cerium-Chromium-Uranium Mixtures. *Anal. Chem.* **1956**, *28* (8), 1338–1340. https://doi.org/10.1021/ac60116a037.

(174) Marple, T. L.; Przybylowicz, E. P.; Hume, D. N. Photometric Titration of Cerium(III). *Anal. Chem.* **1956**, *28* (12), 1892–1894. https://doi.org/10.1021/ac60120a023.

(175) Medalia, L. S. "COLOR STANDARDS" FOR THE COLORIMETRIC MEASUREMENT OF H-ION CONCENTRATION pH 1.2 TO pH 9.8. *J Bacteriol* **1920**, *5* (5), 441–468. https://doi.org/10.1128/jb.5.5.441-468.1920.

(176) Rolia, E.; Dutrizac, J. E. The Determination of Free Acid in Zinc Processing Solutions. *Canadian Metallurgical Quarterly* **1984**, *23* (2), 159–167. https://doi.org/10.1179/cmq.1984.23.2.159.

(177) Wei, Y.; Fang, B.; Arai, T.; Kumagai, M. Electrolytic Oxidation of Ce(III) in Nitric Acid and Sulfuric Acid Media Using a Flow Type Cell. *J Appl Electrochem* **2005**, *35* (6), 561–566. https://doi.org/10.1007/s10800-005-1820-7.

(178) Brodt, G.; Haas, J.; Hesse, W.; Jäger, H.-U. Method for Electrolytic Galvanizing Using Electrolytes Containing Alkane Sulphonic Acid. US6811673B2, November 2, 2004. https://patents.google.com/patent/US6811673B2/en (accessed 2024-11-18).

(179) Yu, H.; Pritzker, M.; Gostick, J. Improving Performance of Hybrid Zn–Ce Redox Flow Battery by Controlling Ion Crossover and Use of Mixed Acid Positive Electrolyte. *J Appl Electrochem* **2024**. https://doi.org/10.1007/s10800-024-02193-x.

(180) Sun, C.; Chen, J.; Zhang, H.; Han, X.; Luo, Q. Investigations on Transfer of Water and Vanadium Ions across Nafion Membrane in an Operating Vanadium Redox Flow Battery. *Journal of Power Sources* **2010**, *195* (3), 890–897. https://doi.org/10.1016/j.jpowsour.2009.08.041.

(181) Cecchetti, M.; Toja, F.; Casalegno, A.; Zago, M. A Comprehensive Experimental and Modelling Approach for the Evaluation of Cross-over Fluxes in Vanadium Redox Flow Battery. *Journal of Energy Storage* **2023**, *68*, 107846. https://doi.org/10.1016/j.est.2023.107846.

(182) Zhao, N.; Platt, A.; Riley, H.; Qiao, R.; Neagu, R.; Shi, Z. Strategy towards High Ion Selectivity Membranes for All-Vanadium Redox Flow Batteries. *Journal of Energy Storage* **2023**, *72*, 108321. https://doi.org/10.1016/j.est.2023.108321.

(183) Jiang, B.; Wu, L.; Yu, L.; Qiu, X.; Xi, J. A Comparative Study of Nafion Series Membranes for Vanadium Redox Flow Batteries. *Journal of Membrane Science* **2016**, *510*, 18–26. https://doi.org/10.1016/j.memsci.2016.03.007.

(184) Xi, J.; Wu, Z.; Qiu, X.; Chen, L. Nafion/SiO2 Hybrid Membrane for Vanadium Redox Flow Battery. *Journal of Power Sources* **2007**, *166* (2), 531–536. https://doi.org/10.1016/j.jpowsour.2007.01.069.

(185) Skyllas-Kazacos, M.; Kazacos, M. State of Charge Monitoring Methods for Vanadium Redox Flow Battery Control. *Journal of Power Sources* **2011**, *196* (20), 8822–8827. https://doi.org/10.1016/j.jpowsour.2011.06.080.

(186) *Modeling Electrical Conductivity in Concentrated and Mixed-Solvent Electrolyte Solutions | Industrial & Engineering Chemistry Research*. https://pubs.acs.org/doi/full/10.1021/ie040144c (accessed 2024-11-18).

(187) Ding, M. S.; von Cresce, A.; Xu, K. Conductivity, Viscosity, and Their Correlation of a Super-Concentrated Aqueous Electrolyte. *J. Phys. Chem. C* **2017**, *121* (4), 2149–2153. https://doi.org/10.1021/acs.jpcc.6b12636.

(188) de Diego, A.; Usobiaga, A.; Fernández, L. A.; Madariaga, J. M. Application of the Electrical Conductivity of Concentrated Electrolyte Solutions to Industrial Process Control and Design: From Experimental Measurement towards Prediction through Modelling. *TrAC Trends in Analytical Chemistry* **2001**, *20* (2), 65–78. https://doi.org/10.1016/S0165-9936(00)00081-9.

(189) *Modification of Nafion® Membrane via a Sol-Gel Route for Vanadium Redox Flow Energy Storage Battery Applications - Huang - 2017 - Journal of Chemistry - Wiley Online Library*. https://onlinelibrary.wiley.com/doi/full/10.1155/2017/4590952 (accessed 2024-11-18).

(190) Mills, A.; McMurray, N. Kinetic Study of the Oxidation of Water by Ce IV Ions Mediated by Activated Ruthenium Dioxide Hydrate. *Journal of the Chemical Society, Faraday Transactions 1: Physical Chemistry in Condensed Phases* **1989**, *85* (8), 2055–2070. https://doi.org/10.1039/F19898502055.

(191) Bouchaud, B.; Balmain, J.; Bonnet, G.; Pedraza, F. pH-Distribution of Cerium Species in Aqueous Systems. *Journal of Rare Earths* **2012**, *30* (6), 559–562. https://doi.org/10.1016/S1002-0721(12)60091-X.

(192) Kok, M. D. R.; Jervis, R.; Tranter, T. G.; Sadeghi, M. A.; Brett, D. J. L.; Shearing, P. R.; Gostick, J. T. Mass Transfer in Fibrous Media with Varying Anisotropy for Flow Battery Electrodes: Direct Numerical Simulations with 3D X-Ray Computed Tomography. *Chemical Engineering Science* **2019**, *196*, 104–115. https://doi.org/10.1016/j.ces.2018.10.049.

(193) Al-Fetlawi, H.; Shah, A. A.; Walsh, F. C. Modelling the Effects of Oxygen Evolution in the All-Vanadium Redox Flow Battery. *Electrochimica Acta* **2010**, *55* (9), 3192–3205. https://doi.org/10.1016/j.electacta.2009.12.085.

(194) Cacciuttolo, Q.; Petit, M.; Pasquier, D. Fast Computing Flow Battery Modeling to Optimize the Choice of Electrolytes and Operating Conditions – Application to Aqueous Organic Electrolytes. *Electrochimica Acta* **2021**, *392*, 138961. https://doi.org/10.1016/j.electacta.2021.138961.

(195) Arenas, L. F.; Ponce de León, C.; Walsh, F. C. Pressure Drop through Platinized Titanium Porous Electrodes for Cerium-based Redox Flow Batteries. *AIChE Journal* **2018**, *64* (3), 1135–1146. https://doi.org/10.1002/aic.16000.

(196) Bernardi, D. M.; Verbrugge, M. W. Mathematical Model of a Gas Diffusion Electrode Bonded to a Polymer Electrolyte. *AIChE Journal* **1991**, *37* (8), 1151–1163. https://doi.org/10.1002/aic.690370805.

(197) Nikiforidis, G.; Berlouis, L.; Hall, D.; Hodgson, D. Evaluation of Carbon Composite Materials for the Negative Electrode in the Zinc–Cerium Redox Flow Cell. *Journal of Power Sources* **2012**, *206*, 497–503. https://doi.org/10.1016/j.jpowsour.2011.01.036.

(198) Leung, P. K.; Ponce de León, C.; Low, C. T. J.; Walsh, F. C. Ce(III)/Ce(IV) in Methanesulfonic Acid as the Positive Half Cell of a Redox Flow Battery. *Electrochimica Acta* **2011**, *56* (5), 2145–2153. https://doi.org/10.1016/j.electacta.2010.12.038.

(199) Nikiforidis, G. *Investigations of the zinc-cerium hybrid flow battery*.

(200) Lee, S. H.; Rasaiah, J. C. Proton Transfer and the Mobilities of the H+ and OH- Ions from Studies of a Dissociating Model for Water. *Journal of Chemical Physics* **2011**, *135* (12). https://doi.org/10.1063/1.3632990.

(201) *Yaws: Yaws" Handbook of thermodynamic and physical... - Google Scholar*. https://scholar.google.com/scholar_lookup?title=Handbook%20of%20Thermodynamic%20and%20Physical%20Properties%20of%20Chemical%20Compounds&publication_year=2003&author=C.L.%20Yaws&author=C.%20Gabbula (accessed 2024-11-10).

(202) Bratsch, S. G. Standard Electrode Potentials and Temperature Coefficients in Water at 298.15 K. *Journal of Physical and Chemical Reference Data* **1989**, *18* (1), 1–21. https://doi.org/10.1063/1.555839.

(203) Nzikou, J. M.; Aurousseau, M.; Lapicque, F. Electrochemical Investigations of the Ce(m)/Ce(Iv) Couple Related to a Ce(Iv)-Assisted Process for SO2/NOx Abatement. *Journal of Applied Electrochemistry* **1995**, *25* (10), 967–972. https://doi.org/10.1007/BF00241592.

(204) Simpson, G. D.; White, R. E. An Algebraic Model for a Zinc/Bromine Flow Cell. *J. Electrochem. Soc.* **1989**, *136* (8), 2137. https://doi.org/10.1149/1.2097226.

(205) Parsons, R. *Handbook of Electrochemical Constants*; Butterworths Scientific and Academic Press, 1959.

(206) Barton, G. W.; Scott, A. C. A Validated Mathematical Model for a Zinc Electrowinning Cell. *Journal of Applied Electrochemistry* **1992**, *22* (2), 104–115. https://doi.org/10.1007/BF01023811.

(207) Kriksunov, L. B.; Bunakova, L. V.; Zabusova, S. E.; Krishtalik, L. I. Anodic Oxygen Evolution Reaction at High Temperatures in Acid Solutions at Platinum. *Electrochimica Acta* **1994**, *39* (1), 137–142. https://doi.org/10.1016/0013-4686(94)85020-8.

(208) Springer, T. E.; Zawodzinski, T. A.; Gottesfeld, S. Polymer Electrolyte Fuel Cell Model. *J. Electrochem. Soc.* **1991**, *138* (8), 2334. https://doi.org/10.1149/1.2085971.

(209) Wei, X.; Desai, D.; Yadav, G. G.; Turney, D. E.; Couzis, A.; Banerjee, S. Impact of Anode Substrates on Electrodeposited Zinc over Cycling in Zinc-Anode Rechargeable Alkaline

Batteries. *Electrochimica Acta* **2016**, *212*, 603–613. https://doi.org/10.1016/j.electacta.2016.07.041.

(210) Arenas, L. F.; León, C. P. de; Walsh, F. C. Mass Transport and Active Area of Porous Pt/Ti Electrodes for the Zn-Ce Redox Flow Battery Determined from Limiting Current Measurements. *Electrochimica Acta* **2016**, *221*, 154–166. https://doi.org/10.1016/j.electacta.2016.10.097.

(211) Carta, R.; Palmas, S.; Polcaro, A. M.; Tola, G. Behaviour of a Carbon Felt Flow by Electrodes Part I: Mass Transfer Characteristics. *J Appl Electrochem* **1991**, *21* (9), 793–798. https://doi.org/10.1007/BF01402816.

(212) Lee, K. M.; Alizadeh, M.; Suzuki, T.; Tsushima, S.; Roberts, E. P. L.; Gostick, J. T. Multiphysics Simulation of Multi-Layered Fibrous Electrodes for the Vanadium Redox Flow Battery. *J. Electrochem. Soc.* **2024**, *171* (9), 090534. https://doi.org/10.1149/1945-7111/ad7c85.

(213) Reed, D.; Thomsen, E.; Viswanathan, V.; Wang, W.; Sprenkle, V. High Current Density Redox Flow Batteries for Stationary Electrical Energy Storate.

(214) Wang, H.; Pourmousavi, S. A.; Soong, W. L.; Zhang, X.; Ertugrul, N. Battery and Energy Management System for Vanadium Redox Flow Battery: A Critical Review and Recommendations. *Journal of Energy Storage* **2023**, *58*, 106384. https://doi.org/10.1016/j.est.2022.106384.

(215) Tian, Y.; Liu, M.; Zhou, X.; Huang, L.; Liu, Z.; An, B. Inhibition of Hydrogen Evolution Reaction on Polypyrrole-Modified Electrode in Acid Media. *J. Electrochem. Soc.* **2013**, *161* (3), E23. https://doi.org/10.1149/2.032403jes.

(216) Bayaguud, A.; Fu, Y.; Zhu, C. Interfacial Parasitic Reactions of Zinc Anodes in Zinc Ion Batteries: Underestimated Corrosion and Hydrogen Evolution Reactions and Their Suppression Strategies. *Journal of Energy Chemistry* **2022**, *64*, 246–262. https://doi.org/10.1016/j.jechem.2021.04.016.

Appendix

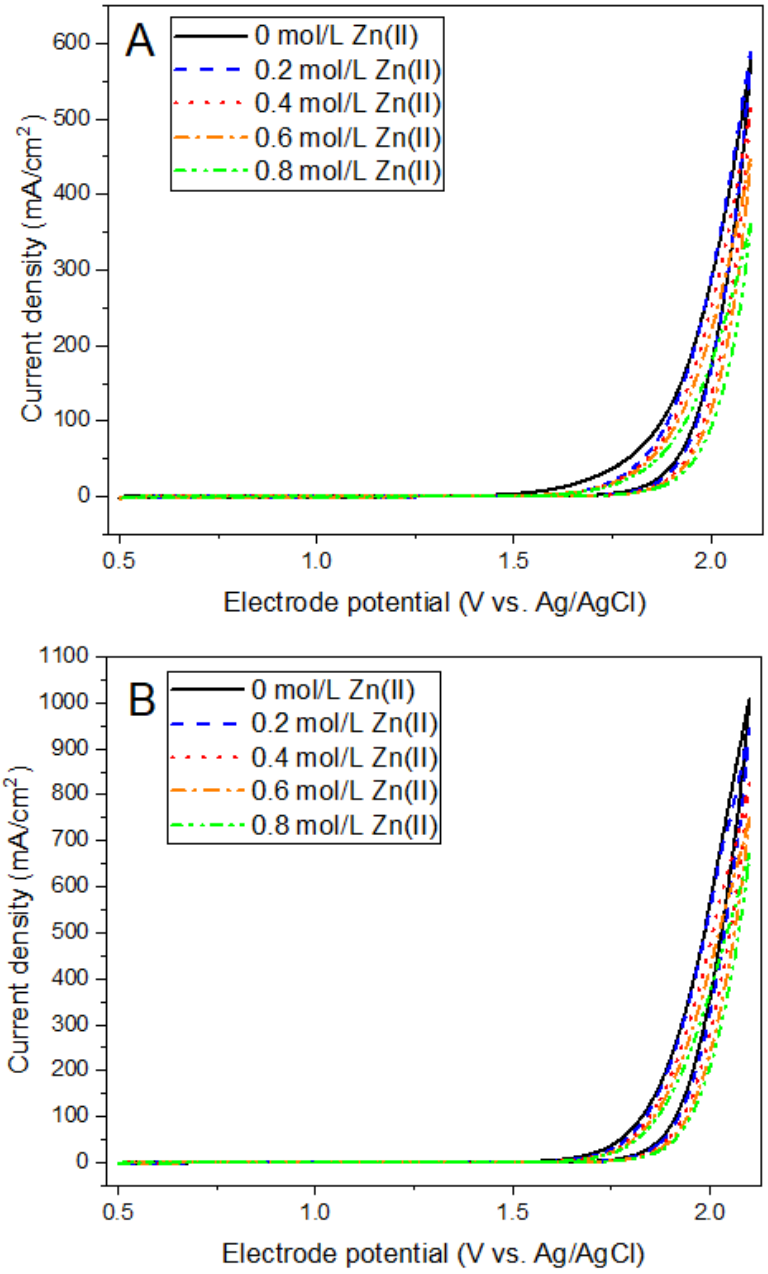


Figure S1. Effect of zinc(II) methanesulfonate addition on the cyclic voltammograms for the oxygen evolution reaction in (A) 4 mol/L MSA and (B) 2/0.5 MA in the absence of Ce(III)/Ce(IV) ions. Scan rate = 50 mV/s.

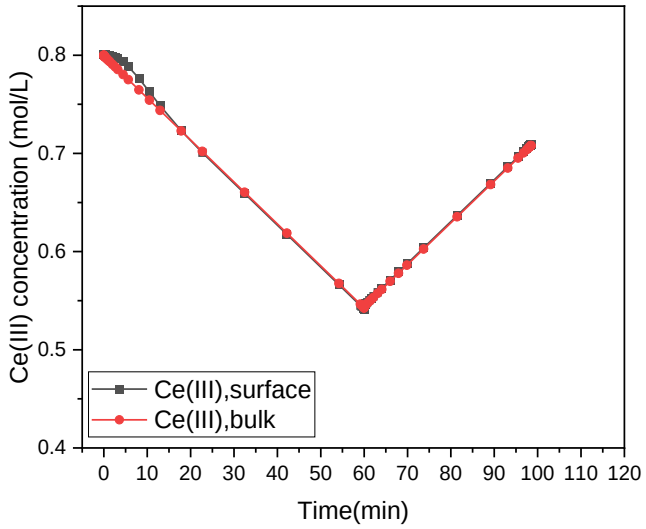


Figure S2. Comparison of computed surface and bulk Ce(III) concentrations in the positive compartment when Pi-Ti micromesh positive electrode is used.

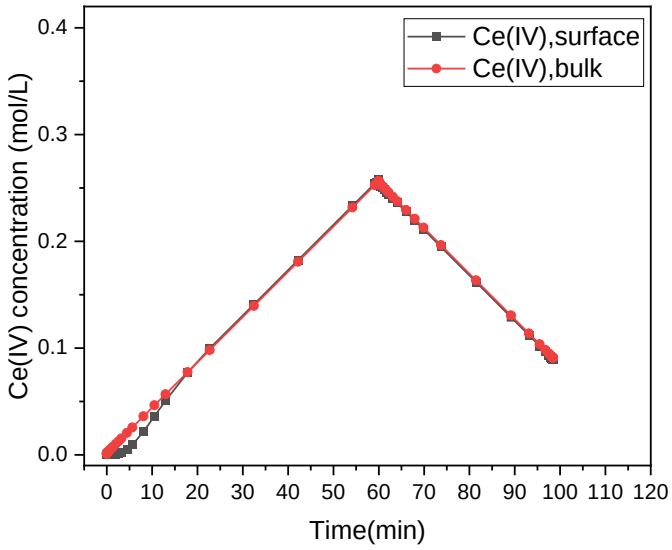


Figure S3. Comparison of computed surface and bulk Ce(IV) concentrations in the positive compartment when Pi-Ti micromesh positive electrode is used.